ON SCATTERING ANISOTROPY FOR ACCURATE MODELING OF RADIATION TRANSFER

by

BRIAN D. HUNTER

A dissertation submitted to the

Graduate School – New Brunswick

Rutgers, The State University of New Jersey

In partial fulfillment of the requirements

For the degree of

Doctor of Philosophy

Graduate Program in Mechanical and Aerospace Engineering

Written under the direction of

Dr. Zhixiong Guo

And approved by

_____

_____

_____

_____

New Brunswick, New Jersey

MAY, 2014

ABSTRACT OF THE DISSERTATION

On Scattering Anisotropy for Accurate Modeling of Radiation Transfer

By BRIAN D. HUNTER

Dissertation Director:

Dr. Zhixiong Guo

It is well known that the discrete-ordinates method (DOM) suffers from two shortcomings: 1) numerical smearing (or false scattering) error due to spatial discretization, and 2) ray effect error due to limited number of discrete angular directions. It is less aware that all numerical methods based on the discretization solution of the integral-differential equation of radiation transfer (ERT), such as the finite volume method (FVM), experience similar issues. In this dissertation, the existence of a third type of numerical error, termed “angular false scattering” for anisotropic scattering media, is revealed and presented for both DOM and FVM. In all practical applications, radiation scattering is anisotropic in nature. Angular discretization of anisotropy may not preserve the scattering phase-function asymmetry factor, resulting in an artificial alteration of medium scattering properties - angular false scattering.

Phase-function normalization was the prevailing approach in DOM to numerically conserve scattered energy. In this dissertation, this technique is employed, for the first time, to simultaneously conserve both scattered energy and asymmetry factor for both DOM and FVM. Traditionally, the solid-angle splitting approach was implemented to conserve scattered energy for FVM. It is found, however, that extremely high splitting levels are required to preserve asymmetry factor for strongly scattering media, substantially increasing computational cost. Here, two novel phase-function normalization techniques are developed for FVM and DOM radiation transfer analysis to specifically mitigate angular false scattering errors by simultaneously conserving scattered energy and asymmetry factor. Normalization approaches are formulated for both diffuse and ballistic radiation transfer. Radiation transfer predictions generated using both the DOM and FVM with the normalization approaches are compared with statistical Monte Carlo predictions to gauge their accuracy and efficiency. Proper phase-function normalization is shown to greatly improve radiation transfer accuracy, while concurrently improving computational efficiency by allowing for substantial reduction in both discrete direction number and solid-angle splitting density. Application of phase-function normalization for ballistic radiation transfer is found to be crucial. Additionally, phase-function normalization allows for accurate conformity between DOM and FVM solutions of the ERT.

Acknowledgments

First and foremost, I would like to offer my sincere gratitude and unending thanks to my dissertation advisor, Dr. Zhixiong Guo, for his tutelage and guidance in my 4 years in his research group. I have never met someone with such a passion for excellence in research and academia that was also so compassionate and understanding in all aspects of life. I am forever indebted to him for making me a better student, a better researcher, and a better overall person. I know that my future success in whatever career path I eventually end up choosing will be in no small part to his hard work and excellence in advising. Words cannot adequately describe my overall gratitude and thanks.

Secondly, I would like to offer my thanks to the remaining members of my dissertation committee: Dr. Prosenjit Bagchi, Dr. Andrew Norris, and Dr. Eugene Speer, for serving on my committee and offering their much appreciated advice and suggestions for how to improve the explanations of my research findings herein. Behind a good student is always an excellent core of professors and advisors, and without their help, advice, and teaching, I would not be the same student I am today. They have made my academic life easier while at Rutgers, which is all anyone can ask for. To them, I offer my unending thanks and appreciation.

I wouldn't be where I am today without my parents, Kevin and Helen Hunter. Throughout all my years of school, from preschool through Ph.D., they have supported me, helped me with any problems I've encountered, given me comfort when I needed it and criticism when it was necessary. They've supported all decisions I've made, good or bad, and have always been there for me whenever I have needed anything. I love you guys, and can't express enough how thankful I am that you are my parents. From interacting with other human

beings (sometimes against my will), I know that I ended up with the cream of the crop (and hey, I guess you did too!).

I would also like to acknowledge and thank ASEE and DoD for bestowing the SMART scholarship upon me in 2011, for funding my research for 3 years, and for providing me with employment at ARDEC at Picatinny in the coming 3 years. My mentor at ARDEC, Mr. Douglas Troast, has been forthcoming and honest about everything I've asked of him, and has been easy to talk to and understanding of some of my personal situations. I look forward to working with and for him for the foreseeable future.

Finally, but not any less importantly, I would like to thank my fiancé, Samantha Yost, for everything she has done for me in the nearly 5 years we have been together. From supporting me when I was having emotional meltdowns, to making me laugh when I was upset, all the way to listening to me ramble about my research when she had no idea what I was going on about, she is the best thing to happen to me in my lifetime. I don't know where I would be without her, and I know that I am a better person because of her. I love you, Samantha. Thanks for being so awesomely awesome.

Dedication

To my parents, Kevin and Helen Hunter, and my fiancé, Samantha.

Table of Contents

List of Tables

List of Figures

Acknowledgment of Previous Publications

The following publications by the author and dissertation advisor are acknowledged, as the following dissertation is partly comprised of material in said publications:

Hunter, B., and Guo, Z., 2011, Comparison of discrete-ordinates method and finite volume method for steady-state and ultrafast radiative transfer analysis in cylindrical coordinates, *Numerical Heat Transfer B*, vol. 59, pp. 339-359.

Hunter, B., and Guo, Z., 2012, Conservation of asymmetry factor in phase function discretization for radiative transfer analysis in anisotropic scattering media, *International Journal of Heat and Mass Transfer*, 2011, vol. 55, nos. 5-6, pp. 1544-1552.

Hunter, B., and Guo, Z., 2012, Reduction of angle splitting and computational time for the finite volume method via phase function normalization, *International Journal of Heat and Mass Transfer*, 2011, vol. 55, nos. 9-10, pp. 2449-2460.

Hunter, B., and Guo, Z., 2012, Phase function normalization for accurate analysis of ultrafast collimated radiative transfer, *Applied Optics*, vol. 51, pp. 2192-2201.

Hunter, B., and Guo, Z., 2012, Phase-function normalization in 3-D discrete-ordinates solution of radiative transfer – Part I: Conservation of scattered energy and asymmetry factor, *Numerical Heat Transfer* B, vol. 62, pp. 203-222.

Hunter, B., and Guo, Z., 2012. Phase-function normalization in 3-D discrete-ordinates solution of radiative transfer – Part II: Benchmark comparisons, *Numerical Heat Transfer B*, vol. 62, pp. 223-242.

Z. Guo and B. Hunter, 2013, Advances in ultrafast radiative transfer modeling and applications: A review, *Heat Transfer Research*, vol. 44, pp. 303-344.

Hunter, B., and Guo, Z., 2013, Comparison of quadrature schemes in DOM for anisotropic scattering radiative transfer analysis, *Numerical Heat Transfer B*, vol. 63, pp. 485-507.

Hunter, B., and Guo, Z., 2014, Normalization of various phase functions for radiative heat transfer analysis in a solar absorber tube, *Heat Transfer Engineering*, vol. 35, no. 6-8, pp. 791-801.

Hunter, B., and Guo, Z., 2014, A new and simple technique to normalize HG phase function for conserving scattered energy and asymmetry factor, *Numerical Heat Transfer B*, vol. 65, pp. 195-217

Hunter, B., and Guo, Z., 2014, Improved treatment of anisotropic scattering for ultrafast radiative transfer analysis, *Journal of Heat Transfer*, *submitted for review.*

Hunter, B., and Guo, Z., 2014, Improved treatment of anisotropic scattering in radiative transfer analysis using the finite volume method, *Heat Transfer Engineering*, *submitted for review.*

Hunter, B., and Guo, Z., 2014, Applicability of phase-function normalization techniques for radiation transfer computation with DOM, *Numerical Heat Transfer B*, *submitted for review*

Computational Workstation Note

For all simulations in this dissertation, the computational workstation used is a Dell Optiplex 780, with an Intel Dual Core processor and 4.0 GB of RAM. All radiation transfer predictions are generated in the FORTRAN computing language, while normalization parameters for Hunter and Guo's 2012 normalization are generated in MATLAB, in order to make use of the built in least-squares and QR factorization scripts. These normalization parameters are then imported back into FORTRAN for further analysis.

CHAPTER 1 : INTRODUCTION

1.1 Background - Radiation Transfer and Applications

In many practical applications, radiation is the dominant mode of heat transfer, with its contributions vastly outweighing those of conduction and convection [Modest 2002, Siegel and Howell 2002]. Some traditional applications where radiation plays a major role are:

- High-temperature combustion [Edwards and Balakrishnan 1973, Taine and Soufiani 1999, Guo and Maruyama 2000, Solovjov and Webb 2001, Seo et al. 2002, Tuncer et al. 2009] and material processing [Dupret et al. 1990, Guo et al. 1998, Chen and Jaluria 2007]
- Fire and flame radiation [de Ris 1979, Tien and Lee 1982, Albini 1985, Shokri and Beyler 1989, Cumber 2000]
- Atmospheric radiation [Angstrom 1924, Elsasser 1942, Bliss 1961, Goody and Yung 1995]
- Solar radiation and renewable energy [Turner 1999, Tzen and Morris 2003, Gratzel 2005]
- Human space exploration [Gordon 1958, Cucinotta and Durante 2006, Durante and Cucinotta 2006]

Additionally, radiation heat transfer plays a major role in both biomedical and industrial processes. In the last few decades, the use of ultrashort-pulsed (USP) lasers has greatly increased for such applications, due to both availability and affordability of equipment and improved intelligence regarding the advantages of such technology. The convergence of a

powerful USP laser beam to a small focal spot can result in optical breakdown due to high energy flux, allowing for the exploration of a brand new window of nonlinear optics. Some important examples of USP laser application are plasma-mediated ablation and material micromachining [Niemz et al. 1991, Liu et al. 1997, Loesel et al. 1998, Hatano et al. 2000, Choi and Grigoropoulos 2002, Hong et al. 2004, Chowdhury et al. 2005, Huang and Guo 2009a, Huang and Guo 2010, Wang and Guo 2010]. The ultrashort pulse duration results in negligible thermal diffusion, as it is much shorter than material thermal diffusion time. Consequently, USP lasers allow for minimization of the thermal and mechanical damage that is a major concern for conventional continuous-wave (CW) lasers.

Perhaps the largest impact of ultrafast laser technology has been on the field of biomedicine [Sajjadi et al. 2013]. The visualization of growths embedded in biological tissue, such has cancerous tumors, via near-infrared optical imaging [Wang et al. 1991, Liu et al. 1993, Yoo and Alfano 1993, Yamada 1995, Yodh and Chance 1995, Alfano et al. 1997, Villringer and Chance 1997, Quan and Guo 2004] has become greatly improved through the use of ultrafast lasers. Additionally, ultrafast laser technology is crucial for many biomedical therapeutic applications, including but not limited to the following:

- Precision laser microsurgery [Anderson and Parrish 1983, Abergel et al. 1986, Arkin et al. 1994, Ridouane and Campo 2006], such as LASIK corneal surgery [Lubatschowski et al. 2003]
- Tissue ablation and microprocessing [Kim et al. 2001, Huang and Guo 2009b]
- Laser-induced hyperthermia [Anghileri and Robert 1986, Jaunich et al. 2008, Jiao and Guo 2011]
- Decontamination of medical devices [Guo et al. 2010, Wang and Guo 2010]

- Laser endodontics [Serafetinides et al. 1999, Strassl et al. 2002]
- Laser tissue welding and soldering [Murray et al. 1989, Bass and Treat 1995, Fried et al. 1999, Kim and Guo 2004]

In all applications where radiation is the driving force, the ability to accurately determine the impact of radiation transfer is crucial for advances in science and technology.

1.2 Numerical Methods for Radiation Transfer

The recent technological advances in the field of radiation transfer have prompted significant increases in numerical research. In many cases, numerical modeling of radiation transfer is a realistic and appreciable alternative to costly or dangerous experimentation, especially for *in vivo* biomedical applications, where safety of the living subject is of the highest importance. In order to determine the overall impact of radiation in a given application, accurate and complete solution of the governing Equation of Radiation Transfer (ERT) is required. For selected simple situations, analytical solutions of the ERT are possible. However, in most practical applications where light scattering exists, the integro-differential nature of the ERT makes analytic solution extremely difficult or impossible, mandating the use of numerical techniques to completely describe radiation processes. Two commonly implemented solution methodologies, due to their relative simplicity, are the Discrete-Ordinates Method (DOM) and the Finite Volume Method (FVM).

1.2.1 The Discrete-Ordinates Method (DOM)

The DOM was first proposed by Chandrasekhar [1960] for determination of atmospheric and astrophysical radiation. Later, Carlson and Lathrop [1968] adapted the DOM as a means of solving the neutron transport equation. Works by Fiveland [1984, 1988] and Truelove [1988]

were among the first to apply the DOM as a solution methodology for the ERT, determining steady-state radiative transfer in both 2-D and 3-D enclosures containing participating media. Menguc and Viskanta [1986], Jamaluddin and Smith [1988], and Jendoubi et al. [1993] laid out the detailed framework for DOM solutions in axisymmetric cylindrical media, in order to more accurately model combustion processes in boilers and furnaces. More recently, some modifications to the DOM have been put forth [Mishra et al. 2006, Mishra and Krishna 2011], in an attempt to increase both computational efficiency and feasibility of implementation.

In order to determine radiant energy propagation with ultrafast speed of light, the DOM can be implemented to solve the time-dependent hyperbolic ERT (TERT). The DOM was first considered for ultrafast radiative transfer in a 1-D planar medium by Mitra and Kumar [1999]. Guo and Kumar [2001,2002] provided the formulation for the transient DOM (TDOM) to investigate ultrafast laser propagation in both 2- and 3-D enclosures described by Cartesian coordinates. Guo and co-authors additionally implemented the TDOM to accurately and efficiently model short-pulsed irradiation of turbid media [Kim and Guo 2007, Jaunich et al. 2008], laser-tissue welding and soldering [Kim and Guo 2004], and pulse train irradiation using Duhamel's superposition theorem [Guo and Maruyama 2000, Akamatsu and Guo 2011]. Further, Sakami et al. [2002] analyzed the ultra-short light pulse propagation in a 2-D rectangular medium using the TDOM, and Das et al. [2003] compared DOM predictions of ultrafast laser propagation through tissue phantoms with experiment, showing accurate agreement.

1.2.2 The Finite Volume Method (FVM)

The first appearance of the FVM as a method of determining radiation heat transfer was in Raithby and Chui [1990], where they presented the initial formulation and analyzed some

benchmark problems for verification. Chui et al. [1992] provided the framework for determining radiative transfer in both axisymmetric and non-axisymmetric cylindrical enclosures using the FVM. Additional works by Chui and co-authors [Chui and Raithby 1993, Chui et al. 1993] extended the FVM for use with non-orthogonal meshes to analyze radiation heat transfer in a pulverized fuel flame. Chai et al. [1994] also extensively analyzed the FVM, solving for radiation heat transfer in irregular geometric enclosures [Chai et al. 1995]. Additional works by Borjini et al. [2007] and Kamel et al. [2006] used the 3-D FVM to determine radiation heat transfer in a baffled combustion chamber containing a non-gray, sooting medium.

Over the years, numerous attempts have been made to improve the FVM for predicting radiation heat transfer. Extension of the FVM for use with unstructured triangular and tetrahedral meshes, similar to those used in computational fluid dynamics, was presented by Murthy and Mathur [1998], with Baek et al. [1998] using non-orthogonal meshes to analyze radiation transfer in a kidney-shaped, 3-D combustion chamber. Chai and Moder [2000] introduced an angular multiblock procedure for the FVM for use with fine angular grids. Kim et al. [2001] and Guedri et al. [2009] further extended the unstructured FVM to enclosures containing obstacles.

Extension of the FVM to determine ultrafast radiation propagation was first outlined by Chai [2003] for a 1-D slab. Further works by Chai and co-authors extended the FVM for ultrafast radiation transfer to both 2-D [Chai 2004] and 3-D [Chai et al. 2004] geometries. The interaction of both single-pulse and pulse-train irradiation with 1-D and 2-D anisotropic media using the transient FVM was investigated by Muthukumaran and Mishra [2008a, 2008b], while Rahmani et al. [2009] investigated the prediction of ultrafast radiant energy transfer with FVM using a generalized computational grid, introducing a novel method of treating control angle overhang.

1.3 Motivation of the Dissertation

The DOM and FVM have been shown to offer a healthy balance between efficiency and accuracy, as compared with other ERT solution methods. More computationally efficient methods, such as the diffusion approximation, suffer from severe limitations in predicting ballistic photon transport the presence of boundaries and absorbing regions [Guo et al. 2003]. Conversely, the Monte Carlo ray-tracing method is considered as a realistic alternative to costly experimentation, but the inherent processes are extremely time-consuming [Guo et al. 2000, Guo et al. 2002, Lu and Hsu 2004, Lu and Hsu 2005]. Study by Mishra et al. [2006] found that the DOM and FVM were computationally efficient and accurate methods for determining short-pulse laser transport through a participating medium.

It is well known that the DOM suffers from two shortcomings: numerical smearing (or called as false scattering) due to spatial discretization practices [Coelho 2002a, Coelho 2002b, Jessee and Fiveland 1997], and ray effect due to the approximation of the continuous angular variation of radiation scattering with a finite number of discrete radiation directions [Chai et al. 1993, Coelho 2002b]. However, it is less known in the field that all numerical methods that solve the ERT using discretization practices, such as the FVM, will also suffer from similar errors. Over the years, many attempts to account for and limit these two discretization errors have been made. Common approaches of reducing numerical smearing involve application of either finer spatial grids or higher-order spatial differencing schemes, while ray effect can be treated by improving angular resolution.

For all practical applications in nature, radiation scattering is anisotropic. During numerical computations of radiation, it is well known that scattered energy must be accurately conserved after angular discretization [Wiscombe 1976, Kim and Lee 1988, Liu et al. 2002,

Boulet et al. 2007, Collin et al. 2011]. Inaccurate conservation of scattered energy can lead to massive errors in radiation transfer predictions, or in extreme cases, divergent iterative solutions. Phase-function normalization has become the prevailing approach to ensure numerically accurate scattered energy conservation after DOM discretization. However, even with scattered energy conservation intact, the DOM still has difficulty predicting radiation transfer accurately in anisotropic media [El Wakil and Sacadura 1992, Chai et al. 1998, Sadoghi 2006, Ma et al. 2013]. Attempts to modify the DOM for computations involving high scattering anisotropy have been made [Korkin et al. 2012], although the root cause behind its difficulty remained unclear for years.

Only recently was it discovered that angular discretization of scattering anisotropy results in change in the physical property of phase-function asymmetry factor, which is the average cosine of scattering angle [Boulet et al. 2007]. Alterations in asymmetry factor after angular discretization results in alteration of medium scattering properties, leading to a third type of discretization error, termed here "**angular false scattering**". Previously published phase-function normalization techniques do not ensure the simultaneous conservation of asymmetry factor and scattered energy after DOM discretization. For the FVM, it is widely assumed that phase-function normalization is unnecessary. Instead, solid-angle splitting [Chui et al. 1992] was used to accurately conserve scattered energy. However, solid-angle splitting may not accurately preserve phase-function asymmetry factor, leading to inaccuracies in FVM predictions.

The ability to accurately predict radiation transfer using approximate numerical methods is critical, especially for biomedical applications. Consider the *in vivo* treatment of cancerous tumors via ultrafast laser hyperthermia. Inaccurate numerical predictions can lead to

costly mistakes in experimental application, including necrosis/thermal damage of healthy, surrounding tissues, or the improper eradication of the dangerous tissue during laser treatment.

To this end, phase-function normalization approaches for the DOM and FVM that accurately conserve both scattered energy and phase-function asymmetry factor are desired, in order to effectively minimize angular false scattering errors and allow for accurate numerical predictions of radiation transfer.

1.4 Goals of the Dissertation

The goals of this dissertation are as follows:

- To introduce the concept of “angular false scattering”, make its existence known in the field of radiation transfer, and illustrate the inadequacies of previously published normalization approaches
- To present the need for additional phase-function treatment in DOM and FVM, in order to obtain accurate solutions to the ERT
- To develop novel phase-function normalization techniques that will accurately conserve scattered energy and phase-function asymmetry factor simultaneously after angular discretization
- To illustrate the ability of proper phase-function normalization to both improve radiation transfer accuracy and improve computational efficiency
- To show the necessity of additional phase-function treatment for problems involving ballistic radiation transport

1.5 Dissertation Overview

The dissertation is laid out in the following manner:

- In Chapter 1, practical applications that require accurate and efficient radiation transfer predictions are presented. A brief history of the DOM and FVM as ERT solution methods is outlined. The motivations behind the study in this dissertation, as well as the dissertation goals, are outlined.
- In Chapter 2, the mathematical formulation of the DOM is presented, in detail, for use in both 2-D axisymmetric cylindrical and 3-D Cartesian enclosures. DOM quadrature schemes, including the traditional S_N and multiple high-order schemes, are discussed. DOM solutions are validated with exact solutions in simple benchmark problems. Radiation transfer predictions in a solar absorber tube are presented, in order to clarify the impact of medium optical thickness, scattering albedo, wall emissivity, and phase-function asymmetry factor.
- In Chapter 3, the mathematical formulation of the FVM is presented in detail. Description of commonly implemented FVM quadrature schemes is outlined. FVM predictions of radiation transfer are validated with experimental, exact, and DOM predictions. An illustration of the two well-known numerical discretization errors (ray effect and numerical smearing/false scattering) is presented. Finally, an analysis of the computational efficiency of the DOM and FVM is presented.
- In Chapter 4, the existence and root cause of angular false scattering, a third type of numerical discretization error, is presented for both the DOM and FVM. The inability of commonly implemented numerical techniques, such as phase-function normalization for DOM and solid-angle splitting for FVM, to accurately

conserve phase-function asymmetry factor after angular discretization is observed. The impact of angular-false scattering errors on both DOM and FVM radiation transfer predictions is witnessed through comparison with statistical Monte Carlo. The misnomer of calling numerical smearing errors as "false scattering" is presented. The need for additional phase-function treatment, in order to conserve both scattered energy and asymmetry factor simultaneously, is presented for both DOM and FVM.

- In Chapter 5, a novel phase-function normalization approach, known as Hunter and Guo's 2012 normalization, which accurately conserves both quantities simultaneously, is formulated for application with both DOM and FVM. Improvements in radiation transfer predictions after application of this approach are presented via comparison with isotropic scaling law and statistical Monte Carlo. The impact of normalization on media with varying optical properties is investigated. Finally, the ability of proper normalization to improve computational efficiency by reducing both required discrete-direction number in the DOM and solid-angle splitting density in the FVM while maintaining solution accuracy is shown.
- In Chapter 6, a second phase-function normalization approach is developed. This approach is able to conserve both relevant quantities simultaneously in a simpler manner. Application of this normalization for DOM using both HG and Legendre phase-functions is presented. Comparisons to both Monte Carlo and high-order FVM are shown, in order to gauge accuracy. A recommendation for when to implement specific normalization techniques is presented.

- In Chapter 7, the necessity for additional phase-function normalization treatment for problems involving ballistic radiation transport is presented. An extension of the normalization approaches outlined in Chapters 5 and 6 is presented for ballistic radiation transport for use in both DOM and FVM. The need for negative intensity correction for convergent ERT solutions is investigated.
- Finally, in Chapter 8, overall conclusions of the dissertation are presented, and an outline of the advantages and disadvantages of specific phase-function normalization techniques is listed.

CHAPTER 2 : THE DISCRETE-ORDINATES METHOD

2.1 Equation of Radiation Transfer

The ultrafast wave-propagation transient ERT (TERT) of radiation intensity *I* in a gray, absorbing-emitting and anisotropically scattering medium can be expressed as follows, using general vector notation [Modest 2002, Guo and Kumar 2001]:

$$\frac{1}{c}\frac{\partial I(\boldsymbol{r},\hat{\boldsymbol{s}},t)}{\partial t}+\hat{\boldsymbol{s}}\cdot\nabla I(\boldsymbol{r},\hat{\boldsymbol{s}},t) = -(\sigma_a+\sigma_s)I(\boldsymbol{r},\hat{\boldsymbol{s}},t)+\sigma_a I_{bk}(\boldsymbol{r},t)+\frac{\sigma_s}{4\pi}\int_{4\pi} I(\boldsymbol{r},\hat{\boldsymbol{s}}',t)\,\Phi(\hat{\boldsymbol{s}}',\hat{\boldsymbol{s}})d\Omega' \tag{2.1}$$

In the preceding equation, $I(\boldsymbol{r},\hat{\boldsymbol{s}},t)$ is the radiative intensity at a given spatial location (defined by position vector $\boldsymbol{r}$) and time t propagating in radiation direction $\hat{\boldsymbol{s}}$, c is the speed of light in the medium, I_{bk} is the blackbody emitting intensity of the medium, σ_a and σ_s are the absorption and scattering coefficients of the medium, respectively, and $\Phi(\hat{\boldsymbol{s}}',\hat{\boldsymbol{s}})$ is the scattering phase-function, determined via Mie theory [Modest 2002]. The two terms on the left-hand side of the equation represent the temporal and spatial gradients of radiation intensity, which are balanced on the right-hand side by three terms: (1) intensity attenuation due to absorption and scattering, (2) intensity augmentation due to blackbody emission, and (3) intensity augmentation due to in-scattering between two radiation directions $\hat{\boldsymbol{s}}'$ and $\hat{\boldsymbol{s}}$. Addition of the time-derivative term is an addition to the steady-state ERT, which represents wave propagation of radiant energy at the speed of light [Guo and Kumar 2001, Guo and Kumar 2002]. Removal of the temporal derivative reduces Eq. (2.1) to the steady-state ERT.

In the presence of radiative scattering ($\sigma_s \neq 0$), Eq. (2.1) is an integro-differential equation, for which analytical solutions are nearly impossible to determine. To this end,

numerical solutions of Eq. (2.1) are desired, in order to accurately represent radiation transfer in a given medium.

2.1.1 Initial and Boundary Conditions

In order to solve Eq. (2.1) to determine radiation transfer in a given medium, both initial and boundary conditions must be specified. In general, the initial condition is given as a known temperature or intensity field in the medium. For ultrafast radiation transfer, this initial condition represents the medium state at t = 0. For steady-state radiation transfer, where the temporal derivative in Eq. (2.1) can be discarded, the initial condition serves as an initial guess for an iterative solution procedure.

A common boundary condition found in radiation transfer analysis is that of an emitting and reflecting wall. The intensity emanating in from a given wall surface location r_w in direction $\hat{\boldsymbol{s}}$ is given by [Guo and Kumar 2001, Guo and Kumar 2002]:

$$I(r_w, \hat{\boldsymbol{s}}) = \epsilon(r_w) I_{bk}(r_w) + \frac{\rho^d(r_w)}{\pi} \int_{\hat{\boldsymbol{n}}\cdot\hat{\boldsymbol{s}}'<0} I(r_w, \hat{\boldsymbol{s}}\,')|\hat{\boldsymbol{n}} \cdot \hat{\boldsymbol{s}}'|\, d\Omega' + \rho^s(r_w, \hat{\boldsymbol{s}}\,)\, I(r_w, \hat{\boldsymbol{s}}^{-1}) \qquad (2.2)$$

where the first term represents emission from the boundary wall, the second term represents the diffuse reflection of incoming intensities, and the third term represents specular reflection. In Eq. (2.2), $\epsilon(r_w)$ and $\rho^d(r_w)$ are the emissivity and diffuse reflectivity at wall location r_w, respectively, $\rho^s(r_w, \hat{\boldsymbol{s}}\,)$ is the specular reflectivity for wall location r_w and direction $\hat{\boldsymbol{s}}$, $\hat{\boldsymbol{n}}$ is the outward unit normal vector at surface location r_w, $|\hat{\boldsymbol{n}} \cdot \hat{\boldsymbol{s}}'|$ is the cosine of the angle between $\hat{\boldsymbol{n}}$ and an arbitrary incoming radiation direction $\hat{\boldsymbol{s}}'$, and the radiation direction $\hat{\boldsymbol{s}}^{-1}$ is the direction that is a mirror-opposite to $\hat{\boldsymbol{s}}$. For a diffusely emitting and reflecting wall, where the intensity leaving the wall is independent of direction, $\rho^s(r_w, \hat{\boldsymbol{s}}\,)$ = 0 [Siegel and Howell 2002].

For interfaces where a mismatch in refractive indices exists, Fresnel reflection must be considered [Kim and Guo 2004]. At such an interface, incident radiation refraction and reflection obey both Snell's law and the Fresnel equation. Under such a boundary condition, reflection is taken as specular, with specular intensity calculated as follows:

$$I(r_w, \hat{\boldsymbol{s}}) = \big(1 - \rho^s(r_w, \hat{\boldsymbol{s}}\,)\big) I_{bk}(r_w) + \rho^s(r_w, \hat{\boldsymbol{s}}\,)\, I(r_w, \hat{\boldsymbol{s}}^{-1}) \tag{2.3}$$

where $\rho^s(r_w, \hat{\boldsymbol{s}}\,)$ is calculated as follows:

$$\rho^s(r_w, \hat{\boldsymbol{s}}\,) = \begin{cases} \dfrac{1}{2}\left[\dfrac{\tan^2\big(\theta_i(\hat{\boldsymbol{s}}) - \theta_r(\hat{\boldsymbol{s}})\big)}{\tan^2\big(\theta_i(\hat{\boldsymbol{s}}) + \theta_r(\hat{\boldsymbol{s}})\big)} + \dfrac{\sin^2\big(\theta_i(\hat{\boldsymbol{s}}) - \theta_r(\hat{\boldsymbol{s}})\big)}{\sin^2\big(\theta_i(\hat{\boldsymbol{s}}) + \theta_r(\hat{\boldsymbol{s}})\big)}\right], & \theta_i(\hat{\boldsymbol{s}}) < \theta_{cr} \\ 1\,, & \theta_i(\hat{\boldsymbol{s}}) \geq \theta_{cr} \end{cases} \tag{2.4}$$

In the above, $\theta_i(\hat{\boldsymbol{s}})$ is the angle of incidence of incoming radiation direction $\hat{\boldsymbol{s}}$, $\theta_r(\hat{\boldsymbol{s}})$ is the refractive angle predicted by Snell's Law, and the critical angle $\theta_{cr} = \sin^{-1}(n_1/n_2)$, where n_1 and n_2 are the refractive indices of the media on either side of the interface.

A special axisymmetric condition must be implemented, for an axisymmetric cylindrical medium, at the radial centerline. This condition is taken as a mirror condition, or a purely specular reflector ($\rho^s = 1$ in Eq. 2.3).

2.1.2 ERT in Cylindrical Coordinates

Consider radiation transfer in a cylindrical enclosure, similar to that shown in Figure 2.1**.** Use of this geometry is common for simulation of ultrafast radiation transfer in biological tissues via pulsed laser heating [Kim and Guo 2004]. In the cylindrical coordinate system, the vectors $\boldsymbol{r}$ and $\hat{\boldsymbol{s}}$ that locate the radiative intensity can be expressed, using cylindrical base vectors $\overrightarrow{e_r}$, $\overrightarrow{e_{\phi_0}}$, and $\overrightarrow{e_z}$, as follows:

$$\boldsymbol{r} = \boldsymbol{r}(r, \phi_0, z) = r\overrightarrow{e_r} + \phi_0\overrightarrow{e_{\phi_0}} + z\overrightarrow{e_z} \tag{2.5a}$$

$$\hat{\boldsymbol{s}} = \hat{\boldsymbol{s}}(\theta, \phi) = \mu\overrightarrow{e_r} + \eta\overrightarrow{e_{\phi_0}} + \xi\overrightarrow{e_z} \tag{2.5b}$$

where r and z are the radial and axial coordinates, ϕ and θ are the azimuthal and polar angles defining radiation direction $\hat{\boldsymbol{s}}$, and ϕ_0 is the spatial azimuthal angle relating $\boldsymbol{r}$ to the Cartesian coordinate system, as seen in Figure 2.2. The azimuthal angle ϕ and spatial azimuthal angle ϕ_0 are related by $\phi = \phi_r - \phi_0$, where ϕ_r is the azimuthal angle relating $\hat{\boldsymbol{s}}$ to the Cartesian coordinate system. The direction cosines relate to the azimuthal and polar angles as $\mu = \sin\theta\cos\phi$, $\eta = \sin\theta\sin\phi$, and $\xi = \cos\theta$.

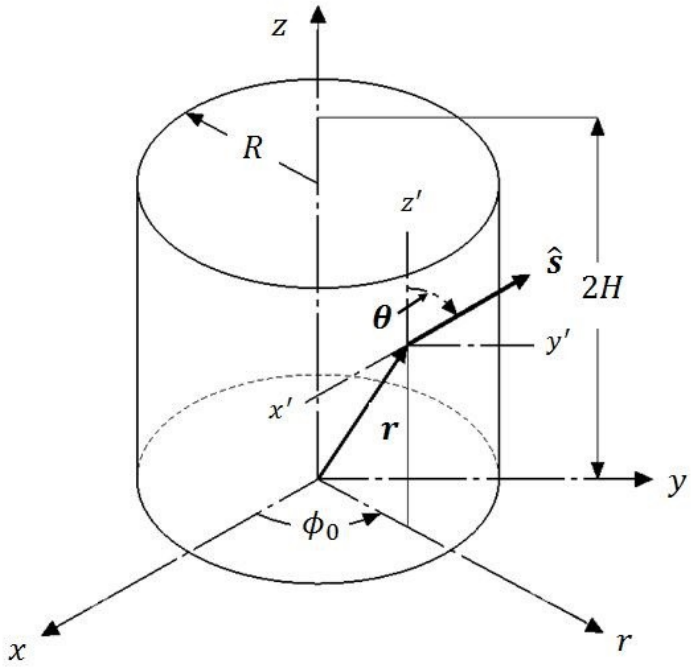

Figure 2.1: Cylindrical geometry and relationship between cylindrical coordinate system and Cartesian coordinate system

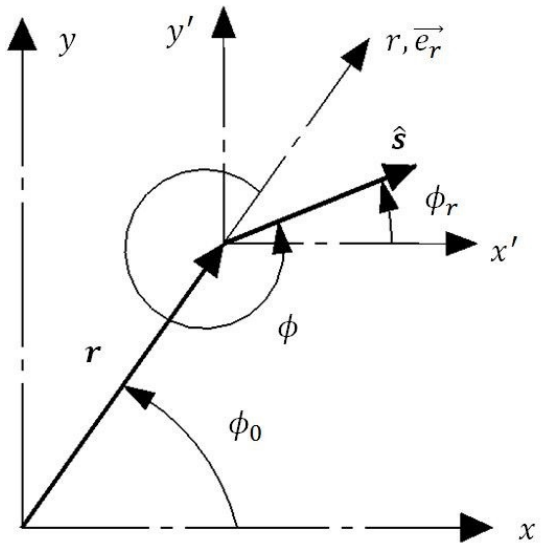

Figure 2.2: Definition of azimuthal angles in the cylindrical coordinate system

For an axisymmetric geometry, intensities are invariant with spatial azimuthal angle ϕ_0 [Menguc and Viskanta 1986]. Thus, intensities corresponding to radiation direction $\hat{\boldsymbol{s}}$ can be obtained by solving the ERT at different values of ϕ_r. However, Chui and Raithby [1992] discovered that a lack of conservation and unphysical directional coupling can occur using this method. Instead, they introduced a simple mapping solution, as illustrated in Figure 2.3. Instead of fixing ϕ_0, ϕ_r for all intensity vectors was set to zero, and the directional intensities can then be calculated by solving the ERT at various values of ϕ_0. Using this notion, intensities become functions of r, z, ϕ, and θ only.

With the preceding information, Eq. (2.1) can be expanded in the cylindrical coordinate system, as follows:

$$\frac{1}{c}\frac{\partial I}{\partial t}+\frac{\mu}{r}\frac{\partial}{\partial r}[rI]-\frac{1}{r}\frac{\partial}{\partial \phi}[\eta I]+\xi\frac{\partial I}{\partial z}=-(\sigma_a+\sigma_s)I+S \tag{2.6}$$

where it is understood that $I = I(r, z, \phi, \theta)$ and $S = S(r, z, \phi, \theta)$. S is comprised of the intensity augmentation terms in Eq. (2.1), and is commonly referred to as the "radiative source term".

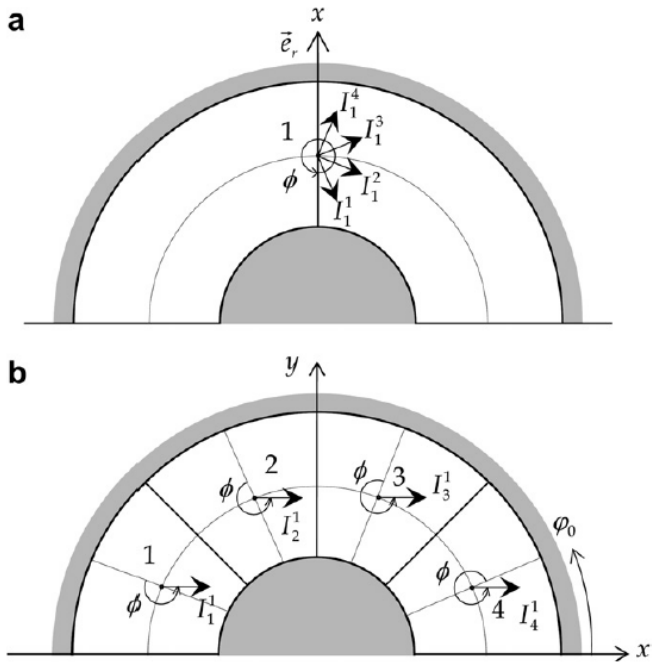

Figure 2.3: Illustration of axisymmetric mapping technique: a) cumbersome mapping with set value of ϕ_0, b) a) axisymmetric mapping technique with ϕ_r = 0 (reproduced from [Kim 1998])

2.1.3 ERT in Cartesian Coordinates

In the 3-D Cartesian coordinate system, the vectors $\boldsymbol{r}$ and $\hat{\boldsymbol{s}}$ are defined as follows, using Cartesian base vectors:

$$\boldsymbol{r} = \boldsymbol{r}(x, y, z) = x\overrightarrow{e_x} + y\overrightarrow{e_y} + z\overrightarrow{e_z} \tag{2.7a}$$

$$\hat{\boldsymbol{s}} = \hat{\boldsymbol{s}}(\theta, \phi) = \mu\overrightarrow{e_x} + \eta\overrightarrow{e_y} + \xi\overrightarrow{e_z} \tag{2.7b}$$

The direction cosines are defined as before. The azimuthal angle ϕ, in this case, is equivalent to ϕ_r in Figure 2.2, and no special treatment is required. With this definition, Eq. (2.1) can be expanded in Cartesian coordinates as follows:

$$\frac{1}{c}\frac{\partial I}{\partial t} + \mu\frac{\partial I}{\partial x} + \eta\frac{\partial I}{\partial y} + \xi\frac{\partial I}{\partial z} = -(\sigma_a + \sigma_s)I + S \tag{2.8}$$

where $I = I(x, y, z, \phi, \theta)$ and $S = S(x, y, z, \phi, \theta)$.

2.2 Solution of ERT Using the Discrete-Ordinates Method

2.2.1 Axisymmetric Cylindrical Medium

Using the DOM, the continuous angular variation of radiative scattering is approximated using a finite set of discrete radiation directions $\hat{\boldsymbol{s}}^{\boldsymbol{l}}$. After directional discretization, Eq. (2.6) can be written in the following manner [Kim and Guo 2004, Jaunich et al. 2008, Jiao and Guo 2009]:

$$\frac{1}{c}\frac{\partial I^l}{\partial t} + \frac{\mu^l}{r}\frac{\partial}{\partial r}[rI^l] - \frac{1}{r}\frac{\partial}{\partial \phi}[\eta^l I^l] + \xi^l\frac{\partial I^l}{\partial z} = -(\sigma_a + \sigma_s)I^l + S^l \ , \qquad l = 1,2,\dots,M \tag{2.9a}$$

$$S^l = \sigma_a I_{bk} + \frac{\sigma_s}{4\pi}\left(\sum_{l'=1}^{M}\Phi^{l'l}I^{l'}w^{l'} + \sum_{B} I^B\Phi^{l^B l}\right) \ , \quad l = 1,2,\dots,M \tag{2.9b}$$

where M is the total number of discrete radiation directions $\hat{\boldsymbol{s}}^{\boldsymbol{l}}$. The in-scattering integral in Eq. (2.6) is replaced in Eq. (2.9b) by discrete quadrature summations over all discrete directions [Fiveland 1987, Fiveland 1988]. In the first summation, which represents the in-scattering of diffuse radiation, $w^{l'}$ is the DOM directional weighting factor associated with radiation direction

$\hat{\boldsymbol{s}}^{\boldsymbol{l'}}$, and $\Phi^{l'l}$ is the discrete scattering phase-function value between incoming radiation direction $\hat{\boldsymbol{s}}^{\boldsymbol{l'}}$ and scattered radiation direction $\hat{\boldsymbol{s}}^{\boldsymbol{l}}$.

The second summation in Eq. (2.9b) represents in-scattering of ballistic radiation [Jendoubi et al. 1993], which becomes critical in applications involving irradiation by collimated solar or laser incidence, or a focused ballistic laser beam cone. In this summation, I^B is the magnitude of the ballistic irradiance (or incident heat flux) at a given medium location, and $\Phi^{l^B l}$ is the ballistic scattering phase-function between the direction of ballistic incidence $\hat{\boldsymbol{s}}^{\boldsymbol{l^B}}$ and radiation direction $\hat{\boldsymbol{s}}^{\boldsymbol{l}}$.

Radiation scattering is described by the Mie phase function Φ, which is highly-oscillatory in nature and can be expressed as an infinite series of Legendre polynomials, as follows:

$$\Phi(\Theta) = 1 + \sum_{i=1}^{\infty} C_i P_i(\cos\Theta) \tag{2.10}$$

where the coefficients C_i are determined via Mie theory, and Θ is the scattering angle between radiation directions $\hat{\boldsymbol{s}}^{\boldsymbol{l'}}$ and $\hat{\boldsymbol{s}}^{\boldsymbol{l}}$. While numerical implementation of the Mie phase function is possible, it can prove to be computationally cumbersome. Commonly, $\Phi(\Theta)$ is approximated by truncating the Legendre series to a finite number of terms, as follows:

$$\Phi_{\mathrm{L}}(\Theta) = 1 + \sum_{i=1}^{N} C_i P_i(\cos\Theta) \tag{2.11}$$

where N is the chosen term of approximation.

Another commonly implemented phase function approximation, due to its ability to accurately capture the strong forward-scattering peak in anisotropic scattering, is the Henyey-Greenstein (HG) phase-function, whose analytical form is as follows:

$$\Phi_{\mathrm{HG}}(\Theta) = \frac{1 - g^2}{[1 + g^2 - 2g\cos\Theta]^{1.5}} \tag{2.12}$$

where the phase-function asymmetry factor g represents the averaged scattering direction cosine, which can be related to the Mie coefficient C_1 through the relation $g = C_1/3$. The asymmetry factor g is a measure of the anisotropy of light scattering. Isotropic scattering, where light scatters equally in all directions, corresponds to g = 0.0. The range of asymmetry factor is $-1.0 \leq g \leq 1.0$, where an asymmetry factor of 1.0 indicates that all light is scattered in the forward direction, and an asymmetry factor of -1.0 indicates that all light is scattered in the backward direction. Most practical participating media scatter light anisotropically, with typical values for biological tissue ranging between $0.8 \leq g \leq 0.99$.

Examples of both Legendre-polynomial and HG phase-functions are plotted in Figure 2.4(a-b). In Figure 2.4a, seven Legendre polynomial phase-functions are shown, which have asymmetry factors of g = 0.4000, 0.485623, 0.669723, 0.7693, 0.818923, 0.84534, and 0.927323. The Mie coefficients C_i associated with these seven phase-function approximations are presented by Kim and Lee [1990] and Lee and Buckius [1982]. In Figure 2.4b, HG phase-functions with g = 0.2000, 0.5000, 0.8000, and 0.9300 are shown, in addition to g = 0.0000 (isotropic scattering), for which the phase function $\Phi = 1.0$ for all directions.

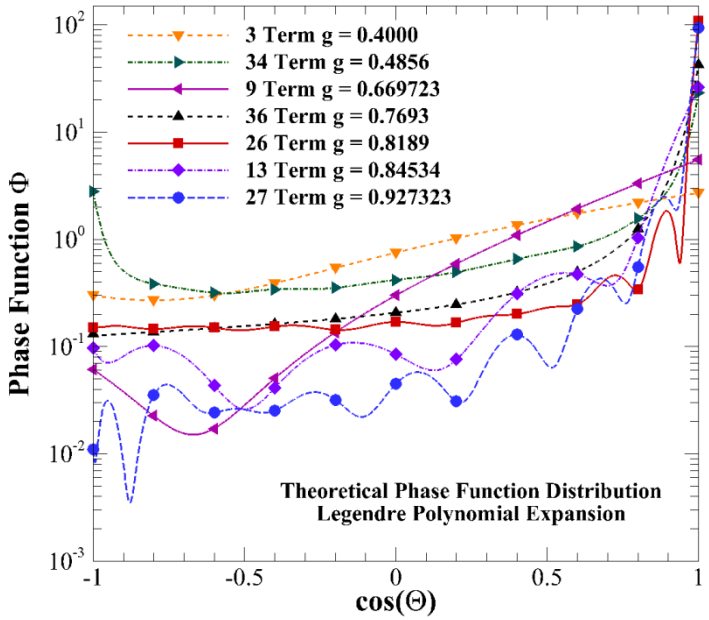

(a)

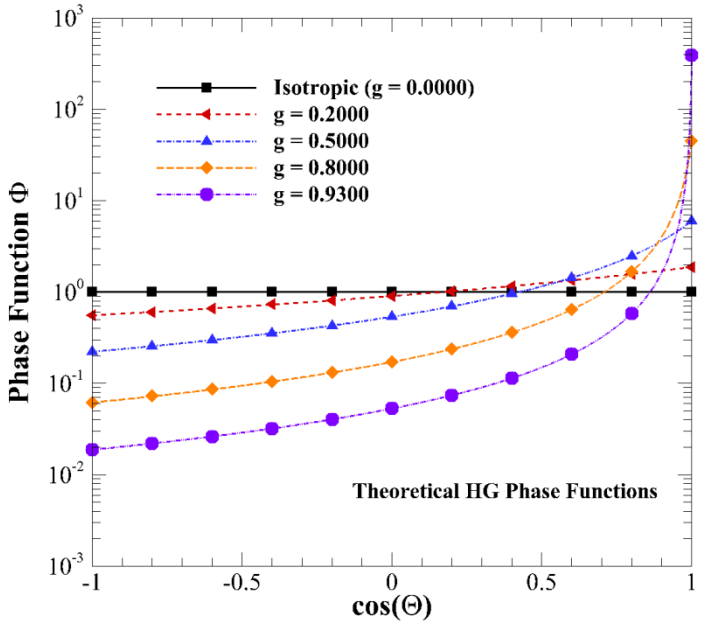

(b)

Figure 2.4: Phase-function distributions: a) Legendre polynomial, b) Henyey-Greenstein

In order to solve Eqs. (2.9a-b), the control-volume method is employed [Modest 2002]. Expanding the ERT over the control-volume in Figure 2.5, and approximating the temporal and

spatial derivatives using traditional differencing techniques [Modest 2002], leads to the following DOM discretization equation for discrete radiation direction $\hat{\boldsymbol{s}}^{\boldsymbol{l}}$:

$$\frac{1}{c\Delta t}\left(I_P^l - I_P^{l0}\right)\Delta V + \mu^l\left(A_n I_n^l - A_s I_s^l\right) - (A_n - A_s)\frac{\alpha^{l+\frac{1}{2}} I_P^{l+\frac{1}{2}} - \alpha^{l-\frac{1}{2}} I_P^{l-\frac{1}{2}}}{w^l} + \xi^l\left(A_t I_t^l - A_b I_b^l\right) = -(\sigma_a + \sigma_s) I_P^l \Delta V + S_P^l \Delta V \tag{2.13}$$

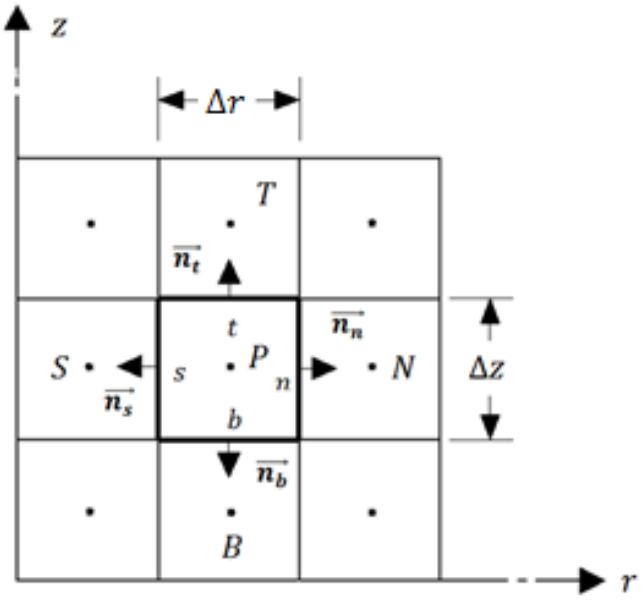

Figure 2.5: Control-volume schematic for 2-D axisymmetric radiation transfer using DOM

As shown in Figure 2.5, $i = n, s, t, b$ are the faces of the control-volume, the subscript P represents the nodal center of the control volume, A_i is the control-volume facial area at control-surface i, and ΔV is the volume of the current control-volume. The temporal derivative is approximated using a forward difference, with I_P^{l0} as the nodal intensity from the previous time-step [Kim and Guo 2004]. For an axisymmetric geometry, where intensities are invariant with ϕ, the facial areas and volumes can be calculated as $A_n = r_n \Delta z_P$, $A_s = r_s \Delta z_P$, $A_t = A_b =$

$r_P \Delta r_P$, and $\Delta V = r_P \Delta r_P \Delta z_P$. For a uniform grid system, as shown in Figure 2.5, Δr_P and Δz_P are invariant across control volumes, and thus are written as Δr and Δz. Additionally, the time step Δt should satisfy the inequality $\Delta t \leq \frac{1}{c} \min(\Delta r, \Delta z)$, so that the traveling distance of radiant energy between successive time steps does not exceed the spatial control volume size [Guo and Kumar 2001].

In an axisymmetric cylindrical geometry, the angular derivative term presents a complication, as the solutions are invariant with azimuthal angle. Carlson and Lathrop [1968] introduced a direct-differencing technique to approximate the angular derivative, as follows:

$$\frac{\partial}{\partial \phi}[\eta^l I^l] \cong \frac{\alpha^{l+\frac{1}{2}} I_P^{l+\frac{1}{2}} - \alpha^{l-\frac{1}{2}} I_P^{l-\frac{1}{2}}}{w^l} \tag{2.14}$$

where the directions $l + \frac{1}{2}$ and $l - \frac{1}{2}$ represent the edges of the angular range of w^l [Jamaluddin and Smith 1988]. The values of a satisfies the following relationship:

$$\alpha^{l+\frac{1}{2}} - \alpha^{l-\frac{1}{2}} = w^l \mu^l \ , \ \ l = 1,2, \dots, M \tag{2.15}$$

with $\alpha^{\frac{1}{2}} = \alpha^{M+\frac{1}{2}} = 0$.

Eq. (2.13) is solved using an iterative sweeping procedure, although relationships between the facial intensities and nodal center intensities are required, in order to limit the number of unknowns in the equation [Jendoubi et al. 1993]. The following weighted relationships can be implemented:

$$\gamma_r I_n^l + (1 - \gamma_r) I_s^l = I_P^l \quad , \quad \mu > 0 \tag{2.16a}$$

$$(1 - \gamma_r) I_n^l + \gamma_r I_s^l = I_P^l \quad , \quad \mu < 0 \tag{2.16b}$$

$$\gamma_z I_t^l + (1 - \gamma_z) I_b^l = I_P^l \quad , \quad \xi > 0 \tag{2.16c}$$

$$(1-\gamma_z)I_t^l + \gamma_z I_b^l = I_P^l \quad , \quad \xi < 0 \tag{2.16d}$$

$$\gamma_\phi I_P^{l+\frac{1}{2}} + \left(1-\gamma_\phi\right) I_P^{l-\frac{1}{2}} = I_P^l \tag{2.16e}$$

The first-order upwind ($\gamma = 1$) and central differencing schemes ($\gamma = 0.5$) are two of the most commonly implemented weighting relationships [Modest 2002], although many other relationships exist. In radiation transfer, the first-order upwind scheme is known as the "step" scheme, while the central differencing scheme is commonly called "diamond".

The intensities for all nodal centers in the medium for a given iteration can be solved using a simple sweeping procedure over the computational domain. There are four possible sweep directions, corresponding to the values of μ and ξ. For example, if both μ and ξ are positive, the solution procedure for that direction will sweep from the radial centerline out to the radial side wall, and from the bottom end wall to the top end wall ($r = 0 \to R, z = 0 \to 2H$, as seen in Figure 2.1). Intensities at upstream boundaries are known, either from boundary conditions, or from solution in adjacent control volumes. The boundary condition given by Eq. (2.2) is discretized as follows, for the radial wall:

$$I_w^l = \epsilon_w I_{bk,w} + \frac{\rho_w^d}{\pi} \sum_{l',\mu^{l'}>0} w^{l'} I^{l'} \left|\mu^{l'}\right|, \quad \mu^l < 0 \tag{2.17}$$

Conditions for the other walls in the enclosure can be obtained by manipulation of the direction cosines in the previous equation. For the sweep where μ and ξ are positive, I_s^l and I_b^l are known, meaning that use of the relationships in Eqs. (2.16a-c) can eliminate all unknowns except I_P^l from Eq. (2.13), allowing us to solve for the nodal center intensity. Eq. (2.13) can be thus be rearranged to solve for I_P^l, for $\mu > 0$, $\xi > 0$:

$$I_P^l = \frac{\left[\frac{\Delta V}{c\Delta t} I_p^{l0} + I_s^l(A) - I_P^{l-\frac{1}{2}}(B) + I_b^l(C) + S_P^l \Delta V\right]}{\left[\frac{\Delta V}{c\Delta t} + \frac{\mu^l A_n}{\gamma_r} - \frac{(A_n - A_s)}{w^l}\left(\frac{\alpha^{l+\frac{1}{2}}}{\gamma_\phi}\right) + \frac{\xi^l A_t}{\gamma_z} + (\sigma_a + \sigma_s)\Delta V\right]} \tag{2.18a}$$

$$A = A_s + \frac{A_n(1-\gamma_r)}{\gamma_r} \tag{2.18b}$$

$$B = \frac{(A_n - A_s)}{w^l}\left(\alpha^{l-\frac{1}{2}} + \frac{\alpha^{l+\frac{1}{2}}(1-\gamma_\phi)}{\gamma_\phi}\right) \tag{2.18c}$$

$$C = A_b + \frac{A_t(1-\gamma_z)}{\gamma_z} \tag{2.18d}$$

A similar procedure can be used to determine the governing equations for I_P^l for the other three sweep combinations. Once I_P^l is known, it can be substituted back into Eqs. (2.16a-e) in order to obtain intensities at the downstream faces, which will become the boundary conditions for adjacent control volumes.

For ultrafast simulations, the intensity field generated after completion of the sweeping procedure over the computational domain for all directions represents a given time t. The solution procedure is then repeated in an iterative manner, with the previously generated intensities used as initial conditions for the next sweep, until the desired simulation time is reached. For steady-state simulations, the intensities generated at each iterative step have no physical meaning, and the iterative procedure must be repeated until a convergence criterion is reached in order to generate the steady-state solution.

After calculation of the intensity field, the net radiative heat fluxes at the radial side and axial end walls can be obtained as follows:

$$Q_r = \sum_{l=1}^{M} \mu^l w^l I^l \quad , \quad Q_z = \sum_{l=1}^{M} \xi^l w^l I^l \tag{2.19}$$

Additionally, the incident radiation G and divergence of radiative heat flux $\nabla \cdot q_r$, which represents energy deposition in the medium, can be calculated as follows:

$$G = \sum_{l=1}^{M} w^l I^l \quad , \quad \nabla \cdot q_r = \sigma_a (4\pi I_{bk} - G) \tag{2.20}$$

2.2.2 3-D Cubic (Cartesian) Medium

After DOM directional discretization, Eq. (2.8) can be written in the following manner [Guo and Kumar 2002]:

$$\frac{1}{c}\frac{\partial I^l}{\partial t} + \mu^l \frac{\partial I^l}{\partial x} + \eta^l \frac{\partial I^l}{\partial y} + \xi^l \frac{\partial I^l}{\partial z} = -(\sigma_a + \sigma_s) I^l + S^l \ , \qquad l = 1,2,\dots,M \tag{2.21a}$$

$$S^l = \sigma_a I_{bk} + \frac{\sigma_s}{4\pi}\left(\sum_{l'=1}^{M} \Phi^{l'l} I^{l'} w^{l'} + \sum_{B} I^B \Phi^{l^B l} \right) \ , \ l = 1,2,\dots,M \tag{2.21b}$$

Expanding Eqs. (2.21a-b) over the control-volume illustrated in Figure 2.6, the discretization equation for discrete direction $\hat{\boldsymbol{s}}^{\boldsymbol{l}}$ becomes:

$$\begin{aligned} &\frac{1}{c\Delta t}\left(I_P^l - I_P^{l0}\right)\Delta V + \mu^l\left(A_n I_n^l - A_s I_s^l\right) + \eta^l\left(A_e I_e^l - A_w I_w^l\right) + \xi^l\left(A_t I_t^l - A_b I_b^l\right) \\ &\qquad = -(\sigma_a + \sigma_s) I_P^l \Delta V + S_P^l \Delta V \end{aligned} \tag{2.22}$$

For a uniform grid system, $A_n = A_s = \Delta y \Delta z,\ A_t = A_b = \Delta x \Delta y,\ A_e = A_w = \Delta x \Delta z,\ \Delta V = \Delta x \Delta y \Delta z$.

Similar to the procedure illustrated for the 2-D axisymmetric cylindrical medium, an iterative sweeping procedure is implemented over the computational domain and discrete

directions, with eight possible sweep directions corresponding to the eight possible sign combinations of μ^l, η^l, and ξ^l.

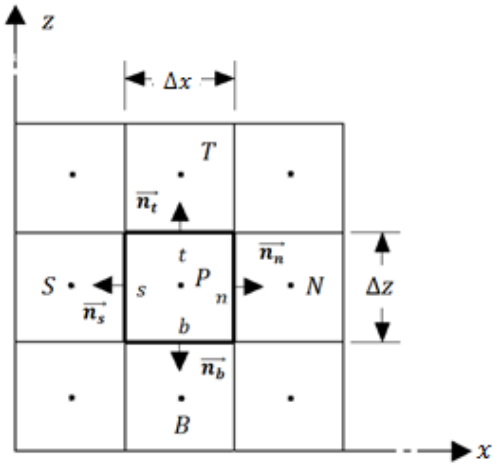

(a)

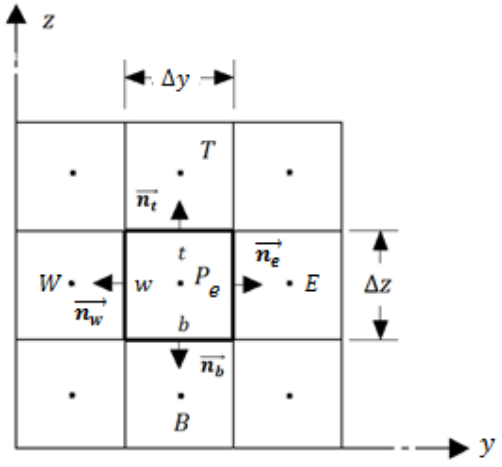

(b)

Figure 2.6: Control volume schematics for 3-D cubic enclosure: a) x-z plane, b) y-z plane

The differencing relationships of Eqs. (2.16a-d) are again used, with x replacing r in Eqs. (2.16a-b), along with the addition of a similar relationship for the y-direction. For the sweep

direction where all direction cosines are positive, Eq. (2.22) can be rewritten to solve for I_p^l as follows:

$$I_P^l = \frac{\left[\frac{\Delta V}{c\Delta t} I_p^{l0} + I_s^l(A) + I_w^l(B) + I_b^l(C) + S_P^l \Delta V\right]}{\left[\frac{\Delta V}{c\Delta t} + \frac{\mu^l A_n}{\gamma_x} + \frac{\eta^l A_e}{\gamma_y} + \frac{\xi^l A_t}{\gamma_z} + (\sigma_a + \sigma_s)\Delta V\right]} \tag{2.23a}$$

$$A = A_s + \frac{A_n(1-\gamma_x)}{\gamma_x}, \qquad B = A_w + \frac{A_e(1-\gamma_y)}{\gamma_y}, \qquad C = A_b + \frac{A_t(1-\gamma_z)}{\gamma_z} \tag{2.23b}$$

The above equation can once again be rewritten for the other seven sweeps. After calculation of the intensity field, the net radiative heat fluxes at the enclosure walls can be calculated as:

$$Q_x = \sum_{l=1}^{M} \mu^l w^l I^l, \quad Q_y = \sum_{l=1}^{M} \eta^l w^l I^l, \quad Q_z = \sum_{l=1}^{M} \xi^l w^l I^l \tag{2.24}$$

while the incident radiation G and divergence of radiative heat flux $\nabla \cdot q_r$ formulae remain unchanged from Eq. (2.20). For a 2-D medium, the formulation is identical, except for the removal of all z-component terms.

2.3 DOM Quadrature Sets

2.3.1 Directional Moment Conditions

In general, the choice of quadrature scheme for the DOM is arbitrary. However, DOM quadrature sets are normally developed around the satisfaction of directional moment conditions [Modest 2002]. After directional discretization, the m^{th}-order moment conditions can be expressed as follows:

$$\frac{1}{4\pi}\sum_{l=1}^{M}\left(\mu^l\right)^m w^l = \frac{1}{4\pi}\sum_{l=1}^{M}\left(\eta^l\right)^m w^l = \frac{1}{4\pi}\sum_{l=1}^{M}\left(\xi^l\right)^m w^l = \begin{cases} 0\ , & m = 1,3,5,7,\ldots \\ \dfrac{1}{m+1}\ , & m = 0,2,4,6,\ldots \end{cases} \tag{2.25}$$

Depending on the value of m, these conditions are typically referred to as odd- or even-moment conditions. A constraint on the values of the weighting factors arises from the simplest moment condition, when m = 0:

$$\frac{1}{4\pi}\sum_{l=1}^{M} w^l = 1 \tag{2.26}$$

This condition makes physical sense, as the weighting factors are the numerical analogs of discrete solid angles. Since the total solid angle is 4π, the weighting factors must obey this condition.

2.3.2 Level-Symmetric Quadrature

Historically, the most commonly implemented quadrature set is the level-symmetric S_N quadrature, where the index N is an even number that relates to the total number of discrete radiation directions as $M = N(N+2)$ [Fiveland 1991]. In the principal octant, discrete directions are arranged on $N/2$ directional levels of constant polar angle (i.e., constant ξ), with $\frac{N}{2} - i + 1$ directions existing on the i^{th} directional level, $i = 1,2,\ldots,N/2$ [Thurgood et al. 1995]. The S_N quadrature fully satisfies reflectional and rotational symmetries about the coordinate axes, and thus only specification of the principal octant is required, as the principal octant directions can be mapped onto the remainder of the unit sphere. Figure 2.7 shows the discretization of the continuous angular variation of radiation scattering (unit sphere) using the S_{12} quadrature ($M = 168$). The directions and weighting factors satisfy both the 0^{th}- and 1^{st}-order moment conditions, as well as all subsequent even conditions ($m \geq 2$ in Eq. (2.23)). Further details on the development and derivation of the S_N quadrature set are readily available in Modest [2002] and Fiveland [1991].

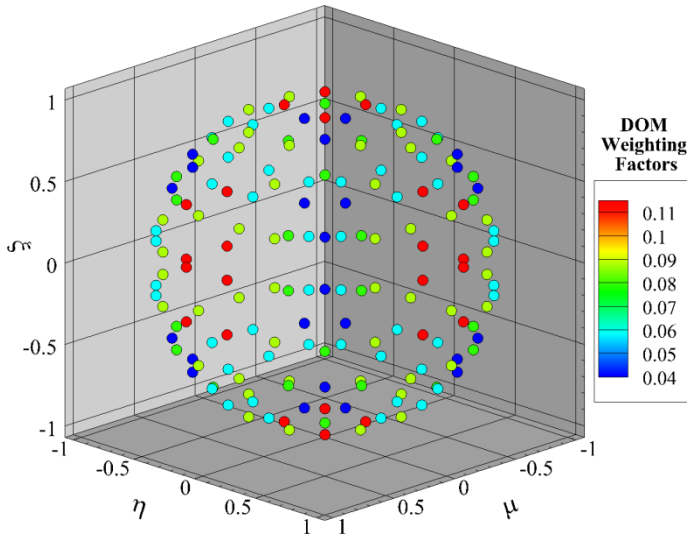

Figure 2.7: S_{12} directional distribution with corresponding DOM weighting factors

More recently, Endo and Yamamoto [2007] developed a new solid angle quadrature set, called the Even-Odd Quadrature (symbolized as EO_N). This quadrature set was developed to satisfy not only even-moment conditions, similar to S_N, but also higher-order odd moment conditions, leading to more accurate radiation transfer predictions than those generated using traditional S_N quadrature.

Both the S_N and EO_N quadrature sets come with a significant mathematical limitation. For $N \geq 20$ ($M \geq 440$), satisfaction of the directional moment conditions lead to physically unrealistic negative weighting factors. Due to this issue, there is an upper limit on the total number of discrete directions that can be used in simulation when these quadratures are considered [Carlson 1971].

2.3.3 Non-Directionally-Limited Quadrature Sets

More recently, DOM quadratures that have no restriction on discrete direction number have been developed, in order to overcome such a major shortcoming [Hunter and Guo 2013].

Two such quadratures, proposed by Longoni and Haghighat [2001] and determined using the Gauss-Legendre quadrature technique [Carlson 1971], are the Legendre-Equal Weight (P_N-EW) and Legendre-Chebyshev (P_N-T_N) quadrature sets. These two quadrature sets have the same level arrangement and direction numbers as previously described for the S_N quadrature, although the directions and weighting factors differ. For both quadrature sets, the values of ξ_i in the principal octant corresponding to the i^{th} level of constant polar angle are taken to be the $N/2$ positive roots of $P_N(x)$, the N^{th}-order Legendre polynomial, with $\xi_1 < \xi_2 < \cdots < \xi_{\frac{N}{2}}$. The weighting factor w_i corresponding to a given direction on the i^{th} polar level is calculated as follows:

$$w_i = \frac{\pi}{\left(\frac{N}{2} - i + 1\right)\left(1 - \xi_i^2\right)\left[\left(\frac{dP_N}{dx}\right)_{x=\xi_i}\right]^2}, \qquad i = 1, \ldots, \frac{N}{2} \tag{2.27}$$

where $\frac{N}{2} - i + 1$ is the total number of equally-weighted directions on each polar level.

For the P_N-EW quadrature, the azimuthal angle is determined using equal partitioning of the octant for a given polar level, whereas for the P_N-T_N quadrature the azimuthal angles on each level are taken as the roots of the Chebyshev polynomials of the first kind. Thus, the azimuthal angle corresponding to the j^{th} direction on the i^{th} polar level becomes:

$$\phi_{i,j} = \begin{cases} \dfrac{j\pi}{2\left[\frac{N}{2} - i + 2\right]}, & P_N - EW \\ \dfrac{\pi[N + 3 - 2i - 2j]}{2[N + 2 - 2i]}, & P_N - T_N \end{cases} \tag{2.28}$$

where $i = 1, \ldots, \frac{N}{2}$ and $j = 1, \ldots, \frac{N}{2} - i + 1$. Once the azimuthal angle is known, the remaining direction cosines μ and η are easily determined through the relationships listed earlier. Both the P_N-EW and P_N-T_N quadrature sets accurately satisfy the zeroth and first order moment

conditions, and the P_N-T_N quadrature also completely satisfies even-moment condition for all direction cosines. The P_N-EW quadrature similarly satisfies even-moment conditions for ξ, but the equipartitioning of azimuthal angle produces noticeable errors in the even-moment summations for μ and η.

Two additional quadrature sets, the Triangle Tessellation (T_N) and Spherical Ring Approximation ($SRAP_N$), which are purely geometric in construction, have been developed as a means of countering directional limitations due to moment condition satisfaction. In the T_N quadrature, developed by Thurgood et al. [1995], the unit sphere surface is divided into $M = 8N^2$ regions, where $N \geq 1$. Construction of the quadrature set can be achieved in three steps:

(1) The principal octant is mapped onto an equilateral basal triangle, with vertices at points (1,0,0), (0,1,0), and (0,0,1)

(2) The equilateral triangle is tessellated into N^2 smaller equilateral triangles, whose side lengths are equal to L/N, where L is the basal triangle side length

(3) The tessellations are mapped from a flat surface onto the unit sphere

Using this method, the direction cosines for each region can be calculated using a simple mapping:

$$\mu = \frac{x_c}{\sqrt{x_c^2 + y_c^2 + z_c^2}}, \qquad \eta = \frac{y_c}{\sqrt{x_c^2 + y_c^2 + z_c^2}}, \qquad \xi = \frac{z_c}{\sqrt{x_c^2 + y_c^2 + z_c^2}} \tag{2.29}$$

where (x_c, y_c, z_c) is the centroid of the tessellated triangle in the basal plane. The weighting factors corresponding to a given discrete direction is calculated as the area of the mapped spherical triangle through which that direction passes. Using reflectional and rotational symmetry, the directions and weights for the remaining octants are easily determined.

Li et al. [1998] introduced a second purely geometric DOM quadrature set, known as the $SRAP_N$, where $N \geq 2$. To determine the quadrature, the surface of the unit sphere in the principal octant is divided into N spherical "rings", with the topmost "ring" reducing to a crown. Working downwards from the crown element, each spherical ring is divided into additional spherical elements. The number of elements in successive spherical rings constitutes an arithmetic progression, starting with two elements in the topmost crown, with every successive ring containing one additional element. Using this manner of division, each element will have an equal solid angle, and thus an equal elemental surface area.

Determination of the discrete directions for a given element entails location of the centroid (x_c, y_c, z_c) of the elemental solid angle. These coordinates are then transformed using Eq. (2.29) into direction cosine form. As with the T_N quadrature, the weighting factors correspond to the elemental surface area. Since all elements in this quadrature set have identical surface areas, every direction is equally weighted. The total number of directions in the $SRAP_N$ quadrature across all octants is $M = 4N(N+3)$, and thus the weighting factor for each discrete direction becomes $w = 4\pi/M$.

Figures 2.8(a-e) depict the principal octant directional distributions and weighting factors for the S_{16}, EO_{16}, P_{16}-T_{16}, T_6, and $SRAP_7$ quadrature sets, respectively [Hunter and Guo 2013]. All quadrature sets have M = 288 discrete directions, except for $SRAP_7$ (M = 280). The weighting factors are indicated by the spectrum shading of each point in the plots. The directional distribution of the T_6 quadrature set reflects the use of triangular elements, and is the only set that does not exhibit specific levels of constant polar angle. It is interesting to note that the magnitude of the maximum weighting factor is very similar for the non-limited

quadrature sets ($w_{max} \sim 0.045 - 0.06$), while the maximum weighting factors are larger for S_N and EO_N ($w_{max} \sim 0.08 - 0.09$).

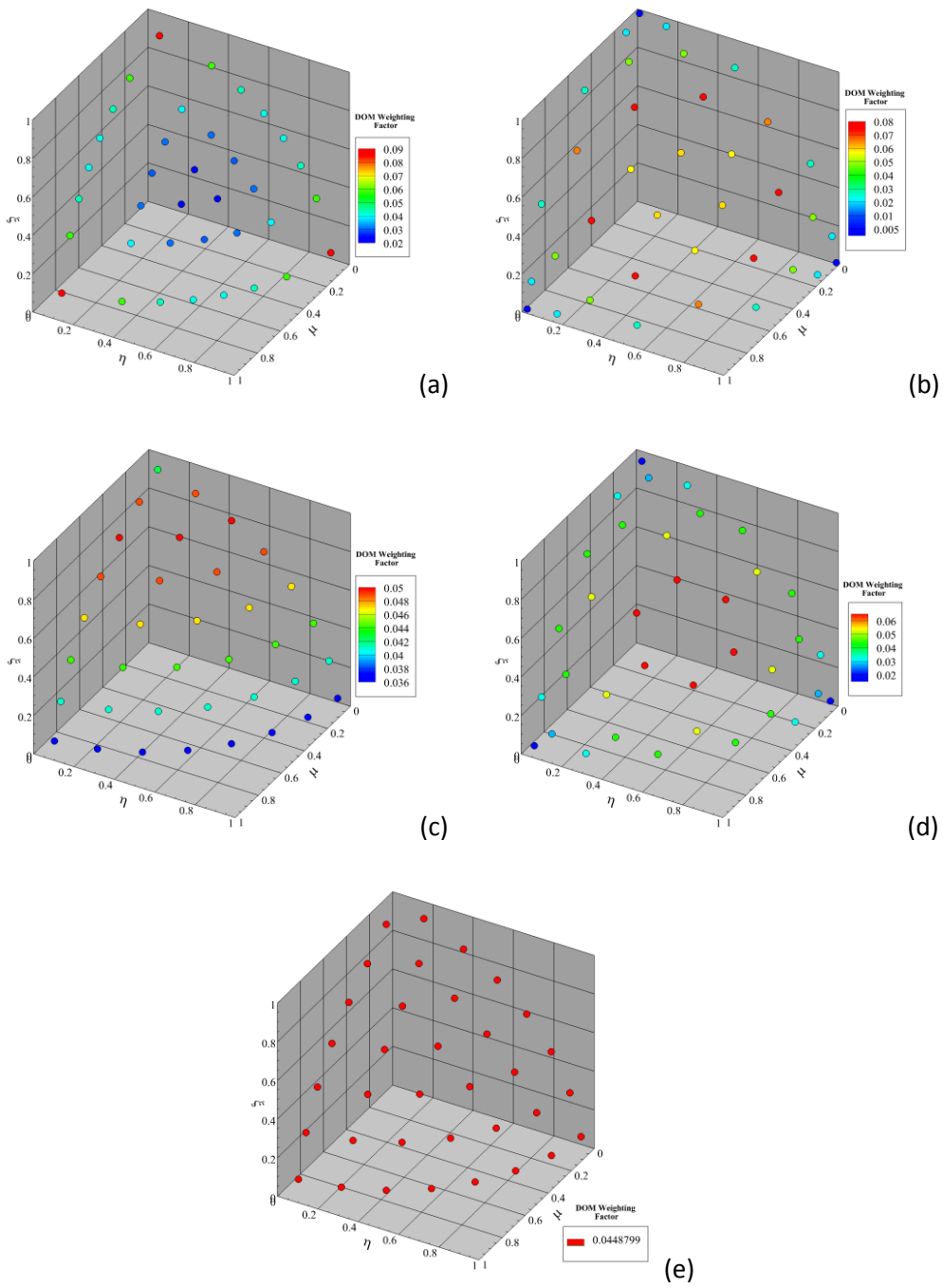

Figure 2.8: Principal octant direction distributions: a) S_{16}, b) EO_{16}, c) P_{16}- T_{16}, d) T_6 e) $SRAP_7$

2.4 Radiation Transfer Predictions using DOM

2.4.1 Validation with Exact Solutions

Comparison of DOM radiation transfer predictions with analytical solutions to the ERT, in simple situations where an analytical solution is possible, is a preferred method of DOM validation. To this end, radiation transfer in two benchmark problems is considered here [Hunter and Guo 2011]. The first test problem involves radiation transfer in a purely absorbing cylindrical medium. For a purely absorbing medium, the single-scattering albedo $\omega = \frac{\sigma_s}{\sigma_a + \sigma_s}$, which is a ratio of scattering efficiency to total extinction efficiency, is equal to 0. The chosen cylindrical enclosure has a unity aspect ratio (i.e., $\frac{R}{H} = 1.0$). The boundary walls are taken to be cold ($T = 0$), diffuse, blackbody emitters (ϵ_w = 1.0, $\rho^d = \rho^s = 0.0$), while the medium is taken to be hot, with a prescribed initial temperature of T_{med}. To simplify analysis, the radial and axial coordinates are nondimensionalized as $r^* = \frac{r}{R}, z^* = \frac{z}{H}$.

Non-dimensional radial heat flux at the radial side wall $Q_R^*(z^*) = Q_R(z^*)/\sigma T_{med}^4$, calculated for three different optical thicknesses $\tau = (\sigma_a + \sigma_s)R = 0.1, 1.0,$ and 5.0, is plotted in Figure 2.9. Due to symmetry, only the range $0 \leq z^* \leq 1.0$ is required for analysis. The steady-state results for the DOM are compared with the readily-available exact solution [Kim 2008], which can be easily calculated using the Beer-Lambert Law [Modest 2002]. The computational grid was divided into $(N_r \text{ x } N_z) = (150 \text{ x } 150)$, in order to minimize errors due to poor spatial discretization, while the DOM S_{16} quadrature is used to better represent the continuous angular variation of radiation scattering. To minimize computational time for this steady-state case, the time derivative in Eq. (2.9a) was ignored.

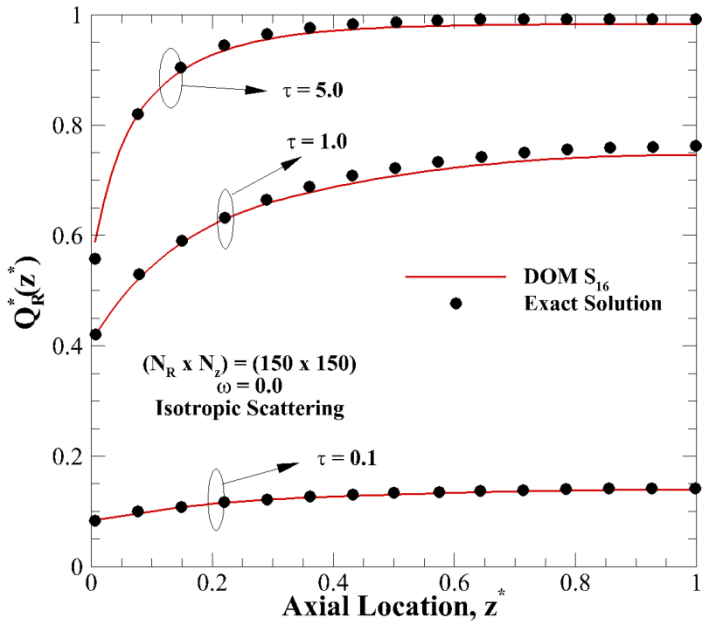

Figure 2.9: Comparison of steady-state $Q_R^*(z^*)$ generated using DOM with exact solution [Kim 2008] in purely absorbing medium for various optical thicknesses

As seen in Figure 2.9, the present solution generated using the DOM is found to be accurate when compared to the exact solution. For all optical thicknesses, the maximum discrepancy between the DOM and exact solution occurs at $z^* = 1.0$, with maximum percent differences of 0.85%, 2.14%, and 1.69% seen for $\tau = 0.1, 1.0,$ and 5.0, respectively. Due to the inherent need to discretize in both the spatial and angular domain, errors of this small magnitude between numerical and analytical solutions are well within the range of acceptability.

The second benchmark problem analyzed for DOM validation is that of a purely scattering medium ($\omega = 1.0$) in a 2-D, square enclosure, with side length L. DOM solutions for such an enclosure can be determined following the procedure outlined in Section 2.2.2, provided that all terms involving the z-direction are removed. Non-dimensionalization of the

spatial coordinates $x^* = x/L$, $y^* = y/L$ is implemented. The optical thickness of the medium is set at $\tau = 1.0$, and scattering is taken to be isotropic. All walls are taken to be diffuse, blackbody emitters. The medium, and three walls are taken as cold, while the wall at x^* = 0.0 is taken to be hot, with unity emissive power ($E_{bw} = \sigma T_w^4$ = 1.0).

A comparison of steady-state, non-dimensional heat flux Q generated using the DOM with the readily-available exact solution [Crosbie and Schrenker 1984] is presented in Figure 2.10. The heat flux is non-dimensionalized by the wall emissive power. Heat fluxes at both the source wall ($x^* = 0$) and the opposite wall ($x^* = 1.0$) are presented. The spatial grid implemented for the analysis is (N_x x N_y) = $(107 \text{ x } 107)$, and results are presented both for the S_{16} and EO_{16} quadratures.

Heat fluxes generated at the source wall with both DOM quadratures are accurate within 0.50% (at maximum) to the exact solution, and the S_{16} and EO_{16} results differ from each other by a maximum of 0.22%. At x^* = 1.0, both S_{16} and EO_{16} are accurate to within 1% near the wall center ($y^* = 0.5$). However, differences of up to 7% between S_{16} and EO_{16} exist, due to physically unrealistic bumps in the S_{16} profile. In general, the EO_{16} quadrature predicts more accurately (~2.5% at maximum) to the exact solution than S_{16} (~8.0% at maximum), which may be due in part to the better satisfaction of higher-order odd-moment conditions, as described in Section 2.3.2.

Figure 2.11 presents transient heat flux profiles for the same benchmark problem as Figure 2.10, in order to gauge the impact of non-dimensional time $t^* = c\Delta t/L$ on DOM heat flux predictions. The computational grid used in the transient simulation is (N_x x N_y) = $(57 \text{ x } 57)$, and thus the non-dimensional time-step is taken to be $\Delta t^* = 0.07$, in order to satisfy $\Delta t^* \leq \min(\Delta x^*, \Delta y^*)$. DOM heat flux profiles are presented using the EO_{16} quadrature for four non-

dimensional times: $t^* = 0.375, 0.75, 1.5,$ and 7.5. The exact steady-state solution of Crosbie and Schrenker [1984] is also plotted as a reference.

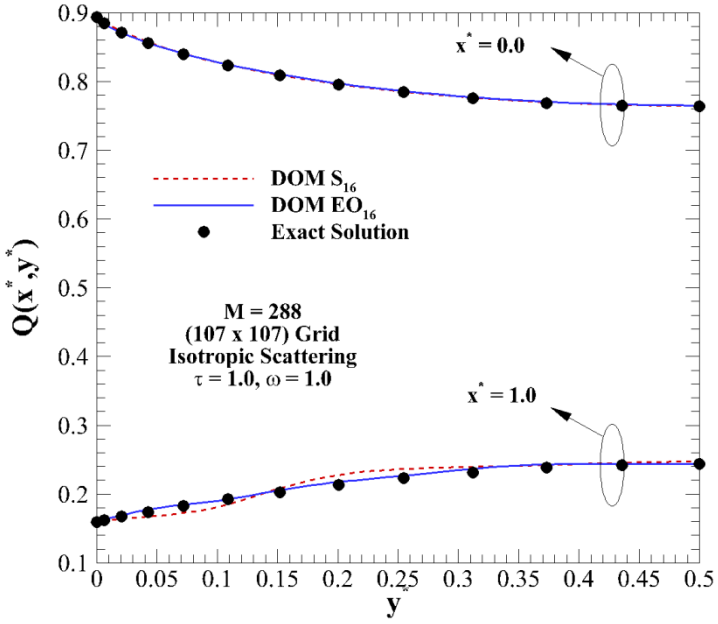

Figure 2.10: Comparison of steady-state Q(x*, y*) generated using DOM with exact solution [Crosbie and Schrenker 1984] in purely scattering medium

At the source wall ($x^* = 0.0$), the non-dimensional heat flux Q starts at a value near unity, and decreases for all times t^*, corresponding to radiant energy propagation into the medium and away from the wall. At the opposite wall (x^* = 1.0), heat flux is initially zero, and increases with increasing t^*, corresponding to radiant energy propagation into the wall. Heat flux is negligible at the early nondimensional times, due to the fact that the radiant energy has not had enough time to propagate through the medium. As time increases, and radiant energy makes its way to the enclosure wall, heat flux rapidly increases towards the exact steady-state solution. For both the source and opposite wall, heat flux profiles generated at large t^* match

accurately to the exact solution of Crosbie and Schrenker [1984], and exactly match the steady-state solution generated when the time-derivative is dropped from the ERT.

All in all, the accuracy of DOM predictions in both the absorbing cylinder (Figure 2.9) and the scattering square medium (Figures 2.10 and 2.11) to exact solutions of the ERT provide the necessary validation for use of the DOM in predicting radiation transfer.

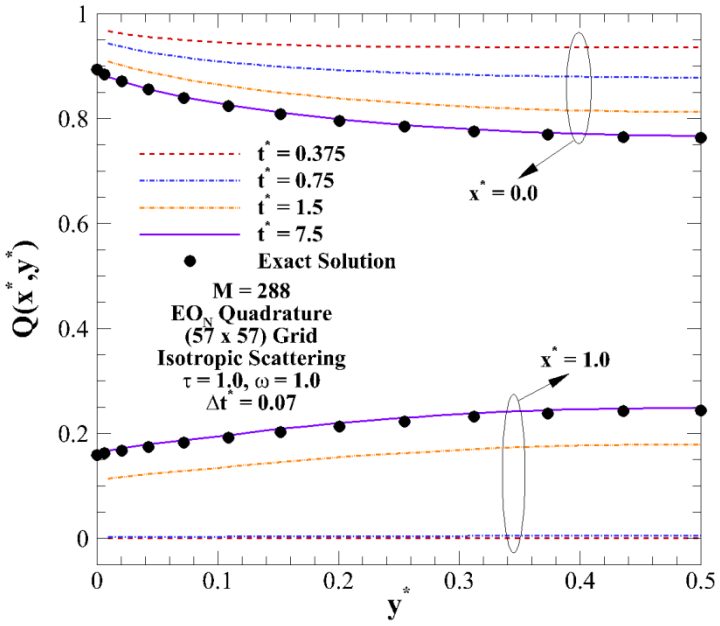

Figure 2.11: Transient comparison of $Q(x^*, y^*)$ generated using DOM with exact solution [Crosbie and Schrenker 1984] in purely scattering medium at various non-dimensional times t^*

2.4.2 Radiation Transfer in Solar Absorber Tube

The use of solar energy in place of traditional fossil fuels has become a largely researched area in the past two decades, due to governmental and environmental concerns over pollution and global warming. In solar reactors and power plants, solar radiation is absorbed by solar absorber tubes via the use of reflectors and concentrators [Li et al. 2010, Wang et al. 2010], in order to heat a working fluid, such as molten salt or thermal oil. Many

different materials can be added to the inside of an absorber tube, in order to increase thermal efficiency of the solar power plant [Karni et al. 1998] by allowing for higher working temperatures and large solar fluxes.

Radiation transfer in a solar absorber tube is analyzed here using the DOM [Hunter and Guo 2014a], with a parametric study performed to gauge how different material properties impact the absorption of radiative energy. Radiation transfer in an absorber tube component in a solar energy power plant is modeled using an axisymmetric cylindrical enclosure containing a homogeneous participating medium, with optical thickness $\tau = (\sigma_a + \sigma_s)R$, scattering albedo ω, asymmetry factor g, and inner radial wall surface emissivity ϵ_w. The absorber tube has radius R and length L. To account for the neglecting of end effects (because a real absorber tube is quite long), the end walls of the tube are treated as mirrors (i.e., perfectly specular reflecting with $\rho_w^s = 1.0$). Use of mirror conditions at the end wall also means that changes in tube aspect ratio can be neglected. Solar radiant heating is approximated as a diffuse boundary condition on the side wall of the enclosure ($\rho_w^s = 0,\ \rho_w^d = 1 - \epsilon_w$), with temperature T_w typically in the range between 500K and 1200K in a real solar absorber, depending on the receiver condition. The wall of the absorber tube is usually metallic and thin, so that heat loss due to conduction through the wall is negligible. Moreover, the medium is assumed to be cold throughout to show solar radiative heat transfer only.

In Figures 2.12-2.15, the impact of variation in asymmetry factor, optical thickness, scattering albedo, and wall emissivity on non-dimensional radiative energy absorption rate $g_{rad}^* = (\nabla \cdot q_r)R/(4\pi I_{bw})$, where the energy deposition $\nabla \cdot q_r$ is calculated using Eq. 2.20 and non-dimensionalized by the wall emissive power and absorber tube radius. The spatial grid used for the simulations is $(N_r \text{ x } N_z)$ = 40 x 40, and the DOM EO_{16} quadrature set is implemented, in order to limit errors due to poor odd moment-condition satisfaction.

Figure 2.12 plots the variation of radiative energy absorption rate with non-dimensional r^* for absorber materials with different asymmetry factors g. The absorber material has a specified optical thickness τ = 10.0, scattering albedo $\omega = 0.92$, and radial wall emissivity $\epsilon_w = 0.92$. Variations in asymmetry factor between g = 0.4 and 0.927323 are achieved by varying the medium scattering phase function among the seven Legendre-polynomial functions shown in Figure 2.4a.

Near the center of the tube (r^* = 0), the amount of energy absorbed by the medium increases as asymmetry factor increases. This is due to the fact that as scattering becomes more highly anisotropic, radiant energy is scattered away more strongly from the heated absorber tube wall, leading to higher intensity values near the radial centerline, and lower intensity values near the heat source. This explains the opposite trend at the tube surface, where the largest radiative energy absorption rate occurs for the smallest g. A higher absorption rate near the tube center is paramount, in order to provide more energy to the working fluid for later use in a solar power plant. Thus, a material that scatters energy in a strongly-forward manner is desirable for lining the inside of a solar absorber tube.

Figure 2.13 examines the impact of optical thickness on radial profiles of non-dimensional radiative energy absorption rate. The side-wall emissivity and scattering albedo are kept constant at $\epsilon_w = 0.99$ and $\omega = 0.92$, while the scattering phase function applied is the 27-term g = 0.927323, as Figure 2.12 showed that increase in g leads to increased energy absorption. Near the heated surface, increases in optical thickness produce increases in energy absorption rate. For optical thickness less than τ = 10.0, radiant energy is able to propagate strongly throughout the entire medium, leading to flatter radial energy absorption rate profiles. Conversely, for an extremely thick medium with τ = 100, the energy absorption rate at the side wall is five orders of magnitude higher than at the radial centerline. For these properties, the

optimal optical thickness is $\tau \cong 10$, as that provides the largest absorption rate near the tube center.

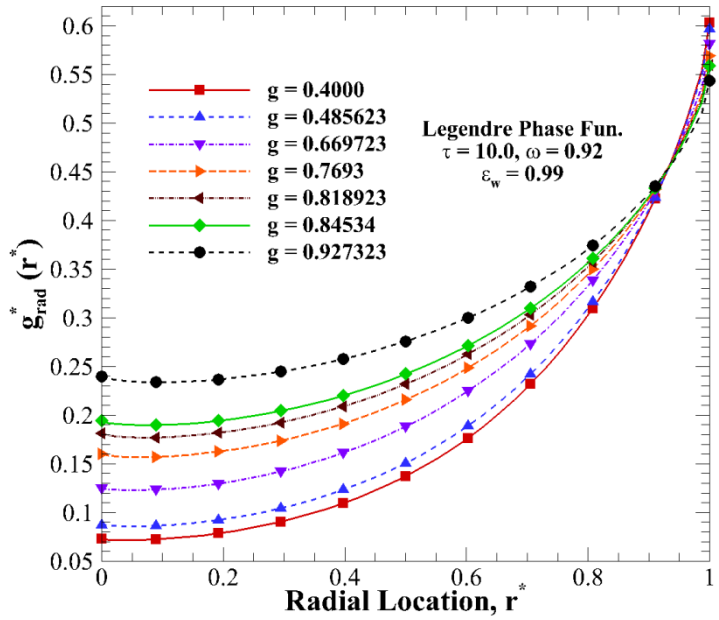

Figure 2.12: Radiative energy absorption rate vs. radial location with varying asymmetry factor

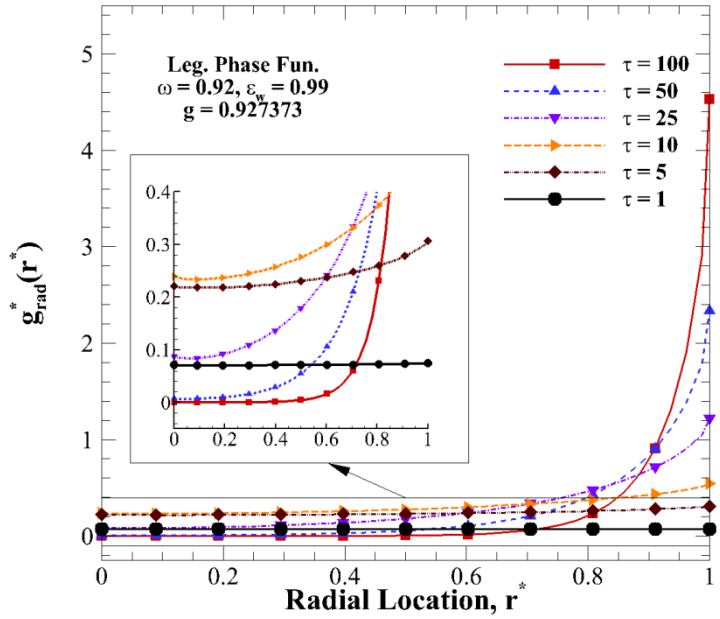

Figure 2.13: Radiative energy absorption rate vs. radial location for various optical thicknesses with g = 0.927323

The variation of $g_{rad}^{*}(r^{*})$ with medium scattering albedo ω is presented in Figures 2.14a and 2.14b. The optical thickness is set at $\tau = 1.0$ in Figure 2.14a, and τ = 10.0 in Figure 2.14b. The side wall emissivity and asymmetry factor are kept constant at ϵ_w = 0.92 and g = 0.927323. For the thinner medium in Figure 2.14a, we see that increases in scattering albedo produce decreases in energy absorption rate for all radial locations, due to the fact that an increase in scattering albedo directly corresponds to a reduction in the medium's ability to absorb radiant energy. For the optically thicker medium in Figure 2.14b, the energy absorption rate is highly concentrated near the heated wall, excluding the case where ω = 0.98. For the thinner medium, the optical scattering albedo is $\omega \cong$ 0.68, while $\omega \cong$ 0.92 is optimal for maximization of radiative energy absorption near the radial centerline.

Finally, the impact of absorber wall emissivity ϵ_w on absorption rate is analyzed in Figure 2.15. Optical thickness and scattering albedo are kept constant at τ = 10.0 and ω = 0.92, while asymmetry factors of g = 0.4, 0.7693, and 0.927323 are applied. The emissivity of the wall is varied between ϵ_w = 0.80, 0.90, and 0.99. For all asymmetry factors, energy absorption rate increases with increasing wall emissivity. For lower asymmetry factors, the difference in energy absorption between the three emissivities is small, while an increase in asymmetry factor leads to an increase in energy absorption rate difference between ϵ_w= 0.99 and ϵ_w = 0.80. It is clear that, in order to maximize absorption rate near the tube center, a higher wall emissivity is desired.

In general, overall energy absorption near the absorber tube center (i.e., the location of the flowing working fluid in a solar power plant) increases with increasing medium optical thickness, wall emissivity and asymmetry factor, and decreases for increasing scattering albedo.

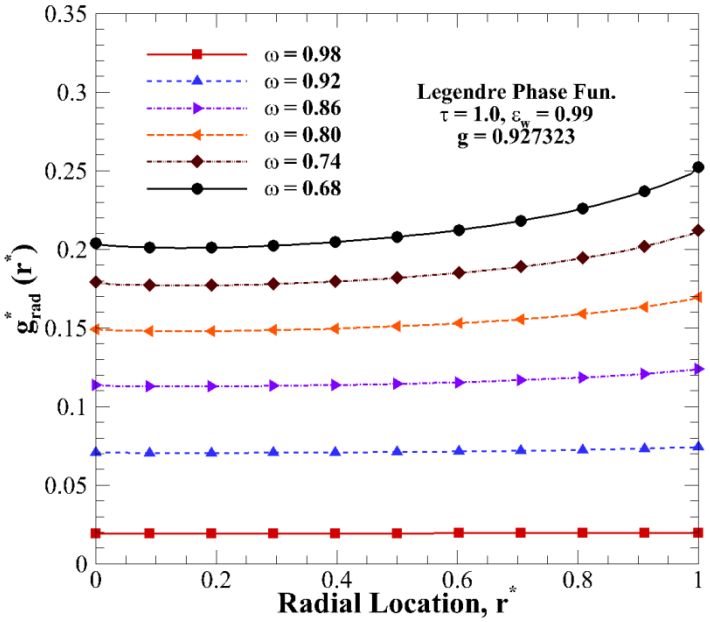

(a)

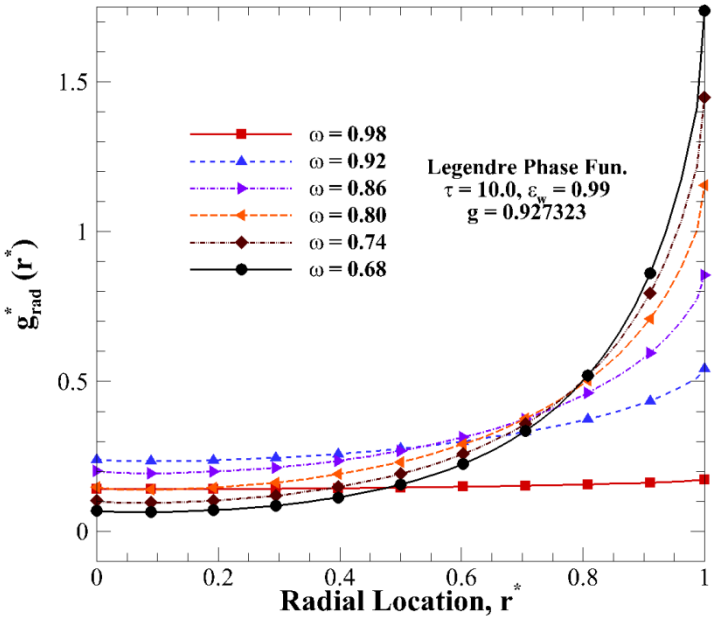

(b)

Figure 2.14: Radiative energy absorption rate vs. radial location for various scattering albedos with g = 0.927323 and a) τ = 1 and b) τ = 10

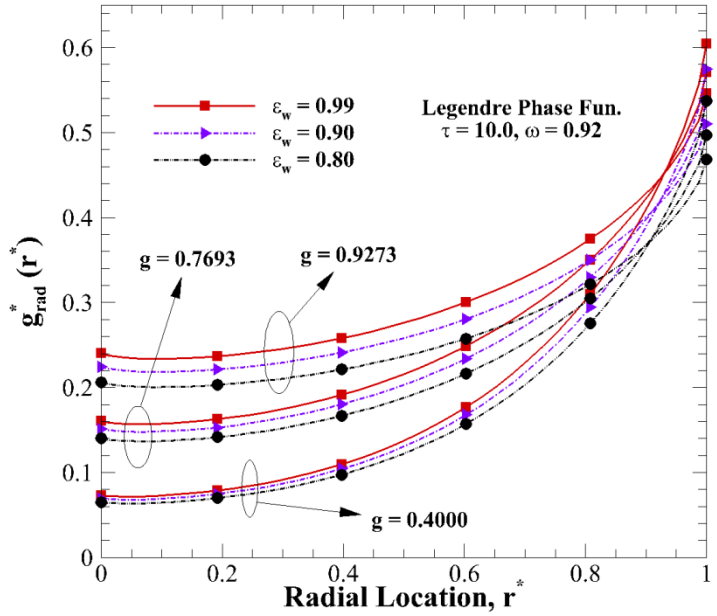

Figure 2.15: Radiative energy absorption rate vs. radial location for varying side wall emissivity

2.5 Summary

In Chapter 2, the formulation for solution of the time-dependent, hyperbolic Equation of Radiation Transfer (TERT) using the Discrete-Ordinates Method (DOM) is presented for both 2-D axisymmetric cylindrical enclosures and 2-D/3-D enclosures described using Cartesian coordinates. Discretization equations for the DOM are developed using the control-volume method, and the marching solution procedure is discussed. Types of approximations to the Mie scattering phase-function, which are more computationally efficient than exact implementation, are introduced. A discussion on the requirements of DOM quadrature (discrete directions) is outlined, with the major issue of directional limitation for typical level-symmetric quadratures stressed. DOM solutions in both purely absorbing and scattering media are compared to readily available exact solutions, as a method of validation. Finally, a parametric study of material properties in a solar absorber tube is presented using the DOM, in order to visualize the impact of optical thickness, scattering albedo, wall emissivity, and asymmetry factor on radiative energy

absorption. It is found that the DOM is able to accurately predict radiation transfer with minimal error.

CHAPTER 3 : THE FINITE VOLUME METHOD

3.1 Solution of ERT Using the Finite Volume Method

3.1.1 2-D Axisymmetric Cylindrical Medium

The FVM discretization equation can be determined using a control-volume approach. The TERT of Eq. (2.1) is integrated over an arbitrary control volume, defined by volume ΔV and solid angle $\Delta\Omega^l$ [Chai and Patankar 2000], as follows:

$$\frac{1}{c}\frac{\partial}{\partial t}\int_{\Delta\Omega^l}\int_{\Delta V}(I^l)dVd\Omega^l + \int_{\Delta\Omega^m}\int_{\Delta V}(\nabla\cdot\hat{\boldsymbol{s}})I^l dVd\Omega^l = \int_{\Delta\Omega^l}\int_{\Delta V}[-(\sigma_a+\sigma_s)I^l + S^l]\,dVd\Omega^l \tag{3.1}$$

where $\hat{\boldsymbol{s}}\cdot\nabla I^l = (\nabla\cdot\hat{\boldsymbol{s}})I^l$ and , $I^l = I(r,\hat{\boldsymbol{s}}^{\boldsymbol{l}},t)$ A typical control volume for an axisymmetric cylindrical enclosure is shown in Figure 3.1, and the discrete solid angle $\Delta\Omega^l$ corresponding to radiation direction $\hat{\boldsymbol{s}}^{\boldsymbol{l}}$ is shown in Figure 3.2 [Hunter and Guo 2011]. Through use of Gauss' divergence theorem [Chai et al. 1994], the second volume integral can be rewritten as an area integral, and Eq. (3.1) can be rewritten as follows:

$$\frac{1}{c}\frac{\partial}{\partial t}\int_{\Delta\Omega^l}\int_{\Delta V}(I^l)dVd\Omega^l + \int_{\Delta\Omega^m}\int_{\Delta A}I^l\left(\hat{\boldsymbol{s}}^l\cdot\hat{\boldsymbol{n}}\right)dAd\Omega^l = \int_{\Delta\Omega^l}\int_{\Delta V}[-(\sigma_a+\sigma_s)I^l + S^l]\,dVd\Omega^l \tag{3.2}$$

Under the assumption that intensity is constant within a given control volume and control solid angle, Eq. (3.2) can be expressed as follows, for discrete direction $\hat{\boldsymbol{s}}^{\boldsymbol{l}}$:

$$\frac{1}{c}\frac{\partial I^l}{\partial t}\Delta V\Delta\Omega^l + \sum_i I_i^l\Delta A_i D_i^l = -(\sigma_a+\sigma_s)I^l\Delta V\Delta\Omega^l + S^l\Delta V\Delta\Omega^l \tag{3.3}$$

where the area integral has been replaced by a summation over the i faces of the given control volume, and ΔA_i is the surface area of control-volume face i. For the control volume in Figure

3.1, the facial areas and volume can be calculated as follows: $\Delta A_n = r_n \Delta\phi \Delta z, \Delta A_s = r_s \Delta\phi \Delta z$, $\Delta A_t = \Delta A_b = 0.5 * (r_n^2 - r_s^2)\Delta\phi, \Delta A_e = \Delta A_w = \Delta r \Delta z$, and , $\Delta V = \Delta A_t \Delta z$.

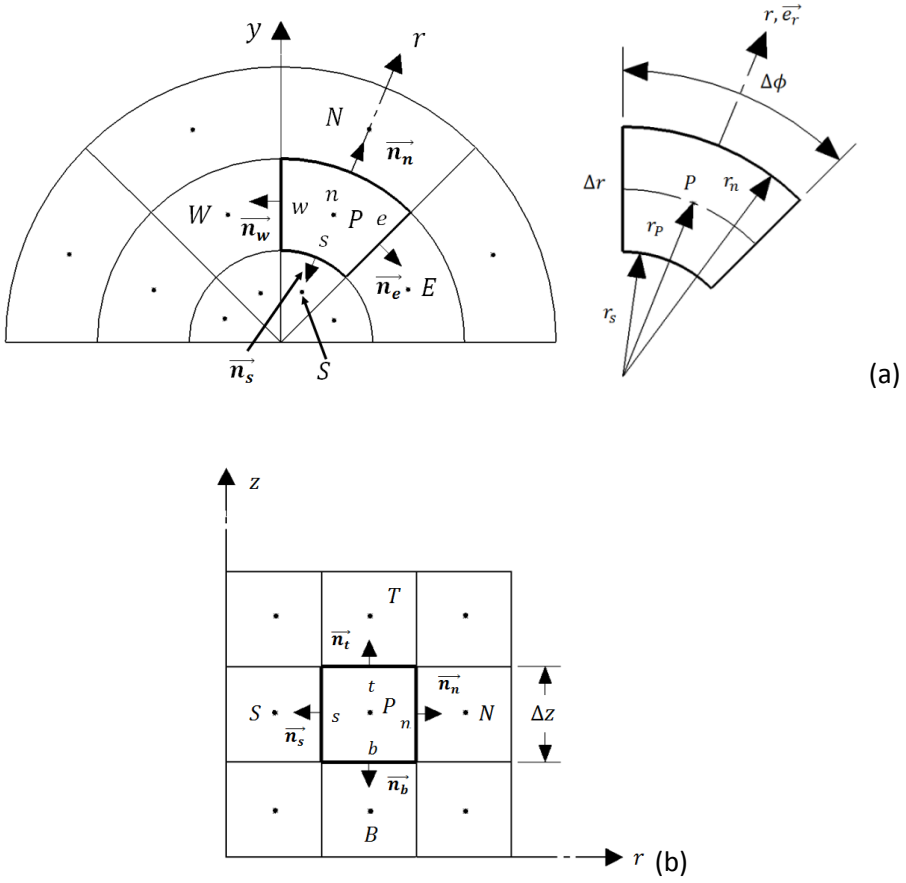

Figure 3.1: Schematics of a typical control-volume: (a) top view (b) side view in r-z plane

The discrete solid angle $\Delta\Omega^l$, as shown in Figure 3.2, is defined as:

$$\Delta\Omega^l = \int_{\Delta\Omega^l} d\Omega^l = \int_{\phi^{l-}}^{\phi^{l+}} \int_{\theta^{l-}}^{\theta^{l+}} \sin\theta \, d\theta \, d\phi = (\cos\theta^{l-} - \cos\theta^{l+})(\phi^{l+} - \phi^{l-}) \tag{3.4}$$

where $\phi^{l+}, \phi^{l-}, \theta^{l+}$, and θ^{l-} are the azimuthal and polar angles defining the edges of the discrete solid angle. The source term S^l is calculated as follows:

$$S^l = \sigma_a I_{bk} + \frac{\sigma_s}{4\pi}\left(\sum_{l'=1}^{M} \bar{\Phi}^{l'l}\, I^{l'} \Delta\Omega^{l'} + \sum_{B} I^B \bar{\Phi}^{l^B l}\right) \tag{3.5}$$

where $\bar{\Phi}^{l'l}$ is the average scattering phase function between discrete direction $\hat{\boldsymbol{s}}^{\boldsymbol{l'}}$ and $\hat{\boldsymbol{s}}^{\boldsymbol{l}}$. The directional weight at control volume face i in direction $\hat{\boldsymbol{s}}^{\boldsymbol{l}}$, represented by the symbol D_i^l, is an analog to the discrete direction weight w^l in the DOM, and can be calculated for each control volume face using the following integral expansion:

$$D_i^l = \int_{\phi^{l-}}^{\phi^{l+}} \int_{\theta^{l-}}^{\theta^{l+}} \left(\hat{\boldsymbol{s}}^l \cdot \hat{\boldsymbol{n}}_i\right) \sin\theta \; d\theta \; d\phi \tag{3.6}$$

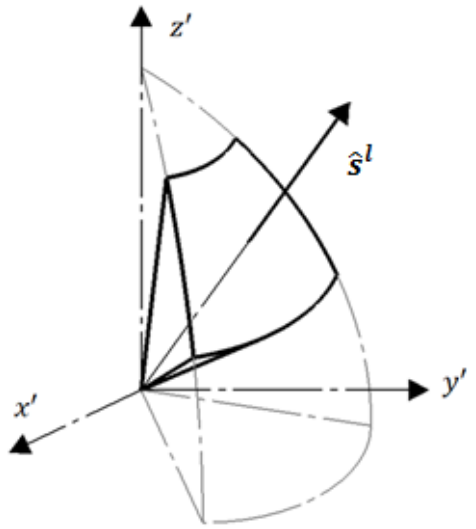

Figure 3.2: Discrete solid angle $\Delta\Omega^l$

For the "north" face in the control volume shown in Figure 3.1 ($i = n$), the normal vector is $\hat{\boldsymbol{n}}_n = \overrightarrow{e_r}$, and thus the dot product $\hat{\boldsymbol{s}}^l \cdot \hat{\boldsymbol{n}}_n = \sin\theta\cos\phi$. Substituting into Eq. (3.6), the north directional weight becomes:

$$D_n^l = \left(\sin\phi^{l^+} - \sin\phi^{l^-}\right) * \left[\frac{1}{2}\left(\theta^{l^+} - \theta^{l^-}\right) - \frac{1}{4}\left(\sin 2\theta^{l^+} - \sin 2\theta^{l^-}\right)\right] \tag{3.7}$$

Using this notion, the directional weights for the other remaining control-volume faces in Figure 3.1 become:

$$D_s^l = -D_n^l = \left(\sin\phi^{l^-} - \sin\phi^{l^+}\right) * \left[\frac{1}{2}\left(\theta^{l^+} - \theta^{l^-}\right) - \frac{1}{4}\left(\sin 2\theta^{l^+} - \sin 2\theta^{l^-}\right)\right] \tag{3.8a}$$

$$D_t^l = -D_b^l = \left(\phi^{l+} - \phi^{l-}\right) * \left[\frac{1}{2}\left(\sin^2\theta^{l+} - \sin^2\theta^{l-}\right)\right] \tag{3.8b}$$

$$D_e^l = \left(\cos\phi^{l+1} - \cos\phi^{l}\right)\left[\frac{1}{2}\left(\theta^{l^+} - \theta^{l^-}\right) - \frac{1}{4}\left(\sin 2\theta^{l^+} - \sin 2\theta^{l^-}\right)\right] \tag{3.8c}$$

$$D_w^l = \left(\left(\cos\phi^{l-1} - \cos\phi^{l}\right)\right)\left[\frac{1}{2}\left(\theta^{l^+} - \theta^{l^-}\right) - \frac{1}{4}\left(sin\, 2\theta^{l^+} - sin\, 2\theta^{l^-}\right)\right] \tag{3.8d}$$

In the directional weights for the "east" and "west" face, ϕ^{l+1} corresponds to the azimuthal angle for the discrete direction on the next azimuthal level, where $\phi^{(l+1)-} = \phi^{l+}$ in Figure 3.3. Conversely, ϕ^{l-1} corresponds to the azimuthal angle for the discrete direction on the previous azimuthal level, where $\phi^{(l-1)+} = \phi^{l-}$ in Figure 3.3. Further explanation of these directional weights is presented by Kim [1998].

A special consideration is required when describing the scattering phase function for the FVM [Chai and Patankar 2000]. The average scattering phase function from solid angle $\Delta\Omega^{l'}$ into solid angle $\Delta\Omega^{l}$ can be accurately calculated as [Chui et al. 1992]:

$$\overline{\Phi}^{l'l} = \frac{1}{\Delta\Omega^{l'}\Delta\Omega^{l}} \sum_{l_s=1}^{M_s} \sum_{l_s'=1}^{M_s^l} \Phi^{l_s' l_s} \Delta\Omega^{l_s'} \Delta\Omega^{l_s} \tag{3.9}$$

where the solid angles $\Delta\Omega^{l'}$ and $\Delta\Omega^{l}$ have been subdivided into M_s' and M_s smaller sub-angles $\Delta\Omega^{l_s'}$ and $\Delta\Omega^{l_s}$, respectively. The importance of this approach will be later discussed in Chapter 4. An illustration of the solid-angle splitting technique is shown in Figure 3.4.

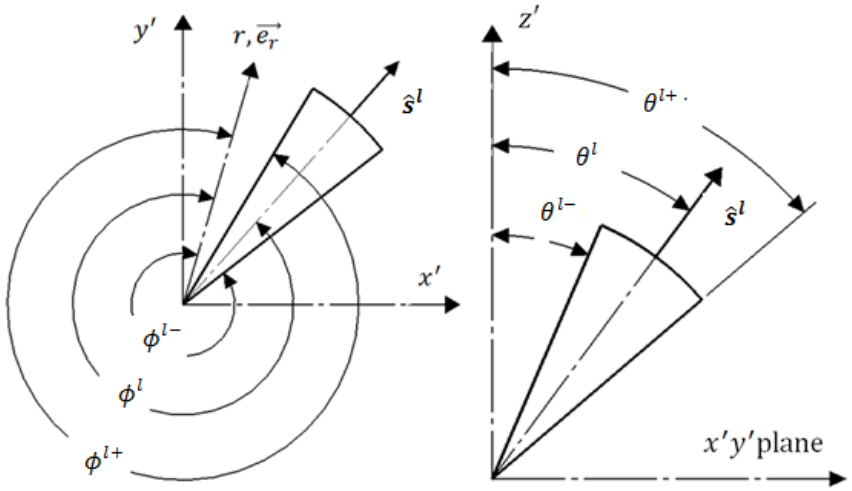

Figure 3.3: Definitions of polar and azimuthal edge angles for a discrete solid angle

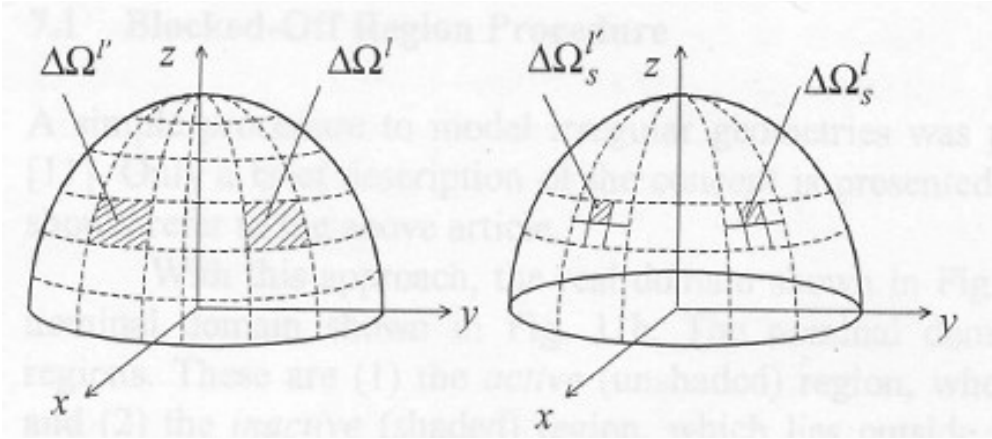

Figure 3.4: Illustration of solid-angle splitting for average scattering phase function (reproduced from Chai and Patankar [2000]

Using a control-volume approach, and further expanding Eq. (3.3) over the control volume in Figure 3.1, the discretization equation for the FVM becomes:

$$\frac{1}{c\Delta t}\left(I_P^l - I_P^{l0}\right)\Delta V \Delta\Omega^l + I_n^l \Delta A_n D_n^l + I_s^l \Delta A_s D_s^l + I_t^l \Delta A_t D_t^l + I_b^l \Delta A_b D_b^l + I_e^l \Delta A_e D_e^l + I_w^l \Delta A_w D_w^l = -(\sigma_a + \sigma_s) I_P^l \Delta V \Delta\Omega^l + S_P^l \Delta V \Delta\Omega^l \tag{3.10}$$

As outlined in the DOM, the temporal derivative is approximated using a forward-difference in time.

Eq. (3.10) is more readily solvable if it is written in terms of nodal intensities $I = N, S, T, B, E, W$, as opposed to facial intensities $i = n, s, t, b, e, w$ [Ben Salah et al. 2004]. There are many possible schemes to relate nodal intensities to facial intensities, in order to transform Eq. (3.10) into the desired form. The simple step scheme, which guarantees universally that all intensities will remain positive during the iterative solution process, relates the nodal intensities I_I to the facial intensities I_i in the following manner [Modest 2002]:

$$I_i^l D_i^l = I_P^l \max\left(D_i^l, 0\right) - I_I^l \max\left(D_i^l, 0\right) \tag{3.11}$$

Use of the maximum function allows for Eq. (3.11) to be appropriate regardless of sweep direction.

Special treatment is required for the faces $i = e, w$. In the step scheme, the west facial intensity is a known quantity, due to the sweeping scheme, where the west face on the current control volume is the east face of the previous control volume in the sweep. The east facial intensity is unknown, and is approximated in the step scheme as the intensity at the center of the current control volume. Thus, the east and west facial intensities become:

$$I_e^l = I_P^l \quad , \qquad I_w^l = I_W = I_P^{l-1} \tag{3.12}$$

where the superscript $l-1$ designates that the nodal intensity be taken from the previous control volume in the azimuthal angle sweep.

Applying the relationships of Eq. (3.11) and (3.12) to Eq. (3.10) leads to the following equation for the intensity in discrete direction $\hat{\boldsymbol{s}}^{\boldsymbol{l}}$ at nodal center:

$$I_P^l = \frac{\left[\alpha_N I_N^l + \alpha_S I_S^l + \alpha_T I_T^l + \alpha_B I_B^l - \Delta A_w D_w^l I_P^{l-1} + (\sigma_a + \sigma_s) S_P^l \Delta V \Delta\Omega^l + \frac{\Delta V \Delta\Omega^l}{c\Delta t} I_P^{l0}\right]}{\frac{\Delta V \Delta\Omega^l}{c\Delta t} + \sum_{i=n,s,t,b} \max\left(\Delta A_i D_i^l, 0\right) + (\sigma_a + \sigma_s)\Delta V \Delta\Omega^l + \Delta A_e D_e^l} \tag{3.12a}$$

$$\alpha_I^l = \max(-\Delta A_i D_i^l, 0) \tag{3.12b}$$

$$S_P^l = \sigma_a I_{bk,P} + \frac{\sigma_s}{4\pi} \sum_{l'=1}^{M} \bar{\Phi}^{l'l} I_P^{l'0} \Delta\Omega^{l'} \tag{3.12c}$$

The formulation in Eqs. (3.12a-c) is valid for all sweep directions. As an illustration, if we are sweeping inward from the radial side wall and downward from the top surface, i.e. $D_n^l < 0, D_t^l < 0$, Eq. (3.12a) would reduce to the following:

$$I_P^l = \frac{\left[-\Delta A_n D_n^l I_N^l - \Delta A_t D_t^l I_T^l - \Delta A_w D_w^l I_P^{l-1} + (\sigma_a + \sigma_s) S_P^l \Delta V \Delta\Omega^l + \frac{\Delta V \Delta\Omega^l}{c\Delta t} I_P^{l0}\right]}{\frac{\Delta V \Delta\Omega^l}{c\Delta t} + \Delta A_s D_s^l + \Delta A_b D_b^l + (\sigma_a + \sigma_s)\Delta V \Delta\Omega^l + \Delta A_e D_e^l} \tag{3.13}$$

where I_N^l, I_T^l, and I_P^{l-1} are known intensities from either prescribed boundary conditions or intensity calculation at previous adjacent control volumes. The sweeping scheme and iterative solution procedure is identical to that outlined in the previous chapter for the DOM, so it will not be repeated here.

After the intensity field is generated, heat fluxes in the radial and axial directions can be calculated as follows:

$$Q_r = \sum_{l=1}^{M} I^l \, D_n^l \quad , \quad Q_z = \sum_{l=1}^{M} I^l D_t^l \tag{3.14}$$

while the incident radiation G can be calculated as

$$G = \sum_{l=1}^{M} I^l \, \Delta\Omega^l \tag{3.15}$$

3.1.2 3-D Cubic (Cartesian) Enclosure

In Cartesian coordinates, the ERT is expanded over the control volume shown previously in Figure 2.6. The expanded equation is exactly the same as Eq. (3.3) above, while the discretization equation of Eq. (3.10) is also still valid. The expressions for the weighting factors D_i^l are also identical to those listed in Eqs. 3.7 and 3.8(a-d), with the only difference being that the azimuthal angles ϕ^{l-}, ϕ^l, and ϕ^{l+} are measured from the x'-axis in Figure 3.3, as opposed to the r-axis, as shown for the axisymmetric cylindrical medium.

Applying the step scheme of Eq. (3.11) to all facial intensities $i = e, w, n, s, t, b$, the discretization equation of Eq. (3.10) can be rewritten as follows:

$$I_P^l = \frac{\left[\sum_{I=N,S,T,B,E,W} \alpha_I I_I^l + (\sigma_a + \sigma_s) S_P^l \Delta V \Delta\Omega^l + \frac{\Delta V \Delta\Omega^l}{c\Delta t} I_P^{l0}\right]}{\frac{\Delta V \Delta\Omega^l}{c\Delta t} + \sum_{i=n,s,t,b,e,w} \max\left(\Delta A_i D_i^l, 0\right) + (\sigma_a + \sigma_s)\Delta V \Delta\Omega^l} \tag{3.16a}$$

$$\alpha_I^l = \max(-\Delta A_i D_i^l, 0) \tag{3.16b}$$

$$S_P^l = \sigma_a I_{bk,P} + \frac{\sigma_s}{4\pi} \sum_{l'=1}^{M} \bar{\Phi}^{l'l} I_P^{l'0} \Delta\Omega^{l'} \tag{3.16c}$$

where the major difference from the axisymmetric cylindrical enclosure is that the "east" and "west" faces now are treated in the same way as the remaining faces. For the sweep case where $D_n^l > 0, D_t^l < 0$, and $D_e^l < 0$ (which is one of eight possible combinations), the expression for I_P^l becomes:

$$I_P^l = \frac{\left[-\Delta A_s D_s^l I_S^l - \Delta A_t D_t^l I_T^l - \Delta A_e D_e^l I_E^l + (\sigma_a + \sigma_s) S_P^l \Delta V \Delta\Omega^l + \frac{\Delta V \Delta\Omega^l}{c\Delta t} I_P^{l0}\right]}{\frac{\Delta V \Delta\Omega^l}{c\Delta t} + \Delta A_s D_s^l + \Delta A_b D_b^l + \Delta A_w D_w^l + (\sigma_a + \sigma_s)\Delta V \Delta\Omega^l} \tag{3.17}$$

where I_S^l, I_T^l, and I_E^l are the known upstream intensities.

Heat fluxes in the x-, y-, and z- directions are calculated as:

$$Q_x = \sum_{l=1}^{M} I^l D_n^l \quad , \qquad Q_y = \sum_{l=1}^{M} I^l D_e^l \, , \qquad Q_z = \sum_{l=1}^{M} I^l D_t^l \tag{3.18}$$

while the incident radiation G can still be determined using Eq. (3.15).

3.2 FVM Quadrature

Unlike the DOM, in which the quadrature set is specifically developed to satisfy certain moment equations, FVM quadrature is extremely flexible and arbitrary, due to the direct integration of the ERT and direct use of discrete solid angles. One common method of generating FVM discrete directions is to divide the total solid angle of 4π steradians using uniform division of both the polar and azimuthal angles [Chai et al. 1994, Ben Salah et al. 2004]. In this method, the azimuthal angle is divided into N_ϕ equally-spaced directions, and the polar angle is divided into N_θ equally spaced directions. With this approach, $\Delta\phi = 2\pi/N_\phi$ and

$\Delta\theta = \pi/N_\theta$. Figure 3.5a shows the directional distribution using uniformly-spaced azimuthal and polar divisions for $N_\phi = 10, N_\theta = 12$ (M = 120 discrete directions, analog to DOM S_{10} quadrature).

This approach, due to the fact that each polar level has an equal number of azimuthal divisions, can lead to highly non-uniform solid angles [Kim and Huh 2000], which can become a major issue for 3-D problems. This phenomenon is clearly witnessed in Figure 3.5a, where the solid angles range between 0.0256 steradians at the topmost/bottommost polar levels and 0.1618 steradians near the center of the unit sphere. Additionally, division in this manner can lead to discrete directions that have zero direction cosine in one of the ordinate directions, rendering it useless for a marching procedure that dictates marching direction based on direction cosine.

To this end, Kim and Huh [2000] developed a new quadrature scheme for the FVM, called the FT_N-FVM. In this method, the total polar angle θ is divided into an even number N uniformly spaced directional levels. The number of azimuthal divisions corresponding to the N polar levels follows the arithmetic sequence $4, 8, 12, \ldots 2N-4, 2N, 2N-4, \ldots, 12, 8, 4$. The total number of directions becomes $M = N(N+2)$, identical to the number of directions in both the DOM S_N and EO_N quadratures, for the same even index N. As seen in Figure 3.5b, the FT_{10}-FVM angular distribution produces more uniform solid angles than the traditional method shown in Figure 3.5a, with solid angles ranging between 0.0769 and 0.11584 steradians. The improved uniformity of solid angles has been shown by Kim and Huh [2000] to lead to slightly more accurate radiation transfer predictions than the traditional (N_ϕ x N_θ) approach. As previously mentioned, the choice of discrete directions is highly arbitrary in the FVM, so these are only two of many possible discretization approaches.

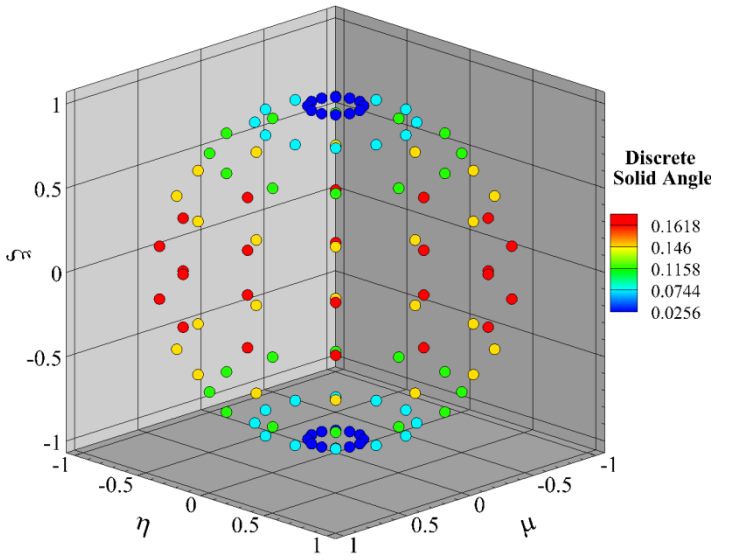

(a)

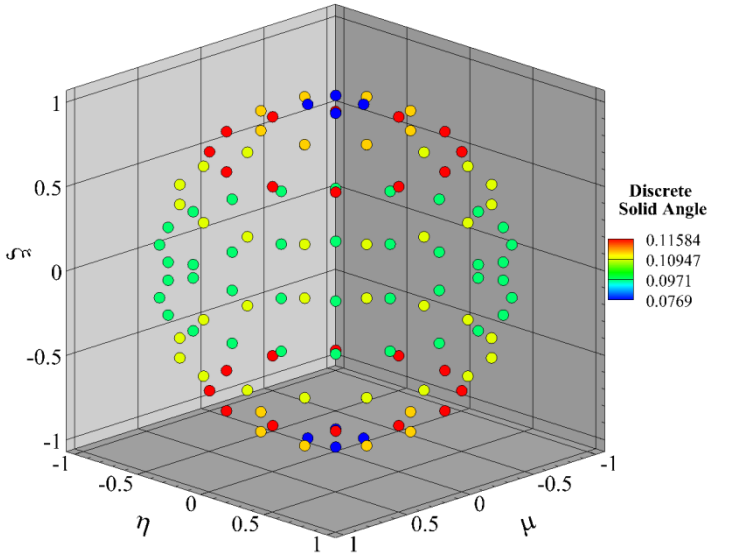

(b)

Figure 3.5: Discrete direction distribution for a) FVM 120 and b) FT_{10}-FVM quadrature (120 discrete directions)

3.3 Radiation Transfer Predictions using FVM

3.3.1 Validation with Experimental, Exact, and DOM Predictions

As a primary method of validating FVM radiative predictions, comparisons to both experimentally determined wall heat fluxes [Wu and Fricker 1971] and DOM predictions for a non-swirling gas flame in the Delft furnace are presented in Figure 3.6(a-b). The horizontal, axisymmetric cylindrical enclosure representing the Delft furnace is taken to have radius $R = 0.45\ m$ and total length $L = 5.1\ m$. The temperatures of the radial side wall ($r = 0.45$ m) and axial wall at $z = 0$ m are held at $T = 425$ K, while the axial wall at $z = 5.1$ m is held at $T = 300$ K. The emissivity of the radial side wall is ϵ_w = 0.8, while the axial walls are taken as blackbody emitters. The medium is approximated as purely absorbing, with $\sigma_a = 0.3\ m^{-1}$. The temperature field inside the furnace [Jamaluddin and Smith 1988] is presented in Figure 3.6a, where all temperatures are listed in Kelvin. The spatial grid used for the simulation is $(N_r \text{ x } N_z) = (3 \text{ x } 17)$, as shown in Figure 3.6a, and M = 288 discrete directions are used to discretize the angular domain. It is observed in Figure 3.6b that the heat flux generated using the FVM with 288 discrete directions is consistent with the experimental data. Additionally, when compared to DOM S_{16}, excellent agreement is witnessed, with differences ranging between 0.3% at z = 0 m to 5.3% at z = 5.1 m. The average difference across the entire furnace length is less than 1%.

Additional validation of FVM radiation transfer predictions is presented for the purely absorbing cylindrical medium (discussed in Section 2.4.1) in Figure 3.7 [Hunter and Guo 2011]. Both the exact solution and the DOM prediction from Figure 2.9 are presented, for comparison. FVM heat fluxes, generated using the traditional (N_ϕ x N_θ) = (16 x 18) and (20 x 24) quadratures (M = 288 and 440) are shown, while the DOM profiles are generated using the S_{16} quadrature.

For all optical thicknesses, FVM heat flux profiles conform accurately to both exact and DOM solutions. The maximum differences between the FVM 288 and DOM S_{16} profiles are 0.73%, 1.57%, and 2.00% for τ = 0.1, 1.0, and 5.0, respectively. The maximum difference between FVM 288 and the exact solution, which occurs for τ = 1.0, is 2.89%.

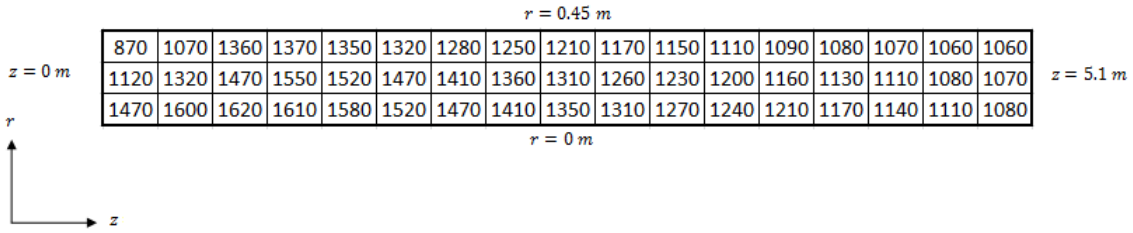

(a)

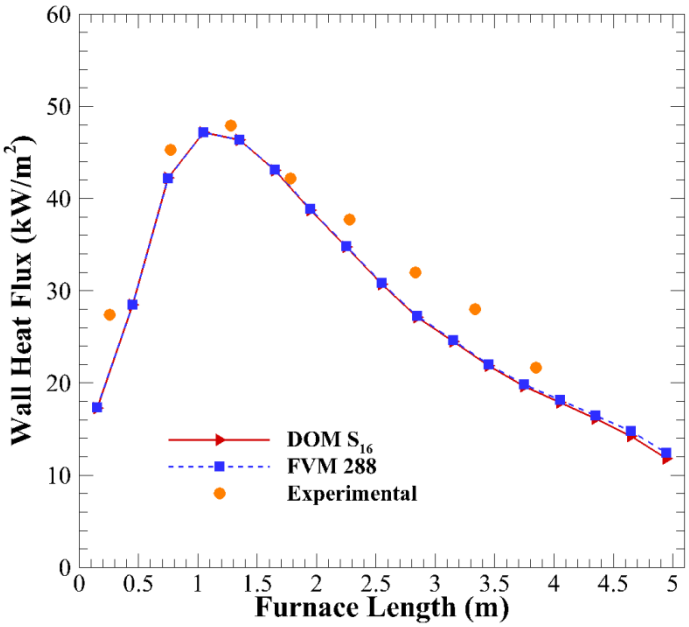

(b)

Figure 3.6: a) Temperature distribution inside Delft furnace [Jamaluddin and Smith 1988], b) Comparison of FVM and DOM heat fluxes with experimentally determined heat fluxes for non-swirling gas in Delft furnace [Wu and Fricker 1971]

As previously mentioned, for the DOM S_N quadrature, finer angular discretization past M = 288 is impossible, due to the appearance of negative weighting factors. However, for the

FVM, the number of discrete directions is unlimited. To this end, FVM heat fluxes with M = 440 are also plotted, in order to illustrate the impact of increasing direction number. The inlay in Figure 3.7 shows that, for $\tau = 1.0$, the FVM with 440 directions more closely conforms to the exact solution than the FVM with 288 directions, but still underpredicts the DOM S_{16} solution by 0.22%. The difference in scheme accuracy is very small for this case, but may arise from the differences in direction choices between the two schemes.

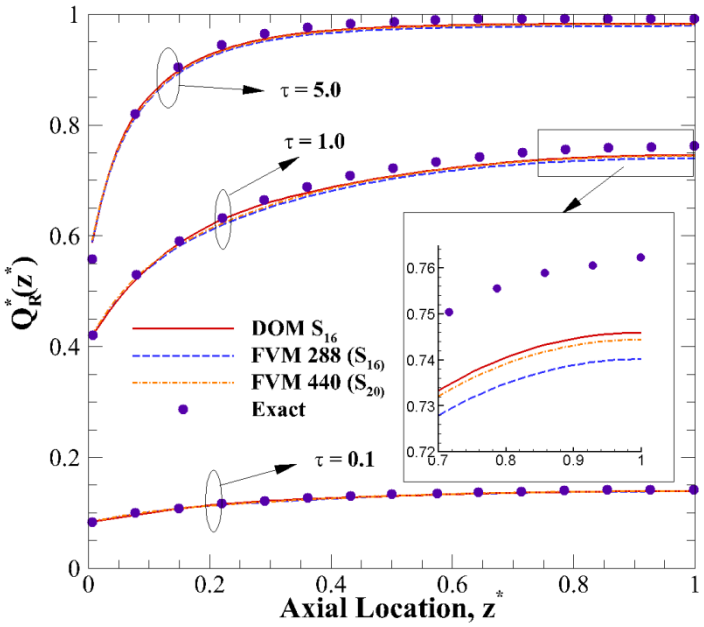

Figure 3.7: Comparison of steady-state $Q_R^*(z^*)$ generated using FVM with exact solution [Kim 2008] and DOM solution in purely absorbing medium for various optical thicknesses

An additional comparison between FVM, DOM, and exact solutions is presented in Figure 3.8 for the purely scattering, 2-D cubic medium previously discussed in Section 2.4.1 and Figure 2.10 for the DOM. At x^* = 0, heat flux generated using the FT_{16}-FVM quadrature conforms to the DOM EO_{16} heat flux within 0.3% for all y^*, indicating excellent agreement between the two numerical methods. At x^* = 1.0, the impact of the difference in the two

methods is more clearly witnessed, although both solutions are accurate in comparison to the exact solution. Differences between FVM and DOM are less than 1.5% at all locations except near y^* = 0, where discrepancies of ~5-7% are witnessed.

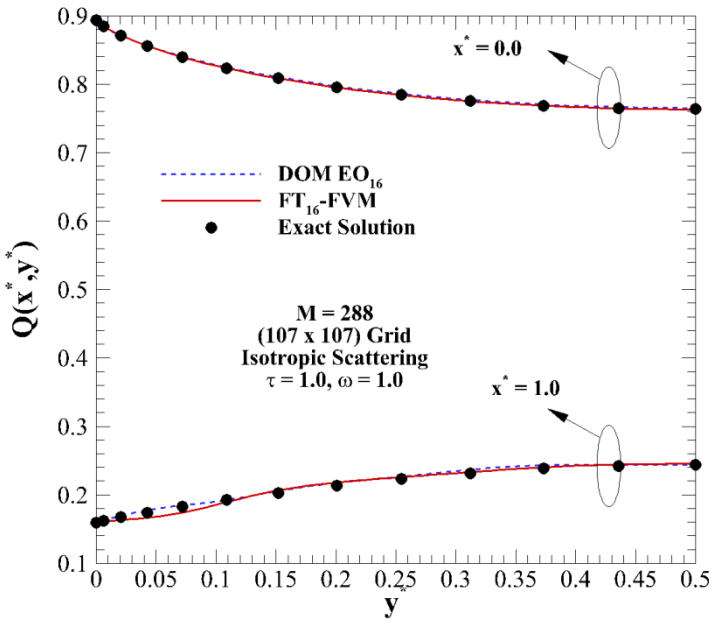

Figure 3.8: Comparison of steady-state Q(x*, y*) generated using FVM with exact solution [Crosbie and Schrenker 1984] and DOM in purely scattering medium

Figure 3.9 plots transient heat fluxes $Q(x^* = 1.0, y)$, generated using the FT_{16}-FVM, and compares them to the exact and DOM solutions previously examined in Figure 2.11. For all non-dimensional times, the FVM and DOM produce similar heat flux profiles, with the only major differences occurring in the range $0 \leq y^* \leq 0.15$ for t^* = 1.5 and 7.5. The accurate conformity of FVM heat flux profiles to experimental data in Figure 3.6 and exact/DOM solutions in Figures 3.7-3.9 gives confidence that the FVM is a suitable method for accurately determining radiation transfer.

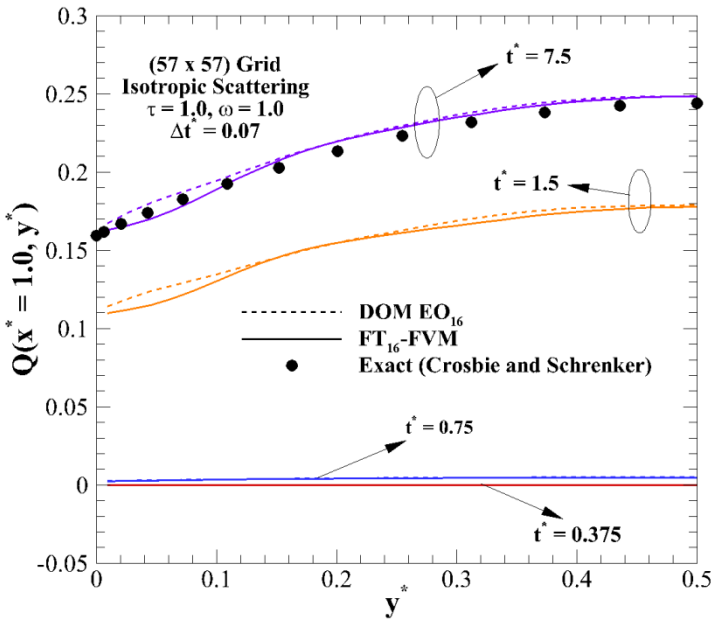

Figure 3.9: Comparison of $Q(x^* = 1.0, y^*)$ at different non-dimensional times between FVM and DOM, and comparison to exact steady-state solution

3.3.2 Illustration of Numerical Discretization Errors

3.3.2.1 Numerical Smearing

Numerical methods for radiation transfer, including the DOM and FVM, suffer from two well-known major shortcomings, due to the necessity of spatial and angular discretization [Chai et al. 1993]. The first type of numerical error, which arises due to spatial discretization and is independent of angular discretization, is numerical smearing [Coelho 2002a]. Numerical smearing is also referred to in literature as numerical scattering or false scattering [Jessee and Fiveland 1997], although these two terms are, in essence, a misnomer, which will be discussed in greater detail in Chapter 4. Numerical smearing can be thought of as the counterpart of false diffusion in computational fluid dynamics, which arises mainly in multidimensional problems where the radiation directions are not directly aligned with spatial grid lines [Coelho 2002a, Chai

et al. 1993]. Numerical smearing errors can be the result of two spatial issues: (1) improper spatial grid resolution, or (2) use of lower-order spatial differencing schemes.

Numerical smearing errors due to improper spatial grid resolution are examined in Figure 3.10a, in which generated FVM heat fluxes $Q(x^*, y^*)$ for the purely scattering, 2-D square medium (outlined in Section 2.4.1) are plotted for various spatial grid resolutions. The spatial grids applied are $(N_x \text{ x } N_y)$ = (7 x 7), (17 x 17), (27 x 27), and (107 x 107), while the number of discrete directions is held constant at M = 288. Additionally, the exact solution of Crosbie and Schrenker [1984] is plotted for comparison. All other medium properties are identical to those described in Section 2.4.1, and are thus not repeated here.

For low spatial resolution, errors due to numerical smearing are extremely evident, with differences from the exact solution reaching maximums of 5.4% and 22.5% for x^* = 0 and 1.0, respectively. Errors at the far wall (x^* = 1.0) are larger than at the source wall (x^* = 0), due to the distance traveled by radiant energy through the medium. Improvement of spatial resolution improves FVM solution accuracy. Use of a grid with high resolution of (107 x 107) reduces the discrepancies at y^* = 0.5 to less than 0.5% for both x^* locations when compared to the exact solution, indicating that numerical smearing error due to improper grid resolution has effectively been minimized. Higher resolution grids will further reduce errors, but come at the cost of substantial increases in required computational memory storage.

The second source of numerical smearing errors stems from the use of lower-order spatial differencing schemes to approximate the spatial gradients of radiative intensity. The step (upwind) and diamond (central) schemes are first-order spatial differencing schemes, which are highly stable [Coelho 2002a]. In these first-order schemes, numerical smearing can be excessive, due radiation across a control volume face being locally treated as one-dimensional

[Coelho 2002a]. Additionally, many first-order spatial differencing schemes result in unbounded intensities that are physically unrealistic [Jessee and Fiveland 1997, Alves et al. 2003].

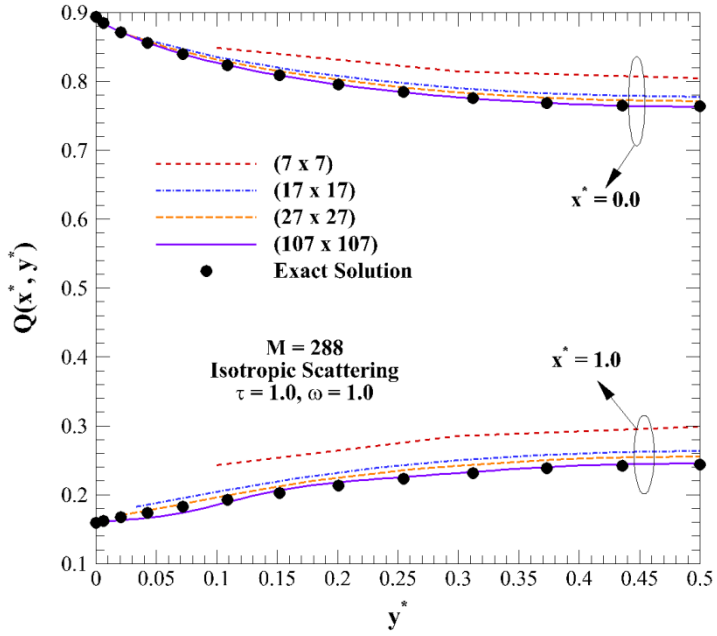

(a)

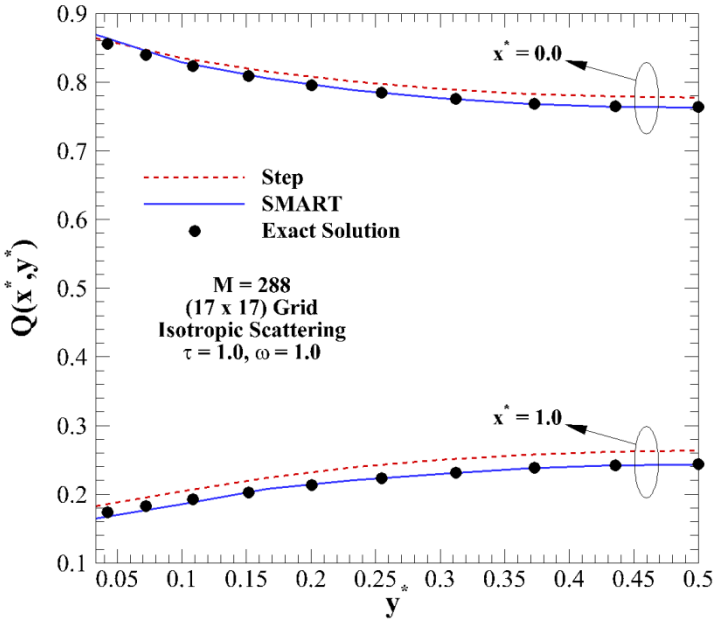

(b)

Figure 3.10: Illustration of numerical smearing due to (a) improper spatial discretization, (b) spatial discretization scheme (exact solution from [Crosbie and Schrenker 1984])

Higher-order differencing schemes, which are bounded, are available for spatial discretization of the ERT. Bounded schemes such as SMART [Gaskell and Lau 1988], MINMOD [Harten 1983], MUSCL [Van Leer 1979], and CUBISTA [Alves et al. 2003], which were developed for computational fluid dynamics, are accurate and numerically stable, and can be readily applied to the ERT for radiation transfer calculation using DOM and FVM [Liu et al. 1996]. High-order spatial differencing schemes can be expressed using the Normalized Variable and Space Formulation (NVSF) of Darwish and Moukalled [1994], which is an extension of Leonard's [1987] Normalized Variable Formulation (NVF). While the formulation of all of the mentioned higher-order differencing schemes can be found in the above references, the formulae describing the third-order SMART differencing scheme is presented herein.

The SMART differencing scheme, as well as other bounded, high-order schemes, express the intensity at a control-volume face i in terms of three spatial nodes: (1) the nodal center of the downstream control volume, designated as D, (2) the nodal center of the upstream control volume, designated as U, and the nodal center of the current control volume, designated as P [Coelho 2002a]. Using the NVSF, the normalized radiation intensity $\tilde{I}$ and normalized spatial coordinate $\tilde{x}$ can be defined as follows:

$$\tilde{I}_j = \frac{I_j - I_U}{I_D - I_U} \quad , \qquad \tilde{x}_j = \frac{x_j - x_U}{x_D - x_U} \tag{3.19}$$

where the spatial coordinates x can correspond to any direction, and should not be confused with the x-direction in Cartesian coordinates, and the variable j is a placeholder variable. As an example, in the NVSF approach, the first-order upwind (step) scheme, where the intensity at face i is equal to the intensity at nodal center P, can be expressed as $\tilde{I}_i = \tilde{I}_P$.

The SMART scheme, as outlined by Gaskell and Lau [1988] and Darwish and Moukalled [1994], follows the following piecewise relationship for the intensity at control-volume face i, to ensure boundedness:

$$\tilde{I}_i = \frac{\tilde{x}_i(1-3\tilde{x}_P+2\tilde{x}_i)}{\tilde{x}_P(1-\tilde{x}_P)}\tilde{I}_P, \quad 0 \le \tilde{I}_P < \frac{\tilde{x}_P}{3} \tag{3.20a}$$

$$\tilde{I}_i = \frac{\tilde{x}_i(1-\tilde{x}_i)}{\tilde{x}_P(1-\tilde{x}_P)}\tilde{I}_P + \frac{\tilde{x}_i(\tilde{x}_i-\tilde{x}_P)}{(1-\tilde{x}_P)}, \quad \frac{\tilde{x}_P}{3} \le \tilde{I}_P < \frac{\tilde{x}_P}{\tilde{x}_i}(1+\tilde{x}_i-\tilde{x}_P) \tag{3.20b}$$

$$\tilde{I}_i = 1, \quad \frac{\tilde{x}_P}{\tilde{x}_i}(1+\tilde{x}_i-\tilde{x}_P) \le \tilde{I}_P < 1 \tag{3.20c}$$

$$\tilde{I}_i = \tilde{I}_P, \quad \tilde{I}_P \le 0 \ \ or \ \ \tilde{I}_P \ge 1 \tag{3.20d}$$

The relationship in Eq. 3.20d states that if the normalized intensity $\tilde{I}_P$ is not between 0 and 1, this scheme reduces down to a first-order upwind scheme.

To further clarify the formulation of the SMART scheme, we can apply it to the control volume in Figure 2.6 for the 3-D enclosure described by Cartesian coordinates. Let's assume we are interested in determining the intensity at the "north" control-volume face n for a sweep in the positive x-direction. In this case,

$$\tilde{I}_n = \frac{I_n - I_S}{I_N - I_S} \quad , \qquad \tilde{x}_n = \frac{x_n - x_S}{x_N - x_S} \quad , \quad \tilde{I}_P = \frac{I_P - I_S}{I_N - I_S} \quad , \quad \tilde{x}_P = \frac{x_P - x_S}{x_N - x_S} \tag{3.21}$$

For a non-uniform grid, substitution of Eq. (3.21) into Eqs. (3.20a-d) will give the SMART scheme formulation. For uniform grids, $\tilde{x}_n = 0.75$, $\tilde{x}_P = 0.50$, and Eqs. (3.20a-d) and (3.21) can be simplified to the following expressions for the "north" control-volume face in Figure 2.6:

$$\tilde{I}_n = 3\tilde{I}_P, \quad 0 \le \tilde{I}_P < \frac{1}{6} \tag{3.22a}$$

$$\tilde{I}_n = \frac{3}{4}\tilde{I}_P + \frac{3}{8}, \quad \frac{1}{6} \le \tilde{I}_P < \frac{5}{6} \tag{3.22b}$$

$$\tilde{I}_n = 1, \quad \frac{5}{6} \le \tilde{I}_P < 1 \tag{3.22c}$$

$$\tilde{I}_n = \tilde{I}_P, \quad \tilde{I}_P \le 0 \ \ or \ \ \tilde{I}_P \ge 1 \tag{3.22d}$$

This ends the development of the 3rd-order SMART spatial differencing scheme.

Numerical smearing errors due to use of a low-order spatial differencing scheme are examined in Figure 3.10b for the same problem as Figure 3.10a. Heat flux profiles $Q(x^*, y^*)$, generated using the FVM with the first-order step and 3rd-order SMART spatial differencing schemes, are plotted against the exact solution to gauge their accuracy. Heat flux profiles generated using the step scheme are shown to overpredict the exact solution at both x^*, with maximum differences of 1.9% and 8.4% seen for x^* = 0.0 and 1.0, respectively. Heat fluxes generated with the 3rd-order SMART scheme at the same grid resolution conform much more accurately to the exact solution, with differences of less than 0.5% witnessed for both x^* at the wall center (y^* = 0.5), indicating that the use of a bounded, higher-order spatial differencing scheme is effective in minimizing numerical smearing error. Numerical smearing appears in both the FVM and DOM, and since numerical smearing depends only on spatial discretization, it will not impact one scheme differently from the other, as long as the same spatial differencing is implemented. Thus, only results for the FVM are presented here, for brevity.

3.3.2.2 Ray Effect

The second well-known numerical error inherent in the FVM and DOM is known as ray effect, and is an error that occurs solely due to angular discretization of the continuous angular variation of radiation scattering [Chai et al. 1993]. Coarse angular discretization may not be able to accurately represent the propagation of radiant energy, which can lead to physically unrealistic bumps and oscillations in heat flux profiles [Chai et al. 1993]. Ray effect can be effectively minimized via refinement of the angular discretization (i.e., use of a higher discrete direction number), in order to more accurately represent the continuous variation [Raithby 1999]

An illustration of ray effect error due to improper angular discretization in the purely scattering problem described in Section 2.4.1 and analyzed for numerical smearing in the previous section is presented in Figure 3.11. Heat flux profiles $Q(x^*, y^*)$ are generated using the FVM with the first-order step scheme and spatial grid $(N_x \text{ x } N_y)$ = (107 x 107) for various discrete direction numbers. The FT_N-FVM quadrature is used to discretize the angular domain, with M = 24, 80, 168, 288, and 1088 directions implemented. As before, the exact solution of Crosbie and Schrenker [1984] is plotted for comparison purposes.

Errors due to ray effect are minimal at the source wall (x^* = 0), with differences greater than 1% witnessed only for the lowest angular resolution. At the far wall, however, the impact of ray effect is clearly witnessed. For low angular resolution, ray effect error has manifested as unrealistic bumps in heat flux profiles. For M = 24, FVM heat flux overpredicts the exact solution by 10% at the wall center (y^* = 0.5), while underpredictions of greater than 25% are witnessed in the range $0.2 \leq y^* \leq 0.3$. As angular resolution is refined, these unrealistic oscillations reduce, and the FVM heat fluxes approach the exact solution. For an extremely high

discrete direction number (M = 1088), differences between the exact solution and FVM are less than 0.5% at all locations except near y^* = 0, where a maximum difference of 1.7% is witnessed.

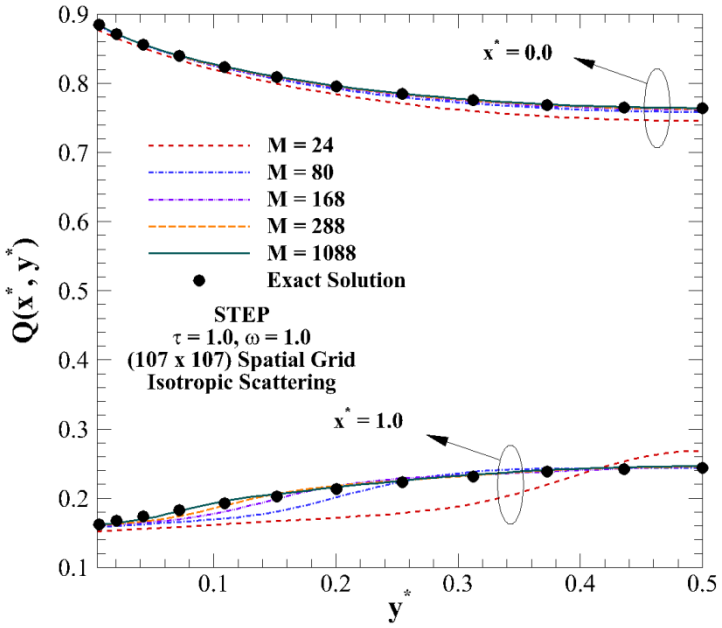

Figure 3.11: Illustration of ray effect in the FVM due to improper angular discretization in an optically thinner, purely scattering medium (exact solution from [Crosbie and Schrenker 1984])

As previously mentioned, ray effect is a consequence of angular discretization, and is not impacted by spatial discretization. For numerical smearing, FVM and DOM are equally impacted, assuming the same spatial discretization scheme is used for both numerical methods. This is not the case for ray effect, as illustrated in Figure 3.12, as the inherent differences between the DOM and FVM quadrature schemes lead to differences in ray effect error on heat flux at the far wall $Q(x^* = 1.0, y^*)$. For M = 24, DOM EO_N heat flux overpredicts FT_N-FVM heat flux by between 8-38%. More interestingly, for M = 80, the unrealistic oscillations/bumps in the profile appear in different locations for the FVM and DOM profiles. At y^* = 0.129, FVM heat flux underpredicts the DOM by 15%, while at y^* = 0.30, the FVM overpredicts DOM by 7%.

Increasing the discrete direction number to M = 288 effectively minimizes ray effect in both numerical methods, leading to similar heat flux profiles and accurate conformity to the exact solution.

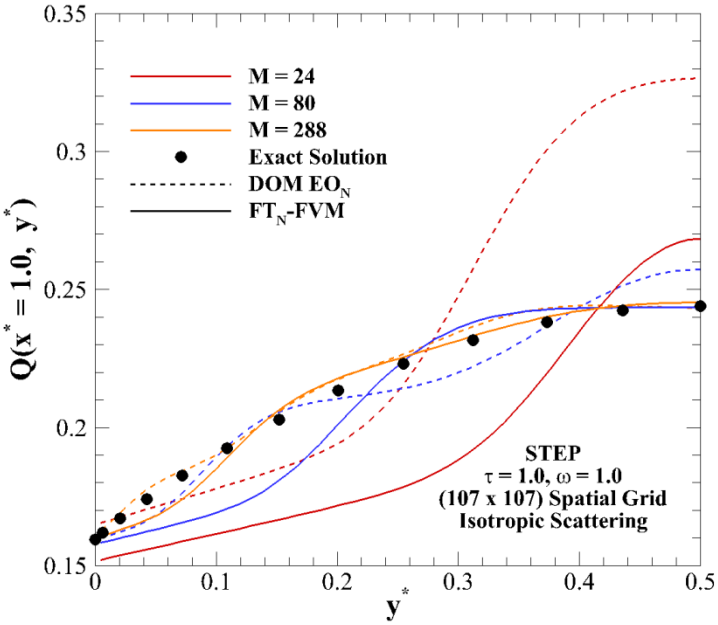

Figure 3.12: Impact of ray effect on DOM and FVM on heat fluxes in an optically thinner, purely scattering medium (exact solution from [Crosbie and Schrenker 1984])

As noted by Chai et al. [1993], ray effect is more prominent for optically thin media, and is effectively mitigated for media with high optical thickness. This fact is illustrated in Figures 3.13a-b, in which heat fluxes at the far wall are plotted for three optical thicknesses: τ = 1.0, 4.0, and 10.0. For the step scheme in Figure 3.13a, increase in optical thickness clearly reduces errors due to ray effect. For the two higher optical thicknesses, the physically unrealistic bumps in heat flux profile are minimized/eliminated, and FVM heat fluxes conform accurately to the exact solution.

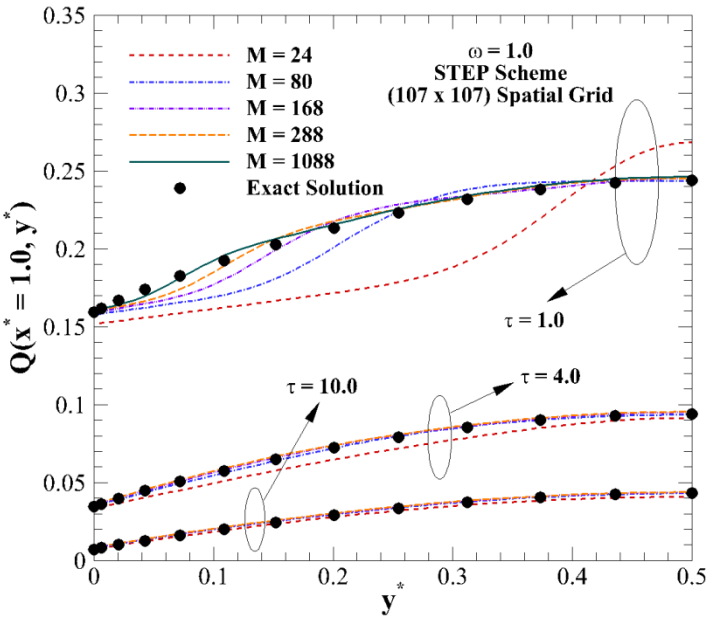

(a)

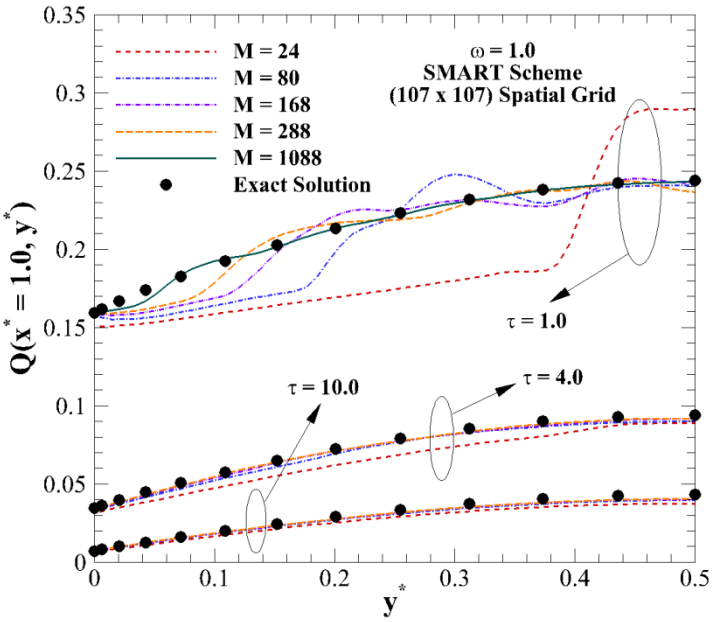

(b)

Figure 3.13: Examination of impact of optical thickness on FVM ray effect errors for Q(x^* = 1.0, y^*) with various discrete direction numbers for a) 1st-order step and b) 3rd-order SMART scheme

An interesting phenomenon is witnessed in Figure 3.13b, where the 3rd-order SMART differencing scheme is used to discretize the spatial domain. At τ = 1.0, oscillations in heat flux

profiles still appear, as they did for the step scheme in Figure 3.13a. However, the oscillations are much more frequent, and the magnitude of ray effect error appears to be significantly larger than witnessed in Figure 3.13a. This result may seem contradictory, at first, when considering the results from Figure 3.10, where the SMART scheme produced more accurate results than the step scheme due to minimization of numerical smearing. However, the appearance of more unstable oscillations in heat flux for the higher-order scheme illustrates the combined effects of numerical smearing and ray effect [Coelho 2002b]. For the step scheme, numerical smearing and ray effect errors are both fairly prominent, but they, in essence, "cancel" each other out. In other words, numerical smearing error acts in an opposite manner, helping to smooth out the oscillations resultant from ray effect error. When the SMART scheme is applied, numerical smearing error is minimized, and there is no mechanism to reduce the errors due to ray effect. The reduction of the combined error effects results in greater ray effect error for the higher-order SMART scheme, as witnessed in Figure 3.13b. Increase in optical thickness is able to minimize ray effect error, similar to the results seen for the step scheme

3.3.3 Computational Efficiency Analysis of FVM and DOM

The results presented in Sections 3.3.1 and 3.3.2 illustrate that the FVM and DOM are both able to accurately predict radiation transfer, with limitations in accuracy occurring due to numerical discretization errors. In addition to comparing physical results, it is important to analyze the computational efficiency of both methods. This can be accomplished by analyzing both CPU convergence times and computational memory requirements for both schemes [Hunter and Guo 2011]. In order to accurately compare committed memory between each method, only variables and arrays in the numerical code that are necessary for execution are included, and double-precision is used for all real numbers in the analysis. Computational

memory requirements and CPU times are generated for radiation transfer in an absorbing-scattering, axisymmetric cylindrical enclosure of unity aspect ratio (geometry similar to that in Figure 2.1). All walls are taken as black, the axial end walls are cold, and the radial side wall is hot with unity emissive power. The medium is taken as cold, with optical thickness τ and scattering albedo ω, and scattering is taken to be isotropic for all cases. The step scheme is used for spatial discretization for all forthcoming results.

Figure 3.14 plots the variation of committed memory usage with change in angular quadrature. Four different spatial grids were used for the analysis, ranging from $(N_r \text{ x } N_z) =$ 150 x 150 to 400 x 400, in order to tax the computational resources. The S_N quadrature is implemented for the DOM, while the ($N_\phi \; x \; N_\theta$) quadrature is implemented for the FVM. In general, for both the FVM and DOM, committed memory increases with refinement of both angular and spatial resolutions. The ratio between FVM and DOM committed memory is also plotted for the four spatial grids. The FVM/DOM committed memory ratio is identical for all four spatial grids, indicating that spatial grid refinement has an equal effect on both DOM and FVM committed memory. Conversely, as angular quadrature increases, the ratio between FVM and DOM committed memory increases in a logarithmic fashion, increasing from 1.38 to 1.90 as discrete direction number increases from M = 24 to 288.

The increase in FVM/DOM committed memory ratio with increasing quadrature can be attributed to the difference in angular discretization. In the DOM, the angular derivative is approximated using angular differencing coefficients, as explained in Chapter 2. These coefficients allow for the problem to be solved as a two-dimensional problem (intensities are only required in the (r, z) directions). However, in the FVM, the angular derivative is calculated using neighboring control volumes in the azimuthal direction. Because of this, intensities need

to be stored for the (r, ϕ, z) directions, leading to increased array sizes, and thus a large increase in memory usage as the number of total directions increases.

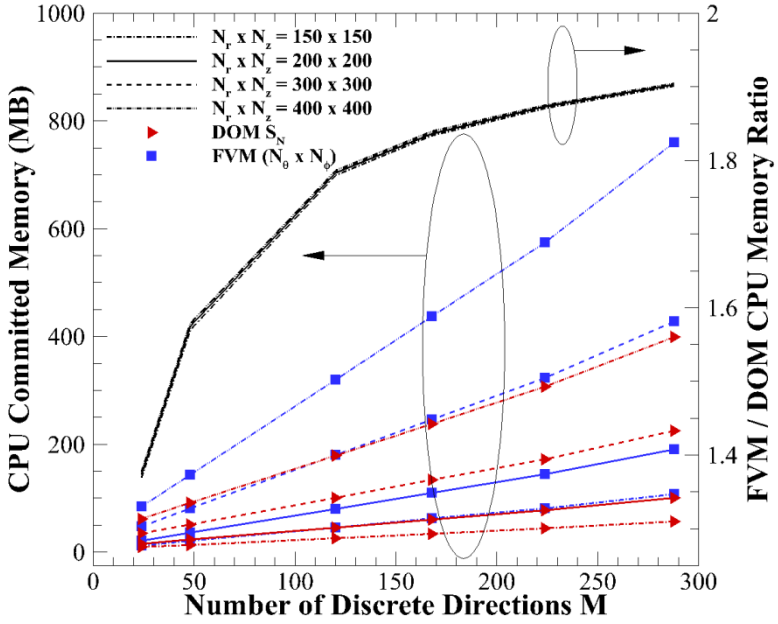

Figure 3.14: Variation of DOM and FVM CPU committed memory (MB) with angular discretization

Figure 3.15 plots FVM and DOM steady-state convergence times versus spatial grid number for a purely scattering medium (ω = 1.0) with optical thickness τ = 1.0. The number of discrete directions is held constant at M = 288. As spatial grid number is increased, a parabolic increase in convergence time is seen. The ratio between FVM and DOM convergence time is fairly constant for all analyzed grid numbers. The FVM/DOM time ratio is 1.11 for N_r = N_z = 150, and 1.07 for the three finer grids. As with committed memory, refinement of the spatial grid seems to have an equal effect on the convergence time of both the FVM and DOM.

Figures 3.16(a-b) display the effect of scattering albedo and extinction coefficient on FVM and DOM steady-state convergence times. As scattering albedo increases from 0 to 1, steady-state convergence time increases due to the dependence of the source term in the

governing equation on scattering albedo. Similarly, as optical thickness increases, convergence time increases, due to the fact that it takes longer for radiant energy to propagate through an optically thick medium. The ratio between FVM and DOM convergence time is plotted for all cases in both figures. Regardless of the scattering albedo or optical thickness chosen, the computational time ratio between the FVM and DOM remains nearly constant, ranging from 1.10 to 1.15.

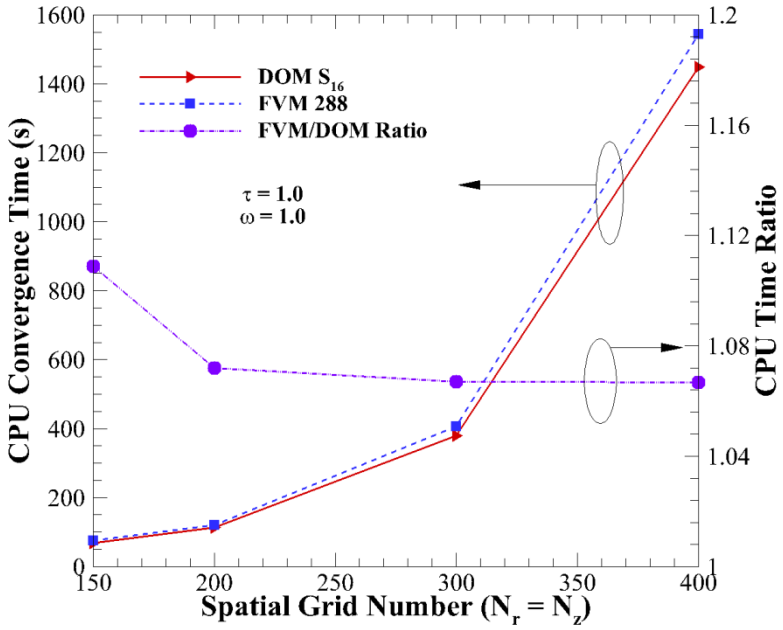

Figure 3.15: Variation of CPU convergence time with spatial grid number for M = 288

These results are inconsistent with basic computational time comparisons in previous literature results, which determined the ratio between FVM and DOM convergence time to range from 1.5 to 2, depending on the scattering albedo, optical thickness and quadrature scheme [Chai et al. 1994, Kim and Baek 1997]. The discrepancy between the current results and the previous literature publications can be attributed to dramatic increases in both CPU memory storage and processing power, especially with the advent of Dual Core processors. For ease of

visualization, CPU committed memory values (in MB) for various angular and spatial resolutions are tabulated in Table 3.1, while CPU convergence times (in seconds) for various optical thicknesses and scattering albedos are tabulated in Table 3.2.

In Table 3.3, required computation memory (in MB) for both the FVM and DOM are tabulated for various discrete direction numbers and spatial grids in a 3-D cubic medium. For all grids and discrete direction numbers, the FVM and DOM use nearly identical memory. The ratios between FVM and DOM memory for all cases are between 1.00 and 1.01, indicating that either method is efficient in terms of memory for 3-D problems. These results differ strongly from the 2-D axisymmetric results, but reaffirm that the DOM is of equal or better efficiency in terms of computational memory. Results for computational convergence time are similar to that shown for the 2-D axisymmetric medium.

All in all, the DOM appears to be a more computationally efficient method, as the FVM requires more memory and computational convergence time in all cases [Hunter and Guo 2011]. However, the flexibility of FVM quadrature may be more desirable than minor savings in computational resources, especially due to the fact that high speed processors allow for more computationally intensive processes to be solved relatively quickly.

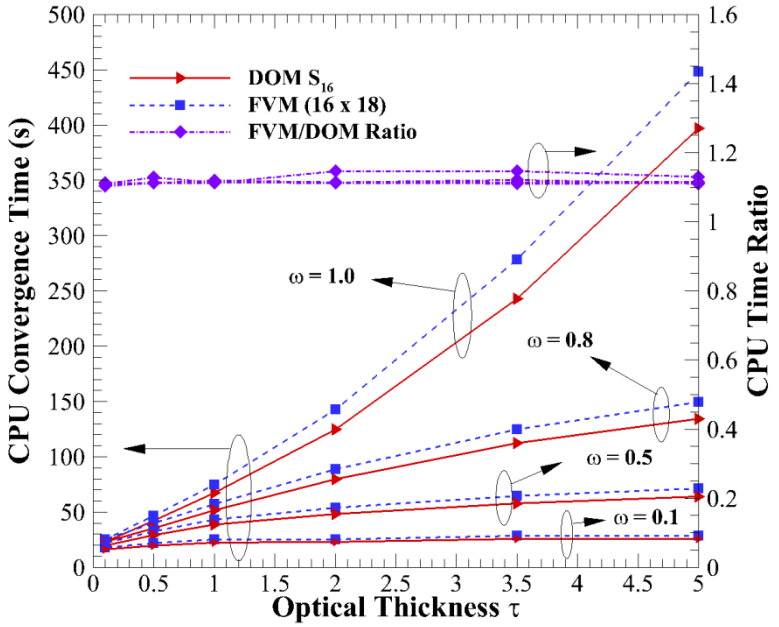

(a)

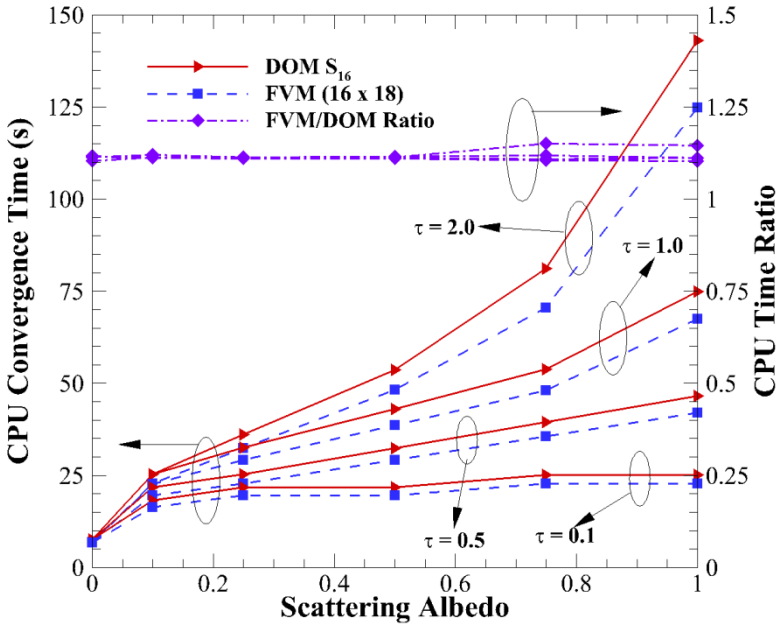

(b)

Figure 3.16: Variation of DOM and FVM computational convergence times with a) optical thickness and b) scattering albedo

Table 3.1: CPU committed memory (MB) for FVM and DOM vs. angular discretization

Quadrature		CPU Committed Memory (MB)											
		Grid = 150 x 150			Grid = 200 x 200			Grid = 300 x 300			Grid = 400 x 400		
N	M	FVM	DOM	Ratio	FVM	DOM	Ratio	FVM	DOM	Ratio	FVM	DOM	Ratio
4	24	12.20	8.91	1.37	21.45	15.61	1.37	47.85	34.74	1.38	84.79	61.52	1.38
6	48	20.47	13.04	1.57	36.14	22.95	1.57	80.88	51.26	1.58	143.51	90.88	1.58
8	80	45.29	25.45	1.78	80.21	44.99	1.78	180.00	100.82	1.79	319.68	178.96	1.79
12	168	61.86	33.74	1.83	109.63	59.70	1.84	246.10	133.87	1.84	437.15	237.70	1.84
14	224	81.20	43.41	1.87	143.96	76.86	1.87	323.24	172.45	1.87	574.23	306.25	1.88
16	288	107.50	56.55	1.90	190.59	100.18	1.90	427.97	224.80	1.90	760.29	399.27	1.90

Table 3.2: CPU convergence times (seconds) for FVM and DOM for various scattering albedos and optical thicknesses

CPU Convergence Times (s)												
	$\omega = 1.0$			$\omega = 0.8$			$\omega = 0.5$			$\omega = 0.1$		
τ	FVM	DOM	Ratio	FVM	DOM	Ratio	FVM	DOM	Ratio	FVM	DOM	Ratio
5.0	448.14	396.85	1.13	149.57	134.11	1.12	71.29	64.19	1.11	28.86	25.96	1.11
3.5	278.34	242.88	1.15	124.89	112.13	1.11	64.54	57.60	1.12	28.75	25.91	1.11
2.0	143.02	124.86	1.15	88.87	79.92	1.11	53.63	48.17	1.11	25.26	22.70	1.11
1.0	74.94	67.39	1.11	57.22	51.37	1.11	43.06	38.63	1.11	25.29	22.59	1.12
0.5	46.58	41.90	1.11	39.98	35.46	1.13	32.32	29.09	1.11	21.70	19.52	1.11
0.1	25.15	22.79	1.10	25.23	22.73	1.11	21.70	19.55	1.11	18.14	16.32	1.11
	$\tau = 2.0$			$\tau = 1.0$			$\tau = 0.5$			$\tau = 0.1$		
ω	FVM	DOM	Ratio	FVM	DOM	Ratio	FVM	DOM	Ratio	FVM	DOM	Ratio
1.00	143.02	124.86	1.15	74.94	67.39	1.11	46.58	41.90	1.11	25.15	22.79	1.10
0.75	81.15	70.57	1.15	53.76	48.11	1.12	39.44	35.59	1.11	25.10	22.71	1.11
0.50	53.63	48.17	1.11	43.06	38.63	1.11	32.32	29.09	1.11	21.70	19.55	1.11
0.25	35.99	32.34	1.11	32.45	29.14	1.11	25.22	22.73	1.11	21.68	19.52	1.11
0.10	25.26	22.70	1.11	25.29	22.59	1.12	21.70	19.52	1.11	18.14	16.32	1.11
0.00	7.52	6.82	1.10	7.53	6.76	1.11	7.55	6.77	1.12	7.53	6.74	1.12

Table 3.3: Comparison of CPU committed memory (in MB) between FVM and DOM in a 3-D cubic enclosure for various discrete direction numbers and spatial grids

	Computational Memory (MB)								
	(17 x 17 x 17)			(22 x 22 x 22)			(27 x 27 x 27)		
M	DOM	FVM	Ratio	DOM	FVM	Ratio	DOM	FVM	Ratio
24	3.42	3.41	1.00	6.05	6.05	1.00	10.2	10.2	1.00
48	5.25	5.25	1.00	10.0	10.0	1.00	17.4	17.4	1.00
80	7.70	7.75	1.01	15.2	15.3	1.00	27.1	27.2	1.00
168	14.7	14.9	1.01	29.9	30.0	1.00	54.0	54.2	1.00
288	24.6	25.1	1.02	50.3	50.9	1.01	90.8	91.5	1.01

3.4 Summary

In Chapter 3, the formulation for solution of the TERT using the Finite Volume Method (FVM) is presented for both 2-D axisymmetric cylindrical enclosures and 2-D/3-D enclosures described using Cartesian coordinates. Discretization equations for the FVM are developed using the control-volume method, and the marching solution procedure is discussed. FVM radiation transfer predictions are validated with experimental data for the Delft furnace, as well as exact solutions to the ERT in purely absorbing and purely scattering media. Additionally, comparisons between FVM and DOM radiation transfer predictions are made. A discussion of two major types of numerical error, known as numerical smearing and ray effect, is examined in detail for both FVM and DOM, and . Finally, an examination of computational convergence times and CPU committed memory requirements for the FVM and DOM is presented. It is found that FVM is an accurate method for determining radiation transfer. Numerical smearing errors impact both FVM and DOM in a similar manner, with reduction of numerical smearing occurring with both spatial grid refinement and use of higher-order spatial differencing schemes. Ray effect impacts FVM and DOM radiation transfer results differently, due to the difference in angular discretization. The combined effects of numerical smearing and ray effect are evident when higher-order schemes are implemented. For all tested cases, the DOM uses less memory and requires less computational time than the FVM, although the FVM is more flexible in nature, and therefore may still be the more desirable method, depending on the problem at hand.

CHAPTER 4 : ANGULAR FALSE SCATTERING IN RADIATION TRANSFER

4.1 Angular False Scattering in the Discrete-Ordinates Method

4.1.1 Conservation of Scattered Energy and Asymmetry Factor

Mathematically, the scattering phase function $\Phi(\hat{\boldsymbol{s}}', \hat{\boldsymbol{s}})$ can be thought of as a probability density function, which governs the probability of a photon (traveling in radiation direction $\hat{\boldsymbol{s}}'$) being scattered into radiation direction $\hat{\boldsymbol{s}}$. By definition, any probability density function $R(x)$ must satisfy a normalization condition, which can be written as follows:

$$\int_{-\infty}^{\infty} R(x)dx = 1 \tag{4.1}$$

Eq. (4.1) states that the sum of all probabilities in probability space must be equal to unity. The scattering phase function $\Phi(\hat{\boldsymbol{s}}', \hat{\boldsymbol{s}})$, as a probability density function, must therefore satisfy a similar normalization condition over angular space. This condition can be written as follows:

$$\frac{1}{4\pi}\int_{4\pi} \Phi(\hat{\boldsymbol{s}}', \hat{\boldsymbol{s}})d\Omega = 1 \tag{4.2}$$

Eq. (4.2) is, in fact, a constraint on total scattered energy in the system, as it guarantees that the total probability of a photon traveling in radiation direction $\hat{\boldsymbol{s}}'$ being scattered into direction $\hat{\boldsymbol{s}}$ will be equal to one.

Using the DOM, the conservation of scattered energy condition of Eq. (4.2) can be discretized in the following manner [Kim and Lee 1988]:

$$\frac{1}{4\pi}\sum_{l=1}^{M}\Phi^{l'l}w^{l}=1\,,\qquad l'=1,2,\dots,M \tag{4.3}$$

It is well known that Eq. (4.3) must be accurately satisfied, in order to generate accurate radiation transfer predictions [Kim and Lee 1988, Chai et al. 1994, Boulet et al. 2007]. For isotropic scattering ($\Phi^{l'l}$ = 1), Eq. (4.3) reduces to the 0th-order moment condition of Eq. (2.26), and is thus automatically satisfied by any properly derived DOM quadrature set. However, for anisotropic scattering, this constraint may not be accurately satisfied after DOM discretization, especially for strong-forward phase-functions [Boulet et al. 2007, Collin et al. 2011].

In order to better illustrate this, consider the DOM discretization equations of Eqs. (2.21a-b). These equations can be rewritten in the following manner [Chai et al. 1998]:

$$\frac{1}{c}\frac{\partial I^{l}}{\partial t}+\mu^{l}\frac{\partial I^{l}}{\partial x}+\eta^{l}\frac{\partial I^{l}}{\partial y}+\xi^{l}\frac{\partial I^{l}}{\partial z}=-(\sigma_a+\sigma_{sm})I^{l}+S^{l}\,,\qquad l=1,2,\dots,M \tag{4.4a}$$

$$S^{l}=\sigma_a I_{bk}+\frac{\sigma_s}{4\pi}\left(\sum_{\substack{l'=1\\ l'\neq l}}^{M}\Phi^{l'l}I^{l'}w^{l'}+\sum_{B}I^{B}\Phi^{^{l^B}l}\right)\,,\quad l=1,2,\dots,M \tag{4.4b}$$

$$\sigma_{sm}=\sigma_s(1-\frac{1}{4\pi}w^{l}\Phi^{ll}) \tag{4.4c}$$

Extraction of the forward-scattering term $\frac{1}{4\pi}w^{l}\Phi^{ll}$ from the scattering summation was suggested by Chai et al. [1998], who showed that treating forward-scattering as transmission through use of a modified scattering coefficient σ_{sm} improves computational efficiency.

Since the modified scattering coefficient is an attenuation term in Eq. (4.4a), physically its value should never be negative; otherwise, it becomes a “false” source that augments intensity in the medium [Hunter and Guo 2012d]. Thus, a necessary condition using the DOM becomes

$$\left(1-\frac{1}{4\pi}w^{l}\Phi^{ll}\right)\geq 0\ , \qquad l=1,2,\ldots,M \tag{4.5}$$

which can be rearranged in the following manner:

$$\Phi^{ll}\leq\frac{4\pi}{w^{l}}\ , \qquad l=1,2,\ldots,M \tag{4.6}$$

Eq. (4.6) provides a necessary limiting condition for the value of the forward peak of the phase function, based strictly on the DOM quadrature weights. For lower-order quadrature (where weighting factors are larger), this limiting condition will be highly restrictive. Additionally, if Eq. (4.6) is not satisfied, and the false source appears, the conservation of scattered energy in the system will automatically be broken, as satisfaction of Eq. (4.3) will become impossible.

It is important to determine exactly where Eq. (4.6) is violated, in order to provide a preliminary range where additional treatment to the scattering phase function is absolutely required to maintain scattered energy conservation and eliminate the false source [Hunter and Guo 2012d]. For the HG phase-function approximation, Eq. (4.6) can be rewritten as follows:

$$\frac{(1+g)}{(1-g)^{2}}\leq\frac{4\pi}{\max\left(w^{l}\right)} \tag{4.7}$$

Use of the maximum weighting factor for a given DOM quadrature scheme will determine the maximum value of g for which the inequality will be satisfied, shedding light on a preliminary range where significant concern over scattered energy conservation is valid.

Table 4.1 examines the maximum value of HG asymmetry factor g below which Eq. (4.7) will be satisfied for various quadrature sets, ranging from S_2 (8 discrete directions) to S_{16} (288 discrete directions). The maximum values of weighting factor w^{l}, as well as the maximum possible values of diffuse phase function Φ^{ll}, are also listed. Use of low discrete direction

number puts a strong restriction on asymmetry factor, with a maximum g of 0.7314 for M = 24. As discrete direction number increases, the maximum value of g also increases, due to decreases in the maximum weighting factor value. For M = 288 discrete directions, which is the directional limit for the S_N quadrature, asymmetry factors above 0.8870 violate Eq. (4.7), and thus the scattered energy condition of Eq. (4.3). Many practical participating media, including biological tissue, can have $g \geq 0.9000$, meaning that accurate prediction of radiation transfer using the S_N quadrature will be impossible without some additional treatment.

Table 4.1: Examination of maximum HG asymmetry factor below which Eq. (4.7) is satisfied for DOM S_N quadrature with various discrete direction numbers

N	# Directions	Max Weight Factor	Max Φ^{II}	Max g
2	8	1.570796	8.0000	0.5586
4	24	0.523599	24.000	0.7314
8	80	0.461718	27.217	0.7467
10	120	0.148395	84.682	0.8521
12	168	0.111154	113.05	0.8713
14	224	0.097659	128.68	0.8792
16	288	0.085065	147.73	0.8870

As previously discussed, several quadratures exist where there is no limit on discrete direction number [Hunter and Guo 2013]. Figure 4.1 examines the maximum HG asymmetry factor below which Eq. (4.7) is satisfied for the four non-limited quadratures presented in Section 2.3.3. As a comparison, the results from the S_N quadrature are also plotted. As seen in Figure 4.1, the four non-limited quadratures allow for higher asymmetry factors than the S_N at the S_N directional limit of M = 288, due to the fact that the maximum weighting factors are significantly smaller, as shown in Figure 2.8. The maximum g values for the P_{16}-T_{16}/P_{16}-EW, T_6, and $SRAP_7$ are g = 0.9129, 0.9005, and 0.9061, compared to 0.8870 for S_{16}. In order to

accommodate asymmetry factors of g = 0.9500 and below, M = 1088, 1352, and 952 discrete directions are required for P_N-T_N/P_N-EW,T_N, and $SRAP_N$, respectively. While the unlimited directionality of these quadratures can ultimately allow for satisfaction of Eq. (4.7) for any asymmetry factor, the added computational cost for such an increase in direction number makes this approach computationally unreasonable.

N	# of Dir.	S_N		P_N-EW/P_N-T_N		N	# of Dir.	T_N		N	# of Dir.	$SRAP_N$	
		Max w^l	Max g	Max w^l	Max g			Max w^l	Max g			Max w^l	Max g
4	24	0.5236	0.7314	0.5464	0.7260	2	32	0.5513	0.7249	2	40	0.3142	0.7885
8	80	0.4617	0.7467	0.1747	0.8401	3	72	0.2061	0.8269	3	72	0.1745	0.8401
10	120	0.1484	0.8521	0.1174	0.8679	4	128	0.1552	0.8489	4	112	0.1122	0.8708
12	168	0.1112	0.8713	0.0840	0.8877	5	200	0.1009	0.8772	5	160	0.0785	0.8913
14	224	0.0977	0.8792	0.0636	0.9019	6	288	0.0654	0.9005	6	216	0.0582	0.9061
16	288	0.0851	0.8870	0.0498	0.9129	7	392	0.0522	0.9109	7	280	0.0449	0.9173
20	440	-	-	0.0328	0.9290	8	512	0.0401	0.9217	8	352	0.0357	0.9260
24	624	-	-	0.0233	0.9400	9	648	0.0307	0.9314	9	432	0.0291	0.9331
28	840	-	-	0.0174	0.9481	10	800	0.0258	0.9370	11	616	0.0242	0.9389
32	1088	-	-	0.0135	0.9542	11	968	0.0213	0.9426	13	832	0.0204	0.9438
36	1368	-	-	0.0107	0.9591	12	1152	0.0176	0.9478	14	952	0.0132	0.9547
40	1680	-	-	0.0088	0.9630	13	1352	0.0153	0.9513	17	1360	0.0092	0.9620
44	2024	-	-	0.0073	0.9662	14	1568	0.0132	0.9547	18	1512	0.0083	0.9640

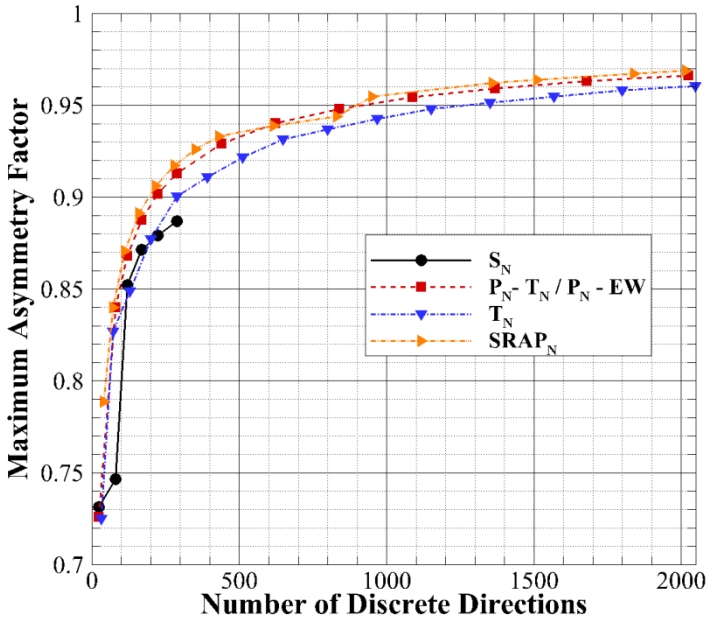

Figure 4.1: Examination of maximum HG asymmetry factor below which Eq. (4.7) is satisfied for DOM with various quadratures and discrete directions

While analysis of the satisfaction of Eq. (4.7) gives an idea of the preliminary range of asymmetry factor where additional phase function treatment is required, in reality the scattered

energy conservation constraint of Eq. (4.2) will be violated for much lower asymmetry factors, due to the fact that Eq. (4.7) only takes into account transmission, and not all other scattered directions.

Figure 4.2(a) examines the conservation of scattered energy (represented by a unity value) versus prescribed HG phase-function asymmetry factor for the S_4, S_8 and S_{12} quadrature sets [Hunter and Guo 2012d]. Scattered energy conservation values are calculated as the left-hand side of Eq. (4.3), and are plotted for all discrete directions $\hat{\boldsymbol{s}}^{l'}$. The appearance of three separate conservation values for S_8 and five values for S_{12} in Figure 4.2(a) stems from the discrete direction weight w^l, as the S_8 and S_{12} quadrature have three and five distinct weighting factors, respectively. For the S_4 quadrature, all directional weights are equivalent.

As seen in the inlay of Figure 4.2(a), scattered energy values start to deviate from unity quickly for the S_4 quadrature set, reaching differences of 0.97% and 1.77% for g = 0.4 and 0.45. For the S_8 quadrature, deviations manifest slightly less rapidly, with a maximum deviation of 1.07% appearing for g = 0.45. As the quadrature increases to S_{12}, the maximum deviation goes to 2.74% at g = 0.75. For all three quadratures, deviations become extreme for highly anisotropic scattering. It is witnessed that scattered energy deviation occurs at for much lower values of g than predicted in Table 1. In general, additional phase-function treatment is required for $g \geq 0.35$, 0.40, and 0.60 for the S_4, S_8, and S_{12} quadratures, respectively, in order to ensure accurate conservation of scattered energy in the system.

Figure 4.2(b) examines the conservation of scattered energy versus prescribed phase-function asymmetry factor for the seven Legendre polynomial phase-functions in Figure 2.4(a).

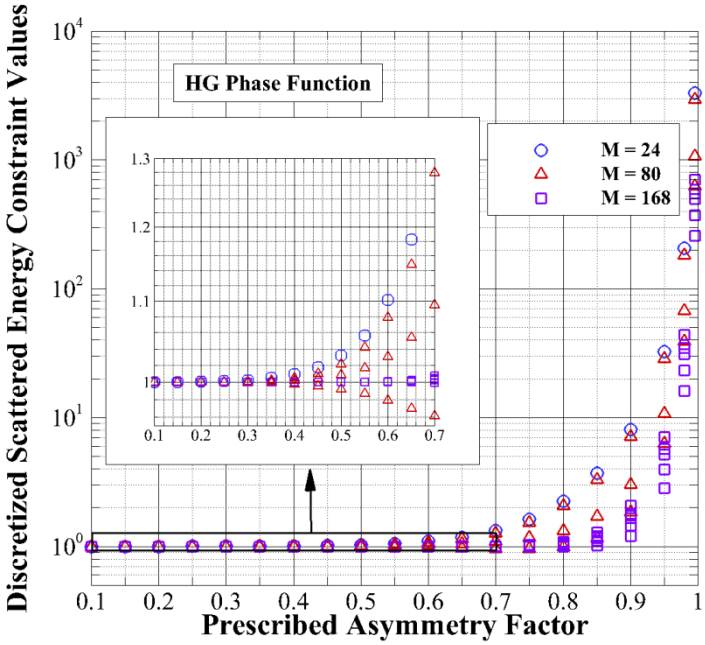

(a)

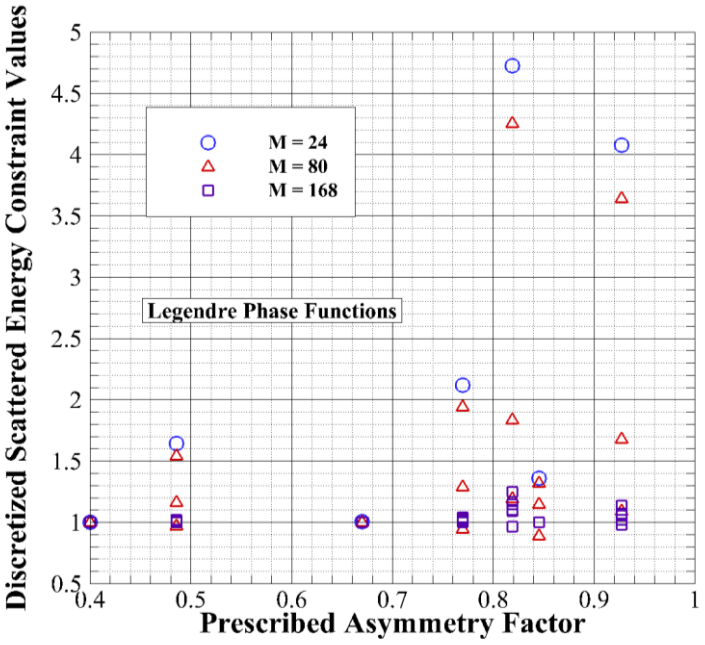

(b)

Figure 4.2: Examination of conservation of scattered energy vs. prescribed phase-function asymmetry factor using DOM S_4, S_8 and S_{12} quadratures: a) HG phase-function, b) Legendre phase-functions

For all three quadratures, scattered energy is conserved within 0.0001% for g = 0.4000, and within 0.75% for g = 0.6697. However, large deviations are witnessed for the remaining Legendre phase-functions. For the S_4 quadrature, deviations range from 64.3% for g = 0.4856 to a maximum of 372.5% occurring for g = 0.8189. Results are similar for the S_8 quadrature set, with deviations ranging from 54.2% to 325.3%. When the quadrature is increased to S_{12}, accurate convergence is realized for g = 0.84534, in addition to g = 0.4000 and 0.6697, and a maximum deviation of 24.6% occurs for g = 0.8189.

For the Legendre phase function, errors in conservation of scattered energy do not follow the strictly increasing pattern witnessed for the HG phase function [Hunter and Guo 2012d]. This phenomenon stems from both the exact shape of the Legendre phase function, as well as the number of terms in the expansion. For the HG phase function, phase-function shape is directly tied to the value of phase-function asymmetry factor. For the Legendre phase function, however, both the number of terms and the magnitude of the coefficients of the higher order terms have a large impact on the exact shape of the phase function, including the severity and number of oscillations present. Since the asymmetry factor is determined solely by the coefficient C_1 ($g = C_1/3$), two phase functions with identical asymmetry factors may have significantly different shapes and oscillatory behavior, due to differences in the higher-order terms or the actual number of terms in the expansion. This leads to the nonlinear correlation between scattered energy conservation and asymmetry factor.

The results from Figures 4.2(a-b) indicate that conservation of scattered energy becomes a significant issue for anisotropic scattering after DOM discretization. Non-conservation of scattered energy for anisotropic scattering can lead to significant errors in radiation transfer predictions, and is likely to result in divergent iterative solutions to the ERT.

Thus, some form of phase function treatment which adjusts for these discrepancies and preserves Eq. (4.3) is necessary.

As mentioned in Section 2.2.1, the phase function asymmetry factor g is a measure of the average cosine of scattering angle, which can be expressed as follows in integral form:

$$g = \frac{1}{4\pi}\int_{4\pi} \Phi(\hat{\boldsymbol{s}}', \hat{\boldsymbol{s}}) \cos\Theta(\hat{\boldsymbol{s}}', \hat{\boldsymbol{s}})\, d\Omega \tag{4.8}$$

Discretizing Eq. (4.8) using the DOM leads to the following expression for g [Hunter and Guo 2012a]

$$\frac{1}{4\pi}\sum_{l=1}^{M} \Phi^{l'l} \cos\Theta^{l'l}\, w^{l} = g\,, \qquad l' = 1,2,\ldots,M \tag{4.9}$$

Eq. (4.9) can thus be considered a constraint on phase-function asymmetry factor. After discretization, this constraint should be accurately satisfied, in order to preserve the scattering properties of the prescribed phase function.

An examination of the conservation of HG asymmetry factor after DOM discretization using the S_4, S_8, and S_{12} quadratures is presented in Figure 4.3. Conservation of asymmetry factor is calculated by averaging the directional values of the summation in Eq. (4.9), and then dividing that average by the prescribed asymmetry factor [Hunter and Guo 2012d]. A ratio of unity indicates accurate conservation (i.e., $g_{discretized} = g_{prescribed}$). For all quadratures, similar correlations to those seen for scattered energy conservation in Figure 4.2a are witnessed. As g increases, there is a strict increase in the deviation from true conservation of asymmetry factor, and a refinement of the angular quadrature results in reduction of conservation deviations at all prescribed asymmetry factors.

For the S_4 quadrature, deviations in asymmetry factor conservation manifest more quickly than the scattered energy deviations seen in Figure 4.2a. For example, at g = 0.40, the deviation from asymmetry factor conservation is 3.3%, as opposed to the 0.97% difference witnessed for scattered energy. In addition, a visible discrepancy is witnessed for g = 0.20. For the S_8 and S_{12} quadratures, deviations of greater than 1% are first attained for g = 0.60 and 0.75, respectively. As asymmetry factor increases to g = 0.90, extreme deviations in discretized asymmetry factor are witnessed, with a deviation of 70.3% occurring for the S_{12} quadrature.

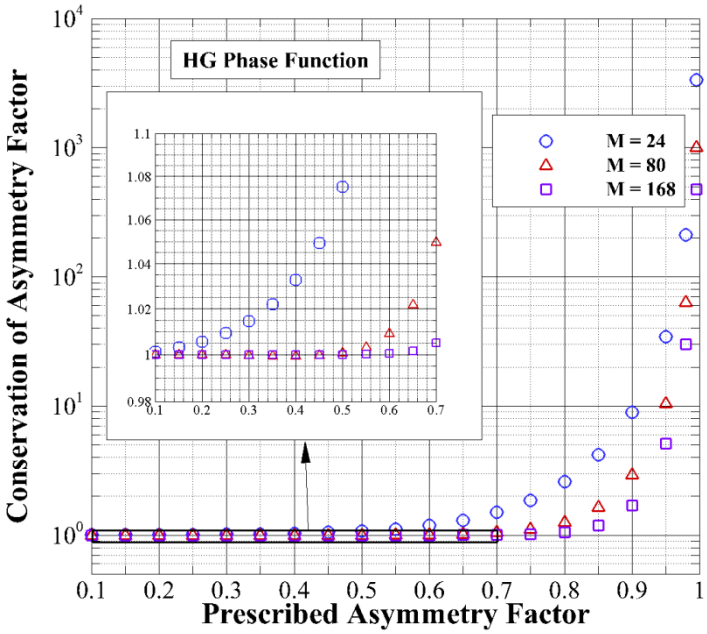

Figure 4.3: Examination of conservation of phase-function asymmetry factor vs. prescribed phase-function asymmetry factor for HG phase-function with DOM S_4, S_8 and S_{12}

Figures 4.4(a-b) examine the conservation of asymmetry factor for the seven Legendre phase functions for the S_4 and S_{12} quadratures, respectively. Conservation ratios determined using Eq. (4.9) are examined for each individual radiation direction $\hat{\boldsymbol{s}}^{l'}$, and are plotted against the cosine of polar angle θ. For the S_4 quadrature, changes in polar angle do not impact the

conservation of asymmetry factor, due to the fact that all directional weighting factors are identical. Accurate conservation is witnessed for the g = 0.4000 expansion. For the g = 0.6697 expansion, the discrepancy in asymmetry factor conservation is 2.1%, which is larger than the 0.75% deviation in scattered energy witnessed in Figure 4.2b. Large discrepancies occur for the remaining five phase functions, with the degree of deviation corresponding to the patterns witnessed in Figure 4.2b.

For the S_{12} quadrature, conservation ratios show a dependence on the polar angle of the discrete direction, due to the fact that the discrete weighting factors $w^{l'}$ vary with polar angle for this quadrature. The discrepancies in asymmetry factor conservation for S_{12} are much smaller than those seen for S_4. Asymmetry factor is accurately conserved, for all polar angles, for the g = 0.4000, 0.6697, and 0.8453 phase functions, conforming to the results seen in Figure 4.2b for scattered energy. The largest deviation occurs for g = 0.8189, reaching a maximum of 30.8%. The results from Figures 4.2b and 4.4(a-b) indicate that additional treatment is required to conserve both scattered energy and asymmetry factor for all phase functions except g = 0.4000 for the S_4 scheme, while for the S_{12} quadrature, attention is required only for g = 0.4856, 0.7693, 0.8189, and 0.9273.

In order to accurately predict radiation transfer in anisotropically scattering media, the breakdowns in conservation of both scattered energy and asymmetry factor must be addressed.

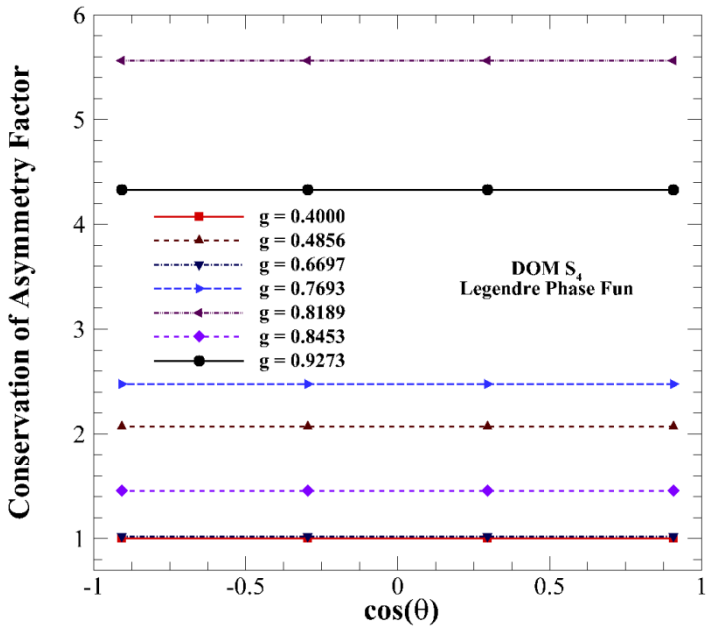

(a)

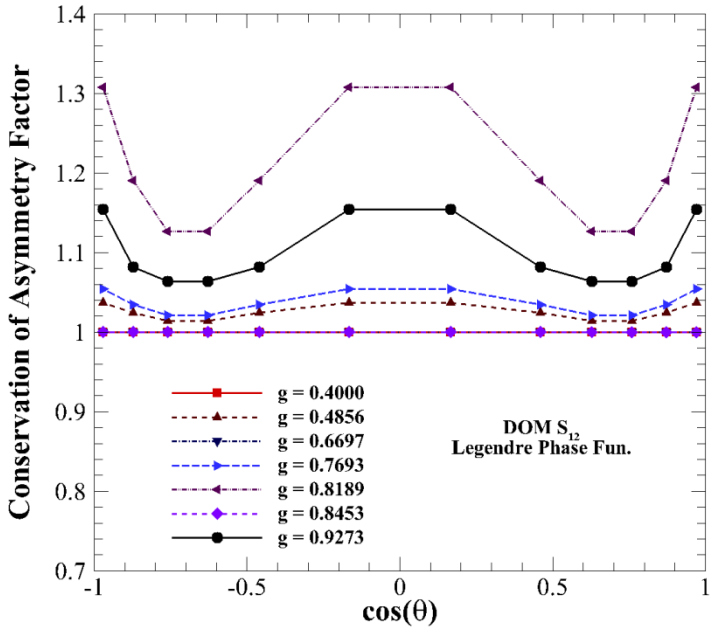

(b)

Figure 4.4: Examination of conservation of phase-function asymmetry factor vs. prescribed phase-function asymmetry factor for Legendre phase-functions with DOM S_4 and S_{12}

4.1.2 Phase-Function Normalization to Conserve Scattered Energy

In order to ensure that scattered energy is conserved in the system so that convergent ERT solutions can be obtained, the scattering phase function Φ can be normalized. Previous publications have provided normalization techniques that allow for accurate satisfaction of Eq. (4.3). The most common approach is to normalize the phase function using a common approach from probability theory, as follows [Kim and Lee 1988, Liu et al. 2002]

$$\widetilde{\Phi}^{l'l} = \Phi^{l'l} * \left(\frac{1}{4\pi} \sum_{l=1}^{M} \Phi^{l'l} w^{l} \right)^{-1} \tag{4.10}$$

By multiplying $\Phi^{l'l}$ by the inverse of the scattered energy summation value, the normalized scattering phase function $\widetilde{\Phi}^{l'l}$ is guaranteed to accurately satisfy Eq. (4.3) for each discrete direction $\hat{\boldsymbol{s}}^{\boldsymbol{l'}}$. This term is akin to a "normalizing constant" for a probability distribution function. Another approach, introduced by Wiscombe [1976], uses specific corrective factors for each individual direction to ensure the conservation of Eq. (4.3). Using this approach, the phase function is normalized as [Wiscombe 1976]

$$\widetilde{\Phi}^{l'l} = (1 + \kappa^{l} + \kappa^{l'}) \Phi^{l'l} \tag{4.11}$$

where κ^{l} and $\kappa^{l'}$ are solutions to the system of equations

$$\frac{1}{4\pi} \sum_{l=1}^{M} (1 + \kappa^{l} + \kappa^{l'}) \Phi^{l'l} w^{l} = 1 \,, \qquad l' = 1,2, \dots, M \tag{4.12}$$

Both approaches result in similar conservation of scattered energy in the system, allowing for convergent ERT solutions [Chai et al. 1994]. Since both of these normalizations produce similar

results, only the scattered energy normalization of Eq. (4.10) will be considered for further analysis. The normalization approach of Eq. (4.10) can be considered as a directional averaging of scattered energy, and thus this technique will be referred to as "scattered energy averaging" in the remainder of this dissertation.

4.1.3 Angular False Scattering

While scattered energy averaging is mathematically able to accurately conserve scattered energy in the system, an analysis of conservation of discretized phase function asymmetry factor is required, to ensure that medium scattering properties are retained after angular discretization [Hunter and Guo 2012a, Hunter and Guo 2012b, Hunter and Guo 2012d]. Figures 4.5(a-b) plot discretized phase function asymmetry factor versus prescribed asymmetry factor for both HG and Legendre phase functions, generated using the DOM S_4, S_8, and S_{12} quadratures.

For the HG phase-function in Figure 4.5a, it is witnessed that the discretized asymmetry factor overpredicts the prescribed value by 1.2% at g = 0.3000 for the S_4 quadrature, with error in asymmetry factor reaching 14.8% for g = 0.8000 (resulting in a discretized asymmetry factor of 0.9186). For the S_8 quadrature, an overprediction of 1% is not reached until g = 0.7000, with the maximum difference of 6.48% occurring for g = 0.9000. For the S_{12} quadrature, a maximum difference of 4.2% is witnessed for g = 0.9000, with discrepancies first reaching 1% for g = 0.8000. As scattering becomes extremely anisotropic ($g > 0.9000$), the difference between discretized and prescribed asymmetry factors steadily decrease, due to the fact that asymmetry factor is limited to a maximum value of unity.

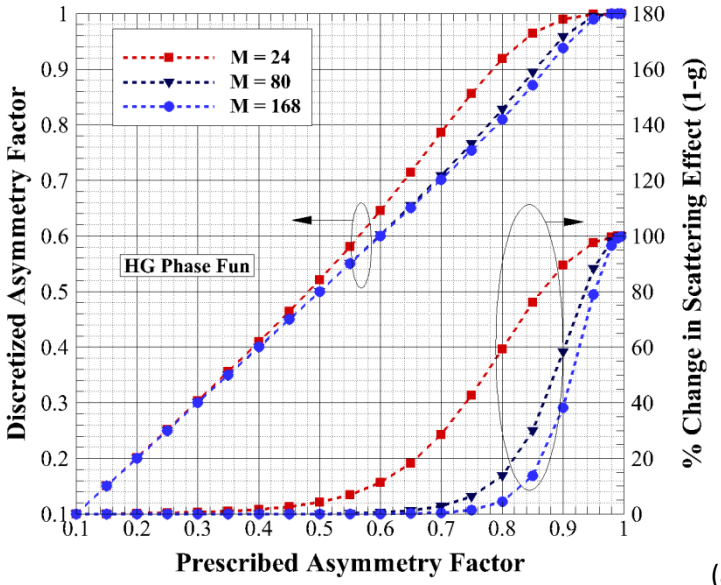

(a)

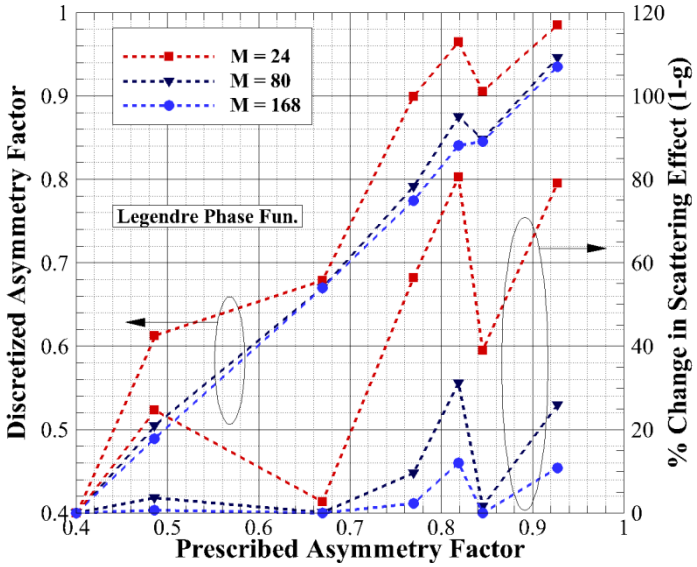

(b)

Figure 4.5: Comparison of discretized and prescribed asymmetry factor and change in scattering effect after application of scattered energy averaging for a) HG phase-functions and b) Legendre phase-functions

While differences of these magnitudes may not seem critical, radiation transfer predictions in strongly-scattering media can be vastly impacted by even minor changes in asymmetry factor when *g* is close to unity [Hunter and Guo 2012e]. This is because overall change in scattering effect due to asymmetry factor adjustment is manifested in the difference

in (1-g), according to the isotropic scaling law [Guo and Maruyama 1999, Guo and Kumar 2000]. To this end, the percentage change in (1-g) after directional discretization, which can be calculated as $100\% * \left(\frac{(1-g_{discretized})-(1-g_{prescribed})}{(1-g_{prescribed})}\right)$, is also presented in Figure 4.5a. Differences in scattering effect of >20% are seen for $g >$ 0.6500, 0.8000, and 0.8500 for the three quadratures, respectively. As prescribed asymmetry factor increases, scattering effect change becomes extremely large, reaching 97.5%, 88.3%, and 78.8% for g = 0.9500 for the three quadratures.

A similar plot for the Legendre phase functions is presented in Figure 4.5b. Asymmetry factor is effectively conserved for all DOM quadrature sets for g = 0.4000. For g = 0.6697, asymmetry factor is effectively conserved within 0.03% for both S_8 and S_{12}, but a 1.29% difference (leading to a discretized value of 0.6784) is witnessed for S_4. The largest differences in discretized asymmetry factor for S_8 and S_{12} occur for g = 0.8189 (corresponding to the largest discrepancies in scattered energy conservation), reaching values of 6.88% and 2.64%, respectively. The percent changes in scattering effect corresponding to the deviations in g are greater than 10% for all quadratures for both g = 0.8189 and 0.9273.

Additional visualization of the lack of asymmetry factor conservation can be seen in Figures 4.6(a-d), which plot discretized phase-function values, generated using the DOM S_4, S_8, S_{12} and S_{16} quadratures, for various HG phase function approximations against the theoretical prescribed values. For a prescribed g = 0.5000 in Figure 4.6(a), the discretized phase function values accurately conform to the prescribed phase function, with only minimal deviation witnessed for the lowest directional order (discretized g = 0.5210). As prescribed g is increased, however, the discretized phase function values start to deviate greatly from the prescribed phase-function. For g = 0.9500, the prescribed asymmetry factor is altered greatly to

discretized values of g = 0.9987, 0.9942, 0.9894, and 0.9828 for the four quadratures, respectively. Significant errors are witnessed for all direction numbers, corresponding to the results presented in Figure 4.5a.

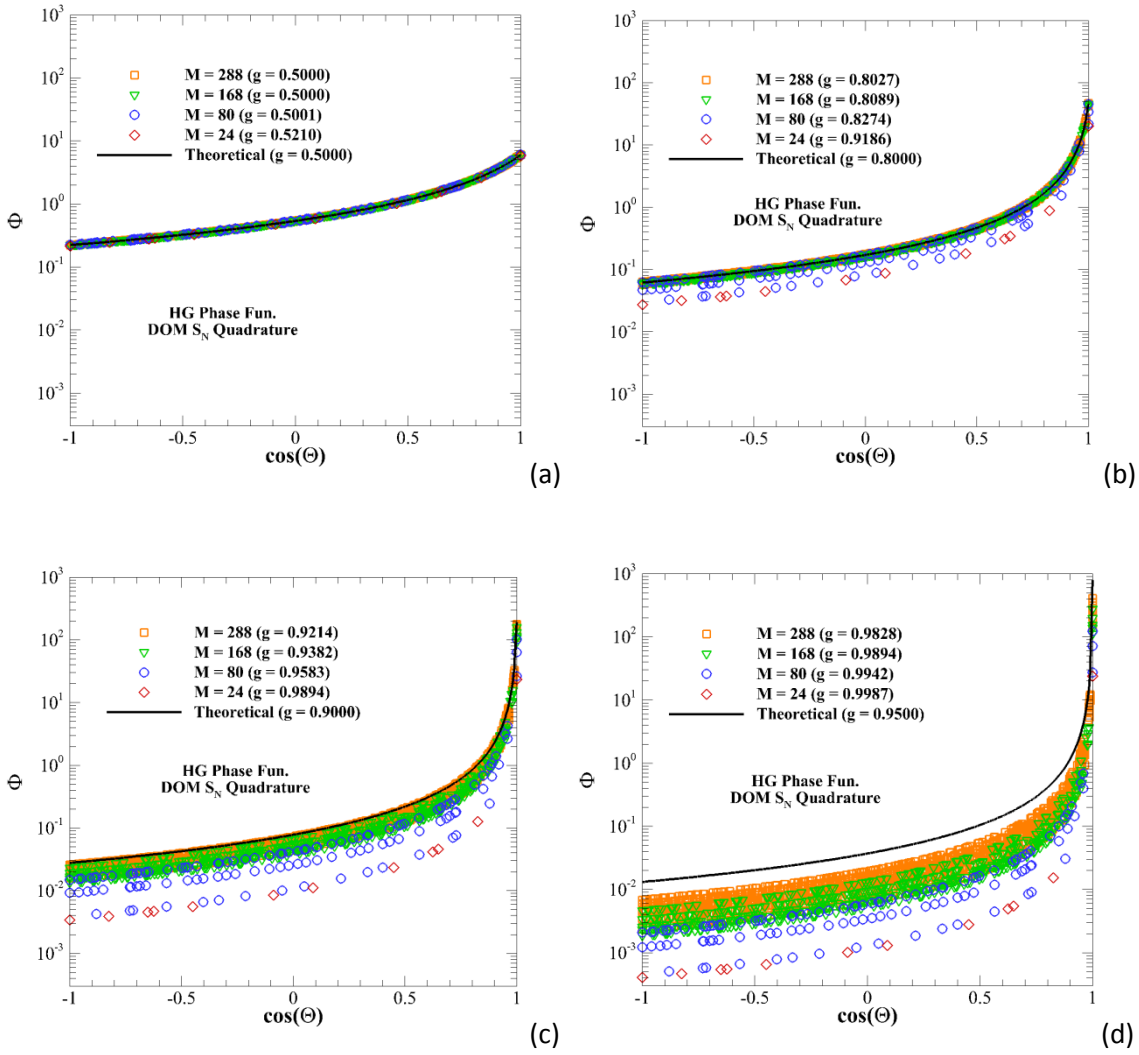

Figure 4.6: Discretized HG phase-function values for a) g = 0.5000, b) g = 0.8000, c) g = 0.9000, and d) g = 0.9500

Similar visualizations for four Legendre polynomial phase functions (g = 0.4856, 0.8189, 0.84534, and 0.9273) are presented in Figures 4.7(a-d). The results conform to those shown in Figure 4.5b, indicating that the exact shape and oscillatory behavior of the phase function has an

impact on conservation of asymmetry factor. The g = 0.4856 phase function, due to the shape including a forward- and backward-scattering peak, shows a much larger deviation in discretized phase function values than those witnessed for the HG g = 0.5000 phase function in Figure 4.6a. The largest discrepancies occur for g = 0.8189 for all quadratures, while only minimal differences occur for g = 0.84534 (significant deviation in g only witnessed for M = 24). For g = 0.8189 and 0.9273, discrete direction numbers below M = 168 are not able to accurately represent the true phase-function shape, due to strong oscillatory behavior.

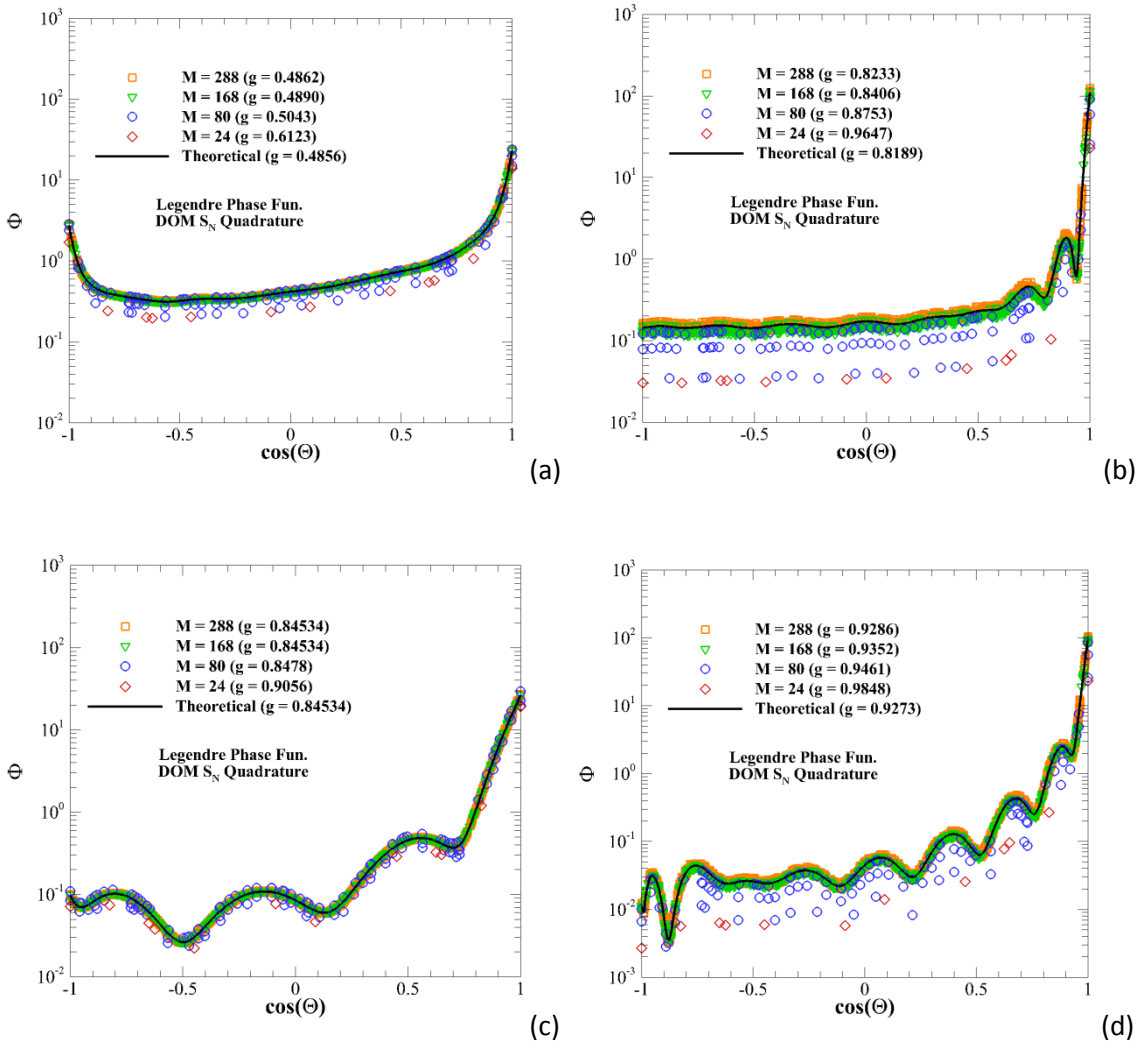

Figure 4.7: Discretized Legendre phase-function values for a) g = 0.4856, b) g = 0.8189, c) g = 0.84534, and d) g = 0.9273

4.1.3.1 The "False Scattering" Misnomer

Alteration of the phase-function asymmetry after angular discretization can dramatically change the scattering properties of the medium, leading to drastic errors in radiation transfer predictions. Errors of this type are termed as "**angular false scattering**" errors [Hunter and Guo 2012d, 2012e, 2013, 2014b], or false scattering errors due to angular discretization. As mentioned in Section 3.3.2.1, numerical smearing has been referred to as "**false scattering**" in the past [Chai et al. 1993], as the errors appear to emulate unrealistic and nonphysical scattering behavior. However, calling numerical smearing errors by the name "false scattering" is, in essence, a ***misnomer***, as numerical smearing depends solely on spatial discretization, and is not impacted in any way by angular discretization or the scattering phase function. In the author's opinion, errors due to lack of asymmetry factor conservation should be referred to as "**false scattering**", as they result from a direct alteration of scattering behavior in the medium. The term "false scattering" should, therefore, not be used as a synonym for numerical smearing. However, as the use of the term "false scattering" has become widespread in the field, the true false scattering errors presented in Figures 4.5-4.7 will henceforth be referred to as "angular false scattering", as to limit confusion.

4.1.4 Impact of Angular False Scattering on DOM Radiation Transfer Predictions

4.1.4.1 Comparison with Isotropic Scaling Law

As a preliminary investigation of the impact of angular false scattering, radiation transfer predicted using the DOM with scattered energy averaging can be compared to predictions generated using the isotropic scaling law [Guo and Maruyama 1999, Guo and Kumar 2000]. The isotropic scaling law allows any anisotropic scattering phase-function Φ to be

approximated as isotropic ($\Phi^* = 1$) by artificially scaling the optical thickness and scattering albedo of the medium as follows:

$$\tau^* = \tau(1 - g\omega)\,, \qquad \omega^* = \frac{\omega(1-g)}{1-g\omega} \tag{4.13}$$

Approximation of this type leads to a much quicker convergence time than the traditional approach [Guo and Maruyama 1999]. The isotropic scaling law has been shown to produce accurate radiation transfer predictions for steady-state, forward scattering problems, especially for optically thick media [Kamdem Tagne and Ballis 2005]. However, caution must be exercised when using the isotropic scaling law, as Guo and Maruyama [1999] and Guo and Kumar [2000] illustrated its impropriety for transient problems (especially at small times), due to the decrease in photon flight distance and time inherent with the reduced optical thickness τ^*. While the isotropic scaling law cannot be used in place of traditional anisotropic scattering for many problems, it can be used to help clarify the impact of angular false scattering errors [Hunter and Guo 2012a, Hunter and Guo 2012b]

The benchmark problem chosen for comparison of DOM and isotropic scaling results is radiation transfer in a 2-D, axisymmetric cylindrical enclosure housing a purely scattering medium (ω = 1.0) that has optical thickness τ and scatters light anisotropically according to the HG phase function with asymmetry factor g. The radial side wall of the enclosure is taken as a diffuse emitter, with unity emissive power, while the axial end walls are cold and black. The medium is also taken as cold. A spatial grid of (N_r x N_z) = 40 x 80 was implemented to eliminate grid dependence and minimize numerical smearing error, while M = 288 discrete directions were used to minimize ray effect errors.

Figures 4.8(a-b) compares non-dimensional radial side wall heat flux $Q_R^*(z^*)$ generated using the DOM with scattered energy averaging with results generated using the isotropic scaling law. The heat flux is non-dimensionalized by the radial side wall emissive power. The medium optical thickness is taken as τ = 25.0, while the HG asymmetry factor is prescribed as g = 0.9000 in Figure 4.8a and g = 0.9500 in Figure 4.8b.

When scattered energy averaging is applied in Figure 4.8a, the discretized asymmetry factor is altered from g = 0.9000 to 0.9214, resulting in an overprediction of isotropic scaling results of up to 17%. When compared to isotropic scaling results generated using the altered asymmetry factor g = 0.9214, differences are significantly reduced to a maximum of 6%. In Figure 4.8b, the normalized DOM overpredicts isotropic scaling heat flux generated at the prescribed g = 0.9500 by a maximum of 20.4%, while conforming almost exactly to the isotropic scaling heat flux generated at the discretized g = 0.9830 (percent differences of less than 0.5% at all locations except near z^* = 0). These results give confidence that DOM predictions generated using scattered energy averaging exhibit scattering properties that conform to the altered asymmetry factor, illustrating the critical impact of angular false scattering.

Figure 4.9 plots the percent difference in $Q_R^*(z^*)$ between the DOM with scattered energy averaging and the isotropic scaling law for various optical thicknesses with HG g = 0.9500. For τ = 1.0, the DOM conforms accurately to the isotropic scaling results within 1% at all axial locations. In an optically thinner medium, radiant energy is able to propagate further into the medium before it encounters a scattering event, meaning that the impact of the altered asymmetry factor is physically mitigated. As optical thickness increases, significant increases in difference between DOM and isotropic scaling are witnessed, due to the increased number of scattering events in the medium. Maximum differences reach 3.2%, 13.1%, and 25.2% for τ = 5,

15, and 25, respectively. The results from Figure 4.9 indicate that angular false scattering errors due to a lack of asymmetry factor conservation have a major impact on radiation transfer in optically thicker media, and should not be ignored [Hunter and Guo 2012a].

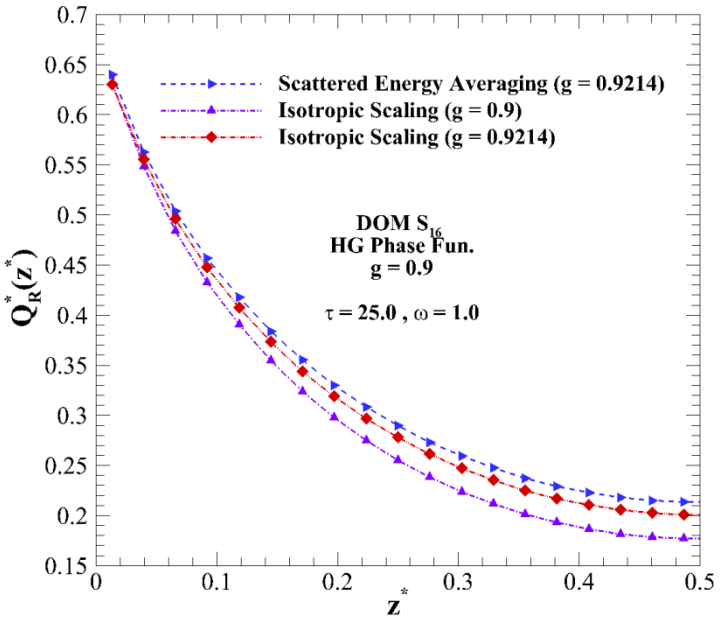

(a)

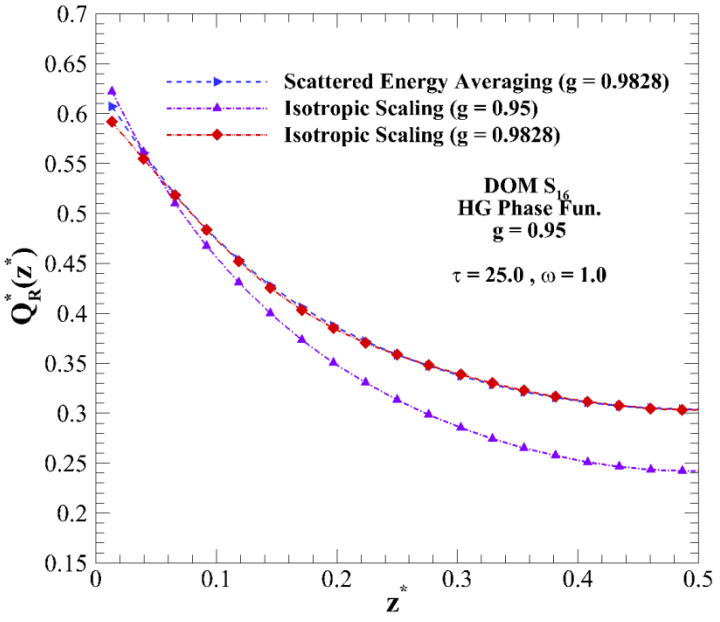

(b)

Figure 4.8: Comparison of $Q_R^*(z^*)$ generated with DOM S_{16} quadrature using scattered energy averaging with isotropic scaling predictions for HG a) g = 0.9000 and b) g = 0.9500

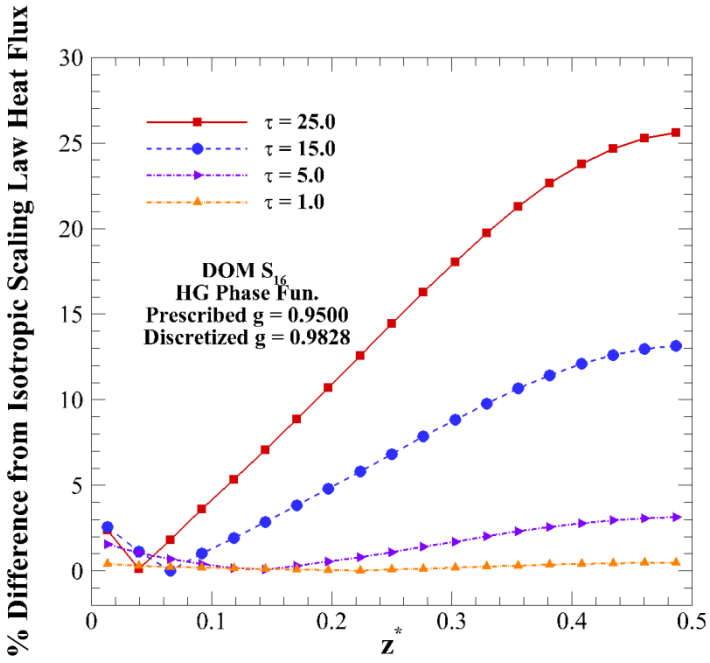

Figure 4.9: Percent difference in $Q_R^*(z^*)$ between DOM S_{16} with scattered energy averaging and isotropic scaling solution for HG g = 0.9500 with varying optical thickness

4.1.4.2 Comparison with Monte Carlo

The comparisons to the isotropic scaling law in Figures 4.8 and 4.9 give a preliminary indication of the issues caused by angular false scattering. However, additional validation is necessary, due to the fact that the isotropic scaling law is an artificial method of treating scattering anisotropy. To this end, comparisons to radiation transfer results generated using the statistical Monte Carlo (MC) method are presented in the following figures, in order to further validate the necessity of minimizing angular false scattering [Hunter and Guo 2012e].

The MC, details of which can be found in Modest [2002], has been extensively used as a method for determining both steady-state [Maltby and Burns 1991, Walters and Buckius 1992, Farmer and Howell, 1994, Yang et al. 1995, Howell 1998] and ultrafast radiation transfer [Flock et al. 1989, Hasegawa et al. 1991, Guo et al. 2000, Guo et al. 2002] in participating media. While

the MC does suffer from shortcomings such as statistical error and lack of computational efficiency, it does not involve angular discretization, and thus will not be influenced by angular false scattering. Additionally, the MC has the ability to handle almost any geometric or physical condition, and is thus commonly implemented as a realistic alternative to experimentation.

The benchmark problem considered for MC comparison is radiation transfer in a 3-D cubic enclosure housing a purely scattering medium (ω = 1.0), with optical thickness τ = 10.0. The medium scatters radiant energy anisotropically according to the HG phase-function approximation. All spatial coordinates are non-dimensionalized by the cube edge length, as described in Section 2.4.1. The medium is taken as cold, and all walls are taken as blackbody emitters. The wall at z^* = 0 is taken to be hot, with unity emissive power, and all other enclosure walls are cold. To ensure minimization of numerical smearing, the spatial grid is taken as $\left(N_x \text{ x } N_y \text{ x } N_z\right)$ = (27 x 27 x 27). For this benchmark problem, MC results computed with over 4 million quanta for each reference control-volume are presented by Boulet et al. [2007].

Figure 4.10 compares radiative heat fluxes $Q(x^*, y^* = 0.5, z^* = 1)$, calculated at the centerline of the wall opposite from the diffuse source, generated using the DOM S_{12} quadrature with scattered energy averaging to the readily available MC benchmark solutions. Results are presented for g = 0.2000, 0.8000, and 0.9300. For weakly-forward scattering (g = 0.2000), DOM heat fluxes conform accurately to the published MC predictions, with differences of between 1-5% witnessed. Errors of ~5% between DOM and MC predictions are not unreasonable, due to DOM discretization errors, as well as statistical errors existing in MC practice [Hunter and Guo 2012e]. Additionally, as seen in Figure 4.5a, asymmetry factor is not significantly altered after DOM discretization for weakly-forward scattering, so accurate conformity between DOM and MC isn't surprising.

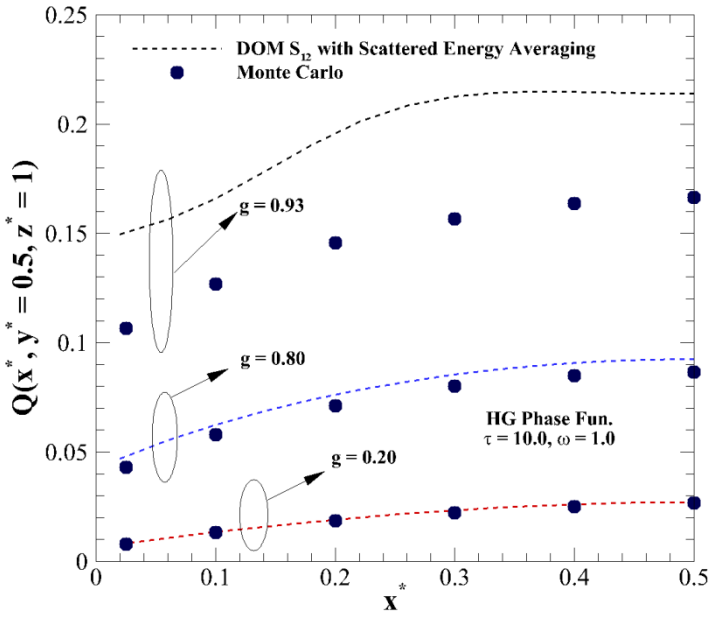

Figure 4.10: Comparison of Q(x*, y* = 0.5, z* = 1.0) generated using DOM S_{12} with scattered energy averaging vs. Monte Carlo solution [Boulet et al. 2007] for HG g = 0.2000, 0.8000, and 0.9300

As asymmetry factor increases to g = 0.8000, discrepancies between DOM and MC increase to 6-9%, corresponding to the small alteration in discretized asymmetry factor to g = 0.8089 (change in scattering effect (1-g) of 4.5%). Further increase of g to 0.9300 results in the DOM massively overpredicting the benchmark MC results by between 28-36%. Application of scattered energy averaging results in a discretized asymmetry factor of g = 0.9735, which corresponds to a 62.1% change in scattering effect (1-g). Errors due to angular false scattering are extremely evident in Figure 4.10, highlighting a major issue for modeling of radiation transfer in highly anisotropic scattering media.

Figures 4.11(a-d) show a comparison of DOM and MC heat fluxes $Q(x^*, y^* = 0.5, z^* = 1.0)$ generated using various DOM quadrature schemes [Hunter and Guo 2013]. Heat fluxes generated using the S_N, P_N-T_N, P_N-EW, T_N, and $SRAP_N$ quadratures are presented for the strong-

forward scattering case (g = 0.9300) analyzed previously. Results are presented for M = 24, 80, 168, and 288 discrete directions in Figures 4.11(a-d), respectively, for the S_N, P_N-T_N, and P_N-EW quadratures. For the geometric T_N and $SRAP_N$ quadratures, the direction numbers are not exactly the same as for the other three quadratures, and thus the closest possible direction numbers are implemented.

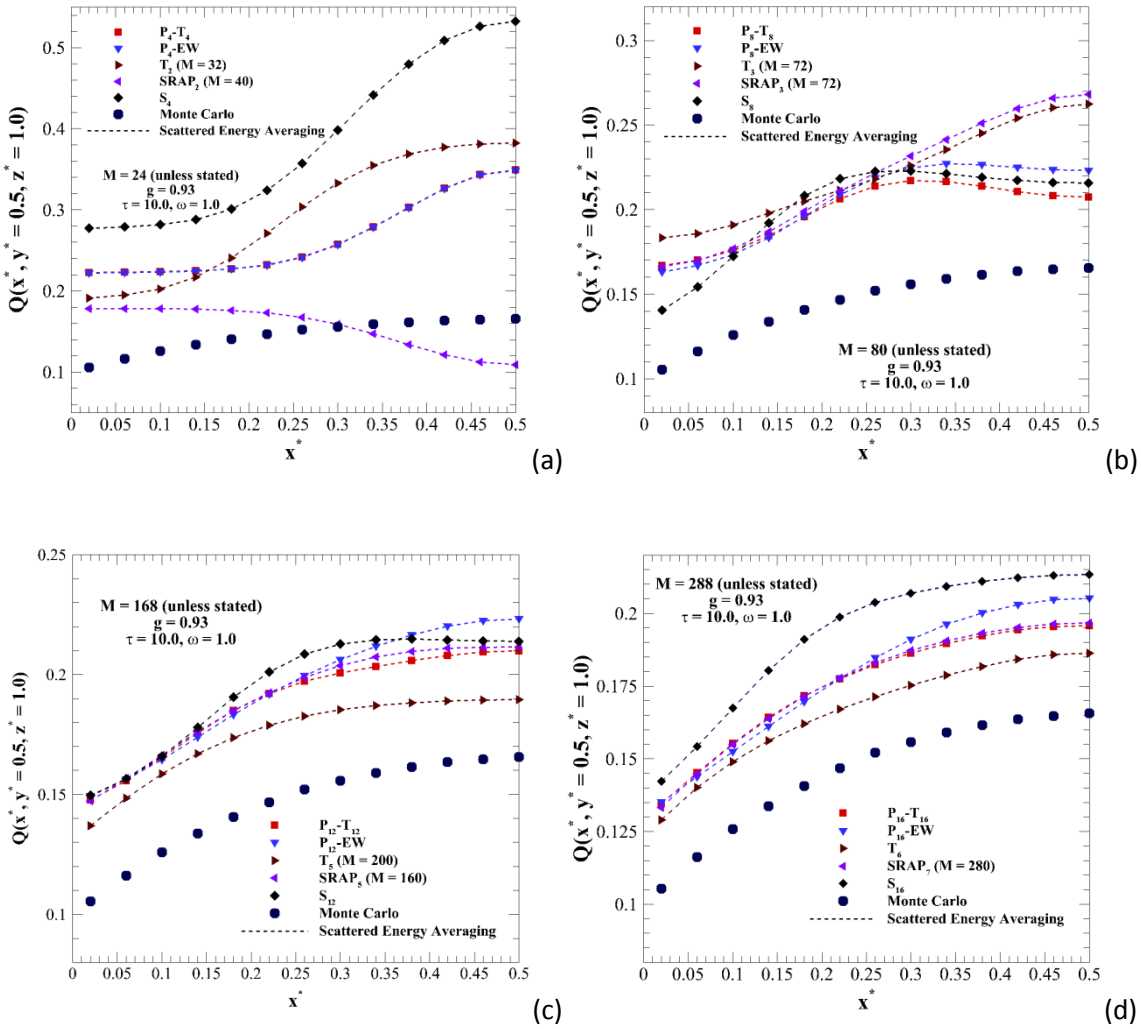

Figure 4.11: Comparison of Q(x*, y* = 0.5, z* = 1.0) generated using DOM with scattered energy averaging with Monte Carlo [Boulet et al. 2007] for various DOM quadratures with a) M = 24, b) M = 80, c) M = 168, and d) M = 288 discrete directions

In Figure 4.11a, radiative heat fluxes are presented for DOM quadrature with discrete direction number on the order of the S_4 quadrature (M = 24). The T_2 (M = 32) and $SRAP_2$ ($M = 40$) quadrature sets are applied for this analysis, as their direction numbers are the closest possible to that of the S_4 quadrature. DOM heat flux profiles generated with scattered energy averaging differ greatly from the reference MC solution for all quadratures, with maximum differences ranging between 69%-222%. All quadratures overpredict the MC heat flux at all medium locations except for $SRAP_2$. In fact, the $SRAP_2$ profile does not make physical sense, as the heat flux should be highest at x^* = 0.50 in this situation.

As quadrature is increased to the order of S_8 (M = 80) in Figure 4.11b, the maximum differences reduce to between 49-74%. Further increase in discrete direction number to the order of S_{12} (M = 168) and S_{16} (M = 288) in Figures 4.11c-d reduces the maximum differences between DOM and MC to 40-42% and 22-36%, respectively, corresponding to the improvements in discretized asymmetry factor with improved resolution of the continuous angular variation of radiation scattering.

For the results in Figure 4.11d, it appears that the four non-directionally limited quadratures conform to MC solutions with equal or higher accuracy than the S_N quadrature, which can possibly be explained by the fact that these quadratures more accurately approximate higher-order even- and odd- moments. However, the errors between DOM and MC still have significant magnitude, indicating that for $M \leq$ 288, angular false scattering will be a major issue for any DOM quadrature scheme [Hunter and Guo 2013].

4.1.5 Angular False Scattering in Non-Directionally Limited Quadratures

Figures 4.5-4.7 indicate that increasing discrete direction number allows for more accurate representation of the original medium scattering properties after DOM discretization. While the S_N quadrature is directionally-limited to 288 discrete directions, where angular false scattering is highly evident, non-limited quadratures may afford the capability to effectively minimize angular false scattering errors simply by increasing angular resolution to a high enough degree [Hunter and Guo 2013]. To this end, Figure 4.12 plots the percent change in scattering effect (1-g) for the four non-limited quadrature sets versus number of discrete directions using a prescribed HG phase-function approximation with g = 0.9300. As a comparison for lower-order quadrature, S_N results up to the directional limit are also plotted.

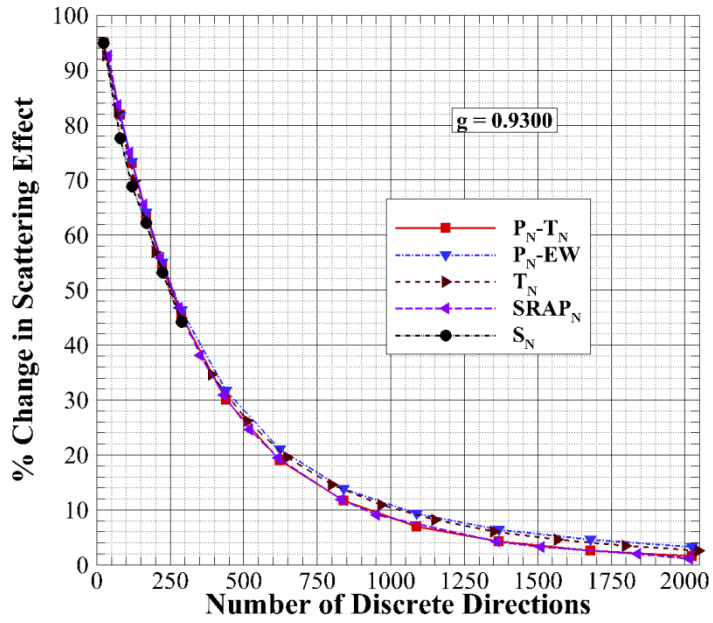

Figure 4.12: Inspection of scattering effect change with increase in DOM discrete direction number for non-limited DOM quadratures with HG g = 0.9300

Up to the directional limit of M = 288, all five quadrature sets exhibit similar behavior, with dramatic decreases in scattering effect change occurring with direction number increase. Deviations of >90% are witnessed for the lowest-order quadrature for all schemes. At the S_N directional limit, application of scattered energy averaging reduces scattering effect change to between 44-47% for the five quadratures. Changes in scattering effect of less than 10% are first realized around M = 1000 for the four non-limited quadratures, while increase in directions to >2000 results in scattering effect changes of between 1-3%, indicating that some error due to angular false scattering may exist even for an extremely high directional order. Substantial increases in direction number result in the percent change in scattering effect converging towards 0%, indicating a possible distinct advantage of non-limited quadrature sets.

Figures 4.13(a-b) examine the percent difference in heat flux $Q(x^*, y^* = 0.5, z^* = 1.0)$ between the reference MC and DOM solutions vs. the discrete direction number at two different values of x^*: x^* = 0.10 and 0.50, respectively. The heat fluxes are generated using the four non-limited quadrature sets with application of scattered energy averaging. In Figure 4.13a, increase in direction number when scattered energy averaging is applied causes differences between MC and DOM to decrease for all quadrature sets, corresponding to the decrease in scattering effect change in Figure 4.12. However, it is important to note that the percent differences do not converge to zero. Instead, they slowly converge to a slightly negative percentage, due to statistical/numerical errors inherent in both MC and DOM methods. For example, at discrete direction number M ~ 2000, the percent differences between MC and DOM heat fluxes are between 0 and -1.2%. In order to obtain heat fluxes that differ by less than 5%, between M = 750 and 1000 directions must be used, depending on the quadrature set.

Results are similar for x^* = 0.50 in Figure 4.13b. For this location, more prominent discrepancies between the four quadrature sets exist after application of scattered energy averaging. The P_N-EW quadrature more greatly overpredicts the MC solution than the other quadrature sets over the range of discrete directions. In fact, while other quadratures have started to underpredict the MC solution at high directional order, heat fluxes generated by the P_N-EW have converged more slowly, and continue to overpredict the MC solution at high direction number. In order to obtain a percentage difference of less than 5%, M = 1368 is required for P_N-EW, while other quadratures only require 500-850 directions.

The advent of non-limited directional quadrature sets also provides the possibility that, with sufficiently large discrete direction number, both scattered energy and asymmetry factor may be accurately conserved *without* the use of any additional phase-function treatment. It is possible that angular false scattering can be effectively minimized or eliminated if angular resolution is taken at a fine enough level [Hunter and Guo 2013]. This concept is examined in Figure 4.14, in which DOM heat flux profiles generated with the P_N-T_N quadrature with extremely high direction number and no phase-function normalization are compared to the reference MC solution for g = 0.9300. Heat fluxes are presented for the P_{44}-T_{44}, P_{52}-T_{52}, and P_{64}-T_{64} quadratures, which have M = 2024, 2808, and 4224 discrete directions, respectively.

The three non-normalized profiles show a converging trend as direction number increases. For M = 2024 discrete directions, differences of between 27-30% exist for all locations when compared to the MC, corresponding to distortion of discretized g to a value of 0.9453 (22% change in scattering effect). While scattered energy is conserved well enough that the ERT solution does converge, the angular grid in this case is still too coarse to obtain accurate

radiation transfer solutions. Increase in direction number to M = 2808 reduces the discrepancies to less than 10% for all locations, corresponding to discretized g = 0.9356.

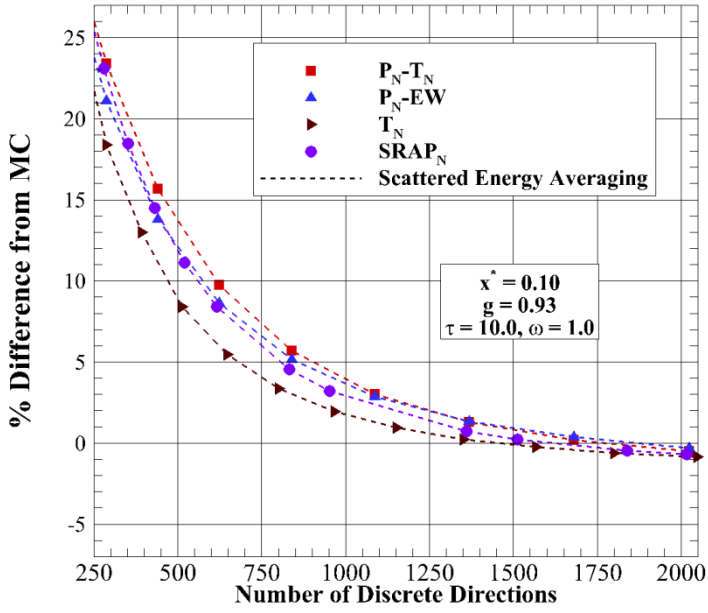

(a)

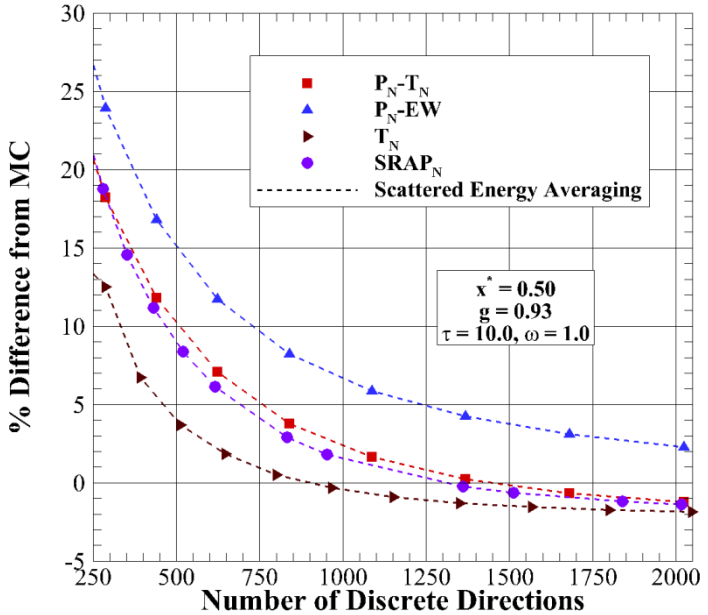

(b)

Figure 4.13: Percent difference in Q(x*, y* = 0.5, z* = 1.0) generated using DOM with scattered energy averaging from Monte Carlo [Boulet et al. 2007] for various DOM quadratures and discrete direction numbers at a) x^* = 0.1 and b) x^* = 0.5

For the extreme M = 4224 quadrature, MC and DOM differ by less than 1.5% for all locations. This solution corresponds to a discretized g = 0.9313, which still results in a 2% change in scattering effect. For comparison, applying scattered energy averaging to this quadrature reduces the discretized g to 0.9301 (0.14% scattering effect change), resulting in heat flux that underpredicts the MC solution by less than 2.5% at all locations, conforming to the results in Figures 4.13(a-b).

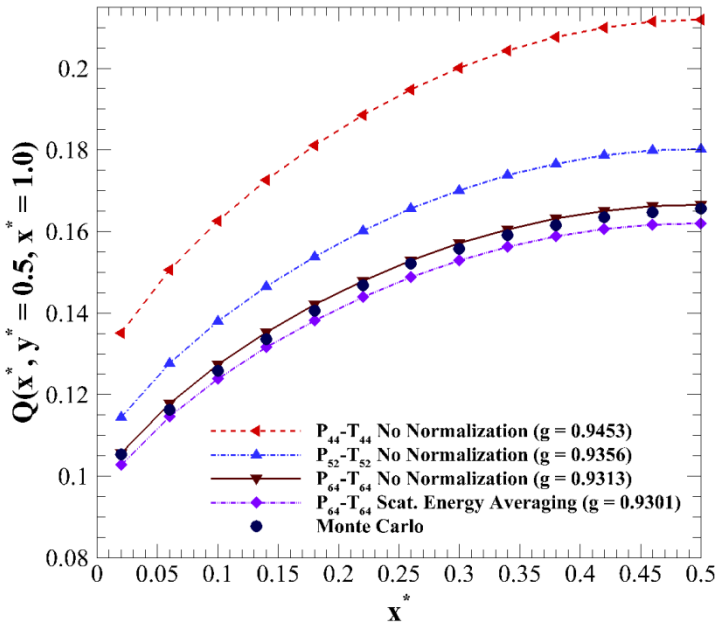

Figure 4.14: Comparison of Q(x*, y* = 0.5, z* = 1.0) generated using DOM without normalization for extremely high discrete direction number

While Figures 4.13-4.14 show that higher-order DOM quadrature sets have the advantage of minimizing angular false scattering error, a major disadvantage of higher-order quadrature sets lies in computational efficiency, as increases in discrete direction number directly result in both higher computational convergence times and greater computational committed memory [Hunter and Guo 2013]. Figure 4.15 examines the computational convergence time, in minutes, versus number of discrete directions for various quadrature sets.

For low direction number, all five quadrature sets converge in similar amounts of time, with convergence times of ~ 13 minutes seen for S_{16} equivalent quadratures.

Convergence time dramatically increases in a non-linear fashion with increase in discrete direction number. For example, looking at the P_N-T_N quadrature, increases in direction number to M = 624, 840, 1088, 1368, and 2024 result in convergence times of 98, 195, 325, 557, and 1330 minutes, respectively. Although it is not presented in this figure, obtaining the more accurate non-normalized P_{64}-T_{64} solution in Figure 6 required 7107 minutes (4.94 days) to converge. These extremely high convergence times illustrate the impracticality of using higher-order quadratures to obtain accurate radiation transfer solutions.

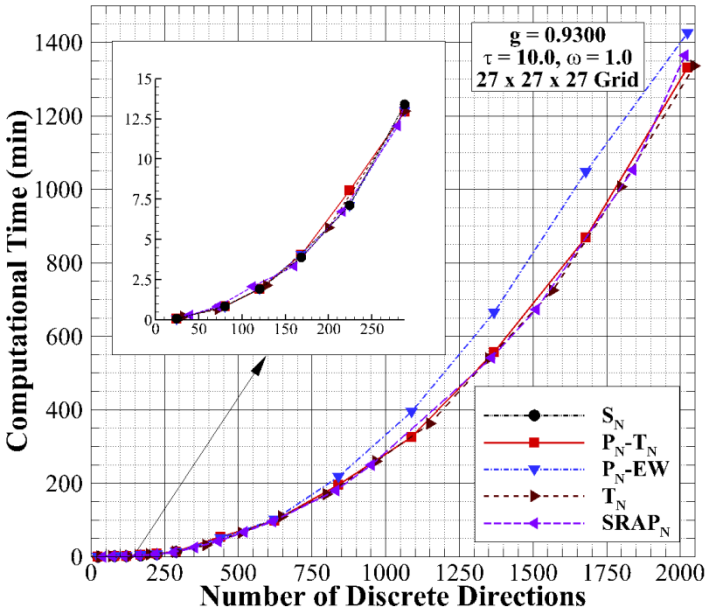

Figure 4.15: Examination of computational time required for use of large discrete-direction number with non-limited quadratures

The overall results in Figures 4.8-4.15 indicate major issues resulting from lack of asymmetry factor conservation after angular discretization. While it is possible to minimize

and/or eliminate angular false scattering errors through use of extreme directional quadratures, it is not an efficient method for generating radiation transfer predictions. In order to limit computational resources to a reasonable amount and maintain accuracy of radiation transfer predictions by limiting angular false scattering, a phase-function normalization technique for DOM that accurately and simultaneously conserves both the scattered energy condition of Eq. (4.3) and the asymmetry factor constraint of Eq. (4.9) is desired. [Hunter and Guo 2012a, Hunter and Guo 2012b, Hunter and Guo 2012e, Hunter and Guo 2013].

4.2 Angular False Scattering in the Finite Volume Method

4.2.1 Conservation of Scattered Energy and Asymmetry Factor

Using the FVM, the scattered energy conservation condition of Eq. (4.3) can be rewritten in the following manner, implementing the averaged scattering phase function as described in Section 3.1.1:

$$\frac{1}{4\pi}\sum_{l=1}^{M}\overline{\Phi}^{l'l}\Delta\Omega^{l}=1\,,\qquad l'=1,2,\ldots,M \tag{4.14}$$

The use of the averaged scattering phase function, introduced by Chui et al. [1992], was suggested as a manner to accurately conserve scattered energy in the system without the necessity of scattered energy averaging as required by the DOM. The theory is that if a fine enough solid-angle splitting grid is defined, scattered energy will be accurately conserved.

This theory is examined in Figure 4.16, where the dependence of scattered energy conservation on the number of solid angle sub-angles is examined after FVM discretization [Hunter and Guo 2014d]. The continuous angular variation is discretized into M = 24, 48, 80, 168, and 288 discrete directions (N = 4,6,8,12,16 in the FT_N-FVM quadrature). Each solid angle

is subdivided into ($N_{s\phi}$ x $N_{s\theta}$) sub-angles, with $N_{s\phi}$= $N_{s\theta}$, ranging from (2 x 2) to (24 x 24) divisions. Scattered energy conservation is presented for the HG phase function approximation with asymmetry factor g = 0.9300.

For a given number of directions M, an increase in the number of sub-angles reduces the discrepancy in discretized scattered energy conservation. In order to conserve scattered energy accurately within 0.001%, ($N_{s\phi}$ x $N_{s\theta}$) = (24 x 24), (20 x 20), (20 x 20), (12 x 12), and (12 x 12) sub-angles are required for M = 24, 48, 80, 168, and 288, respectively. It is seen in Figure 4.16 that the solid-angle splitting technique of Chui et al. [1992] is indeed able to accurately conserve scattered energy without requiring additional phase-function treatment, provided that a fine-enough sub-angle density is applied.

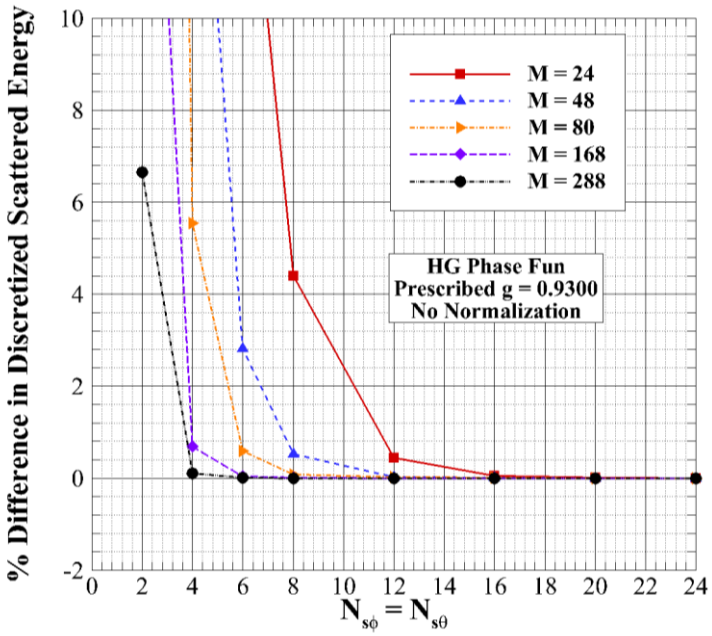

Figure 4.16: Examination of percent difference in scattered energy conservation versus solid-angle splitting number for HG g = 0.9300

Using the FVM, the phase-function asymmetry factor conservation condition of Eq. (4.9) can be reformulated as [Hunter and Guo 2012b, Hunter and Guo 2014d]

$$\frac{1}{4\pi}\sum_{l=1}^{M}\bar{\Phi}^{l'l}\cos\Theta^{l'l}\,\Delta\Omega^{l}=g\,,\qquad l'=1,2,\ldots,M \tag{4.15}$$

The solid-angle splitting technique of Chui et al. [1992] has been assumed previously to conserve phase-function asymmetry factor [Boulet et al. 2007, Collin et al. 2011], and that no additional treatment is required to accurately predict radiation transfer. Analysis of this notion is presented in Figure 4.17(a-b), which illustrate the deviation from asymmetry factor conservation and change in scattering effect for the same conditions as Figure 4.16 [Hunter and Guo 2014d].

For lower amounts of sub-angles, significant deviations from asymmetry factor conservation are witnessed for all directional quadratures in Figure 4.17a. However, instead of converging towards 0% as seen for scattered energy in Figure 4.16, discretized asymmetry factor converges to a value slightly less than the prescribed g = 0.9300. For $(N_{s\phi}$ x $N_{s\theta})$ = (24 x 24), the discretized asymmetry factors for M = 24, 48, 80, 168, and 288 attain values of g = 0.8855, 0.9024, 0.9113, 0.9198, and 0.9237, respectively, indicating that asymmetry factor is not accurately conserved through use of solid-angle splitting, and that the technique of Chui et al. [1992] is not sufficient to accurately satisfy Eqs. (4.14) and (4.15) concurrently. The changes in scattering effect (1-g) corresponding to the alteration of asymmetry factor in Figure 4.17a are plotted in Figure 4.17b. At the splitting levels required to conserve scattered energy within 0.001% discussed previously, changes in scattering effect of 63.6%, 39.3%, 26.7%, 14.4%, and 9.0% are witnessed for M = 24, 48, 80, 168, and 288, respectively, indicating the potential danger of even minor changes in asymmetry factor.

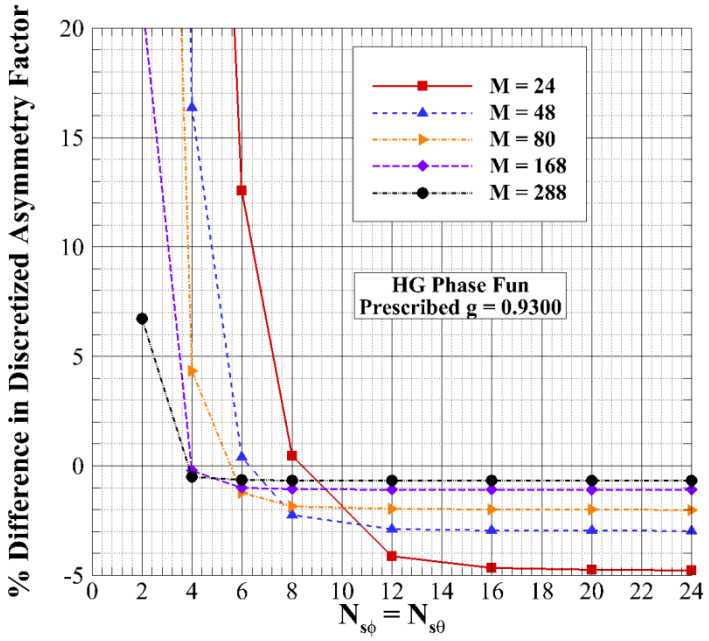

(a)

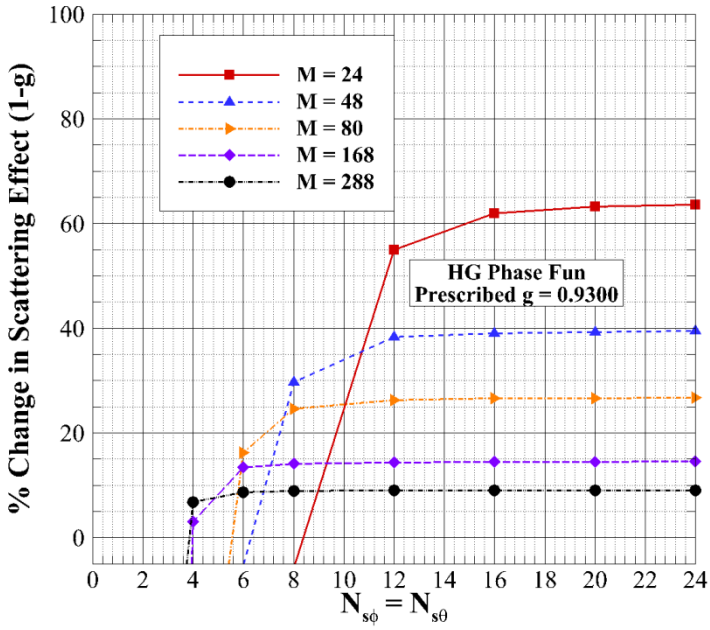

(b)

Figure 4.17: Examination of a) percent difference in asymmetry factor and b) percent change in scattering effect versus solid-angle splitting number for HG g = 0.9300

Table 4.2 compares prescribed and discretized asymmetry factors after FVM discretization with M = 288 and (24 x 24) solid-angle splitting. For weakly-forward scattering, slight discrepancies in asymmetry factor are witnessed, with changes in scattering effect <1% occurring for $g \leq$ 0.5000. For extreme forward scattering (g = 0.9500), change in scattering effect reaches 12.8%, corresponding to discretized asymmetry factor g = 0.9436. Comparing these results to those generated using the DOM with scattered energy averaging in Figure 4.5a, it is seen that scattering effect change is greatly lessened using the FVM with solid-angle splitting, although the scattering effect changes are still large enough to cause some concern.

Table 4.2: Comparison of prescribed and actual phase function asymmetry factor after FVM discretization with M = 288 and $(N_{s\phi}$ x $N_{s\theta})$ = 24 x 24 solid-angle splitting and the percent difference in scattering effect associated with asymmetry factor discrepancy

Prescribed g	**0.1000**	**0.2000**	**0.3000**	**0.4000**	**0.5000**	**0.6000**	**0.7000**	**0.8000**	**0.9000**	**0.9500**
Actual g	0.0991	0.1983	0.2975	0.3967	0.4956	0.5946	0.6938	0.7930	0.8926	0.9436
Prescribed (1-g)	0.9000	0.8000	0.7000	0.6000	0.5000	0.4000	0.3000	0.2000	0.1000	0.0500
Actual (1-g)	0.9009	0.8017	0.7025	0.6033	0.5044	0.4054	0.3062	0.2070	0.1074	0.0564
% Diff (1-g)	**0.10**	**0.21**	**0.36**	**0.55**	**0.88**	**1.35**	**2.07**	**3.52**	**7.40**	**12.80**

Figures 4.18(a-b) plot the percent difference from scattered energy and asymmetry factor conservation, respectively, for the 26-term g = 0.9273 Legendre polynomial phase function with M = 288 discrete directions for various discrete direction polar angle θ [Hunter and Guo 2012b]. In Figure 4.18a, only slight deviations in scattered energy conservation occur for minimal solid angle splitting. For (4 x 4) splitting, the maximum percent difference from conservation is only 0.25%, while increasing splitting to (24 x 24) decreases the maximum difference to 0.007%. It appears that use of proper sub-angle resolution conserves scattered energy accurately for both HG and Legendre phase functions. However, when examining asymmetry factor conservation, percent differences for (24 x 24) splitting range between -0.25%

and -1.4%, indicating that the discretized asymmetry factor underpredicts the prescribed asymmetry factor, conforming to the results from the HG phase function.

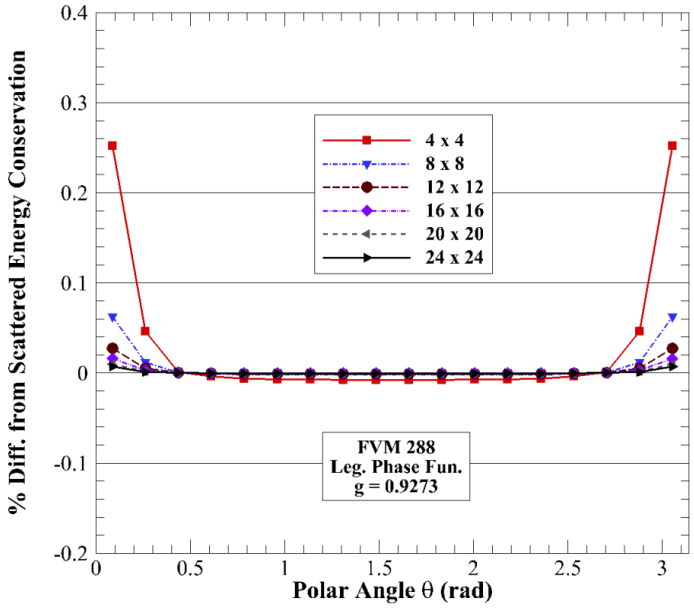

(a)

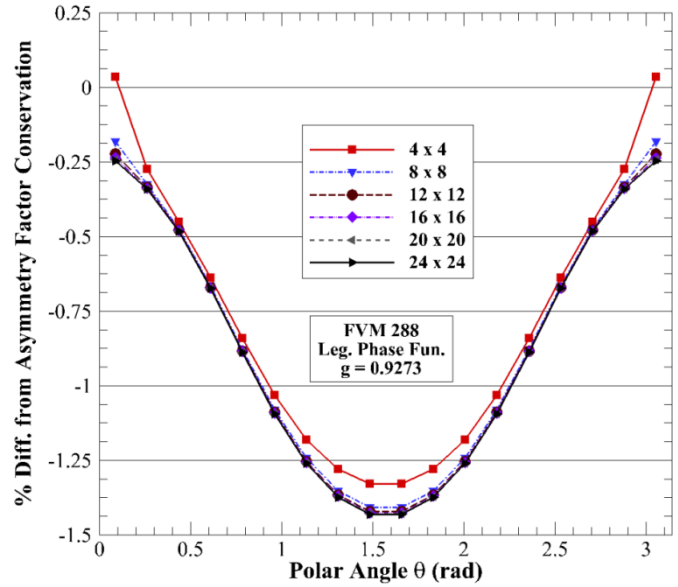

(b)

Figure 4.18: Examination of a) percent difference from scattered energy conservation and b) percent difference from asymmetry factor conservation for Legendre g = 0.9273 phase function with various solid angle splitting levels

Table 4.3 lists the maximum percentage difference from both scattered energy and asymmetry factor conservation at various degrees of solid-angle splitting when the HG phase-function approximation is applied. Prescribed asymmetry factors of g = 0.8000, 0.9000, 0.9500, and 0.9800 are investigated.

Table 4.3: Comparison of conservation of scattered energy and asymmetry factor after FVM discretization at various solid angle splitting levels for g = 0.8000, 0.9000, 0.9500 and 0.9800

g	Scattered Energy - Maximum % Difference from Conservation						
	Solid Angle Splitting - ($N_{s\phi}$ x $N_{s\theta}$)						
	2 x 2	4 x 4	8 x 8	12 x 12	16 x 16	20 x 20	24 x 24
0.8000	0.492	0.118	0.029	0.013	0.007	0.005	0.003
0.9000	7.54	0.264	0.065	0.029	0.016	0.010	0.007
0.9500	65.6	8.13	0.278	0.042	0.024	0.015	0.010
0.9800	600	119	17.7	4.24	1.13	0.305	0.083
	Asymmetry Factor- Maximum % Difference from Conservation						
0.8000	-0.886	-1.39	-1.46	-1.48	-1.48	-1.48	-1.49
0.9000	7.62	-0.936	-1.31	-1.32	-1.33	-1.33	-1.34
0.9500	68.6	7.73	-0.755	-1.04	-1.06	-1.06	-1.07
0.9800	612	121	17.5	3.71	0.496	-0.472	-0.590

For all asymmetry factors tested, a finer splitting grid produces more accurate conservation of scattered energy. In addition, a significant increase in the deviation from accurate scattered energy conservation is seen as asymmetry factor increases. For example, for g = 0.8000, solid-angle splitting of (2 x 2) produces a maximum difference of less than 0.5%, whereas the differences for g = 0.9500 and 0.9800 reach extreme values of 65.6% and 600%, respectively. For extremely high g = 0.9800, more than (24 x 24) splitting is required to accurately conserve scattered energy. For all asymmetry factors, noticeable deviations from unity in asymmetry factor conservation are witnessed. For (24 x 24) splitting, underpredictions of greater than 1% are witnessed for g = 0.8000, 0.9000, and 0.9500, leading to significant changes in scattering effect.

A comparison of discretized phase-function values, generated using the FVM with (24 x 24) solid-angle splitting and HG asymmetry factor g = 0.9300, to the theoretical phase function is presented in Figure 4.19 for various discrete directions numbers. Comparing the results for the FVM to the DOM results in Figure 4.6, it appears that use of solid-angle splitting has greatly improved the conformity of discretized values to the prescribed phase function for all directional orders, although some artificial oscillations are witnessed near the forward-scattering peak. These artificial oscillations appear as overpredictions to the theoretical phase function, which correspond to reductions in overall phase-function asymmetry factor. The largest errors are observed for M = 24, where the limited number of directions is not able to accurately correspond to the true phase-function shape after splitting.

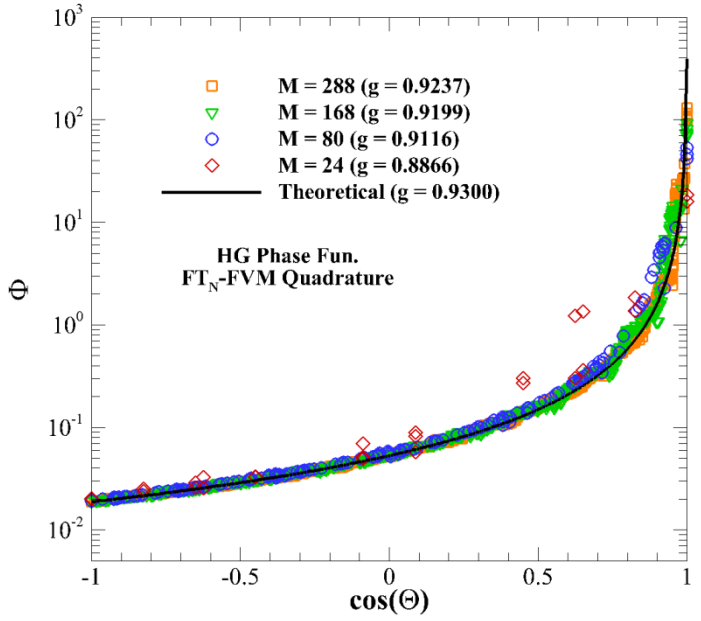

(a)

Figure 4.19: Discretized phase-function values for HG g = 0.9300 after FVM discretization with (24 x 24) splitting

While the results from Figures 4.16-4.19 and Tables 4.2 and 4.3 give the preliminary validation for the necessity of additional phase-function treatment in the FVM, analysis of radiation transfer predictions generated using the FVM are necessary for further justification [Hunter and Guo 2012b, Hunter and Guo 2014d].

4.2.2 Comparison of FVM Radiation Transfer Predictions with Monte Carlo

Figure 4.20 compares heat fluxes $Q(x^*, y^* = 0.5, z^* = 1.0)$, generated using the FVM with M = 168 and (16 x 16) solid-angle splitting (to ensure energy conservation), with published MC results for the benchmark problem described in Section 4.1.4.2 (cubic enclosure with one hot wall). DOM predictions generated with scattered energy averaging, originally presented in Figure 4.10, are replotted in Figure 4.20. Prescribed HG asymmetry factors are varied as g = 0.2000, 0.8000, and 0.9300 [Hunter and Guo 2012e, Hunter and Guo 2014d].

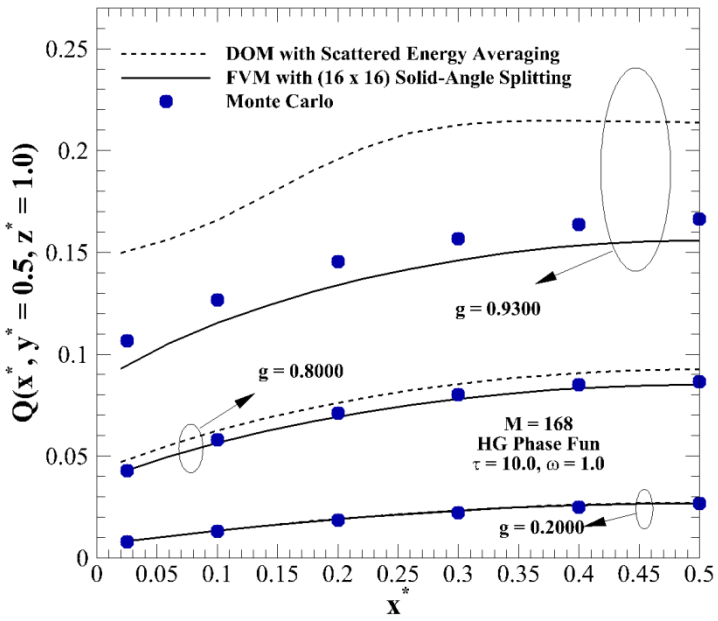

Figure 4.20: Comparison of Q(x*, y* = 0.5, z* = 1.0) generated using FVM with no normalization and (16 x 16) angle splitting with Monte Carlo [Boulet et al. 2007] and DOM S_{12} with scattered energy averaging for HG g = 0.2000, 0.8000, and 0.9300

For weakly-forward scattering, FVM heat fluxes conform almost identically to the DOM (within 1%) and to MC (between 1-5%). When g is increased to 0.8000, deviations between FVM, DOM, and MC start to manifest. The FVM heat flux profile (discretized g = 7900, scattering effect change of 5%) underpredicts MC by between 2-4%. Conversely, the DOM heat flux profile generated in Figure 4.10 overpredicted MC by 6-8%. More drastic differences occur for g = 0.9300. Use of scattered energy averaging with the DOM (discretized g = 0.9735) resulted in overpredictions of between 28-36% when compared to the MC. Use of solid-angle splitting in the FVM results in a discretized asymmetry factor of 0.9198, leading to underpredictions of between 6-12% as compared with MC. As expected, use of solid-angle splitting allows for more accurate prediction of radiation transfer with the FVM than available using the DOM, where normalization is absolutely required to conserve scattered energy, although the discrepancies are still significant due to lack of asymmetry factor conservation [Hunter and Guo 2014d].

Figure 4.21 investigates the impact of angular discretization on FVM heat flux with g = 0.9300. Solid angle splitting of (24 x 24) for M = 24, (20 x 20) for M = 48 and 80, and (16 x 16) for M = 168 is applied to both normalized and non-normalized profiles, in order to accurately conserve scattered energy even without normalization. As compared to the reference MC values [Boulet et al. 2007], increase in discrete direction number is able to reduce FVM underpredictions, due to a reduction in angular false scattering errors. Differences range between 18-37%, 17-27%, 12-20%, and 5-12% for M = 24, 48, 80, and 168, respectively.

An investigation of the impact of solid-angle splitting resolution on radiation transfer results in the cubic benchmark problem is presented in Figures 4.22(a-d) [Hunter and Guo

2014d]. In said figures, percentage differences between FVM and MC heat fluxes are plotted for various levels of solid-angle splitting. Percentage differences are presented for M = 24, 80, 168, and 288 in Figures 4.22(a-d), respectively.

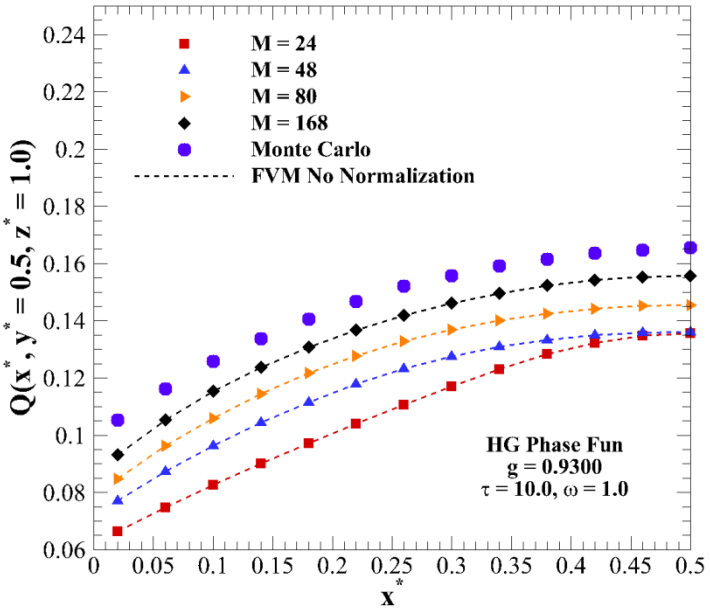

Figure 4.21: Comparison of Q(x*, y* = 0.5, z* = 1.0) generated using FVM with no normalization with Monte Carlo [Boulet et al. 2007] for various discrete direction numbers with HG g = 0.9300

For all directional orders, increasing solid-angle splitting resolution results in percent differences converging to a negative value. For M = 24 and 80, heat flux profiles generated with (8 x 8) solid-angle splitting appear to conform substantially more accurately to MC heat flux predictions than higher splitting levels. However, (8 x 8) splitting is not sufficient to conserve scattered energy accurately for these directional orders, meaning that radiation transfer predictions generated using said splitting are not to be taken as accurate. As discussed in the results shown in Figure 4.16, solid angle splitting of (24 x 24), (20 x 20), (12 x 12), and (12 x 12) are required to accurately conserve scattered energy within 0.001%. For splitting levels higher

than these, no noticeable change in percent differences are noticed, and thus further refinement is unnecessary. The differences between FVM and MC are still significant at the splitting levels where scattered energy is accurately conserved for all discrete direction numbers, due to angular false scattering, indicating the importance of accurately conserving phase-function asymmetry factor [Hunter and Guo 2014d].

Based on the trends in Figures 4.17(a-b), further increase in discrete direction number beyond 288 should further reduce the discrepancy between discretized and prescribed asymmetry factor for high solid-angle splitting. It is therefore possible, with a sufficient number of discrete directions, that scattered energy and asymmetry factor can be accurately conserved without requiring further treatment, as discussed for the DOM with non-limited quadratures [Hunter and Guo 2013, Hunter and Guo 2014d]. This theory is investigated in Figure 4.23, wherein FVM heat fluxes generated using M = 168, 288, 624, 1088, and 2024 discrete directions are plotted in comparison with the reference MC solutions.

Increasing discrete direction number to M = 624, 1088, and 2024 results in discretized asymmetry factors of g = 0.9270, 0.9280, and 0.9290, respectively, showing that direction increase will reduce the change in scattering effect. When corresponding FVM heat fluxes are compared to MC, it is seen that an increase in directions reduces angular false scattering error, with average differences of 3.0%, 2.4%, and 2.2% witnessed for the three direction numbers, respectively. Further increase in direction past M = 2024 would further reduce angular false scattering errors, but at a drastic computational cost. The three profiles corresponding to the previously mentioned direction numbers took 5650, 16520, and 65400 seconds to converge, respectively, indicating the impracticality of simply increasing discrete direction number to counter angular false scattering errors. However, the results in Figure 4.23 also give confidence

that conservation of g after discretization will produce accurate results when compared to MC solutions.

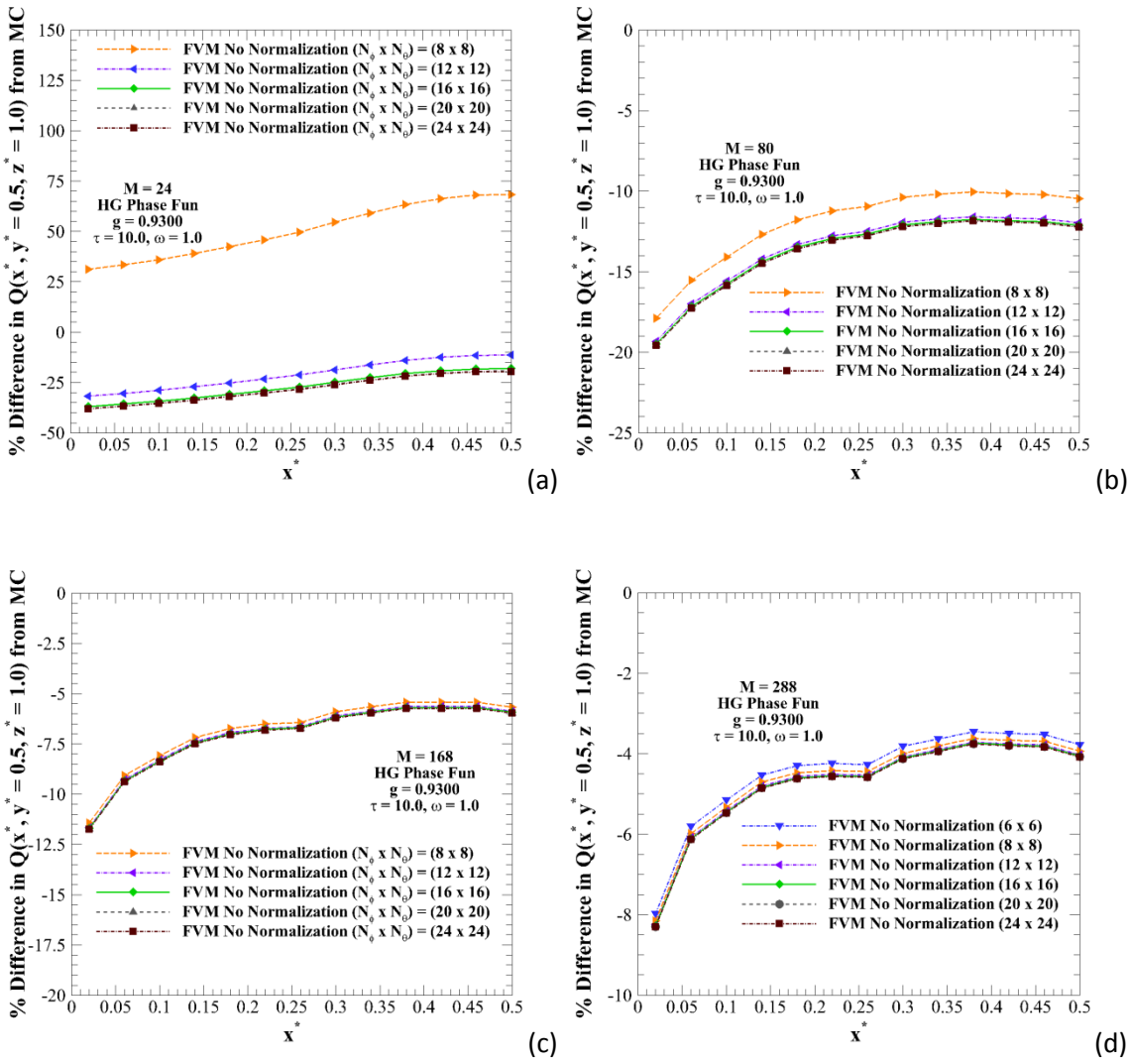

Figure 4.22: Comparison of Q(x*, y* = 0.5, z* = 1.0) generated using FVM with various solid angle splitting levels to Monte Carlo [Boulet et al. 2007] with a) M = 24, b) M = 80, c) M = 168, and d) M = 288

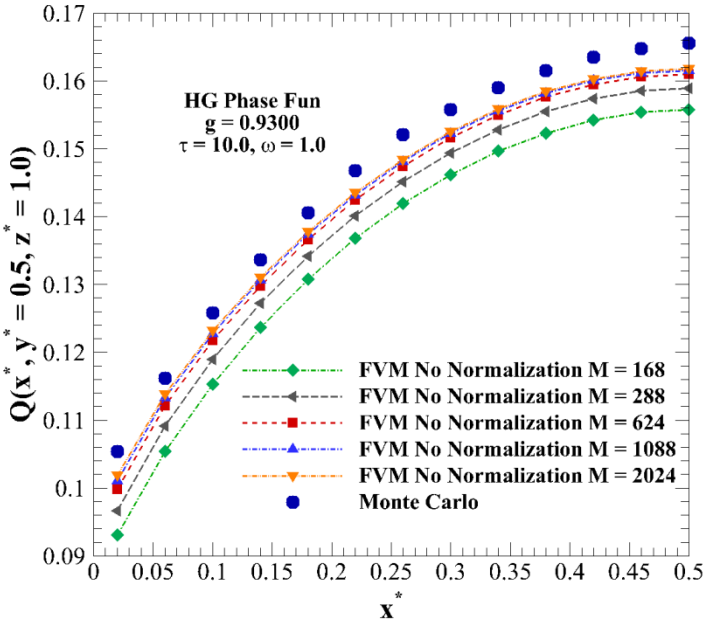

Figure 4.23: Comparison of Q(x*, y* = 0.5, z* = 1.0) generated using FVM with high discrete direction number

4.3 Summary

In this chapter, the concept of angular false scattering, and the root cause of this new type of discretization error, is discussed. The well-known issue of scattered energy conservation in the DOM is addressed, and phase-function normalization is introduced as the common method of correction. The necessity of accurate phase-function asymmetry factor conservation to retain medium scattering properties is presented. A comparison of radiation transfer results generated with scattered energy averaging with both isotropic scaling results and Monte Carlo simulations is presented, in order to illustrate the importance of accurately conserving both scattered energy and phase-function asymmetry factor.

For the FVM, the necessity behind the use of solid-angle splitting to accurately conserve scattered energy is shown. However, the notion that this technique also conserves asymmetry

factor is dispelled. It is seen that the FVM, as well as the DOM, suffer from errors due to angular false scattering, which stem from lack of phase-function asymmetry factor conservation. In general, when compared to MC, FVM errors are not as large as DOM, as a result of using fine solid-angle splitting grids. However, the errors between FVM and MC are significant enough to warrant additional attention.

All in all, use of either scattered energy averaging or solid-angle splitting is not enough to ensure that radiation transfer predictions are of the highest accuracy, and additional phase-function treatment is required to guarantee that both scattered energy and asymmetry factor are accurately conserved after directional discretization.

CHAPTER 5 : HUNTER AND GUO'S 2012 NORMALIZATION: A NORMALIZATION APPROACH TO SIMULTANEOUSLY CONSERVE SCATTERED ENERGY AND ASYMMETRY FACTOR

5.1 Mathematical Formulation

The results presented in Chapter 4 indicate the importance of conserving both scattered energy and phase-function asymmetry factor after directional discretization using either the DOM or FVM, in order to limit numerical error due to angular false scattering. The commonly-implemented scattered energy averaging of Eq. (4.10) is able to satisfy the scattered energy constraint of Eq. (4.3); however the prescribed asymmetry factor is not retained. For the FVM, solid-angle splitting ensures accurate energy conservation, but leads to underpredictions in asymmetry factor. To improve radiation transfer predictions in these numerical methods, a phase-function normalization technique that ensures the numerically accurate conservation of Eqs. (4.2) and (4.8) after discretization of the continuous angular variation of radiation scattering is desired.

To this end, it is proposed that the scattering phase function $\Phi^{l'l}$ be normalized in the following manner, for all discrete radiation directions $\hat{\boldsymbol{s}}^{\boldsymbol{l'}}$:

$$\widetilde{\Phi}^{l'l} = \left(1 + A^{l'l}\right)\Phi^{l'l} \tag{5.1}$$

where the normalization parameters $A^{l'l}$ correspond to radiation scattering between two discrete radiation directions $\hat{\boldsymbol{s}}^{\boldsymbol{l'}}$ and $\hat{\boldsymbol{s}}^{\boldsymbol{l}}$. The normalized phase-function $\widetilde{\Phi}^{l'l}$ satisfies the following three conditions:

$$\frac{1}{4\pi}\sum_{l=1}^{M}\widetilde{\Phi}^{l'l}w^{l}=1 \tag{5.2a}$$

$$\frac{1}{4\pi}\sum_{l=1}^{M}\widetilde{\Phi}^{l'l}\cos\Theta^{l'l}\,w^{l}=g \tag{5.2b}$$

$$\widetilde{\Phi}^{l'l}=\widetilde{\Phi}^{ll'} \tag{5.2c}$$

The constraints of Eqs. (5.2a) and (5.2b) are simply the discretized scattered energy and asymmetry factor conservation conditions of Eqs. (4.3) and (4.9), respectively. Eq. (5.2c) is a symmetry condition, ensuring that the phase-function value between two discrete directions is identical regardless of which directions are the incoming and outgoing directions (i.e., the phase-function value depends solely on scattering angle). The constraints of Eqs. (5.2a) and (5.2b) are written here for the DOM. For the FVM, the constraints can be obtained with the simple substitution of the discrete solid angle $\Delta\Omega^{l}$ for the DOM weighting factor w^{l}, and the average scattering phase function $\overline{\Phi}^{l'l}$ for $\Phi^{l'l}$ in Eq. (5.1).

In order to solve for the normalization parameters $A^{l'l}$ that will ensure conservation of scattered energy and asymmetry factor simultaneously, the system of equations comprised of Eqs. (5.1) and (5.2a-c) can be rewritten in the following matrix/vector form:

$$\boldsymbol{U}\vec{a}=\vec{b} \tag{5.3}$$

In Eq. (5.3), $\boldsymbol{U}$ is a normalization coefficient matrix, $\vec{a}$ is a vector of normalization parameters $A^{l'l}$, and $\vec{b}$ is a vector. Examples of $\boldsymbol{U}$, $\vec{a}$, and $\vec{b}$ are presented in Table 5.1, for the DOM S_2 (M = 8) quadrature.

Table 5.1: Illustration of normalization matrices for Hunter and Guo's 2012 normalization for DOM S_2: a) coefficient matrix $\boldsymbol{U}$, b) normalization parameter vector $\vec{a}$, c) vector $\vec{b}$

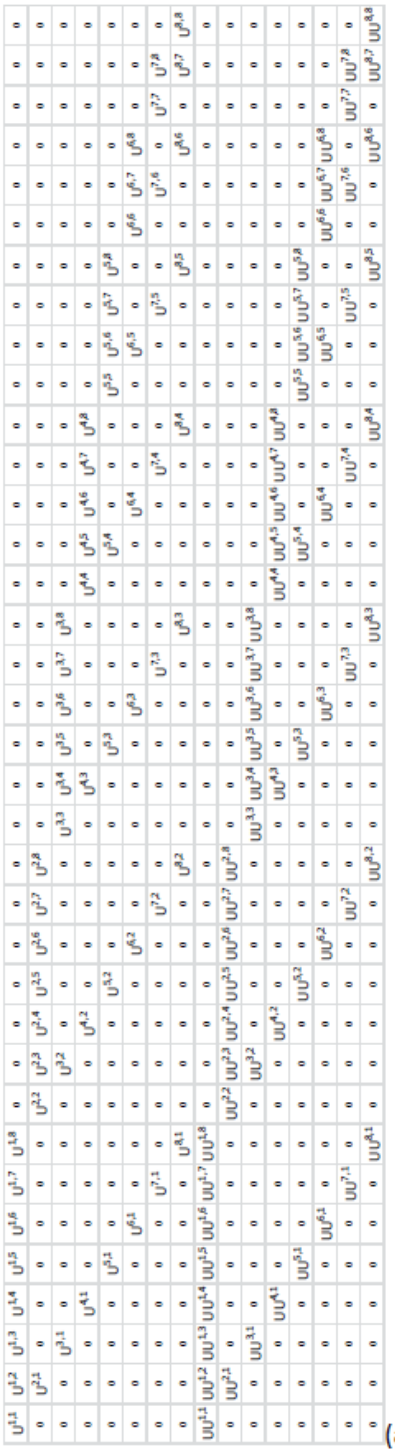

(a)

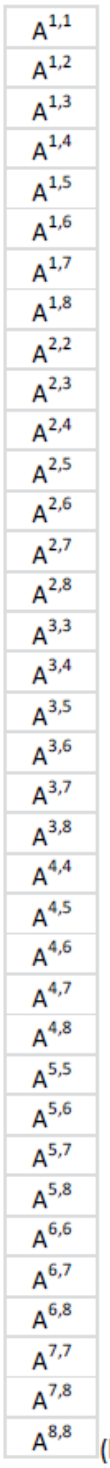

(b)

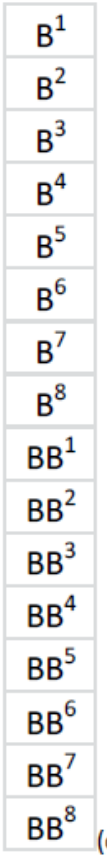

(c)

In the normalization coefficient matrix $\boldsymbol{U}$, the coefficients $\mathrm{U}^{i,j}$ and $\mathrm{UU}^{i,j}$ in Table 5.1a are calculated as:

$$\mathrm{U}^{i,j} = \Phi^{ij} w^j \tag{5.4a}$$

$$\mathrm{UU}^{i,j} = \Phi^{ij} \cos\Theta^{ij}\, w^j \tag{5.4b}$$

In the normalization parameter vector $\vec{a}$, the coefficients $\mathrm{A}^{i,j}$ in Table 5.1b represent the normalization parameter A^{ij}:

$$\mathrm{A}^{i,j} = A^{ij} \tag{5.5}$$

Finally, in the vector $\vec{b}$, the coefficients B^i and BB^i in Table 5.1c are calculated as:

$$\mathrm{B}^i = 4\pi - \sum_{l=1}^{M} \Phi^{il} w^l \tag{5.6a}$$

$$\mathrm{BB}^i = 4\pi g - \sum_{l=1}^{M} \Phi^{il} \cos\Theta^{il}\, w^l \tag{5.6b}$$

In Eqs. (5.4)-(5.6), the indices i and j both range between 1 and M, the total number of discrete directions. The symmetry condition of Eq. (5.2c) allows the restriction of $i \leq j$ in Eq. (5.5) only.

Eq. (5.3) represents an underdetermined system, as there are more unknowns than equations. The total number of unknowns in the system is $M(M+1)/2$, while the total number of equations is $2M$ (M from scattered energy, and M from asymmetry factor). Use of the symmetry condition allows for a reduction in the number of unknowns from M^2 to $M(M+1)/2$. This system has an infinite number of possible solutions mathematically, although one

solution will have the smallest residual error. This solution, known as the "minimum-norm" solution, will minimize the values of $A^{l'l}$ while simultaneously maintaining conservation of the necessary constraints.

To find the minimum norm solution of the system, numerical techniques such as QR factorization can be implemented [Vandenberghe 2011]. Using QR factorization, the (m x n) normalization coefficient matrix $\boldsymbol{U}$ can be decomposed as

$$\boldsymbol{U} = QR \tag{5.7}$$

where Q is an (m x n) orthogonal matrix, and R is an upper triangular (n x n) matrix. The minimum norm solution of the system of equations $QR\vec{a} = \vec{b}$ can then be computed as:

$$\vec{a} = Q^T \vec{b}\, R^{-1} \tag{5.8}$$

Additional solution methods, such as least-squares, are also available to determine the minimum-norm solution, but will not be discussed here, for brevity.

As seen in Table 5.1a, the normalization coefficient matrix $\boldsymbol{U}$ is a sparse matrix, with only $2M^2$ of the $M^3 + M^2$ elements having a nonzero value. Therefore, the fraction of non-zero elements is on the order of M^{-1}. For small systems, such as that presented in Table 5.1 for the S_2 quadrature, computational memory storage will not be an issue. However, for larger systems, care must be taken to avoid issues with computational memory overflow. In order to maximize computational efficiency, the coefficient matrix can be defined as *sparse*, so that memory is only reserved for the non-zero terms. This will reduce the total memory required to store $\boldsymbol{U}$ from $O(M^3)$ to $O(M^2)$.

Table 5.2 lists the computational memory storage required to store matrix $\boldsymbol{U}$, in both full- and sparse-form, for various discrete direction numbers. In addition, the percentage of non-zero elements is listed. For 24 total directions, only 8% of the coefficient matrix elements are non-zero, and sparse storage of the coefficient matrix reduces memory storage by 63%. The total memory at such directional levels is not a concern. However, as the number of directions increases, a major issue is memory storage is encountered. For example, in order to store the coefficient matrix for M = 2024 discrete directions (where ~0.1% of all elements have a non-zero value), over 61 GB of RAM is required, which is roughly 8-12 times the memory storage capacity of the average CPU nowadays. Use of sparse storage reduces this memory requirement to 0.282 GB, a reduction of 99.5% which allows the matrix to be easily stored on average computational workstations. The data in Table 1 indicate the importance of proper sparse matrix storage for efficient application of this normalization approach.

Table 5.2: Computational memory analysis of normalization parameter coefficient matrix $\boldsymbol{U}$

N	M	% of Non-Zero Elements in Coeff. Matrix	Coeff. Matrix Memory (GB)		% Savings w. Sparse
			Full	Sparse	
4	24	8.00	1.07E-04	3.97E-05	63.0
8	80	2.47	3.86E-03	4.41E-04	88.6
10	120	1.65	1.30E-02	9.93E-04	92.4
12	168	1.18	3.55E-02	1.95E-03	94.5
14	224	0.89	8.41E-02	3.46E-03	95.9
16	288	0.69	1.79E-01	5.72E-03	96.8
20	440	0.45	6.36E-01	1.33E-02	97.9
24	624	0.32	1.81E+00	2.68E-02	98.5
28	840	0.24	4.42E+00	4.86E-02	98.9
32	1088	0.18	9.60E+00	8.16E-02	99.2
36	1368	0.15	1.91E+01	1.29E-01	99.3
40	1680	0.12	3.53E+01	1.95E-01	99.4
44	2024	0.10	6.18E+01	2.82E-01	99.5
52	2808	0.07	1.65E+02	5.43E-01	99.7
64	4224	0.05	5.62E+02	1.23E+00	99.8

The mathematical formulation of the normalization technique in Eqs. (5.1)-(5.6) guarantees that scattered energy and asymmetry factor will be accurately conserved after directional discretization, regardless of medium properties, scattering phase-function approximation, and directional quadrature. It is important to note that the normalization parameters for this approach can be pre-generated for a given phase-function and DOM quadrature, and are independent of medium optical properties. Using the sparse matrix approach, additional computational times to determine the normalization parameters are negligible, with less than 10 seconds required to determine normalization parameters for M = 288 discrete directions.

The normalization approach in Eqs. (5.1)-(5.6) was initially developed in early 2011, and was first published in 2012 for use in determining radiation heat transfer in axisymmetric cylindrical enclosures using the DOM [Hunter and Guo 2012a] and FVM [Hunter and Guo 2012b]. This approach was later extended for use in 3-D DOM [Hunter and Guo 2012d, Hunter and Guo 2012e, Hunter and Guo 2013] and 3-D FVM [Hunter and Guo 2014d]. Due to the date of initial publication, the normalization technique described above is referred to as "Hunter and Guo's 2012 normalization" in the remainder of the dissertation.

5.2 Application for DOM Radiation Transfer Predictions

5.2.1 Improvement in Discretized Phase-Function Values

As a validation of Hunter and Guo's 2012 normalization, discretized phase-function values generated using the DOM S_N quadrature with HG asymmetry factors of g = 0.5000, 0.8000, 0.9000, and 0.9500 are presented in Figures 5.1(a-d) for various discrete direction numbers after application of Hunter and Guo's 2012 normalization. Comparing Figures 5.1(a-d) to the previously presented discretized phase-function values after application of scattered

energy averaging in Figures 4.6(a-d), vast improvement is witnessed for g = 0.8000, 0.9000, and 0.9500. For all four phase-functions tested, asymmetry factor is accurately conserved regardless of discrete direction number, leading to accurate conformity of the discretized phase-function values to the theoretical values.

Figures 5.2(a-d) present discretized phase-function values, generated using the DOM S_N quadrature with application of Hunter and Guo's 2012 normalization, for the Legendre g = 0.4856, 0.8189, 0.84534, and 0.9273 phase-functions, respectively.

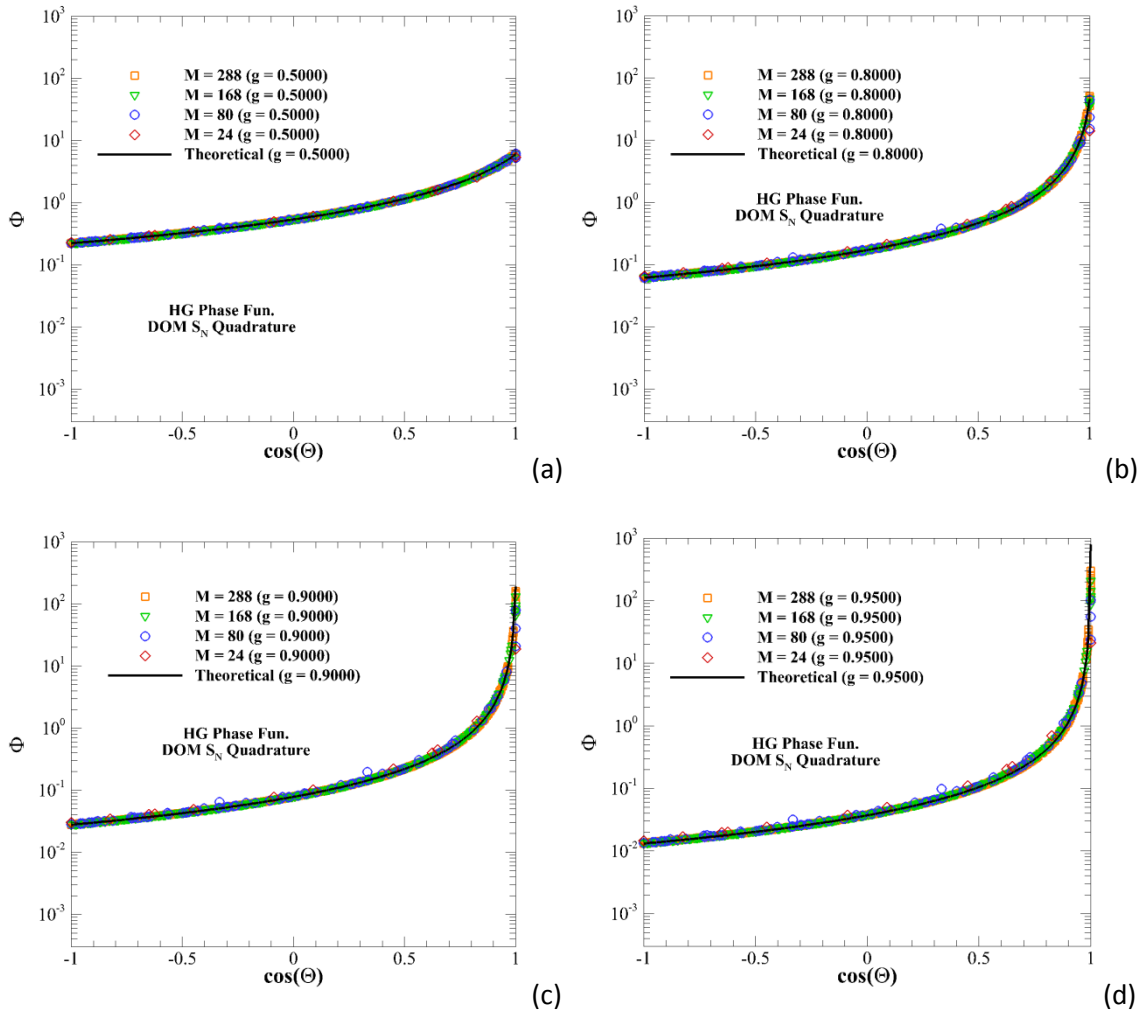

Figure 5.1: Discretized HG phase-function values for a) g = 0.5000, b) g = 0.8000, c) g = 0.9000, and d) g = 0.9500

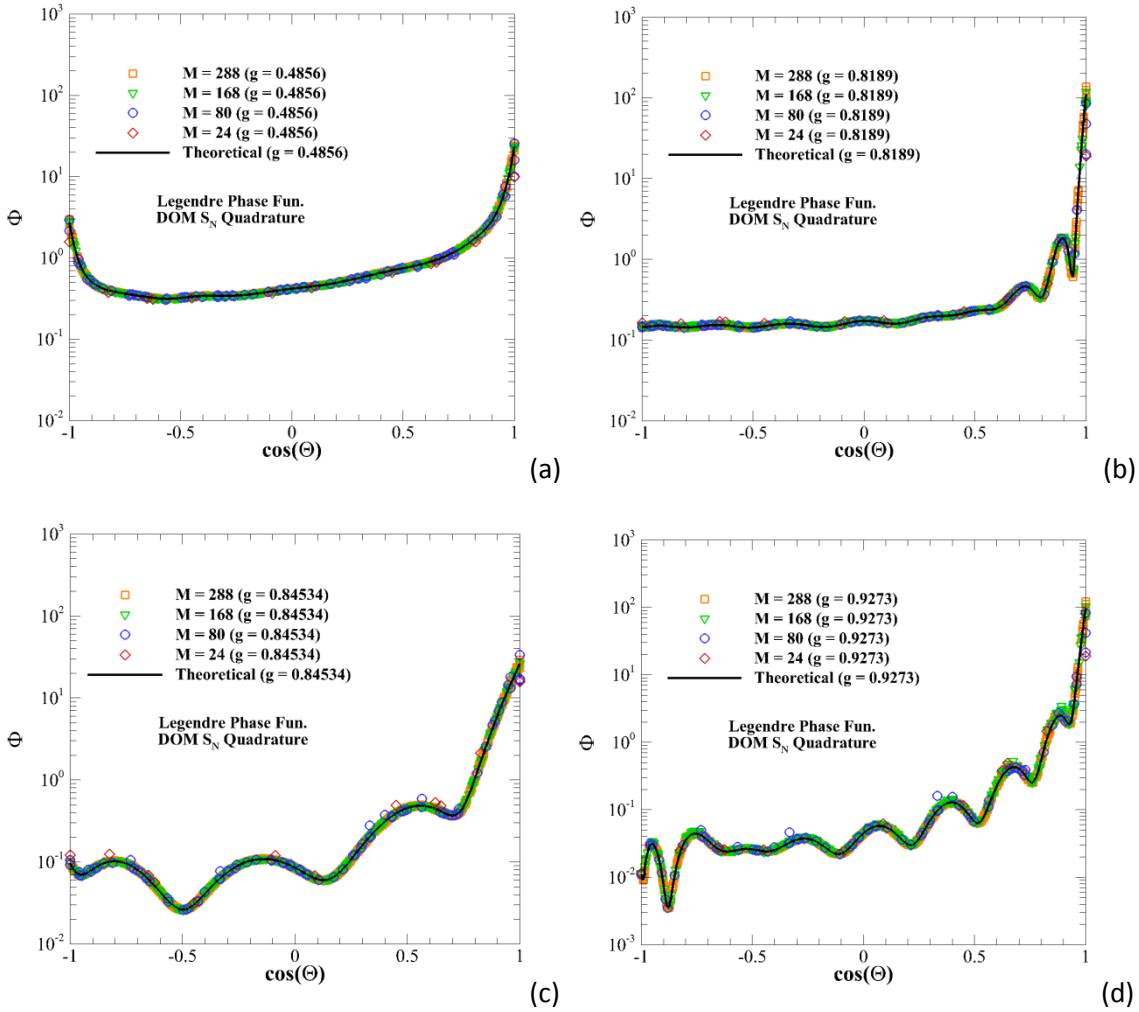

Figure 5.2: Discretized Legendre phase-function values for a) g = 0.4856, b) g = 0.8189, c) g = 0.84534, and d) g = 0.9273

Once again, for all four phase-functions, asymmetry factor is accurately conserved for all discrete direction numbers. Additionally, and perhaps more importantly, application of Hunter and Guo's 2012 normalization allows for more accurate representation of the true phase-function shape, including oscillatory behavior, for all directional orders. When scattered energy averaging was applied, the discretized phase-function values shown in Figure 4.7 for low-order quadrature were not able to either conserve asymmetry factor or accurately represent the true phase-function shape. The noticeable improvement in discretized phase-function values for

both HG and Legendre phase-functions offers promise that angular false scattering errors will be effectively minimized in corresponding radiation transfer calculations if Hunter and Guo's 2012 normalization is implemented prior to analysis.

5.2.2 Comparison to Isotropic Scaling Law

As an initial indication of the impact of Hunter and Guo's 2012 normalization on radiation transfer predictions, Figure 5.3 plots the percentage difference in $Q_R^*(z^*)$ between the DOM using S_{16} quadrature with Hunter and Guo's 2012 normalization and isotropic scaling law predictions for the same problem as described in Section 4.1.4.1 and analyzed in Figure 4.9 (axisymmetric cylindrical medium with a hot radial side wall). Differences are calculated for various medium optical thicknesses, and for the HG phase-function approximation with g = 0.9500. Results for scattered energy averaging presented in Figure 4.9 can be used as an additional comparison [Hunter and Guo 2012a].

For the thinnest medium investigated (τ = 1.0), differences between the isotropic scaling law and DOM are less than 1% for all medium locations, a similar result as seen for scattered energy averaging in Figure 4.9. As previously mentioned, for optically thinner media, very few scattering events are encountered as energy passes through the medium, and thus angular false scattering errors are naturally mitigated. As optical thickness increases, the differences witnessed in Figure 5.3 attain much lower values than in Figure 4.9. Errors are less than 5% for all locations for all medium optical thicknesses when Hunter and Guo's 2012 normalization is applied, and g is conserved to 0.9500. Conversely, when scattered energy averaging is applied, and the discretized g is altered to 0.9828, errors of >10% and >25% are witnessed for τ = 10.0 and 25.0, respectively, in Figure 4.9. The conservation of g inherent in Hunter and Guo's 2012 normalization allows for a retention of scattering properties, which directly corresponds to

mitigation of angular false scattering errors and an improvement of radiative heat fluxes when compared to the isotropic scaling law.

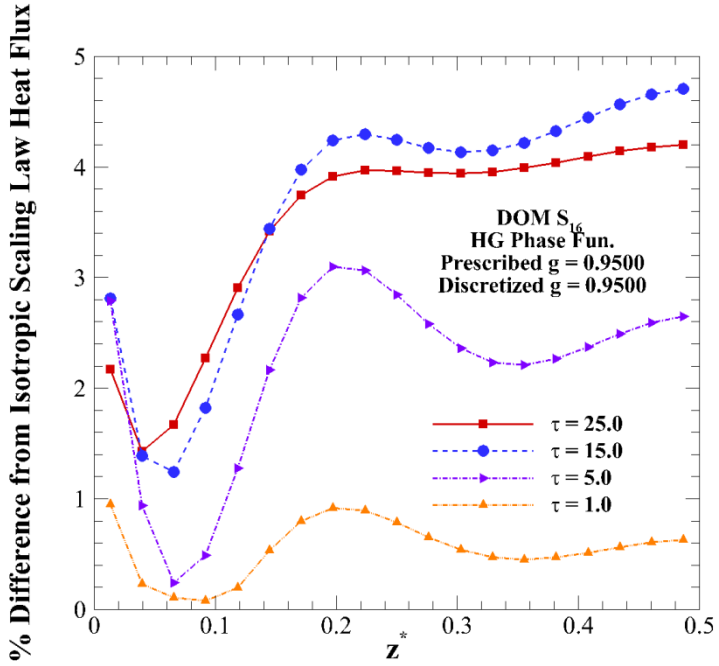

Figure 5.3: Percent difference in $Q_R^*(z^*)$ between DOM S_{16} with Hunter and Guo's 2012 normalization and isotropic scaling solution for HG g = 0.9500 with varying optical thickness

5.2.3 Comparison to Monte Carlo

In Figure 5.4, a comparison of radiative heat fluxes $Q(x^*, y^* = 0.5, z^* = 1.0)$ generated using the DOM S_{12} quadrature with benchmark Monte Carlo [Boulet et al. 2007] results is presented for the 3-D cubic enclosure with one hot wall, as described in detail in Section 4.1.4.2. DOM results are presented for both Hunter and Guo's 2012 normalization and scattered energy averaging (which are originally plotted in Figure 4.10). As in Figure 4.10, heat fluxes are presented for HG g = 0.2000, 0.8000, and 0.9300 [Hunter and Guo 2012e].

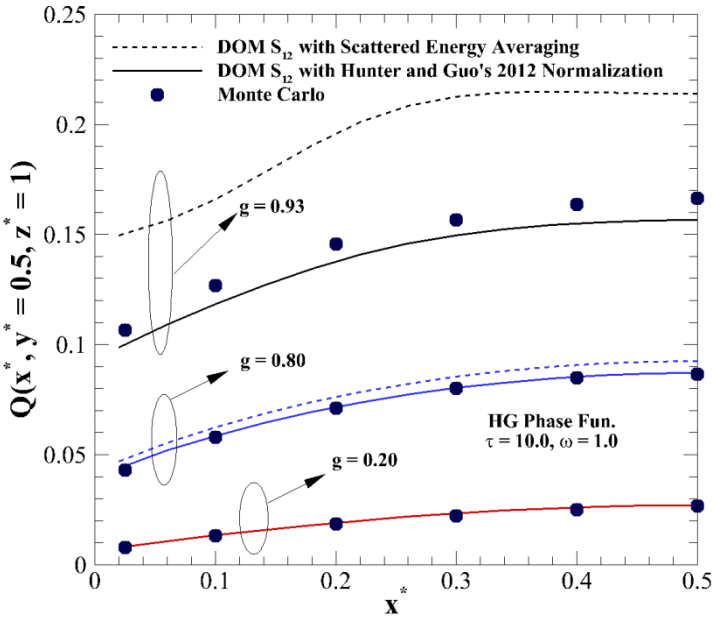

Figure 5.4: Comparison of Q(x*, y* = 0.5, z* = 1.0) generated using DOM S_{12} with Hunter and Guo's 2012 normalization vs. Monte Carlo solution [Boulet et al. 2007] for HG g = 0.2000, 0.8000, and 0.9300

As listed earlier in the discussion of Figure 4.10, DOM heat fluxes generated using scattered energy averaging differ from MC predictions by between 1-5%, 6-8%, and 28-36% for g = 0.2000, 0.8000, and 0.9300, respectively. For weak-forward scattering, DOM heat flux generated using Hunter and Guo's 2012 normalization is nearly identical to that generated using Eq. (4.10), due to the fact that normalization was truly not necessary for this asymmetry factor (as seen in Figures 4.2 and 4.3). For g = 0.8000, the advantage of being able to conserve asymmetry factor after discretization starts to emerge, as Hunter and Guo's 2012 normalization allows for DOM heat fluxes to conform accurately to MC within 1% at all locations. Further, for g = 0.9300, Hunter and Guo's 2012 normalization is able to reduce the ~30% differences witnessed for scattered energy averaging to between 4-7%, depending on medium location. Differences of this magnitude are reasonable between MC and DOM, due to the differences in

methodology and inherent numerical and statistical errors. The large improvement in conformity to MC indicates that angular false scattering errors are greatly reduced when Hunter and Guo's 2012 normalization is implemented.

Building on the results in Figure 5.4, Figures 5.5(a-b) investigate the impact of phase-function normalization technique on $Q(x^*, y^* = 0.5, z^* = 1.0)$ in the cubic medium with strong-forward scattering (g = 0.9300) for the five DOM quadrature schemes outlined in Section 2.3 [Hunter and Guo 2013]. DOM results with scattered energy averaging, originally presented in Figures 4.11(a-b), are overlaid in Figures 5.5(a-b) for comparison to Hunter and Guo's 2012 normalization, as well as the benchmark MC solution. Results are presented discrete direction numbers on the order of M = 24 and 80 in Figures 5.5(a-b), respectively. For the geometrically-determined quadratures (T_N and $SRAP_N$), the discrete direction number is taken to be the closest possible to these two values.

In both figures, application of Hunter and Guo's 2012 normalization appears to improve the accuracy of DOM radiative heat flux in comparison to MC. For M = 24 in Figure 5.5a, application of Hunter and Guo's 2012 normalization results in maximum percentage differences of 92.9%, 18.9%, 16.7%, 41.1%, and 23.8% for S_4, P_4-EW, P_4-T_4, T_2, and $SRAP_2$, respectively, illustrating a vast improvement over the errors witnessed for scattered energy averaging. While the solutions are vastly improved in Figure 5.5a, errors in comparison to MC still have high magnitude, although the source of such errors is not angular false scattering (as asymmetry factor is conserved). These errors can be traced to ray effect, as a small number of directions are being used to approximate the total solid angle 4π. These errors cannot be eliminated by phase-function normalization.

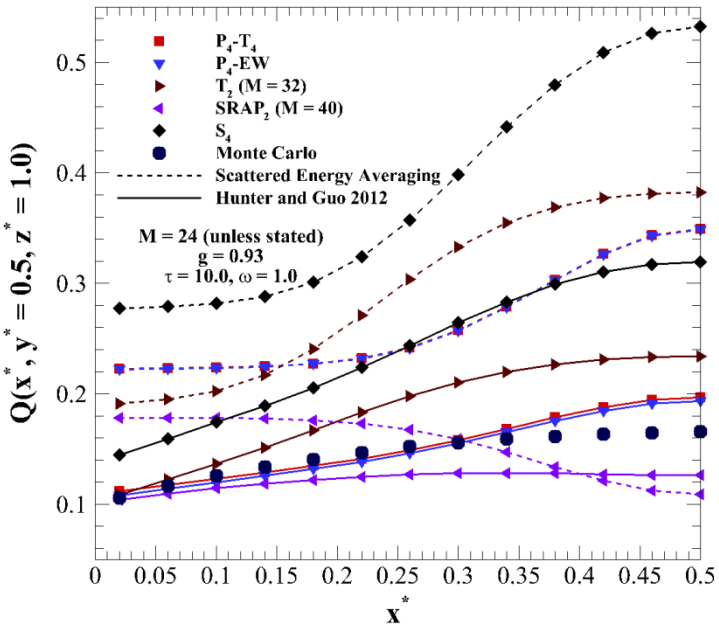

(a)

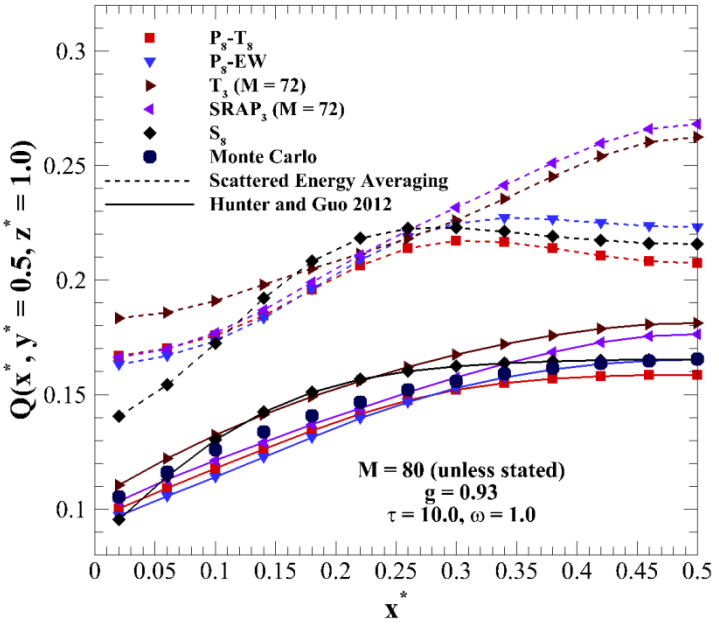

(b)

Figure 5.5: Comparison of Q(x*, y* = 0.5, z* = 1.0) generated using DOM with Hunter and Guo's 2012 normalization with Monte Carlo [Boulet et al. 2007] for various DOM quadratures with a) M = 24 and b) M = 80

Increasing discrete direction number to the order of M = 80 in Figure 5.5b helps to mitigate errors due to ray effect, allowing for easier illustration of angular false scattering errors and the impact of asymmetry factor conservation. For all DOM quadratures, heat fluxes generated with Hunter and Guo's 2012 normalization differ from MC by less than 10% at all locations, while those generated with only scattered energy averaging attain much larger errors of between 50-62%.

For Figures 5.6(a-b), instead of directly plotting heat flux, the percent difference in heat flux from the reference MC solution is directly presented for the same problem as Figures 5.5(a-b), with discrete direction numbers taken on the order of M = 168 and 288, respectively. DOM heat flux results generated with scattered energy averaging were previously presented in Figures 4.11(c-d) for these quadratures and directional orders, and have been reformulated as percent differences for the following analysis.

In Figure 5.6a, application of Hunter and Guo's 2012 normalization produces heat fluxes that differ by less than 7% (in absolute value) from the reference MC solution. Except for a small portion of x^* for the T_5 quadrature, DOM heat fluxes underpredict the MC value at all locations, mirroring the results shown in Figure 5.3. Recalling the data originally presented in Figure 4.11c, lack of asymmetry factor conservation results in significant angular false scattering errors, with differences of between 30-42% observed.

A final increase in discrete direction number to the order of M = 288 in Figure 5.6b reduces angular false scattering error even further, with DOM heat flux profiles predicting within 6% in absolute value to MC for all quadratures after application of Hunter and Guo's 2012 normalization. DOM heat fluxes continue to underpredict MC values for all quadratures and locations, with average percent differences of between -0.5% and -3.0%. Lack of asymmetry

factor conservation after application of Eq. (4.10) results in errors of between 22-36%. The results from Figures 5.5(a-b) and Figures 5.6(a-b) further indicate that Hunter and Guo's 2012 normalization can effectively minimize angular false scattering and improve DOM solution accuracy for $M \leq 288$ discrete directions. Errors with respect to MC are reduced to <10% for all cases except for the lowest-order quadrature, where ray effect is dominant.

As presented in Figures 4.11-4.12, increase in the number of discrete directions can effectively reduce errors due to ray effect and angular false scattering, although the extreme direction numbers required to mitigate said errors result in drastic decreases in computational efficiency [Hunter and Guo 2013]. It is of interest, therefore, to investigate how implementation of Hunter and Guo's 2012 normalization impacts heat fluxes at high discrete direction numbers, in order to see if proper asymmetry factor conservation has a positive impact on computational efficiency.

Figures 5.7(a-b) investigate the impact of Hunter and Guo's 2012 normalization on the percent difference in heat flux between DOM and reference MC versus discrete direction number at four different values of x^*: x^* = 0.02, 0.10, 0.30, and 0.50, respectively. The profiles are generated for the four non-limited DOM quadrature sets using either scattered energy averaging (results originally presented in Figures 4.12a-b) or Hunter and Guo's 2012 normalization.

As seen in Figure 5.7a for x^* = 0.02 (and previously pointed out in the discussion of Figure 4.12), in order to obtain heat fluxes that differ by less than 5% from MC when scattered energy averaging is applied, between M = 750 and 1000 discrete directions must be used, depending on quadrature set. Conversely, if Hunter and Guo's 2012 normalization is applied,

absolute differences of less than 5% are obtained for all quadratures except P_N-EW at the S_N directional limit of M = 288.

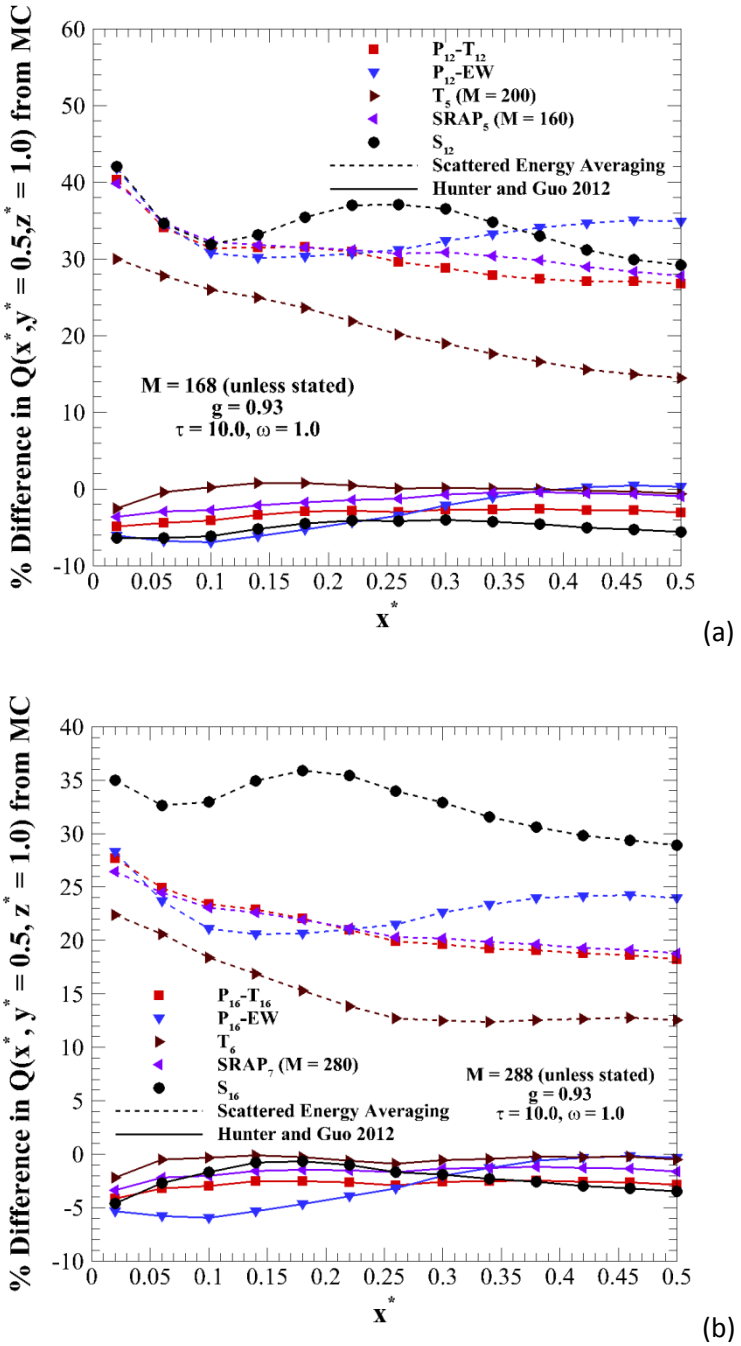

Figure 5.6: Comparison of percent difference in Q(x*, y* = 0.5, z* = 1.0) between DOM with Hunter and Guo's 2012's normalization and Monte Carlo [Boulet et al. 2007] for various DOM quadratures with a) M = 168 and b) M = 288

More interestingly, an increase in discrete direction number does not appear to have a substantial effect on the heat fluxes generated using Hunter and Guo's 2012 normalization. Over the range of discrete directions shown in Figure 5.7a ($24 \leq M \leq 2100$), percent differences for the P_N-T_N, P_N-EW, T_N, and $SRAP_N$ quadratures only improve by 0.9%, 1.1%, 0.1%, and 0.7%, respectively.

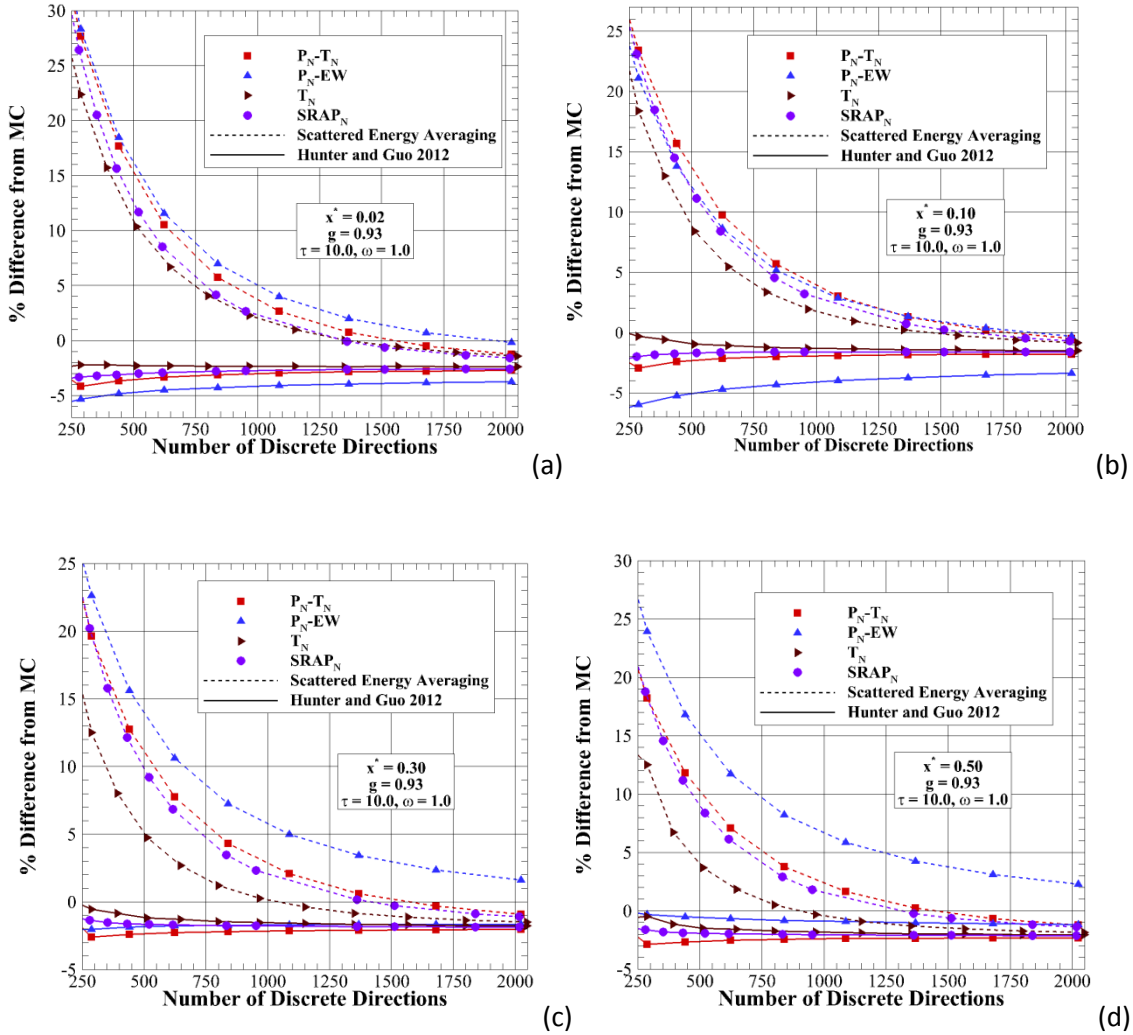

Figure 5.7: Percent difference in Q(x*, y* = 0.5, z* = 1.0) generated using DOM with Hunter and Guo's 2012 normalization from Monte Carlo [Boulet et al. 2007] for various DOM quadratures and discrete direction numbers at a) x* = 0.02, b) x* = 0.1, c) x* = 0.3, and d) x* = 0.5

Similar results are witnessed for the three remaining values of x^* in Figures 5.7(b-d). At the two locations near the wall center (x^* = 0.3 and 0.5), application of Hunter and Guo's 2012 normalization allows for accurate conformity of DOM heat flux to MC within 3% for all discrete direction numbers, with only minimal improvement witnessed over the range of discrete directions tested. The inherent simultaneous conservation of scattered energy and asymmetry factor in Hunter and Guo's 2012 normalization allows for the use of much lower discrete direction numbers than scattered energy averaging, without sacrificing radiation transfer accuracy. Combining these results with the computational time analysis in Figure 4.15, the practicality and efficiency of Hunter and Guo's 2012 normalization becomes evident. For example, as seen in Figures 5.7(a-d), in order to achieve percent differences of 6% of less at all x^*, 840 discrete directions are required for the P_N-T_N quadrature when scattered energy averaging is implemented. Using Hunter and Guo's 2012 normalization, heat fluxes determined for M = 168 in Figure 5.6(a) already attain such an accuracy, allowing for a reduction in computational time of over 98% from ~195 minutes to 4 minutes [Hunter and Guo 2013].

In terms of computational storage, Figure 5.8 examines total DOM computational committed memory (determined through the operating system) for both scattered energy averaging and Hunter and Guo's 2012 normalization versus number of discrete directions. It is important to note that the amount of computational memory depends solely on the spatial and angular resolution, and is independent of quadrature scheme. At low direction number, computational memory for each normalization is comparable. Increase in direction number leads to an increase in computational memory for Hunter and Guo's 2012 normalization over the traditional scattered energy approach, due to the necessity of storing the $O(M^2)$ coefficient matrix. However, this increase in memory is not a major issue, due to the fact that direction number increase does not drastically improve solution accuracy, as seen in Figures 5.7(a-d). As

previously discussed, 840 discrete directions are required to obtain solution accuracy of <6% when compared to MC for the P_N-T_N quadrature using scattered energy averaging, while only 168 directions are required for Hunter and Guo's 2012 normalization. Reduction in discrete direction number from 840 to 168 results in a computational memory savings of 79%, further indicating the advantages of accurately conserving scattered energy and asymmetry factor simultaneously [Hunter and Guo 2013].

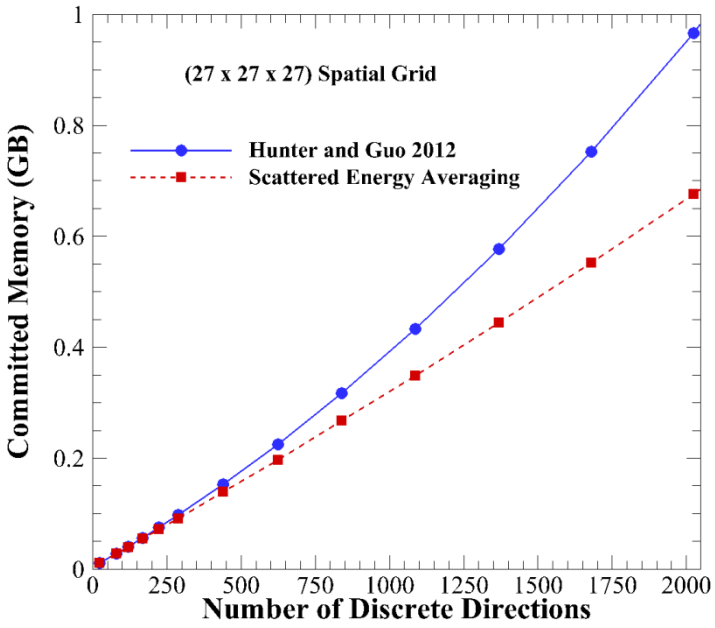

Figure 5.8: Comparison of computational memory (in GB) between DOM with scattered energy averaging and Hunter and Guo's 2012 normalization with varying discrete direction number

5.2.4 Impact of Normalization for Varying Optical Properties

Up to this point, the impact of Hunter and Guo's 2012 normalization has been analyzed for a few specific, benchmark problems. In order to determine when lack of asymmetry factor conservation becomes detrimental to accurate radiation transfer modeling, the impact of

proper phase-function normalization on radiation transfer in media with various optical thicknesses τ and scattering albedos ω is examined in this section [Hunter and Guo 2012e].

Figures 5.9(a-b) investigate the impact of normalization technique on heat flux $Q(x^*, y^* = 0, z^* = 0.5)$ for various medium optical thicknesses τ. Results are presented for a hot medium, of unity blackbody emissive power, surrounded by cold walls (Figure 5.9a), and for a cold medium being diffusely irradiated by one hot wall at x^* = 0 (Figure 5.9b). For both cases, the scattering albedo of the medium is fixed as ω = 0.95, and the 26-term g = 0.8189 Legendre phase-function approximation is implemented. In addition, results are presented for various discrete direction numbers using the S_N quadrature. Heat fluxes generated with the S_{16} quadrature with Hunter and Guo's 2012 normalization are taken as a benchmark or comparison and analysis, as this quadrature most accurately approximates the continuous angular variation of radiation scattering.

For the hot medium in Figure 5.9a, the implemented normalization technique does not have a significant impact for the optically thinner medium (τ = 1.0). The maximum difference between scattered energy averaging and Hunter and Guo's 2012 normalization is 0.3% for S_4, for which an 80.5% change in scattering effect is realized after scattered energy averaging. For optically thinner media, distortions in asymmetry factor do not greatly impact radiation transfer results, due to radiant energy passing freely through the medium without multiple scattering events

As optical thickness increases, total scattering events increase, and the lack of asymmetry factor conservation in scattered energy averaging greatly impacts radiation transfer. When compared to the benchmark case (S_{16} with Hunter and Guo's 2012 normalization), maximum percent differences in heat flux are 18.2%, 9.9%, 2.9%, and 0.9% for S_4-S_{16},

respectively, for τ = 25.0 when scattered energy averaging is applied. Even larger discrepancies are witnessed for the thickest medium (τ = 100.0), with differences of up to 22% for S_4. When Hunter and Guo's 2012 normalization is applied, the differences between all four directional orders are less than 0.7%, indicating that coarser angular resolutions can be implemented without the risk of angular false scattering error.

For the diffuse hot wall (Figure 5.9b), the impact of normalization is again small for the optically thinner medium. However, the choice of discrete direction number has a drastic impact on the physical results. For the S_4 quadrature, it was shown in Figure 4.7 that limited discrete direction numbers were not able to accurately represent the oscillatory behavior of the true phase-function, leading to the noticeable differences in heat flux profile shape of up to 40% when comparing S_4 to S_{16}. Further refinement of quadrature allows for the oscillatory behavior of the phase function to be better represented, and differences when compared to S_{16} decrease dramatically to 5% for S_{12} in both normalization cases.

As optical thickness increases to τ = 25, the impact of altered asymmetry factors in scattered energy averaging become clearly evident. At the far wall, the numerous scattering events encountered as energy propagates away from the source result in extreme differences in heat flux when compared to Hunter and Guo's 2012 normalization. For S_4, heat flux generated using scattered energy averaging is 520% larger than that determined using Hunter and Guo's 2012 normalization. Even for S_{16}, the slight change in discretized g from 0.8189 to 0.8234 produces a 12% difference in heat flux at the far wall, indicating that errors due to lack of asymmetry factor conservation manifest greatly as energy propagates through the medium.

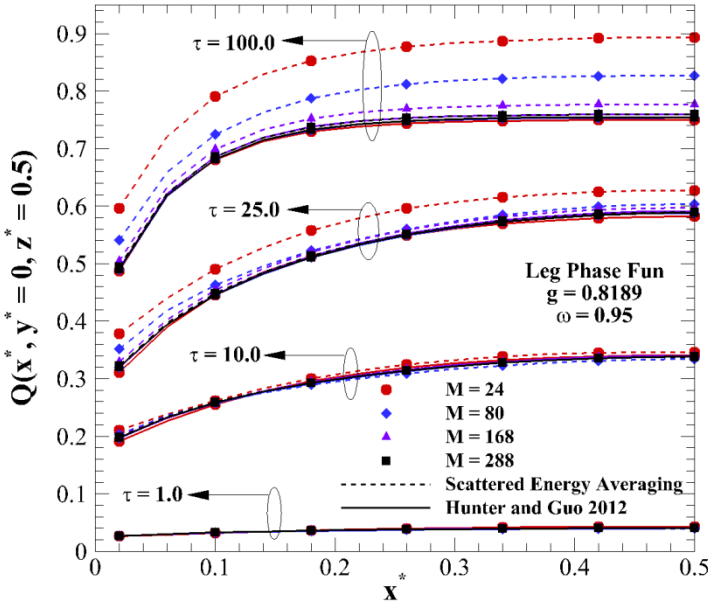

(a)

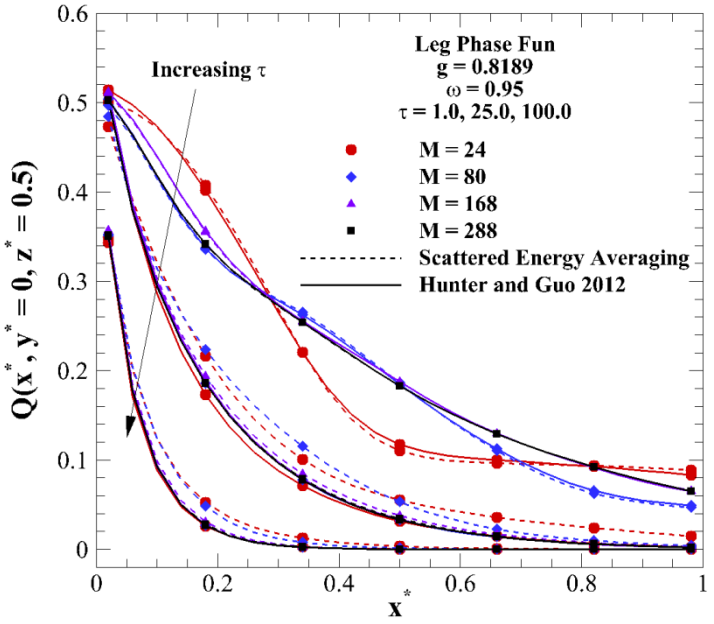

(b)

Figure 5.9: Comparison of Q(x*, y* = 0, z* = 0.5) between DOM with scattered energy averaging and Hunter and Guo's 2012 normalization in a highly scattering medium generated for varying discrete direction number and optical thicknesses with Legendre g = 0.8189 for a) hot medium with cold walls and b) cold medium with hot wall at x* = 0.

When compared to the benchmark case (S_{16} with Hunter and Guo's 2012 normalization), percent differences at the far wall reach maximums of 613%, 92.3%, 36.1%, and 12.0% for S_4-S_{16}, respectively, when scattered energy averaging is implemented. Conservation of asymmetry factor in Hunter and Guo's 2012 normalization reduces the differences to 14.4%, 1.3%, and 1.5% for S_4-S_{12}, where the larger difference for the S_4 quadrature can be attributed to ray effect. The excellent agreement between S_8-S_{16} heat flux profiles with Hunter and Guo's 2012 normalization indicates the importance of conserving asymmetry factor after directional discretization. Results for the extremely thick medium (τ = 100.0) are even more drastic, as differences at x^* = 1.0 reach 31600%, 1920%, 117%, and 28.4% for S_4-S_{16} when scattered energy averaging is applied. Conservation of asymmetry factor with Hunter and Guo's 2012 normalization reduces these discrepancies to 35.1%, 2.4%, and 1.7% for S_4-S_{12}.

Figures 5.10(a-b) examine the impact of normalization on heat flux $Q(x^*, y^* = 0, z^* = 0.5)$ for various medium scattering albedos ω. Results for the hot medium (Figure 5.10a) and the cold medium with a diffusely irradiating hot wall at x^* = 0 (Figure 5.10b) are presented for various DOM S_N discrete direction numbers. The medium is taken to have optical thickness τ = 25.0, and the results are generated using the HG phase-function approximation with g = 0.9000. Heat flux profiles generated with the S_{16} quadrature with Hunter and Guo's 2012 normalization are again taken as a benchmark for comparison.

For the hot medium in Figure 5.10a, scattering albedo is varied between ω = 0.75, 0.90, and 0.95, because lack of conservation of asymmetry factor with scattered energy averaging is not found to have a significant impact for problems where absorption dominates scattering, i.e. $\omega < 0.50$. As scattering becomes dominant, significant discrepancies are witnessed between DOM heat flux profiles generated with the two normalization approaches. When compared to

the benchmark solution, maximum percent differences in heat flux reach 4.7%, 3.9%, 2.6%, and 1.8% for S_4-S_{16}, respectively, when ω = 0.75. Hunter and Guo's 2012 normalization reduces these differences to 1.9%, 0.2%, and 0.7% for S_4-S_{12}, respectively. For ω = 0.95, the maximum differences when compared to the benchmark case increase to 12.4%, 9.8%, 6.5%, and 4.2% for the four directional orders with scattered energy averaging, and drop to 4.4%, 0.2%, and 0.5% for S_4-S_{12} using Hunter and Guo's 2012 approach.

For the diffusely irradiating hot wall in Figure 5.10b, heat fluxes are presented or ω = 0.25, 0.75, and 0.95. For ω = 0.25, the differences between the two normalizations are minimal in the region where heat flux has significant value (less than 7% for all quadrature orders at x^* = 0.20). As scattering albedo increases, differences between the two normalization approaches become noticeable. For ω = 0.95, percent differences at the far wall when compared to the benchmark reach 315%, 64%, 88%, and 54% for S_4-S_{16}, respectively, when scattered energy averaging is applied. In addition, significant discrepancies can be seen in the region x^* = 0.10-0.50, with errors reaching over 40% for the S_8 quadrature. When Hunter and Guo's 2012 normalization is applied, the maximum differences in the medium (which occur at the far wall) drop to 18%, 1.7%, and 2.0% for S_4-S_{12}, respectively.

In general, it is seen in Figures 5.10a-b that normalization to conserve both scattered energy and asymmetry factor becomes critical when medium optical thickness is large (due to the increased number of scattering events) and when scattering albedo approaches unity (where scattering is extremely dominant over absorption in the medium) [Hunter and Guo 2012e].

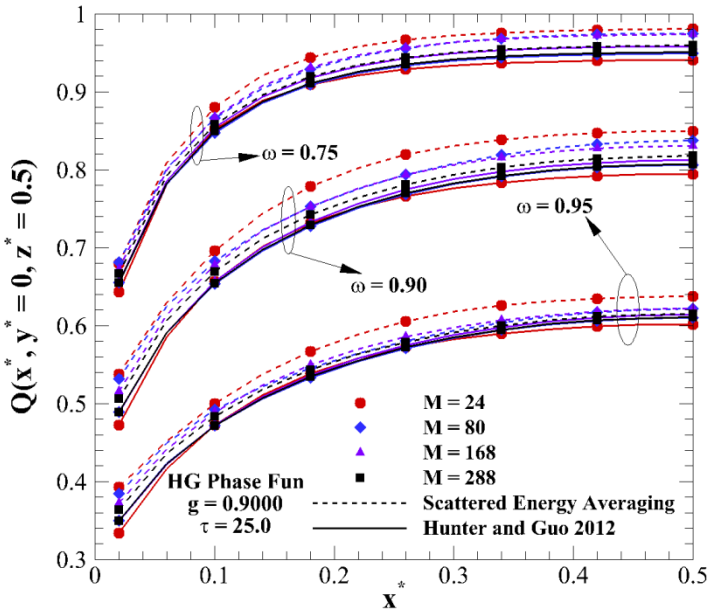

(a)

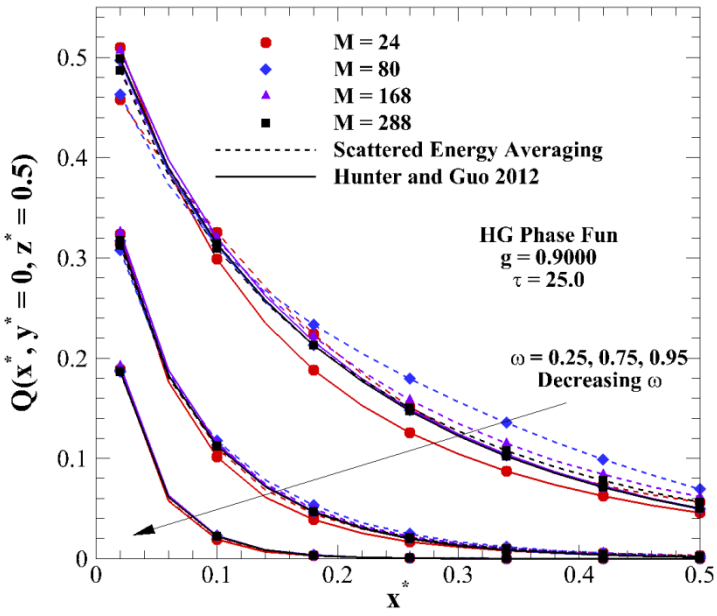

(b)

Figure 5.10: Comparison of Q(x*, y* = 0, z* = 0.5) between DOM with scattered energy averaging and Hunter and Guo's 2012 normalization generated for varying discrete direction number and scattering albedos with HG g = 0.9000 and τ = 25.0 for a a) hot medium with cold walls and b) cold medium with hot wall at x* = 0.

5.3 Application for FVM Radiation Transfer Predictions

5.3.1 Improvement in Discretized Phase-Function Values

As a preliminary validation of Hunter and Guo's 2012 normalization for the FVM [Hunter and Guo 2012b, Hunter and Guo 2014d], discretized phase-function values generated using the FT_N-FVM quadrature scheme are presented for a prescribed HG g = 0.9300 phase function with various discrete direction numbers. (24 x 24) solid-angle splitting is used in order to accurately conserve scattered energy before application of Hunter and Guo's 2012 normalization. High solid-angle splitting resolution allows visualization of improvement solely due to asymmetry factor conservation. For all discrete direction numbers, discretized phase-function values accurately conform to the prescribed values after normalization; a noticeable improvement over the results in Figure 4.19. Slight discrepancies are witnessed for the lowest-order quadrature, which will be further explored later.

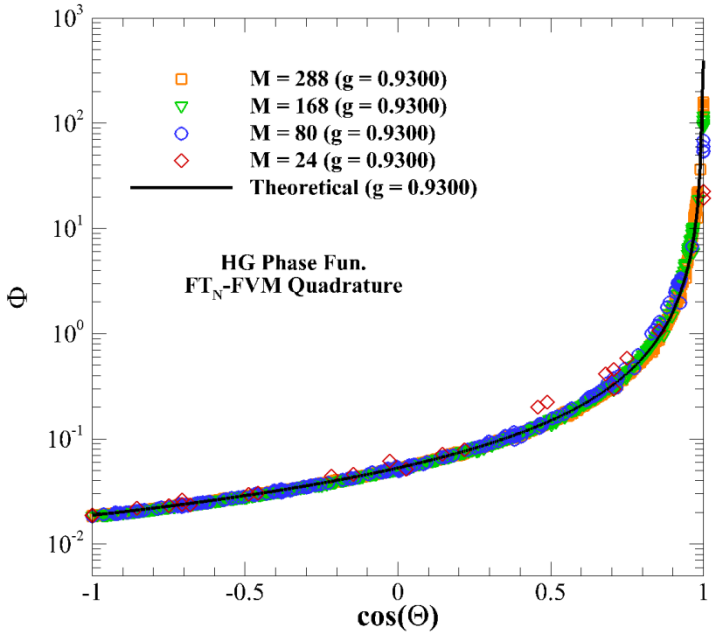

Figure 5.11: Discretized phase-function values for HG g = 0.9300 after FVM discretization with (24 x 24) splitting using Hunter and Guo's 2012 normalization

5.3.2 Comparison to Monte Carlo and DOM

The impact of proper scattered energy and asymmetry factor conservation after discretization is visualized in Figure 5.12, in which FVM heat fluxes $Q(x^*, y^* = 0.5, z^* = 1.0)$ in the cubic enclosure with one hot wall at z^* = 0 are compared to the benchmark MC results [Boulet et al. 2007] for HG g = 0.2000, 0.8000, and 0.9300. M = 168 discrete directions are used, and thus (16 x 16) solid-angle splitting is implemented to accurately conserve scattered energy before normalization is applied. FVM profiles generated without normalization, which were previously plotted in Figure 4.20 in discussion of the necessity of proper normalization, are replotted here for additional comparison [Hunter and Guo 2014d].

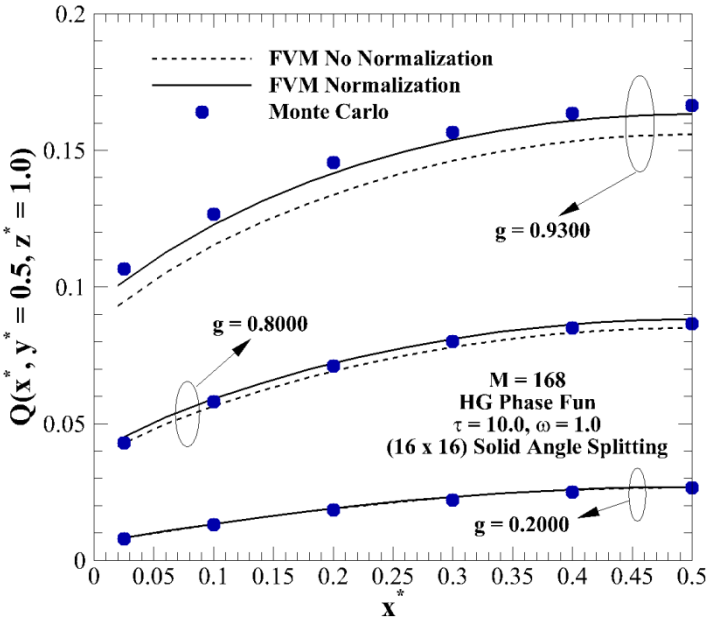

Figure 5.12: Comparison of Q(x*, y* = 0.5, z* = 1.0) generated using FVM with and without Hunter and Guo's 2012 normalization and (16 x 16) angle splitting with Monte Carlo [Boulet et al. 2007] for HG g = 0.2000, 0.8000, and 0.9300

As witnessed for the DOM, FVM profiles are nearly identical for g = 0.2000 both with and without normalization, further reinforcing the notion that normalization is ultimately

unnecessary for weakly-forward scattering phase-functions. For g = 0.8000, heat flux generated using Hunter and Guo's 2012 normalization results in heat fluxes that are between 0-2% higher than MC values, while nonuse of normalization leads to 1-3% underpredictions in heat flux. In general, for this asymmetry factor, both heat flux profiles can be considered as accurate in comparison to MC. For g = 0.9300, however, noticeable improvements are witnessed after application of Hunter and Guo's 2012 normalization. Normalization reduces error with respect to MC to less than 2% for all locations except near x^* = 0, where the maximum difference is 4.6%. Conversely, as originally seen in Figure 4.20, lack of asymmetry factor conservation leads to 6-12% underpredictions in radiative heat flux, corresponding to the 14.6% scattering effect change from the prescribed g = 0.9300 to the discretized 0.9198.

Figure 5.13 reinvestigates the impact of angular resolution on FVM heat flux with g = 0.9300 that was originally presented in Figure 4.21. In Figure 5.13, FVM heat flux profiles are presented both with and without Hunter and Guo's 2012 normalization for M = 24, 48, 80, and 168 discrete directions, respectively. Solid angle splitting of (24 x 24) for M = 24, (20 x 20) for M = 48 and 80, and (16 x 16) for M = 168 is applied to both normalized and non-normalized profiles, in order to accurately conserve scattered energy even without normalization. When normalization is not implemented, large differences of up to 12% with respect to MC are witnessed for M = 168, indicating the prevalence of angular false scattering. Application of normalization greatly improves the conformity greatly for all quadratures but the lowest order, where a difference of near 30% is still witnessed near the wall center. The underlying cause of this large discrepancy near the wall is a result of two underlying errors. The first is ray effect, as discussed earlier for low-directional order. The second underlying cause can be found by examining the values of discretized phase function.

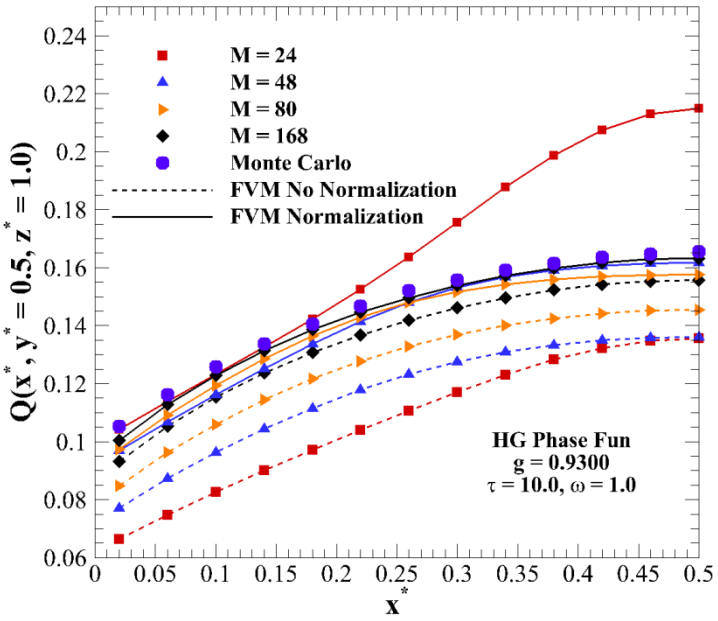

Figure 5.13: Comparison of Q(x*, y* = 0.5, z* = 1.0) generated using FVM with and without normalization with Monte Carlo [Boulet et al. 2007] for various discrete direction numbers with HG g = 0.9300

Figure 5.14a plots the discretized phase function values vs. the cosine of scattering angle both with and without phase-function normalization for M = 24, and compares them to the theoretical HG phase-function values. When normalization is not applied, the phase-function values to not conform accurately to the theoretical phase function, with altered g = 0.8866. After normalization, asymmetry factor is effectively conserved, although the minimal amount of discrete directions in this quadrature order isn't able to accurately represent the true nature of the theoretical phase function shape. Conversely, when a larger number of discrete directions is implemented (M = 168) in Figure 5.14b, both asymmetry factor and phase-function shape are accurately preserved after normalization. Thus, the attained shape of the discretized phase-function values is of extreme importance.

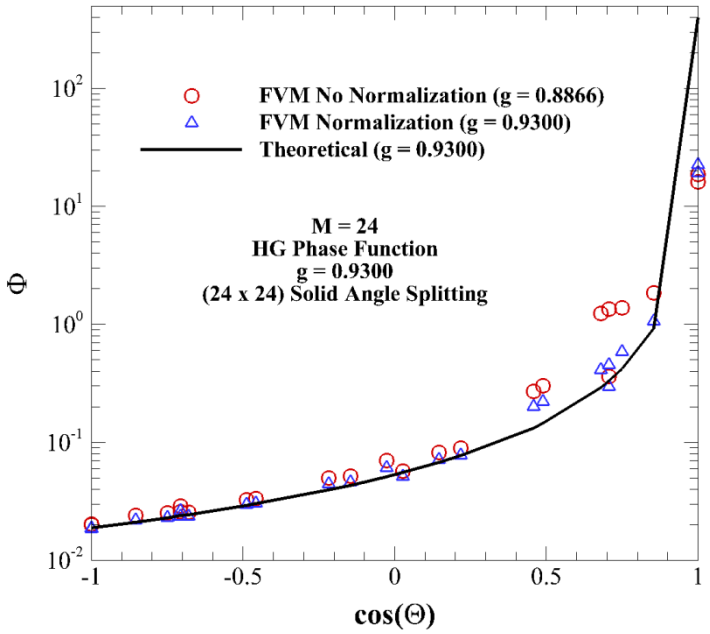

(a)

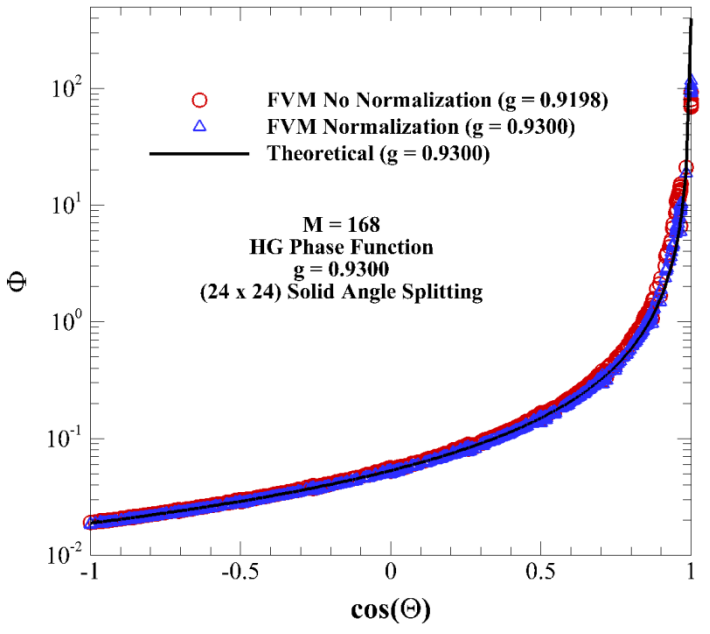

(b)

Figure 5.14: Comparison of discretized HG phase-function values vs. cosine of scattering angle with prescribed g = 0.9300 both with and without phase-function normalization using FVM with a) M = 24 and b) M = 168 discrete directions

Figure 5.15 plots FVM heat fluxes, generated with and without normalization, in an optically thinner medium (τ = 1.0), with all other medium properties are the same as for Figure 5.13. MC results for this optical thickness taken from Boulet et al. [2007] are also presented in Figure 5.15. For the four direction numbers presented (M = 48, 80, 168, and 288), the difference between non-normalized and normalized FVM heat fluxes is minimal, due to the lack of scattering events. However, FVM heat flux profiles exhibit much different behavior and shape than the reference MC values. Physically impossible bumps in heat flux profiles appear due to ray effect, as discussed in Section 3.3.2.2. As direction number is increased, the shape of the FVM heat fluxes appears to converge towards the MC shape, indicating that ray effect is being mitigated with increasing angular resolution. Angular false scattering errors due to lack of asymmetry factor conservation appear to be minimized in an optically thinner medium, although ray effect is still extremely prominent and is of great concern.

Radiation transfer results, determined by solution of the ERT, should be independent of the solution method [Hunter and Guo 2014d]. To this end, a comparison of heat flux values $Q(x^*, y^* = 0.5, z^* = 1.0)$ in the cubic medium with a hot wall at z^* = 0, generated using the FVM with M = 168 discrete directions both with and without phase-function normalization to both MC and DOM S_{12} results are presented in Table 1, in order to further bolster confidence that the generated FVM results are accurate. DOM results are presented for Hunter and Guo's 2012 normalization. All properties, including grid size, scattering albedo, and optical thickness, are identical to those used for Figure 5.13.

The average difference between DOM and FVM is 45% when asymmetry factor is not accurately conserved, which is an inordinately large difference considering the relative similarity of the methods and the fact that they are employed to solve the same equation. Application of

Hunter and Guo's 2012 normalization to both numerical methods reduces the average difference to 3%. Additionally, both methods are accurate to within 7% to MC. The accurate conformity of normalized FVM to both normalized DOM and MC results gives confidence that the scattering properties of the medium are being accurately conserved through use of Hunter and Guo's 2012 normalization. Additionally, the fact that both numerical methods are able to conform to each other highlights a major advantage of phase-function normalization: the ability to use either DOM or FVM to determine accurate radiation transfer.

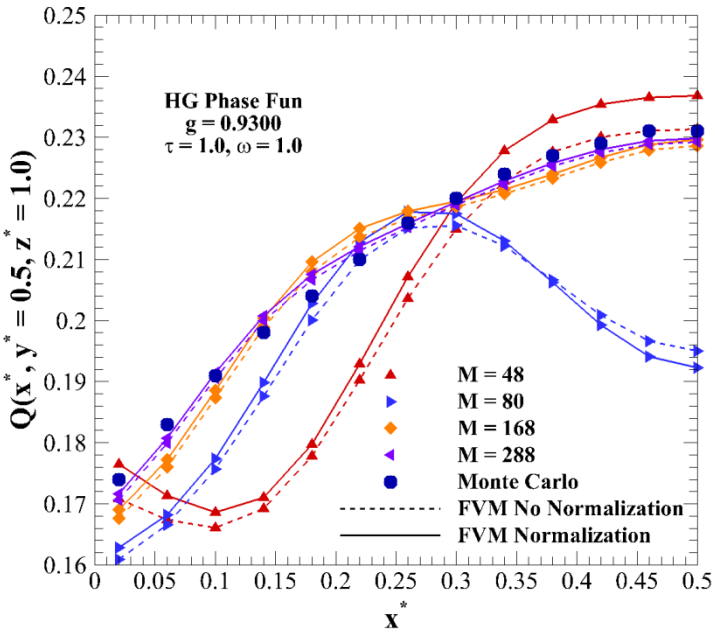

Figure 5.15: Comparison of Q(x*, y* = 0.5, z* = 1.0) generated using FVM with and without normalization and (24 x 24) angle splitting with Monte Carlo [Boulet et al. 2007] for various discrete direction numbers with HG g = 0.9300 in an optically thinner medium (τ = 1.0)

Table 5.3: Comparison of Q(x*, y* = 0.5, z* = 1.0) values generated using DOM and FVM with various normalization techniques to reference MC values [Boulet et al. 2007]

x/L	MC	DOM	FVM	
		Normalization	No Normalization	Normalization
0.02	0.1053	0.0988	0.0930	0.1005
0.10	0.1258	0.1182	0.1153	0.1229
0.14	0.1336	0.1268	0.1237	0.1314
0.22	0.1467	0.1409	0.1368	0.1446
0.30	0.1557	0.1497	0.1461	0.1537
0.38	0.1615	0.1543	0.1523	0.1598
0.42	0.1635	0.1555	0.1542	0.1617
0.50	0.1656	0.1565	0.1558	0.1633

5.3.3 Reduction of Solid-Angle Splitting and Discrete Direction Number

In Figures 4.22(a-d), an analysis of the impact of solid-angle splitting on the difference in heat flux $Q(x^*, y^* = 0.5, z^* = 1.0)$ between non-normalized FVM and MC was presented for four different discrete direction numbers: M = 24, 80, 168, and 288, respectively. This analysis is revisited in Figures 5.16(a-d), where FVM profiles generated with Hunter and Guo's 2012 normalization with both (2 x 2) and (24 x 24) splitting are added for comparison.

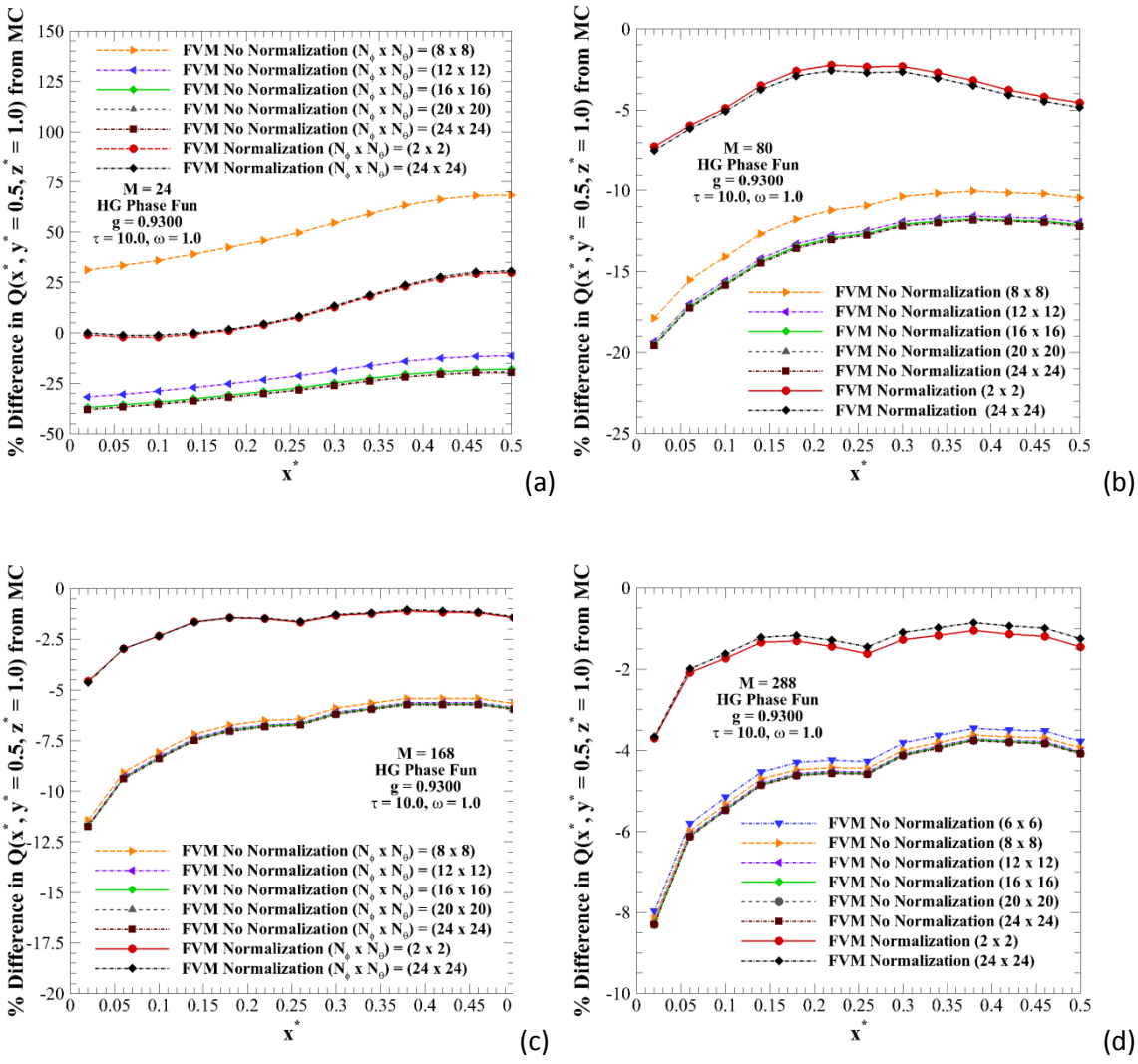

Figure 5.16: Comparison of Q(x*, y* = 0.5, z* = 1.0) generated using FVM with and without Hunter and Guo's 2012 normalization with various solid angle splitting levels to Monte Carlo [Boulet et al. 2007] with a) M = 24, b) M = 80, c) M = 168, and d) M = 288

For low discrete direction number (M = 24), FVM heat flux generated with (24 x 24) splitting and Hunter and Guo's 2012 normalization conform within 5% for locations near the wall. However, as was the case in Figure 5.13, large errors are witnessed near the wall center. For M = 80, 168, and 288, normalized FVM profiles with (24 x 24) splitting predict within 8%, 5%, and 4%, respectively, to the benchmark MC results. Of greater importance, however, is the fact

that FVM profiles generated with both low and high solid-angle splitting densities are nearly identical, with differences of less than 0.5% between (2 x 2) and (24 x 24) for both direction numbers. This indicates that further solid-angle splitting past (2 x 2) is not required to obtain more accurate radiation transfer solutions when implementing normalization.

The ability to produce accurate FVM solutions with minimal solid angle splitting has a distinct advantage when it comes to computational convergence times [Hunter and Guo 2014d]. FVM convergence times for varying numbers of discrete directions and various solid angle splitting levels are presented in Table 5.4 for the problem analyzed in Table 5.3. Computational times using splitting levels ranging from (2 x 2) to (24 x 24) for the non-normalized case are presented, as well as the computational time for Hunter and Guo's 2012 normalization with (2 x 2) splitting.

Table 5.4: Computational convergence times, in seconds, for FVM with and without phase-function normalization at various solid-angle splitting levels and varying number of directions

$(N_{s\phi} \times N_{s\theta})$ / M	No Normalization (sec)								Normalization (sec)
	(2 x 2)	(4 x 4)	(6 x 6)	(8 x 8)	(12 x 12)	(16 x 16)	(20 x 20)	(24 x 24)	(2 x 2)
24	Diverge	Diverge	21.37	14.70	15.38	20.76	33.03	50.86	14.51
48	Diverge	75.21	50.00	47.21	54.40	77.532	124.0	207.0	41.84
80	Diverge	116.5	110.6	113.0	141.8	203.9	335.9	556.6	109.8
168	Diverge	531.0	491.5	514.1	606.7	834.2	1415	2414	497.0
288	1538	1385	1340	1438	1687	2438	4133	7011	1341

When normalization is not applied, (2 x 2) solid angle splitting results in divergent radiation transfer solutions for all direction quadratures except M = 288, corresponding to the lack of scattered energy conservation. In general, refinement of the solid-angle splitting resolution leads to substantial increases in computational convergence time. For M = 288, increase in splitting level from (4 x 4) to (24 x 24) results in a ~400% increase in computational time. Recall from Figure 4.16 that (24 x 24), (20 x 20), (12 x 12), and (12 x 12) splitting is

required to accurately conserve scattered energy for g = 0.9300 when normalization isn't implemented. Use of normalization to conserve asymmetry factor accurately allows for convergence and accuracy with just (2 x 2) splitting, reducing computational times by between 25-250% over the splitting levels required to conserve scattered energy, and highlighting a major advantage of proper phase-function normalization.

A revisit of the analysis in Figure 4.23, in which FVM heat flux profiles generated with extremely high discrete direction numbers were compared to MC results, is presented in Figure 5.17. In addition to the high-direction heat flux profiles generated without normalization in Figure 4.23, FVM solution with normalization at lower discrete direction number (M = 168) is plotted in Figure 5.17. Solid angle splitting of (16 x 16) for *M* = 168 and 288, (8 x 8) for *M* = 624 and 1088, and (4 x 4) for *M* = 2024 is applied to accurately conserve scattered energy. Interestingly enough, the M = 168 FVM profile generated using normalization is more accurate than the three extreme direction cases, with an average percent difference of less than 2% when compared to MC. This profile can be generated, using (2 x 2) splitting, in 497 seconds, respectively, which constitutes a major reduction from the ~5000-65000 seconds required to generate the extreme direction profiles. Thus, use of normalization is both more efficient and more accurate than these higher direction cases [Hunter and Guo 2014d].

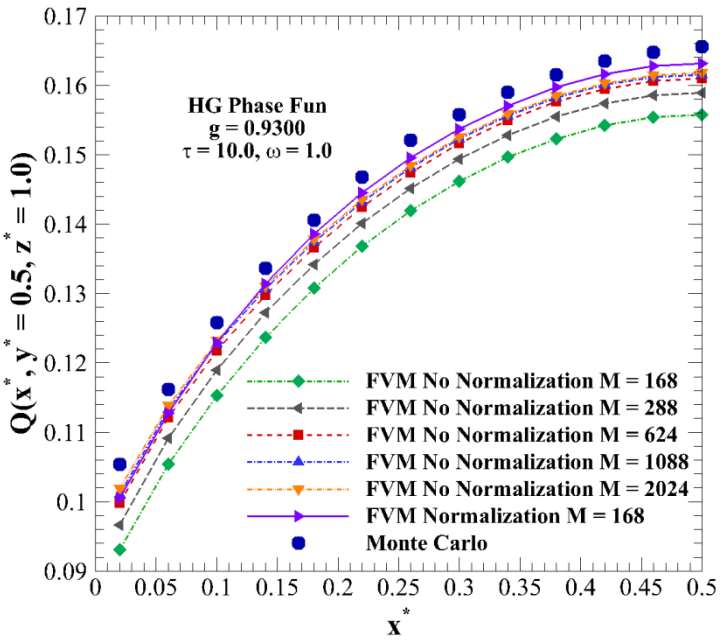

Figure 5.17: Comparison of Q(x*, y* = 0.5, z* = 1.0) between MC solutions [Boulet et al. 2007] and FVM solutions with and without normalization using extremely high-order quadrature

5.4 Summary

In this chapter, a new phase-function normalization approach (called Hunter and Guo's 2012 normalization) is developed for use in both the DOM and FVM as a method to accurately conserve both scattered energy and phase-function asymmetry factor simultaneously. The mathematical model, and an explanation of the method of solution to determine the necessary normalization parameters, is presented in detail. A caution as to the computational memory required to implement Hunter and Guo's 2012 normalization is detailed, and the necessity of using sparse matrix methodology to store the normalization coefficient matrix is presented.

The improvement in discrete phase-function values after application of Hunter and Guo's 2012 normalization is presented for both DOM and FVM, where the conservation of asymmetry factor results in accurate conformity to the prescribed phase function. For the DOM,

comparison between normalized DOM and isotropic scaling law is presented for an axisymmetric medium, where it is found that Hunter and Guo's 2012 normalization greatly improves accuracy over use of scattered energy averaging. Additional comparison with Monte Carlo further validates the use of Hunter and Guo's 2012 normalization to generate accurate heat fluxes and reduce angular false scattering error without requiring an extremely large number of discrete directions. In a parametric analysis, it is found that normalization becomes more critical in optically thick media, and in media where scattering is dominant.

Similar results are encountered for the FVM. When compared to MC, normalization produces much more accurate heat fluxes than when normalization is ignored. Additionally, normalization results in conformity of both DOM and FVM heat fluxes, a result that should occur due to the fact that the two numerical methods are solving the same equation, but was not previously achievable. An additional advantage of normalization is that is greatly reduces the solid-angle splitting density required for accurate radiation transfer prediction.

All in all, the results in Chapter 5 mandate the necessity of accurate conservation of both scattered energy and asymmetry factor after discretization, show that Hunter and Guo's 2012 normalization is able to do so, and validate Hunter and Guo's 2012 normalization as an accurate tool for determining radiation transfer in highly anisotropic scattering media.

CHAPTER 6 : HUNTER AND GUO'S 2014 NORMALIZATION: A SECOND, SIMPLE PHASE-FUNCTION APPROACH FOR ACCURATE RADIATION TRANSFER ANALYSIS USING THE DOM

6.1 Forward-Scattering Term Normalization Techniques

6.1.1 Mishchenko et al.'s Scattered Energy Normalization (Mishchenko E)

As mentioned previously, the scattered energy averaging approach of Eq. (4.10) has been one of the more commonly implemented normalization techniques for the DOM in recent years to ensure convergent DOM solutions. Eq. (4.10) conserves scattered energy through adjustment of every value of $\Phi^{l'l}$ in the system, causing dramatic skews from the prescribed values at all values of scattering angle.

More recently, Mishchenko et al. [1999] introduced another normalization technique, specifically crafted to accurately conserve scattered energy. They noted that, for a strong-forward scattering HG phase function, the magnitude of the forward-scattering term (i.e., $\Phi^{l'l'}$, where $\cos\Theta = 1$) is significantly larger than the remaining discrete phase function values. They determined that this value was the most critical value to adjust in order to conserve scattered energy, a fact that was confirmed earlier in Section 4.1.1 in reference to the modified scattering coefficient.

Thus, rather than normalizing every value of $\Phi^{l'l}$ in the system (as was the case for Eq. (4.10) for scattered energy averaging), Mishchenko et al. [2007] proposed to conserve scattered energy solely through normalization of the forward-scattering phase-function term $\Phi^{l'l'}$, leaving

all other values of $\Phi^{l'l}$ unaltered. Applying this notion, the normalized value of the forward-scattering phase-function term can be expressed as follows:

$$\tilde{\Phi}^{l'l'} = \left(1 + A^{l'}\right)\Phi^{l'l'} \tag{6.1}$$

where $A^{l'}$ is the forward-scattering normalization vector parameter. Using Eq. (6.1) to normalize only the forward-scattering term, the scattered energy condition of Eq. (4.3) can be rewritten as follows, for discrete direction $\hat{\boldsymbol{s}}^{\boldsymbol{l'}}$:

$$\frac{1}{4\pi}\sum_{\substack{l=1 \\ l'\neq l}}^{M} \Phi^{l'l} w^{l} + \frac{1}{4\pi}\left(1 + A^{l'}\right)\Phi^{l'l'} w^{l'} = 1 \tag{6.2}$$

Solving for $A^{l'}$ leads to the following expression for the forward-scattering normalization vector parameter, for discrete direction $\hat{\boldsymbol{s}}^{\boldsymbol{l'}}$:

$$A^{l'} = \left(4\pi - \sum_{l=1}^{M} \Phi^{l'l} w^{l}\right) / \left(\Phi^{l'l'} w^{l'}\right) \tag{6.3}$$

This normalization technique appears to be a simpler alternative to Eq. (4.10), as it conserves scattered energy accurately whilst retaining the values of $\Phi^{l'l}$ for all cases except when $l' = l$. In its present form, Eq. (6.3) is only valid for forward-scattering phase functions ($g > 0$). For backward-scattering phase functions (g < 0), where the strong scattering peak occurs for $\cos\Theta = -1$, Eq. (6.3) must be re-derived so that the backward-scattering phase function term is instead normalized.

While Mishchenko et al.'s normalization does guarantee accurate conservation of scattered energy, it does not mathematically guarantee accurate conservation of phase-function asymmetry factor, and thus angular false-scattering errors will not be effectively mitigated. For further reference, this normalization will be referred to as "Mishchenko's E" normalization.

6.1.2 Kamdem Tagne's Asymmetry Factor Normalization (Kamdem Tagne g)

Recently, Kamdem Tagne [2013] extended the formulation of Mishchenko et al. to develop a new normalization technique that guarantees the preservation of asymmetry factor after discretization. In a similar manner to the formulation discussed in the previous section, Kamdem Tagne focused solely on normalizing the forward-scattering phase function term, as shown in Eq. (6.1). However, instead of using Eq. (4.3) as the basis for determining the forward-scattering normalization parameters, the asymmetry factor conservation condition of Eq. (4.9) is instead used. Implementing the normalization, Eq. (4.9) can be rewritten in the following form, for discrete direction $\hat{\boldsymbol{s}}^{\boldsymbol{l'}}$:

$$\frac{1}{4\pi}\sum_{\substack{l=1\\ l'\neq l}}^{M}\Phi^{l'l}\cos\Theta^{l'l}\,w^{l}+\frac{1}{4\pi}\left(1+A^{l'}\right)\Phi^{l'l'}\cos\Theta^{l'l'}\,w^{l'}=g \tag{6.4}$$

Rearranging Eq. (6.4) and solving for $A^{l'}$, the values of the forward-scattering normalization parameters that will accurately conserve phase-function asymmetry factor can be expressed as follows, for discrete direction $\hat{\boldsymbol{s}}^{\boldsymbol{l'}}$:

$$A^{l'}=\left(4\pi g-\sum_{l=1}^{M}\Phi^{l'l}\cos\Theta^{l'l}\,w^{l}\right)/(\Phi^{l'l'}w^{l'}) \tag{6.5}$$

where the denominator is simplified by the fact that $\cos\Theta^{l'l'}=1$.

This technique has the advantage of being able to accurately conserve phase-function asymmetry factor (meaning that angular false scattering errors will not be present), but it does not mathematically guarantee accurate conservation of scattered energy in the system, a fact that could lead to significant discrepancies in radiation transfer predictions. For future

reference in this work, this normalization will be referred to as "Kamdem Tagne's g" normalization.

Table 6.1 addresses the lack of either scattered energy or asymmetry factor conservation after application of Mishchenko's E and Kamdem Tagne's g normalization [Hunter and Guo 2014b]. In Table 6.1, scattered energy and asymmetry factor values are tabulated for DOM P_N-T_N quadrature indices of N = 4, 6, 8, 12, and 16, corresponding to M = 24, 48, 80, 168, and 288 discrete directions, respectively. Three typical values of HG asymmetry factor are presented: g = 0.6000, 0.8000, 0.9300. As a means of comparison, scattered energy and asymmetry factor conservation values are listed for the DOM both without any phase-function normalization implemented and after application of scattered energy averaging. For the two techniques where scattered energy is conserved, only discretized asymmetry factor values are investigated. Conversely, for Kamdem Tagne's g normalization, only scattered energy discrepancies are listed. In addition, percent differences in scattered energy E and in scattering effect (1-g) are also listed, in order to gauge the significance of lack of parameter conservation.

Table 6.1: Discretized scattered energy and/or asymmetry factor values for various normalization techniques using DOM P_N-T_N quadrature and HG phase function with g = 0.6000, 0.8000, and 0.9300

		No Normalization		Scattered Energy Norm.		Mishchenko E		Kamdem Tagne g	
g	N	Discretized E	Discretized g	Discretized g	% Diff in (1-g)	Discretized g	% Diff in (1-g)	Discretized E	% Diff in E
0.6000	4	1.0741	0.6818	0.6347	8.684	0.6077	1.917	0.9923	0.7669
	6	1.0111	0.6123	0.6056	1.399	0.6012	0.308	0.9988	0.1231
	8	1.0018	0.6021	0.6009	0.237	0.6002	0.053	0.9998	0.0213
	12	1.0001	0.6001	0.6000	0.009	0.6000	0.002	1.0000	0.0008
	16	1.0000	0.6000	0.6000	0.000	0.6000	0.000	1.0000	0.0000
0.8000	4	2.2171	2.0349	0.9177	58.87	0.8177	8.868	0.9823	1.7737
	6	1.4274	1.2346	0.8648	32.38	0.8072	3.604	0.9928	0.7209
	8	1.1695	0.9726	0.8315	15.77	0.8031	1.555	0.9969	0.3110
	12	1.0312	0.8318	0.8066	3.322	0.8006	0.314	0.9994	0.0628
	16	1.0064	0.8065	0.8014	0.703	0.8001	0.068	0.9999	0.0135
0.9300	4	16.524	16.466	0.9965	94.98	0.9414	16.29	0.9886	1.1400
	6	8.3776	8.3149	0.9925	89.26	0.9373	10.43	0.9927	0.7300
	8	5.1532	5.0880	0.9873	81.82	0.9348	6.857	0.9952	0.4800
	12	2.6833	2.6157	0.9746	63.78	0.9324	3.429	0.9976	0.2400
	16	1.8047	1.7360	0.9617	45.36	0.9313	1.857	0.9987	0.1300

Mishchenko's E normalization is able to effectively conserve scattered energy, similar to the scattered energy averaging of Eq. (4.10). However, the fact that nearly all of the discrete phase-function values are preserved during this process leads to much smaller errors in discretized asymmetry factor than witnessed after application of Eq. (4.10). For g = 0.6000, application of Mishchenko's E normalization leads to scattering effect changes of less than 2% for all quadratures, indicating reasonable conservation of asymmetry factor and the resulting mitigation of angular false scattering. In comparison with traditional scattered energy averaging, the differences in scattering effect change are dramatically reduced when only the forward-scattering term is normalized. However, for strong-forward scattering (g = 0.9300), >5% changes in scattering effect are observed for N < 12, with differences of 16.3% and 10.4% occurring for N = 4 and 6, respectively, indicating the potential for the rise of angular false scattering errors.

Kamdem Tagne's g normalization conserves phase-function asymmetry factor, unlike the two previously discussed normalizations, meaning that angular false scattering errors should be effectively minimized. However, conservation of scattered energy in the system is not guaranteed after directional discretization. Discrepancies in scattered energy conservation using Kamdem Tagne's g normalization are not as large as the discrepancies in asymmetry factor and scattering effect when either traditional scattered energy averaging or Mishchenko's E normalizations are implemented. For $g = 0.6000$, energy is only slightly non-conserved for low quadratures. As asymmetry factor is increased, the discrepancies in energy conservation increase, but the values remain less 1% for all quadratures except N = 4. Although the deviations in scattered energy are not of high magnitude, accumulation of errors during computation due to lack of energy conservation can be appreciable and/or lead to divergence of iteration.

6.2 Hunter and Guo's 2014 Normalization

Both Mishchenko's E and Kamdem Tagne's g normalization have an inherent advantage of being simple to implement. However, each of these normalizations are only able to accurately conserve one of the two quantities of interest, indicating possible shortcomings of these simpler phase-function normalizations. Ideally, these two normalizations should be combined in some way, in order to take advantage of the mathematical simplicity while retaining conservation of both scattered energy and asymmetry factor simultaneously after discretization [Hunter and Guo 2014b]

To this end, it is proposed that, in addition to normalizing the forward-scattering phase-function term, the backward-scattering term $\Phi^{l'l^-}$ is also normalized, where the superscript l^- represents the radiation direction directly opposite from $\hat{\boldsymbol{s}}^{\boldsymbol{l'}}$, where $\cos\Theta^{l'l^-} = -1$. Applying this notion, the normalized values of the forward and backward scattering phase function terms can be expressed as follows, for radiation direction $\hat{\boldsymbol{s}}^{\boldsymbol{l'}}$:

$$\tilde{\Phi}^{l'l'} = \left(1 + A^{l'}\right)\Phi^{l'l'} \tag{6.6a}$$

$$\tilde{\Phi}^{l'l^-} = \left(1 + B^{l'-}\right)\Phi^{l'l-} \tag{6.6b}$$

where $B^{l'-}$ is the backward scattering normalization vector parameter. Using Eqs. (6.6a-b), the conservation of scattered energy and asymmetry factor conditions of Eqs. (4.3) and (4.9) can be rewritten in the following form, for discrete direction $\hat{\boldsymbol{s}}^{\boldsymbol{l'}}$:

$$\frac{1}{4\pi}\sum_{\substack{l=1\\ l\neq l'\\ l\neq l^-}}^{M}\Phi^{l'l}w^{l}+\frac{1}{4\pi}\left(1+A^{l'}\right)\Phi^{l'l'}w^{l'}+\frac{1}{4\pi}\left(1+B^{l'^-}\right)\Phi^{l'l^-}w^{l^-}=1 \tag{6.7a}$$

$$\begin{aligned}\frac{1}{4\pi}\sum_{\substack{l=1\\ l\neq l'\\ l\neq l^-}}^{M}\Phi^{l'l}w^{l}\cos\Theta^{l'l}+\frac{1}{4\pi}\left(1+A^{l'}\right)\Phi^{l'l'}w^{l'}\cos\Theta^{l'l'}\\ +\frac{1}{4\pi}\left(1+B^{l'^-}\right)\Phi^{l'l^-}w^{l^-}\cos\Theta^{l'l^-}=g\end{aligned} \tag{6.7b}$$

As this system has $2M$ equations and $2M$ unknowns, it has a unique solution. Simultaneous solution of Eqs. (6.7a-b) leads to the following expressions for the forward- and backward-scattering normalization parameters:

$$A^{l'}=\frac{1}{2\Phi^{l'l'}w^{l'}}\left[4\pi(1+g)-\sum_{l=1}^{M}\Phi^{l'l}w^{l}\left(1+\cos\Theta^{l'l}\right)\right] \tag{6.8a}$$

$$B^{l'^-}=\frac{1}{2\Phi^{l'l^-}w^{l^-}}\left[4\pi(1-g)+\sum_{l=1}^{M}\Phi^{l'l}w^{l}\left(\cos\Theta^{l'l}-1\right)\right] \tag{6.8b}$$

Use of these normalization parameters for all discrete directions $\hat{\boldsymbol{s}}^{\boldsymbol{l'}}$ will guarantee conservation of both scattered energy and asymmetry factor simultaneously, as Hunter and Guo's 2012 normalization also does. Eqs. (6.8a-b) are valid over the entire range of phase-function asymmetry factor $-1\leq g\leq 1$.

This approach was developed in 2013, and was first published in early 2014 [Hunter and Guo 2014b]. Hence, for future reference, this normalization will be referred to as "Hunter and Guo's 2014" normalization.

6.3 Application for DOM with HG Phase Functions

6.2.1 Discretized Phase Function Values

Before analyzing DOM radiation transfer profiles to validate Hunter and Guo's 2014 normalization as an accurate method for modeling scattering anisotropy, an analysis of both the forward- and backward-scattering normalization parameter values is presented in Figures 6.1-6.4, for varying DOM quadrature order and asymmetry factor g.

A common element that exists in all five normalization techniques discussed here is that the forward-scattering phase function term is normalized in some way, in order to artificially reduce the forward-scattering peak such that either scattered energy, asymmetry factor, or both are conserved [Hunter and Guo 2014b]. Figure 6.1 plots the values of the forward-scattering normalization parameters for the DOM P_8-T_8 quadrature (M = 80) for the five normalization techniques using a prescribed HG asymmetry factor of g = 0.9300. The parameters are presented only for directions located in the principal octant, due to DOM directional symmetry. For Hunter and Guo's 2012 normalization, the normalization parameter $A^{l'l'}$ is shown, while for Mishchenko's E, Kamdem Tagne's g, and Hunter and Guo's 2014 normalization, the forward-scattering parameters $A^{l'}$ are plotted. For scattered energy averaging, the normalization value presented is the value of the inverse summation in Eq. (4.10) minus one, in order to make sure that the value is in the same numerical form. A comparison of the forward-scattering normalization parameters in Hunter and Guo's 2014 to the other previously presented techniques will establish a justification behind the mathematical formulation of Hunter and Guo's 2014 normalization.

As seen in Figure 6.1, the parameters generated using Hunter and Guo's 2014 normalization are nearly identical to those generated using both Mishchenko's E and Kamdem

Tagne's g normalizations for all directions. The average values of the forward-scattering normalization parameter for this DOM quadrature and HG asymmetry factor are -0.8427, -0.8436, and -0.8432 for Mishchenko's E, Kamdem Tagne's g, and Hunter and Guo's 2014 normalizations, respectively, indicating that these three normalizations are all similarly attenuating the forward-scattering term. However, the overall asymmetry factor in Mishchenko's E normalization is altered to g = 0.9373, and scattered energy is altered to E = 0.9927 using Kamdem Tagne's g normalization, while both quantities are accurately conserved by both Hunter and Guo's 2012 and 2014 normalizations.

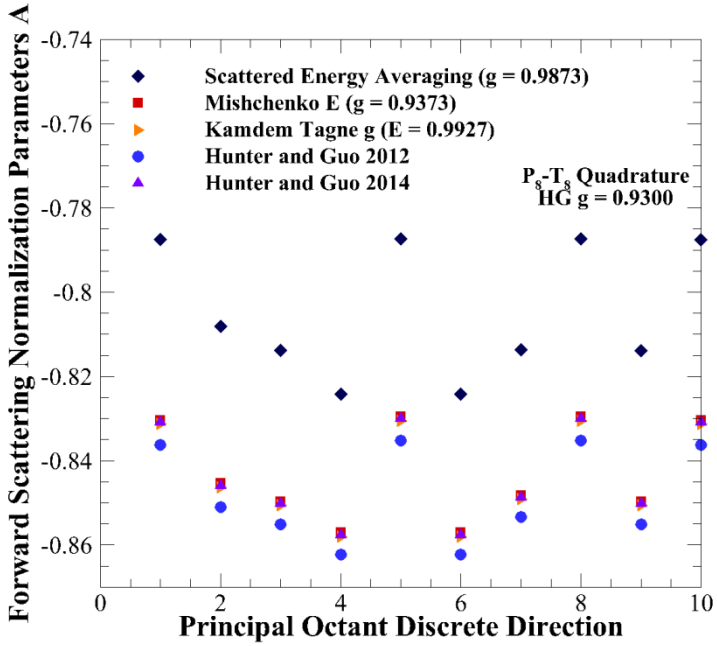

Figure 6.1: Comparison of forward-scattering normalization parameters in the principal octant among various normalization techniques using the P_8-T_8 quadrature (M = 80 discrete directions)

The forward-scattering parameters calculated using Hunter and Guo's 2012 normalization are slightly lower in magnitude than the three previously discussed normalizations, due to the fact that every phase-function term in the system is normalized.

Thus, the drop in forward-scattering phase function term is counteracted by slight increases in the remaining phase-function values in the system. For scattered energy averaging, while at first glance the forward-scattering peak is not reduced as greatly after normalization, the large alteration in g and the resultant angular false scattering errors make this approach less desirable. Hence, from this point further, results will for the traditional scattered energy averaging of Eq. (4.10) will no longer be analyzed.

In Figure 6.2, forward-scattering normalization parameters generated using Mishchenko's E, Kamdem Tagne's g, Hunter and Guo's 2012, and Hunter and Guo's 2014 normalization are presented for the P_{16}-T_{16} quadrature with HG g = 0.9300. As in Figure 6.1 for the P_8-T_8 quadrature, forward-scattering parameters generated with the three forward-scattering normalization techniques are extremely similar, while parameters for Hunter and Guo's 2012 normalization are slightly lower. The absolute values of the normalization parameters for P_{16}-T_{16} are considerably smaller than for P_8-T_8 in Figure 6.1, with average values on the order of -0.59 instead of -0.82. This is due to the decrease in DOM weighting factor value with increase in discrete direction number, as presented in Figure 4.1.

Figures 6.3a-b examine the minimum value of the forward-scattering normalization parameter, as well as the discretized value of the forward-scattering phase-function peak after normalization treatment, versus prescribed HG asymmetry factor after application of the Hunter and Guo's 2014 normalization. The results are presented for the DOM P_N-T_N quadrature with $M = 24$, 48, 80, 168, and 288 discrete directions, respectively. The absolute-values of the forward-scattering parameters decrease with increase in discrete direction number for a given g. Reduction of the forward-scattering peak value by ≥5% (i.e., $A^{l'} < -0.05$) occurs for $g >$ 0.40, 0.55, 0.65, 0.70, and 0.75 for the five discrete direction numbers, respectively. For

$g = 0.9300$, the minimum forward-scattering normalization parameters attain values of -0.9484, -0.9063, -0.8576, -0.7441, and -0.6294 for M = 24-288, respectively, indicating that the forward-scattering peak is more accurately represented by high discrete direction number. As g approaches unity, the forward-scattering normalization parameters approach, but never exceed, negative one. Normalization parameters of <-1 would force the modified scattering coefficient of Eq. (4.4c) to become negative after substitution of $\widetilde{\Phi}^{ll}$, which is physically impossible [Hunter and Guo 2014b].

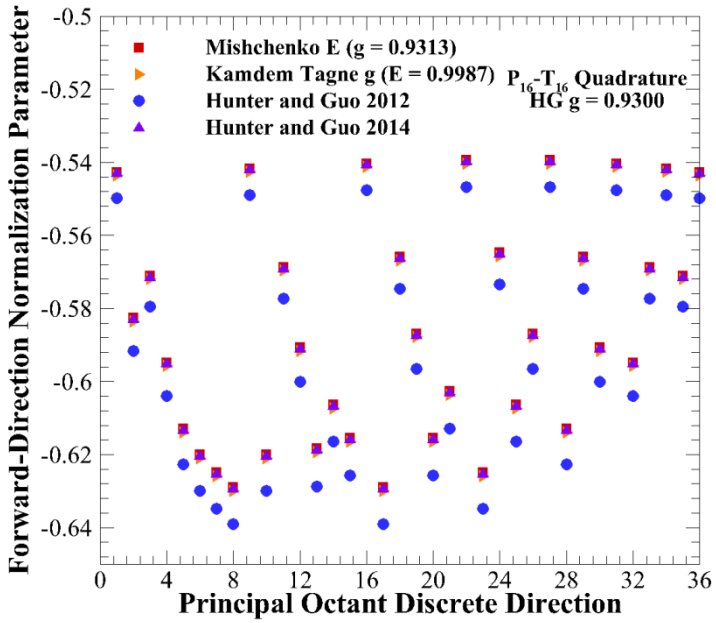

Figure 6.2: Comparison of forward-scattering normalization parameters in the principal octant among various normalization techniques using the P_{16}-T_{16} quadrature (M = 288 discrete directions)

As seen in Figure 6.3b, the discretized values of the forward-scattering peak remain accurate for weakly-anisotropic scattering, but become greatly reduced for strongly anisotropic scattering. For prescribed g = 0.8000, the theoretical forward-scattering peak value from Mie theory with the HG approximation is 45. After application of Hunter and Guo's 2014

normalization, this value is reduced to 15.1, 23.3, 29.8, 38.1, and 42.0 for the five quadrature orders, respectively. For the more extreme case where g = 0.9300, the forward-scattering peak values are reduced from 393.9 to 10.7, 19.7, 30.6, 57.8, and 87.9 for the five discrete direction numbers. As previously discussed in Figures 6.1 and 6.2, all tested normalization approaches also result in similar reductions of the forward-scattering peak values, in order to satisfy the specific conservation constraints. This means that application of any phase-function normalization will result in significant reduction of the forward-scattering peak for strongly-anisotropic scattering.

The new concept introduced in Hunter and Guo's 2014 normalization is the additional normalization of the backward-scattering phase-function term [Hunter and Guo 2014b]. Figures 6.4a-b examine the maximum value of backward-scattering normalization parameters and the discretized value of the backward-scattering phase-function peak after application of normalization. As in Figure 6.3a, the backward parameters in Figure 6.4a have a negligible value for weakly-anisotropic scattering. However, as anisotropy is increased, the values of the backward parameters dramatically increase. An interesting phenomenon occurs for g > 0.90, where the backward parameters for higher-order DOM start to attain larger values than for lower-order DOM. For example, for g = 0.9300, the backward parameters attain values of 7.7, 9.5, 10.5, 10.9, and 10.4, respectively for the five quadratures. This phenomenon is due to the reduction in directional weighting factor magnitude with increasing direction number, combined with the large value of forward-scattering peak for highly anisotropic scattering.

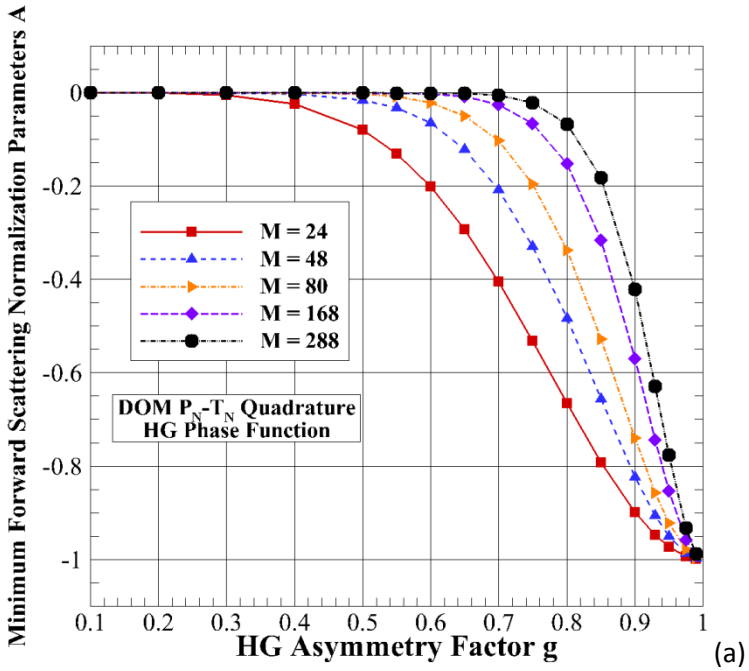

(a)

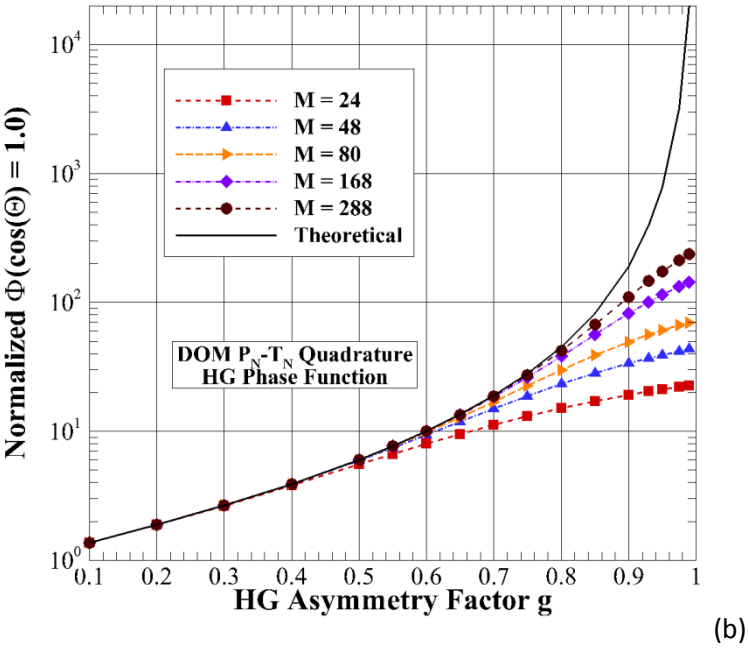

(b)

Figure 6.3: a) Minimum values of forward scattering phase-function normalization parameters and b) normalized forward-scattering discrete phase-function values for various discrete direction numbers versus HG asymmetry factor

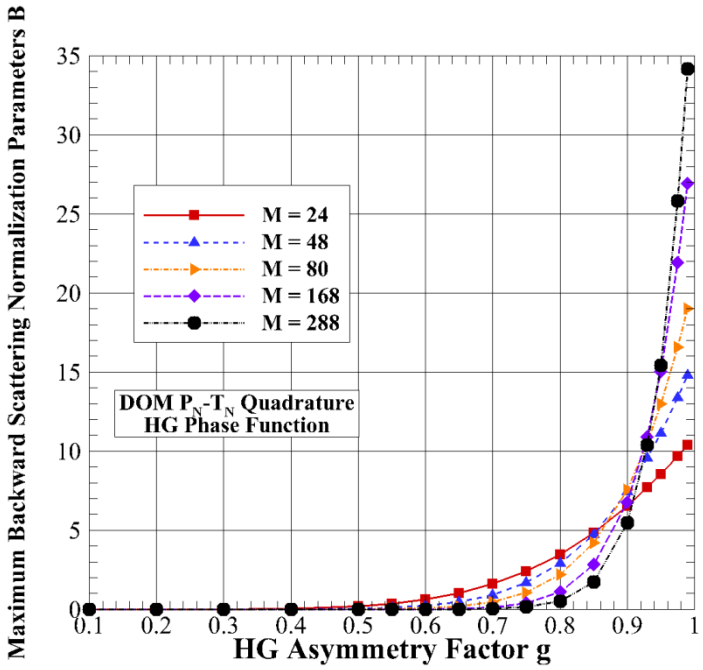

(a)

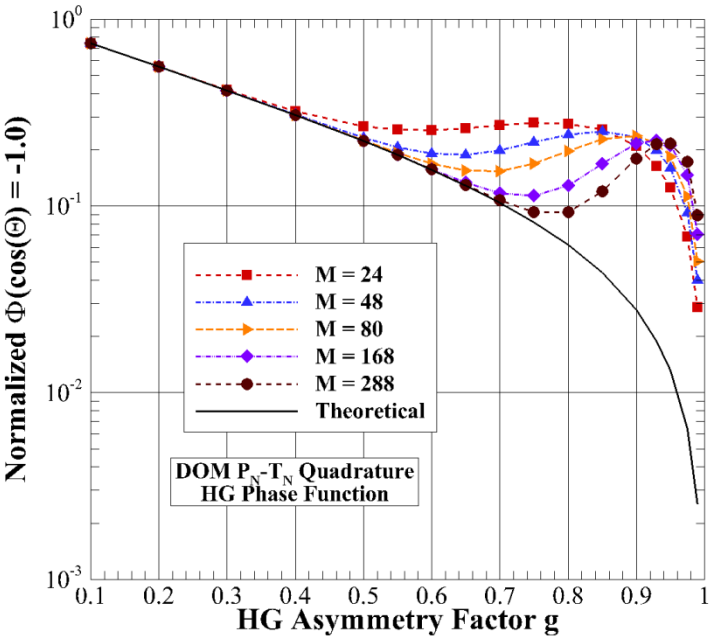

(b)

Figure 6.4: a) Maximum values of backward scattering phase-function normalization parameters and b) normalized backward-scattering discrete phase-function values for various discrete direction numbers versus HG asymmetry factor

The backward-scattering parameters in Figure 6.4a can be in the order of 10 for extremely large g. Looking at Figure 6.4b, parameter values on this order correspond to minor

increases in terms of absolute value change in phase-function. At g = 0.9300, the backward-scattering phase-function value theoretically should be 0.019. After application of the Hunter and Guo's 2014 normalization, this value is increased to 0.179, 0.228, 0.263, 0.301, and 0.309 for the five direction numbers, respectively. While the differences are relatively large, the increased phase-function values are still significantly smaller in magnitude than the forward-scattering peak value for highly-anisotropic scattering. Further, the values are still significantly less than unity, meaning that the impact of such high backward parameters will not be a major concern. It is worth mentioning that Hunter and Guo's 2014 normalization is applicable for backwards-scattering problems where g < 0, with the only difference being that the forward and backward parameters in Figures 6.3a and 6.4a trade values.

6.2.2 Comparison to Monte Carlo and High-Direction FVM

In order to validate use of Hunter and Guo's 2014 normalization for accurate radiation transfer analysis, it is necessary to examine and compare the impact of the various phase-function normalization approaches on actual radiation transfer predictions [Hunter and Guo 2014b]. For this analysis, the benchmark problem involves the 3-D cubic enclosure with a hot wall at z^* = 0, as described for previous analysis of Hunter and Guo's 2012 normalization in Section 5.2.3. As before, the medium is purely scattering (ω = 1.0), has optical thickness τ, and the HG asymmetry factor is taken as g = 0.9300.

Figures 6.5(a-b) present non-dimensional heat fluxes $Q(x^*, y^* = 0.5, z^* = 1.0)$ generated using the DOM with Mishchenko's E, Kamdem Tagne's g, Hunter and Guo's 2012, and Hunter and Guo's 2014 normalization approaches. For this analysis, the optical thickness is τ = 10.0, with reduced optical thickness (1-g)τ = 0.70. DOM results are presented for the P_N-T_N quadrature, with M = 48 and 80 discrete directions implemented in Figures 6.5a and 6.5b,

respectively. As a means of comparison, heat flux profiles generated using both the FVM and MC are also shown. The FVM heat flux was generated using the FT_N-FVM quadrature with M = 2400 discrete directions and (4 x 4) splitting. At this high direction number, the discretized asymmetry factor g = 0.9294, which is very close to the prescribed value of g = 0.9300. The change in scattering effect for the FVM in this case is less than one percent, meaning that angular false scattering should be minimal. The MC heat flux profiles are taken from Boulet et al. [2007], as before.

In Figure 6.5a, results for lower-order M = 48 discrete directions are presented. Heat flux generated using Mishchenko's E normalization, corresponding to a discretized asymmetry factor of g = 0.9373, predict ~4% higher than Hunter and Guo's 2014 normalization, which is consistent with a higher discretized asymmetry factor, as radiant energy more strongly propagates through the medium towards the wall of interest. Conversely, when Kamdem Tagne's g normalization is implemented, heat fluxes are roughly 5% lower than those generated withHunter and Guo's 2014 normalization, corresponding to the underconservation of scattered energy (E = 0.9886).

When comparing Hunter and Guo's 2014 normalization to Hunter and Guo's 2012 normalization, which also conserves both scattered energy and asymmetry factor simultaneously, a maximum discrepancy of just 2.5% is witnessed, with an average difference of 1.4%. For this lower directional order, DOM heat fluxes suffer greatly from ray effect, leading to the differences in heat flux shape when compared to FVM and MC. Heat flux generated with Hunter and Guo's 2014 normalization differs from FVM by between -6.6% and 7.2%, depending on location. It is notable that, while the FVM and MC profiles exhibit similar shapes in general,

they differ by between 2-3% over the range of x^*, due to FVM approximation and MC statistical errors.

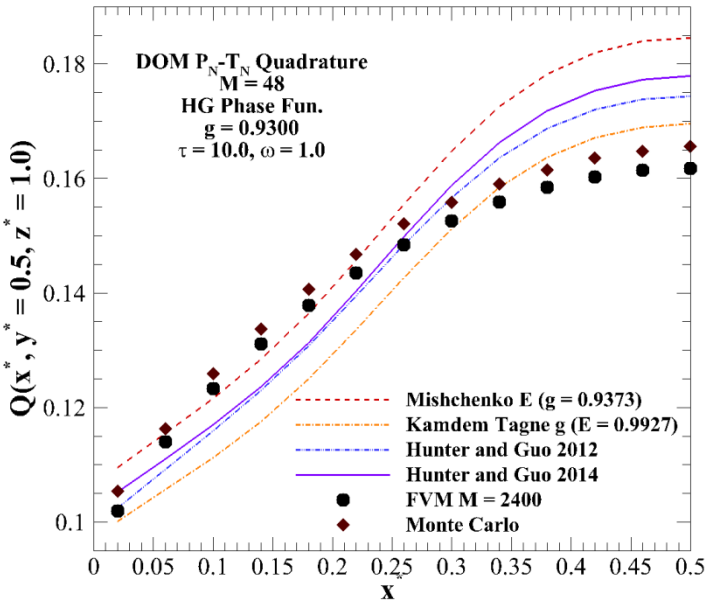

(a)

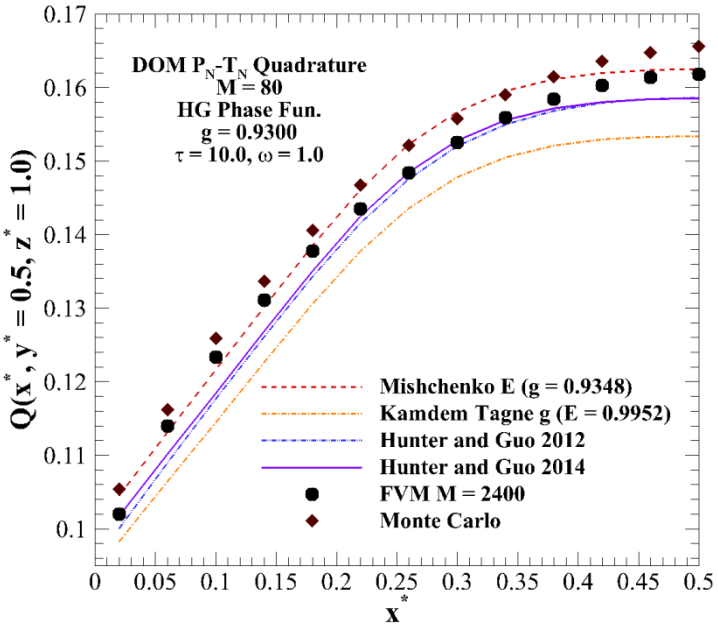

(b)

Figure 6.5: Comparison of Q(x^*, y^* = 0.5, z^* = 1) between DOM solutions generated with various phase-function normalizations and FVM and Monte Carlo predictions using g = 0.9300 with a) M = 48 and b) M = 80

Increase in discrete direction number to M = 80 in Figure 6.5b lessens the impact of ray effect, resulting in DOM heat flux profiles starting to resemble the FVM and MC profiles in general. Use of Mishchenko's E normalization alters the prescribed asymmetry factor to g = 0.9348, resulting in a 2.6% difference when compared to Hunter and Guo's 2014 normalization. The lack of energy conservation in Kamdem Tagne's g normalization results in a differenceof about 3.3%, indicating improvement over Figure 6.5a. The interesting comparison comes when comparing Hunter and Guo's 2014 normalization to Hunter and Guo's 2012 normalization. The differences between these two heat flux profiles are minimal, with an average percent difference of only 0.5%. Additionally, heat flux generated using Hunter and Guo's 2014 normalization conforms fairly accurately to FVM and MC predictions, with average percent differences of 1.5% and 3.7%, respectively.

Figures 6.6a-b analyze the same problem as Figures 6.5a-b, but with increases in discrete direction number to M = 168 and 288, respectively. In Figure 6.6a, an overall reduction in the discrepancies in asymmetry factor and energy conservation for Mishchenko's E and Kamdem Tagne's g normalizations is witnessed. Heat flux generated using Mishchenko's E normalization differs from Hunter and Guo's 2014 normalization by 1.3% on average, corresponding to discretized g = 0.9324. Conversely, Kamdem Tagne's g normalization results in differences of 1.7% on average, corresponding to discretized E = 0.9976.

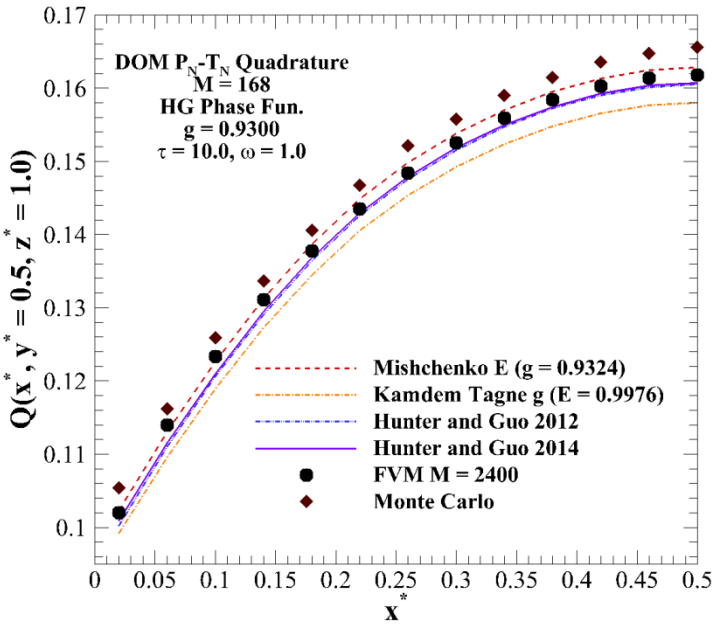

(a)

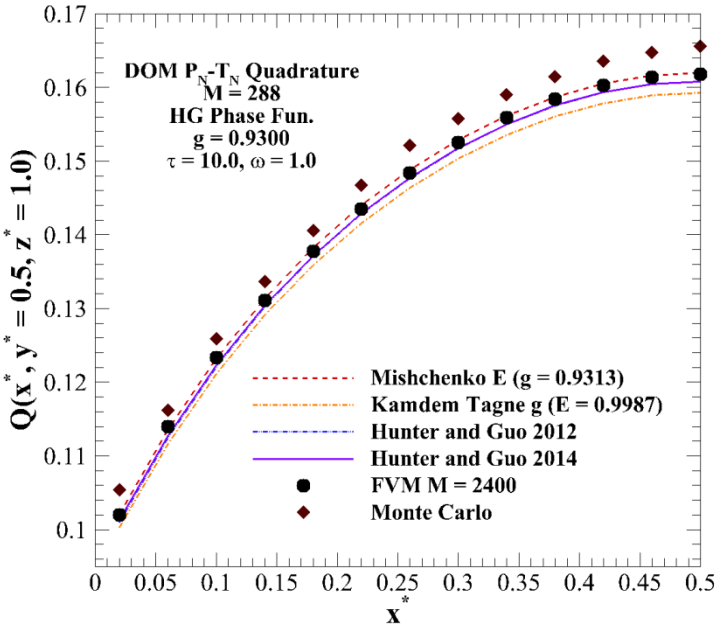

(b)

Figure 6.6: Comparison of Q(x^*, y^* = 0.5, z^* = 1) between DOM solutions generated with various phase-function normalizations and FVM and Monte Carlo predictions using g = 0.9300 with a) M = 168 and b) M = 288

The profiles generated using both Hunter and Guo's 2012 and Hunter and Guo's 2014 normalization are nearly identical, while also conforming accurately to the FVM with large M = 2400 at all locations within 1% on average. This gives extreme confidence that Hunter and Guo's 2014 normalization is able to produce accurate radiation transfer results. Additionally, use of the DOM with normalization presents a distinct advantage in computational efficiency over the extremely high-order FVM. Table 6.2 presents computational convergence times, in minutes, for both the DOM and FVM with varying directional orders versus medium optical thickness. DOM convergence times are presented for Hunter and Guo's 2014 normalization, as times are similar for using other approaches. For M = 168, the DOM using Hunter and Guo's 2014 normalization produces a converged solution in 5.53 minutes, while the FVM with 2400 discrete directions requires 2235 minutes (37.25 hours) to converge. Use of Hunter and Guo's 2014 normalization in conjunction with the DOM reduces computational time by 99.8% without impacting solution accuracy.

A final increase in discrete direction number to M = 288 in Figure 6.6b shows an even greater mitigation of errors between the four normalization approaches. Mishchenko's E normalization (g = 0.9313) and Kamdem Tagne's g normalization (E = 0.9987) differ slightly from Hunter and Guo's 2014 normalization, with an average differences of less than 1%, while Hunter and Guo's 2012 normalization differs less than 0.1% on average. The two normalizations of Hunter and Guo conform extremely accurately (average difference of 0.6%) to the extremely high-direction FVM profile, while providing a distinct advantage in computational efficiency [Hunter and Guo 2014b]. As seen in Table 6.2, while the extremely high-order FVM requires 37.25 hours to converge, the DOM requires only 18.2 minutes.

Table 6.2: Computational convergence times for DOM with Hunter and Guo's 2014 normalization and FVM with minimal solid-angle splitting versus medium optical thickness and discrete direction (a - Convergence time estimated)

Computational Convergence Time (min)				
Method	**M**	**Optical Thickness τ**		
		1.0	10.0	100.0
DOM	48	0.09	0.35	5.19
	80	0.27	1.00	13.7
	168	1.48	5.53	74.5
	288	4.48	18.2	259
FVM	840	36	140	1932
	2400	552	2235	30700[a]

In Figure 6.7, an analysis of the impact of various normalization approaches on radiation transfer in an optically thinner medium is presented. The optical thickness of the medium is taken as τ = 1.0, (1-g)τ = 0.07. DOM Heat fluxes at the far wall centerline are presented for M= 48, 80, and 288 discrete directions, while FVM heat flux with extremely high direction number M = 2400 is also plotted. The asymmetry factor is taken as g = 0.9300. For lower-order DOM (M = 48 and 80), the appearance of physically unrealistic bumps and oscillations in heat flux profiles due to ray effect is substantial. Increase to larger direction number is able to mitigate ray effect errors, and DOM profiles conform accurately to less than 1% on average to the high-order FVM. For all directional orders, profiles generated using Mishchenko's E and Kamdem Tagne's g normalization over- and under-predict Hunter and Guo's normalizations, respectively, mimicking the behaviors from Figures 6.5 and 6.6. However, the thinness of the medium greatly reduces difference between the different normalizations, conforming to the previous results that showed that errors due to skews in E and g after discretization decrease with decreasing optical thickness.

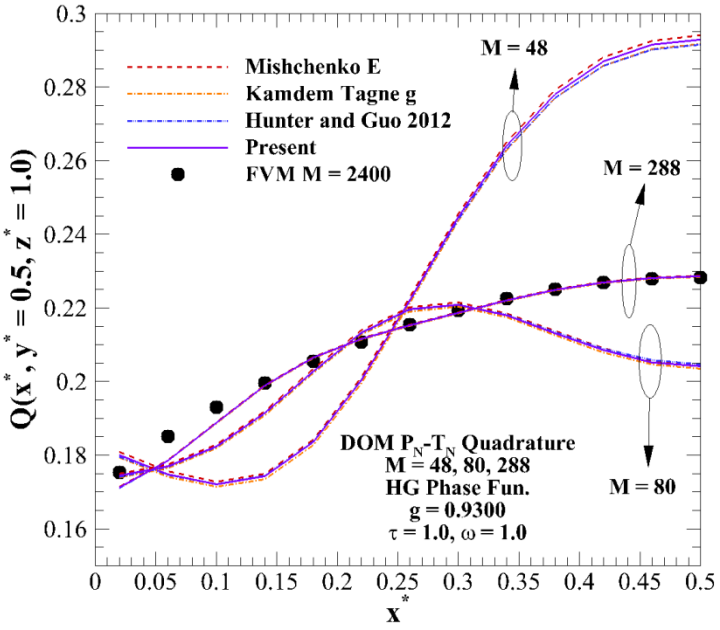

Figure 6.7: Comparison of Q(x*, y* = 0.5, z* = 1) between DOM solutions generated with various phase-function normalizations and FVM predictions using g = 0.9300 with M = 48, 80, and 288 discrete directions in an optically-thinner medium (τ = 1.0)

For many turbid media, such as biological tissue, it is common for the reduced optical thickness (1-τ)g to be >> 1. To this end, Figure 6.8 presents an analysis of the impact of normalization on radiation transfer in an optically-thick medium (τ = 100.0) with prescribed asymmetry factor g = 0.9300. The reduced optical thickness for this medium is 7.0. As a means of validation, FVM heat flux generated using M = 840 discrete directions without normalization and with (8 x 8) solid-angle splitting is also presented. The discretized FVM asymmetry factor at this directional order is g = 0.9280. Increasing the number of FVM directions can improve discretized asymmetry factor, however increase in optical thickness to τ = 100.0 results in a drastic increase in the number of iterations required for convergence from 43 to 590. As seen in Table 6.2, using estimation based on the number of required iterations, use of M = 2400 discrete directions would have required roughly 3 weeks to converge (30,700 minutes). By reducing the

number of FVM discrete directions to M = 840, a converged solution was achieved in 32.2 hours (1932 minutes). By contrast, the DOM with M = 80 produces a converged solution in 13.7 minutes, a reduction of over 99%.

Heat fluxes generated with Mishchenko's E normalization overpredict Hunter and Guo's 2014 normalization, while profiles generated using Kamdem Tagne's g underpredict, similar to the behaviors witnessed in Figures 6.5 and 6.6. However, the large increase in optical thickness has enhanced the impact of scattered energy and asymmetry factor conservation errors. As compared with the FVM, Mishchenko's E normalization overpredicts by an average of 12.6% and 4.3% for M = 48 and 288, respectively. Deviations in scattered energy conservation in Kamdem Tagne's g normalization result in more drastic errors, with underpredictions of 72.0% and 22.3% witnessed for M = 48 and 288. Errors of this magnitude illustrate the criticality of scattered energy conservation for an optically-thick medium, and indicate the impracticality of Kamdem Tagne's g normalization for optically-thick, highly anisotropically-scattering media. Heat fluxes generated using Hunter and Guo's 2014 normalization conform accurately to within 1% of Hunter and Guo's 2012 normalization, and within 2.5% of the higher-direction FVM for all quadratures tested. Additionally, the average difference between Hunter and Guo's 2014 normalization heat fluxes generated using M = 48 and 288 is only 0.70%, indicating that the optically-thick nature of the medium has mitigated ray effect error and that accurate heat fluxes can be achieved with lower-order quadratures. The results from Figures 6.5-6.8 show that ray effect is the dominant source of error for the optically thin media, whereas errors due to lack of E and g conservation dominate for both the optically intermediate and optically thick media.

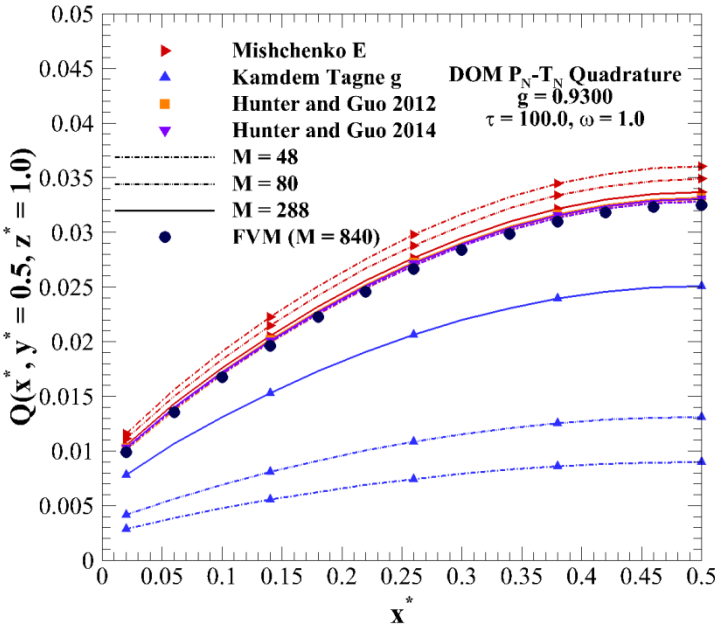

Figure 6.8: Comparison of Q(x*, y* = 0.5, z* = 1) between DOM solutions generated with various phase-function normalizations and FVM predictions using g = 0.9300 with M = 48, 80, and 288 discrete directions in an optically-thick medium (τ = 100.0)

For the HG phase function, Hunter and Guo's 2014 normalization is able to conform accurately to both FVM prediction and DOM prediction generated with the previously introduced Hunter and Guo's 2012 normalization. DOM heat fluxes for which phase-function normalization conserves both E and g simultaneously always lie between the predictions of either conservation alone. While similar heat fluxes are witnessed, Hunter and Guo's 2014 normalization is much simpler to implement, without needing to determine a normalization matrix through pseudo-inversion or least-squares approximation. The mathematical advantage inherent in Hunter and Guo's 2014 normalization make it a desirable technique for determining accurate radiation transfer in highly-anisotropically scattering media.

6.3 Application for DOM with Legendre Phase Functions

6.3.1 Discretized Phase Function Values

In the previous section, Hunter and Guo's 2014 normalization was applied and tested for the HG phase-function approximation, in which the phase-function value changes monotonically with scattering angle. In order to determine the impact of Hunter and Guo's 2014 normalization on oscillatory phase functions that more closely approximate scattering via Mie theory, an analysis of normalization for Legendre-polynomial phase-functions is presented in this section [Hunter and Guo 2014e].

Table 6.3 presents the lack of either scattered energy or asymmetry factor conservation after directional discretization for Mishchenko's E and Kamdem Tagne's g normalizations, as they do not guarantee accurate conservation of both quantities simultaneously. The three prescribed g values correspond to the 9-term g = 0.6697, 26-term g = 0.8189, and 27-term g = 0.9273 Legendre phase-functions originally plotted in Figure 2.4a. E and g values after discretization are tabulated for the DOM EO_N quadrature, with indices N = 4, 6, 8, 10, 12, and 16. Values of E and g are very similar for other DOM quadrature sets, and thus, for brevity, only one quadrature is shown. As an additional means of validation, values without normalization are presented, and percent differences in both E and (1-g) are also tabulated, as in Table 6.1 for the HG phase-function.

For all quadratures and asymmetry factors, Mishchenko's E normalization improves the preservation of phase-function asymmetry factor, while guaranteeing scattered energy conservation. However, the change in scattering effect can be significant, with a maximum of 21% attained for g = 0.9273 with N = 6. Conversely, implementation of Kamdem Tagne's g normalization is able to conserve asymmetry factor accurately, but significant deviations of up

to 1.5% in scattered energy exist. Differences of this magnitude were shown in Figure 6.8 to result in massive radiation transfer errors for optically thick media, and thus they cannot be ignored.

Table 6.3: Scattered energy and/or asymmetry factor values for various normalizations using DOM EO_N quadrature and Legendre phase functions with g = 0.6697, 0.8189, and 0.9273

g	N	No Normalization		Mishchenko E		Kamdem Tagne g	
		Discretized E	Discretized g	Discretized g	% Diff in (1-g)	Discretized E	% Diff in E
0.6697	**4**	1.0075	0.6835	0.6760	1.898	0.9937	0.6269
	6	0.9996	0.6690	0.6694	0.103	1.0003	0.0341
	8	1.0000	0.6697	0.6697	0.000	1.0000	0.0001
	10	1.0000	0.6697	0.6697	0.000	1.0000	0.0000
	12	1.0000	0.6697	0.6697	0.000	1.0000	0.0000
	16	1.0000	0.6697	0.6697	0.000	1.0000	0.0000
0.8189	**4**	4.7249	4.5581	0.8333	7.917	0.9857	1.4335
	6	2.5313	2.3614	0.8302	6.202	0.9888	1.1229
	8	1.9348	1.7580	0.8233	2.396	0.9957	0.4338
	10	1.4546	1.2756	0.8209	1.117	0.9980	0.2023
	12	1.1433	0.9681	0.8248	3.228	0.9942	0.5844
	16	1.0036	0.8232	0.8196	0.369	0.9993	0.0668
0.9273	**4**	4.0767	4.0149	0.9382	14.938	0.9891	1.0856
	6	2.1919	2.1347	0.9428	21.266	0.9845	1.5455
	8	1.7257	1.6592	0.9335	8.507	0.9938	0.6182
	10	1.3079	1.2397	0.9318	6.155	0.9955	0.4473
	12	1.0656	0.9998	0.9342	9.448	0.9931	0.6867
	16	1.0009	0.9285	0.9276	0.343	0.9998	0.0249

When the three mathematically simpler normalizations (Mishchenko's E, Kamdem Tagne's g, and Hunter and Guo's 2014) were applied to the HG phase functions, corrected values of $\widetilde{\Phi}$ were found to be positive for all g values, as shown in Figure 6.3a. For the general Legendre polynomial phase-functions, however, it is found that application of these simpler techniques can, in some cases, lead to either forward- or backward-scattering normalization parameters that are less than -1. This, in turn, leads to physically unrealistic negative values in the normalized phase-function. Table 6.4 lists all of the quadrature schemes and direction numbers for the three Legendre phase-functions where backward normalization parameters of

less than -1 occur for Hunter and Guo's 2014 normalization. For non-listed quadrature schemes and directional orders, backward parameters of <1 were not encountered.

In Figures 6.9(a-b), discretized Legendre phase-function values versus scattering angle cosine generated with Mishchenko's E, Kamdem Tagne's g, Hunter and Guo's 2012, and Hunter and Guo's 2014 normalizations are plotted against the theoretical phase-function values for two cases: the EO_8 quadrature with g = 0.8189, and the EO_{16} quadrature with g = 0.9273.

Table 6.4: List of minimum backward-scattering parameters for normalization of Legendre phase-functions for diffuse radiation using Hunter and Guo's 2014 technique

Quadrature	N	g	Minimum Backward Parameters
P_N-T_N	12	0.9273	-6.659
	16	0.9273	-8.104
S_N	6	0.6697	-1.259
	12	0.9273	-22.71
	16	0.6697	-3.954
	16	0.8189	-3.035
	16	0.9273	-15.99
EO_N	6	0.6697	-1.063
	16	0.8189	-13.49
	16	0.9273	-304.5
EQ_N	16	0.9273	-3.911

In Figure 6.9a, all four normalizations produce similar phase-function values after discretization at most locations, except at the forward- and backward-directions. At $\cos\Theta$ = -1, the impact of the backward-scattering normalization parameters is clearly seen for Hunter and Guo's 2014 normalization, as the phase-function values are skewed to a much higher value. Of more importance, however, is the behavior at $\cos\Theta$ = 1. The inlay in Figure 6.9a shows that the three simpler normalizations result in negative phase-function values in the forward direction, indicating that for Legendre polynomial phase-functions, normalization of solely the forward/backward term(s) might be unsuitable.

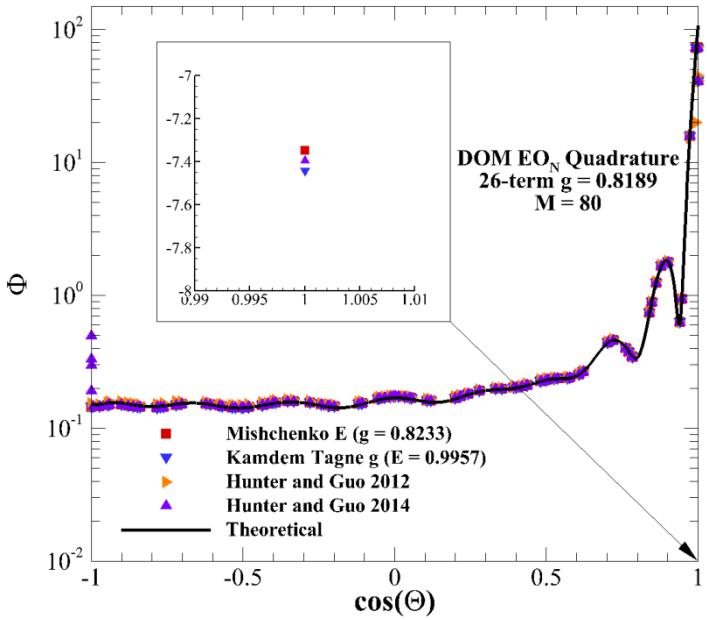

(a)

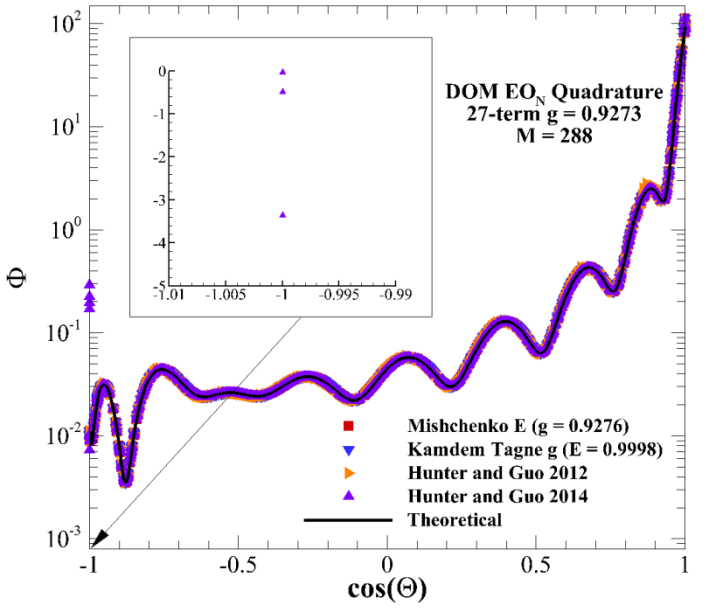

(b)

Figure 6.9: Discretized Legendre phase-function values after normalization using various techniques with a) M = 80 and g = 0.8189, and b) M = 288 and g = 0.9273

In Figure 6.9b, no negative phase-function values are seen for the forward scattering direction. However, as seen in the inlay, large differences between the discretized values

generated with Hunter and Guo's 2014 normalization and the theoretical are witnessed for $\cos\Theta$ = -1, with multiple directions being altered to a negative phase-function value. This error is not present for Mishchenko's E or Kamdem Tagne's g normalization, as they do not involve backward-scattering normalization. Additionally, the negative values for the backward-scattering term are of much lower magnitude than for forward-scattering in Figure 6.9a.

In Figure 6.10, the minimum values of forward-scattering normalization parameter are plotted for the principal octant directions using the EO_8 quadrature with g = 0.8189 for the four normalization techniques. For all 10 principal octant directions, forward parameters for Mishchenko's E, Kamdem Tagne's g, and Hunter and Guo's 2014 normalizations are nearly identical, as witnessed for the HG phase function in Figures 6.1 and 6.2. Parameters of less than -1 occur for three directions, which will result in negative phase-function values. For all but those three directions, Hunter and Guo's 2012 normalization produces nearly identical forward-parameters to the other three approaches. However, for those three directions, Hunter and Guo's 2012 normalization parameters are greater than -1, avoiding the critical issue of negative phase function values. For all other combinations of phase-functions and quadratures, forward-scattering parameters of less than -1 were not witnessed [Hunter and Guo 2014e].

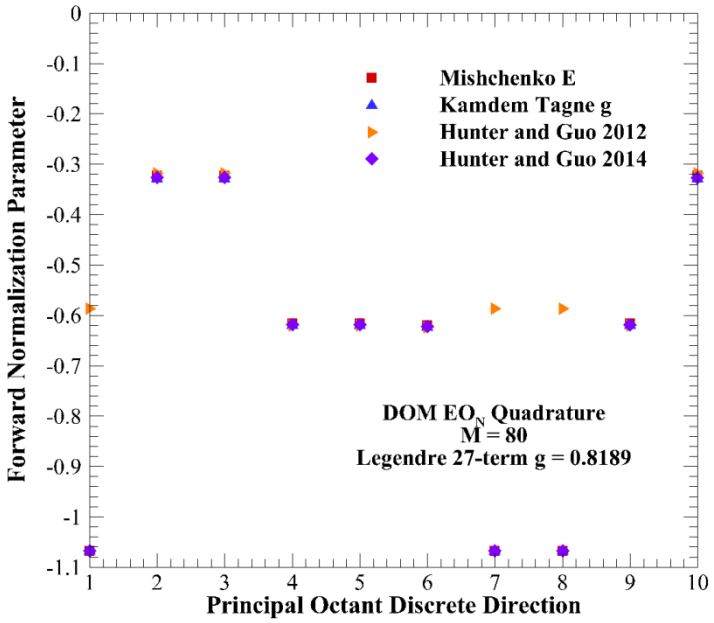

Figure 6.10: Comparison of minimum forward-scattering diffuse radiation normalization parameter using various normalization techniques for the DOM EO_N quadrature with M = 80 and g = 0.8189

6.3.2 Comparison to High-Direction FVM

The appearance of negative phase-function values in the three simpler normalization approaches is a potentially critical issue for determination of accurate radiation transfer using the DOM [Hunter and Guo 2014e]. In order to investigate the impact of negative phase-function values, radiation transfer in the benchmark cubic enclosure with one hot wall at $z^* = 0$ is investigated in this section. All properties are identical to those described earlier in the chapter for the HG phase-function approximation.

During simulation, it was found that negative phase-function values resulted in negative intensity values regardless of spatial differencing scheme, which are extremely unrealistic. Negative intensities tend to occur early in the simulation for a cold medium (where the initial intensity is 0 everywhere except for the hot wall), and disappear as radiant energy propagates

away from the wall. This issue does not occur for every case where forward- or backward-parameters result in negative phase-function values, as factors such as DOM quadrature weighting factors and optical properties play a large role in the intensity values generated from iterative solution of the ERT. However, when intensities do become negative, the solution diverges at the next iteration in the solution procedure, and thus a convergent intensity field cannot be generated. As a means of correcting this issue, the positive scheme [Modest 2002] for negative intensity correction must be implemented, where any negative intensities are set to zero immediately after they are encountered in the calculation.

In Figures 6.11(a-b), non-dimensional heat fluxes Q are calculated using the DOM with the four normalization approaches previously described. The medium optical thickness is taken as τ = 10.0. Results are generated in Figure 6.11a for the EO_8 quadrature with g = 0.8189, and in Figure 6.11b for the EO_{16} quadrature for g = 0.9273. As a means of comparison, FVM heat flux profiles generated using the FT_N-FVM quadrature with M = 840 and (8 x 8) splitting are also plotted, for which scattered energy and asymmetry factor are conserved within 10^{-4}% and 0.25%, respectively, for both phase-functions without application of normalization.

In Figure 6.11a, negative forward-parameters were encountered for the three simpler normalizations. These negative forward-parameters result in negative intensities, mandating the use of negative intensity correction. As Hunter and Guo's 2012 normalization does not require such a correction, it is taken as a validation basis for DOM results. Heat fluxes generated with Hunter and Guo's 2014 normalization with negative intensity correction conform accurately within 1.5% to those generated using Hunter and Guo's 2012 normalization at both y^* locations presented. When Mishchenko's E normalization is implemented, heat fluxes differ from Hunter and Guo's 2012 normalization by ~3%. Conversely, heat fluxes generated using

Kamdem Tagne's g normalization differ by ~5%. When compared to FVM, the four normalizations differ by maximums of 9.0% and 5.5% for y^* = 0.1 and 0.5, respectively. Considering that a low direction number (M = 80) was used to determine the DOM heat fluxes, these are acceptable differences [Hunter and Guo 2014e].

Due to the large absolute values of the backward-scattering normalization parameters in Hunter and Guo's 2014 normalization, it is of interest to examine normalized heat fluxes at the source/hot wall, or $Q(x^*, y^*, z^* = 0)$, in order to determine if large negative parameters result in a significant change in heat flux flowing back into the hot wall. From Figure 6.11b, it is witnessed that results generated using Hunter and Guo's 2014 normalization conform to Hunter and Guo's 2012 normalization and higher-order FVM within 0.2% at all locations. When Mishchenko's E and Kamdem Tagne's g normalizations are implemented, differences are slightly larger (less than 0.5% at maximum). These results indicate that the highly-negative backward-scattering parameters do not have an appreciable impact on transfer predictions at the hot wall [Hunter and Guo 2014e].

Figures 6.12(a-b) present an analysis of the impact of normalization on heat fluxes at the hot wall (Figure 6.12a) and far wall (Figure 6.12b) in an optically thick medium, with τ = 100.0, for the EO_{16} quadrature with g = 0.9273. While DOM profiles generated using the other three normalizations conform to within 2% of each other and within 7% to higher-order FVM at the far wall, and within 1% and 4% at the hot wall, the slight lack of energy conservation inherent in Kamdem Tagne's g normalization results in much larger errors in heat flux, of up to 18% as compared with Hunter and Guo's 2012 normalization at the far wall. Analysis of the optically-thick case indicates the absolute necessity of conserving scattered energy after discretization.

Conversely, small discrepancies in asymmetry factor inherent in Mishchenko's E normalization have only a minimal impact on radiation transfer results.

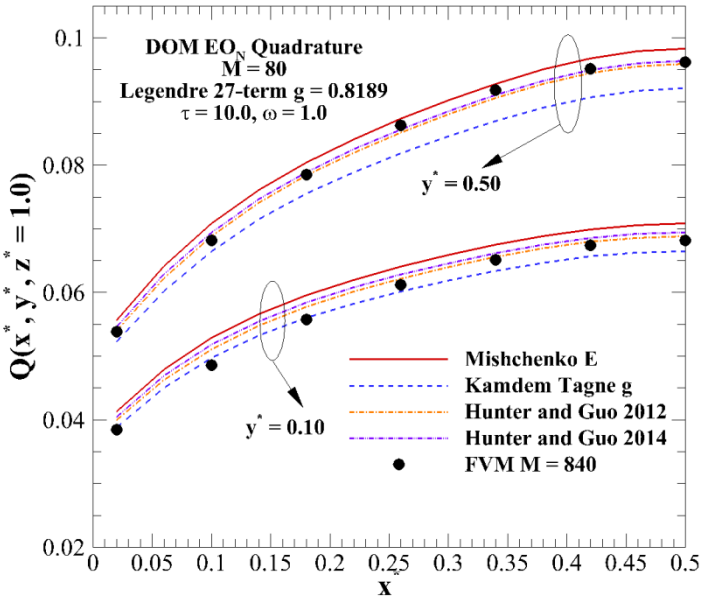

(a)

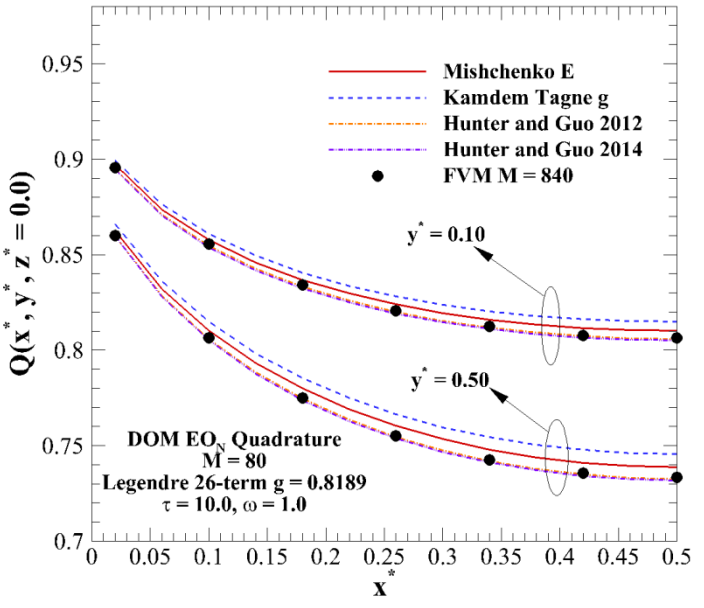

(b)

Figure 6.11: Comparison of heat fluxes generated with FVM and various DOM diffuse radiation normalization techniques: a) $Q(x^*, y^*, z^* = 1.0)$ with M = 80 and g = 0.8189; b) $Q(x^*, y^*, z^* = 0.0)$ with M = 288 and g = 0.9273

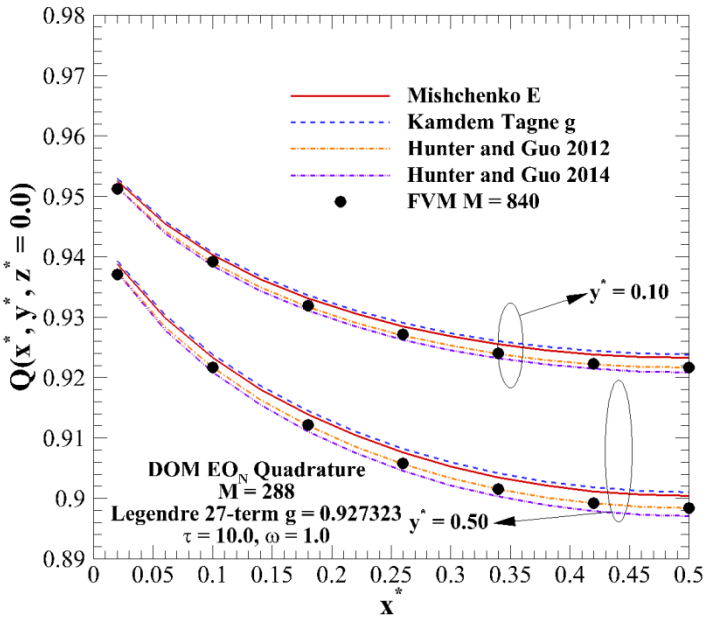

(a)

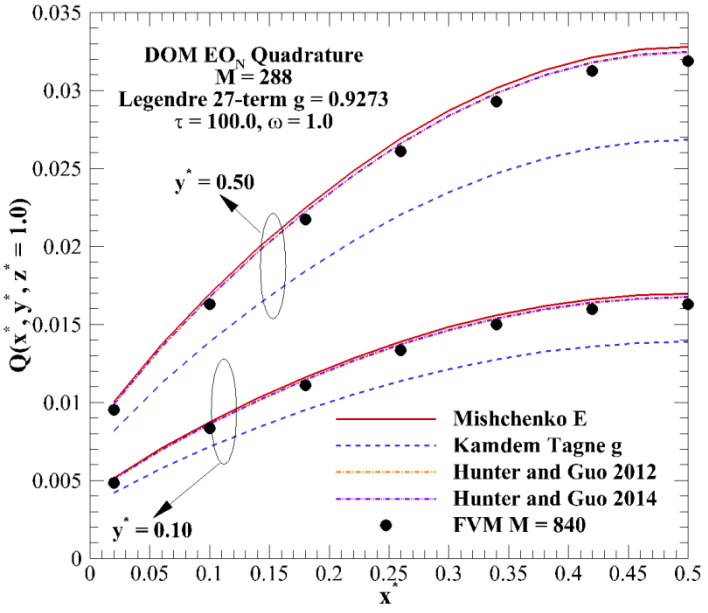

(b)

Figure 6.12: Comparison of a) heat flux Q(x^*, y^*, z^* = 0.0) and b) heat flux Q(x^*, y^*, z^* = 1.0) profiles generated with FVM and various DOM diffuse radiation normalization techniques with M = 288 and g = 0.9273 in an optically thick medium

In general, the results in Figs. 6.11-6.12 show that even though Hunter and Guo's 2014 normalization can result in negative Legendre phase function values in some cases, radiation

transfer predictions are largely unaffected as long as a negative-intensity correction is put in place. Thus, due to its relative simplicity and ability to conserve both scattered energy and asymmetry factor after directional discretization, Hunter and Guo's 2014 normalization is a viable, efficient, and accurate tool for modeling radiation transfer in highly anisotropic scattering media [Hunter and Guo 2014e].

6.4 Summary

In this chapter, a second phase-function normalization technique (called Hunter and Guo's 2014 normalization) that accurately conserves both scattered energy and asymmetry factor after discretization is developed for use with the DOM. This new phase-function normalization technique draws on the ideas presented by Mishchenko et al. and Kamdem Tagne, who developed mathematically simple normalizations to conserve one of the two quantities, but not both. Hunter and Guo's 2014 normalization adjusts the values of both the forward- and backward-scattering phase-function terms, leaving all other terms unaffected. Normalization in this manner differs from Hunter and Guo's 2012 normalization, which accurately conserved both quantities by normalizing every discrete phase-function value in the system.

The values of both forward- and backward-scattering phase function terms application of Hunter and Guo's 2014 normalization were presented for both the HG and Legendre phase-function approximation. For the HG, forward-scattering parameters are always greater than -1, and backward parameters are always positive. Some backward-scattering parameters have a large magnitude (up to 45) for the HG phase-function, although these parameters do not impact radiation transfer predictions. It is seen that radiation transfer predictions generated with Hunter and Guo's 2014 normalization conform accurately to MC, FVM, and DOM predictions

generated with Hunter and Guo's 2012 normalization. Mishchenko's E and Kamdem Tagne's g normalizations result in more significant errors, especially for optically thick media.

For Legendre phase-functions, both forward-scattering and backward-scattering normalization parameters in Hunter and Guo's 2014 normalization can attain values of less than -1, resulting in negative phase-function values. This phenomenon for forward-scattering normalization parameters also occurs for Mishchenko's E and Kamdem Tagne's g normalization, but not for Hunter and Guo's 2012 normalization. It is found that these negative parameters mandate the necessity of using a negative-intensity corrective procedure, in order to obtain convergent solutions of the ERT. If such a correction is implemented, Hunter and Guo's 2014 normalization results in accurate heat flux profiles with respect to FVM and Hunter and Guo's 2012 normalization.

All in all, while it does suffer from the mathematical shortcoming of negative phase-function values, and it requires a negative intensity corrective procedure, Hunter and Guo's 2014 normalization is still a viable alternative to generating accurate radiative heat transfer predictions. The simplicity of implementation over Hunter and Guo's 2012 normalization, which requires matrix solution, makes it a desirable tool for DOM simulation.

CHAPTER 7 : PHASE-FUNCTION NORMALIZATION FOR BALLISTIC RADIATION

7.1 Normalization for Ballistic Radiation in DOM

7.1.1 Ballistic Scattered Energy and Asymmetry Factor Conservation

For problems involving the ultrafast propagation of ballistic radiation [Guo and Hunter 2013], extra care must be taken to ensure that the scattering phase-function for ballistic radiation $\Phi^{l^B l}$ satisfies out-scattered energy and asymmetry factor conservation, in addition to the diffuse counterpart [Hunter and Guo 2012c, Hunter and Guo 2014c]. In order to ensure that ballistic out-scattered energy and asymmetry factor are satisfied, the following constraints on $\Phi^{l^B l}$ must hold after directional discretization, for discrete direction $\hat{\boldsymbol{s}}^{\boldsymbol{l}}$ [Hunter and Guo 2012c]:

$$\frac{1}{4\pi}\sum_{l=1}^{M}\Phi^{l^B l}\,w^l = 1 \tag{7.1a}$$

$$\frac{1}{4\pi}\sum_{l=1}^{M}\Phi^{l^B l}\cos\Theta^{l^B l}\,w^l = g \tag{7.1b}$$

In Eq. 7.1b, $\Theta^{l^B l}$ is the scattering angle between the direction of ballistic incidence $\hat{\boldsymbol{s}}^{\boldsymbol{l^B}}$ and discrete direction $\hat{\boldsymbol{s}}^{\boldsymbol{l}}$.

Consider ballistic incidence propagating through a participating medium in ballistic radiation direction $\hat{\boldsymbol{s}}^{\boldsymbol{l^B}}$. The direction of ballistic incidence, in some cases, will correspond directly to one of the prescribed DOM quadrature directions, as shown on the left-hand side of Figure 7.1. However, it is quite common that the direction of ballistic or collimated incidence will differ from the DOM quadrature, as shown on the right-hand side of Figure 7.1. Thus,

additional treatment to ensure that ballistic out-scattered energy and asymmetry factor are conserved accurately after directional discretization is required.

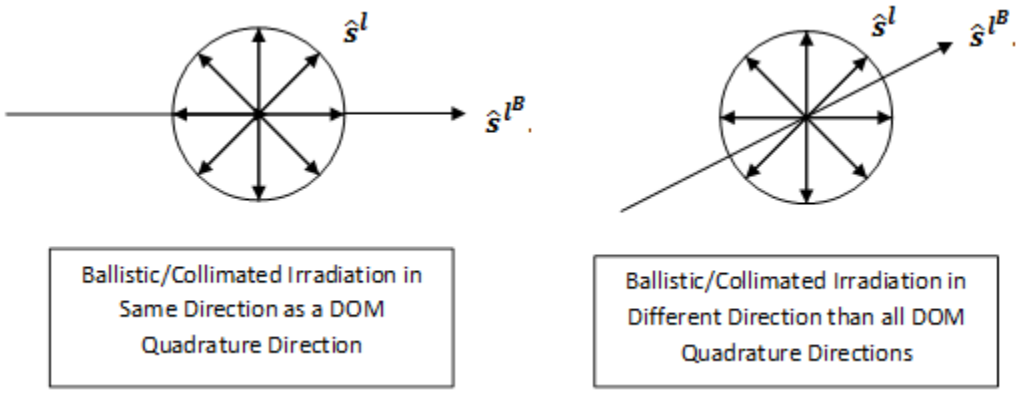

Figure 7.1: Illustration of ballistic direction relation to DOM quadrature directions

A preliminary indication of the necessity of ballistic normalization is presented in Figures 7.2(a-b), in which the conservation of ballistic out-scattered energy is examined versus prescribed HG asymmetry factor for the DOM S_N quadrature [Hunter and Guo 2012e]. The number of discrete directions is varied between M = 24, 80, and 168. Additionally, the direction of ballistic incidence is varied, in order to gauge the effect of incident direction on ballistic out-scattered energy and asymmetry factor conservation. While ballistic incidence does not have to be restricted to a single collimated direction (i.e., a cone of ballistic incidence), collimated incidence is investigated here in order to more clearly present the findings. The azimuthal angle of incidence ϕ_i is varied between 0° (Figure 7.2a) and 45° (Figure 7.2b), while the polar angle of incidence θ_i is taken as 0 (normal incident direction), 10, 30, 45, and 75°, respectively.

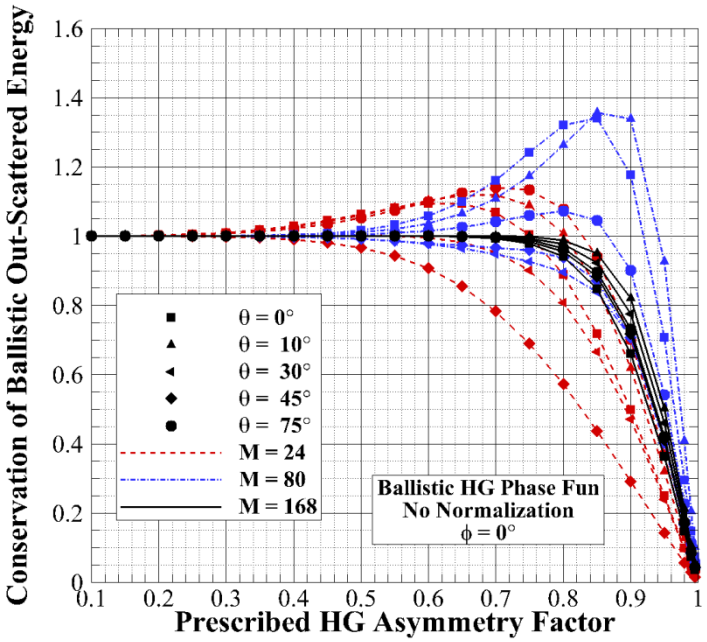

(a)

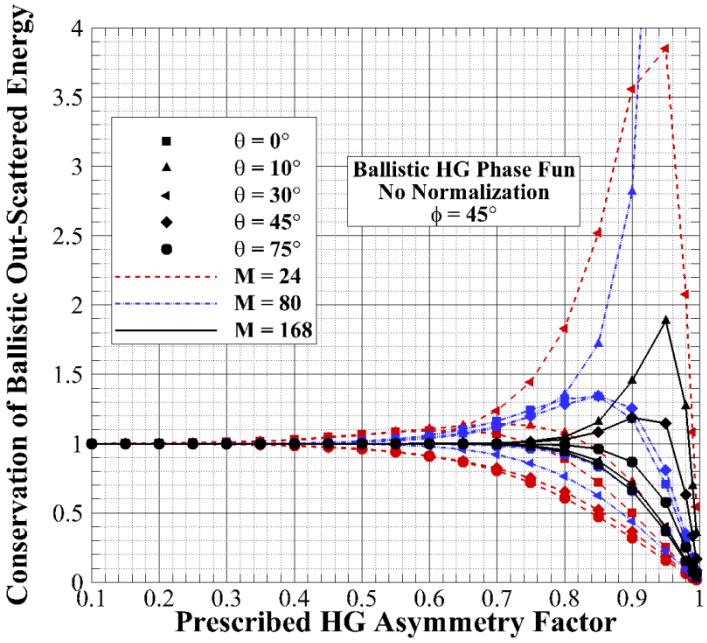

(b)

Figure 7.2: Examination of conservation of ballistic out-scattered energy vs. prescribed HG asymmetry factor for various quadrature sets and ballistic polar angles for ballistic azimuthal angle a) $\phi = 0°$ and b) $\phi = 45°$.

In Figure 7.2a, significant deviations (1% or greater) in the conservation of ballistic out-scattered energy start to appear for $g \geq 0.30$ for M = 24, while deviations for M = 80 and 168 reach >1% for $g \geq 0.45$ and 0.75, respectively. As the prescribed HG asymmetry factor increases further, out-scattered energy becomes extremely non-conserved for all direction numbers and incident angles, with the value of the summation in Eq. (7.1a) plummeting towards zero for extreme-forward scattering. Additionally, it is seen that the polar angle of incidence has a large impact on the conservation of out-scattered energy. For M = 24, deviation from out-scattered energy conservation at g = 0.50 is 6.34% for normal incidence, but less than 0.2% for $\theta_i = 30°$. For M = 80 at g = 0.50, deviations for the same two incident angles are 1.7% and $4*10^{-4}$%, respectively. These differences in out-scattered energy conservation for varying ballistic incident directions stem from the approximation of the continuous angular variation of radiation scattering with the discrete quadrature set. As the number of directions increases, the impact of ballistic incident direction decreases dramatically, due to improved angular discretization.

Similar patterns are witnessed for $\phi_i = 45°$ in Figure 7.2b. Deviations in ballistic out-scattered energy conservation start to become significant at roughly the same asymmetry factors as for $\phi_i = 0°$, with deviations greater than 1% occurring for $g \geq 0.30$, 0.50, and 0.70 for M = 24, 80, and 168, respectively. While the overall pattern in ballistic out-scattered energy conservation is similar to that shown in Figure 7.2a, some significant differences are noticed. For example, for $g \geq 0.90$, massive differences from conservation are witnessed for $\theta_i = 10°$. For g = 0.95, percent differences reach ~90% and ~290% for M = 288 and 24, respectively, while for M = 80, the difference reaches greater than 400%, and it thus not shown in the figure. The results in Figures 7.2(a-b) indicate two important concepts: 1) ballistic out-scattered energy is

not accurately conserved for highly anisotropic scattering and 2) ballistic incident angle has an extremely large impact on out-scattered energy conservation [Hunter and Guo 2012e].

One method of conserving ballistic out-scattered energy is to apply a phase-function normalization approach, similar to that devised for diffuse radiation in Eq. (4.10) [Hunter and Guo 2012c, Hunter and Guo 2012e]. Applying such an approach, the ballistic scattering phase function $\Phi^{l^B l}$ can be normalized in the following manner, to accurately conserve Eq. (7.1a) after directional discretization:

$$\widetilde{\Phi}^{l^B l} = \Phi^{l^B l} * \left(\frac{1}{4\pi} \sum_{l=1}^{M} \Phi^{l^B l} w^l \right)^{-1} \tag{7.2}$$

While Eq. (7.2) will accurately guarantee ballistic out-scattered energy conservation, the formulation may not accurately conserve ballistic asymmetry factor (i.e., Eq. (7.1b) may be violated after application), similar to the discussion in Chapter 4 for diffuse radiation.

The conservation of ballistic asymmetry factor after application of Eq. (7.2), which we will call "Ballistic Scattered Energy Averaging", is investigated in Figures 7.3(a-b). Conservation ratios are again plotted versus prescribed HG asymmetry factor and for varying polar and azimuthal incident angles. In Figure 7.3a, corresponding to azimuthal incident angle $\phi_i = 0°$, extreme deviations from ballistic asymmetry factor conservation are witnessed for all quadrature sets and polar angles as prescribed g increases. For M = 24, deviations of >1% are witnessed for g as small as 0.15, while for M = 80 and 168, deviations of >1% first appear for g = 0.45 and 0.80, respectively. The impact of polar angle is large for lower discrete direction number, with deviations in asymmetry factor ranging from +5.51% to -13.2% for g = 0.70 for M = 24, depending on polar incident angle. The differences caused by changes in incident angle reduce, but do not disappear, with increase in discrete direction number.

As the azimuthal angle of incidence is changed to $\phi_i = 45°$ in Figure 7.3b, the overall trends are similar to those in Figure 7.3a. However, the change in azimuthal angle has greatly impacted asymmetry factor conservation at the various polar angles. The largest change is witnessed for M = 168, where deviations in conservation range from +5.8% at $\theta_i = 0°$ to -3.6% at $\theta_i = 10°$ for g = 0.90.

Noticeable differences are also witnessed when comparing results for specific θ_i between the two azimuthal angles in Figures 7.3(a-b). For example, the discretized asymmetry factor for $\theta_i = 75°$ underpredicts the prescribed value for all g for M = 24 and $\phi_i = 45°$. However, for $\phi_i = 0°$, the results are quite different, with discretized asymmetry factor overpredicting the prescribed value for g < 0.80, and underpredicting for g > 0.80. The results in these two figures show that ballistic scattered energy averaging is not able to accurately conserve ballistic asymmetry factor, and that the direction of ballistic incidence is important.

Further investigations of the impact of ballistic incident direction are presented in Figures 7.4 and 7.5, in which contours of percent difference between discretized and prescribed ballistic asymmetry factor after application of Eq. (7.2) to conserve ballistic out-scattered energy are presented with respect to both azimuthal and polar angle of incidence. Results are presented for the Legendre g = 0.8189 phase-function approximation, with M = 80 and 168 discrete directions implemented for Figures 7.4 and 7.5, respectively. In both figures, the polar (θ_i) and azimuthal (ϕ_i) angles of ballistic incidence are varied between $0 \leq \theta_i, \phi_i \leq 90°$, as the results for the other octants are identical, due to DOM directional symmetry. It should be mentioned that contour plots for both the Legendre and HG phase-function approximations are similar, and thus only Legendre are shown, for brevity.

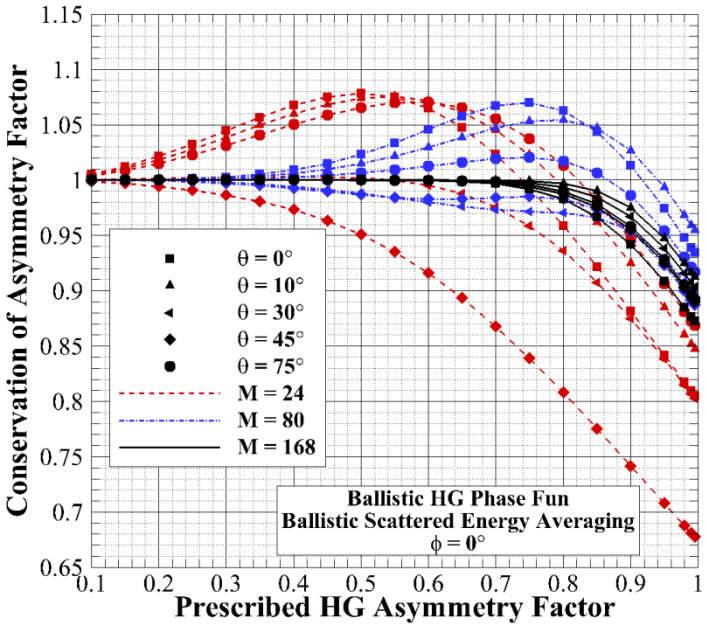

(a)

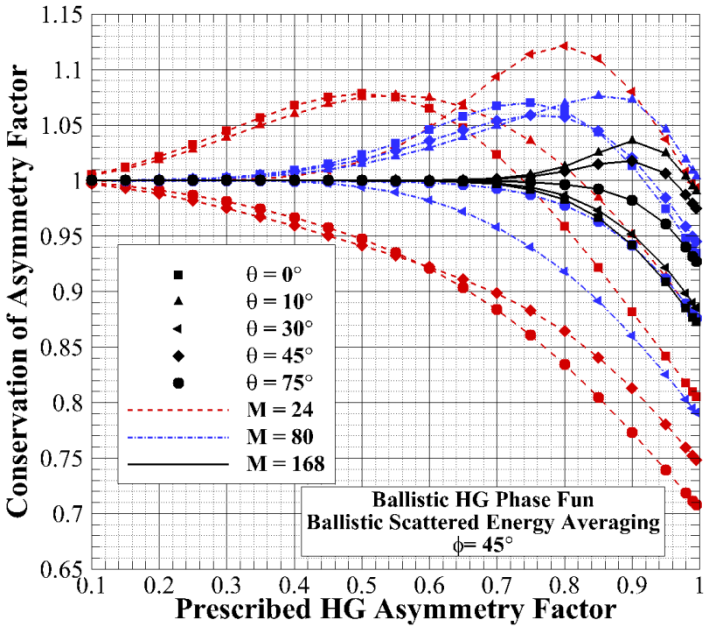

(b)

Figure 7.3: Examination of conservation of ballistic asymmetry factor vs. prescribed HG asymmetry factor for various quadrature sets and ballistic polar angles for ballistic azimuthal angle a) $\phi = 0°$ and b) $\phi = 45°$ after application of ballistic scattered energy averaging

For the Legendre g = 0.8189 phase-function in Figure 7.4, the percentage difference between discretized and prescribed ballistic asymmetry factor ranges between 0.001% and 58.2%, depending on the exact direction of ballistic incidence. For some ballistic incident directions, asymmetry factor is effectively conserved after application of Eq. (7.2), while for others, the skew in phase-function values is extreme. Overall, the average error in ballistic asymmetry factor is 11%. At a fixed azimuthal angle of 45°, the percentage differences range between 0.2% at θ = 81.6° and 58.2% at θ = 33.7°, which indicates that small changes in angle can significantly alter the scattering properties of the ballistic incidence, and mandates the necessity of maintaining accurate asymmetry factor conservation [Hunter and Guo 2012e].

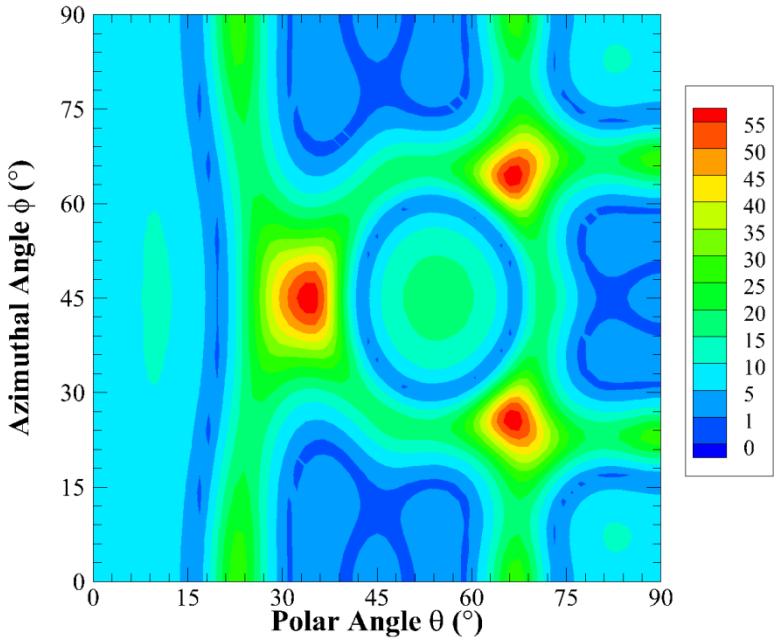

Figure 7.4: Percentage difference of discretized ballistic phase-function asymmetry factor versus azimuthal and polar angle of ballistic incidence with Legendre g = 0.8189 and M = 80

An increase in discrete direction number to M = 168 in Figure 7.5 greatly improves the differences between prescribed and discretized ballistic asymmetry factor. The maximum

difference is only 8.4%, as compared with 58.2% for M = 80 in Figure 7.4. Interestingly, the maximum differences in Figure 7.5 correspond to the extremes in polar or azimuthal angle (either 0 or 90°), while the maximum differences in Figure 7.4 occurred for much different angular combinations. In general, the increase in discrete direction number has improved the conservation of asymmetry factor for all ballistic incident directions over the values witnessed in Figure 7.4, although accurate conservation of Eq. (7.2b) is still not attained.

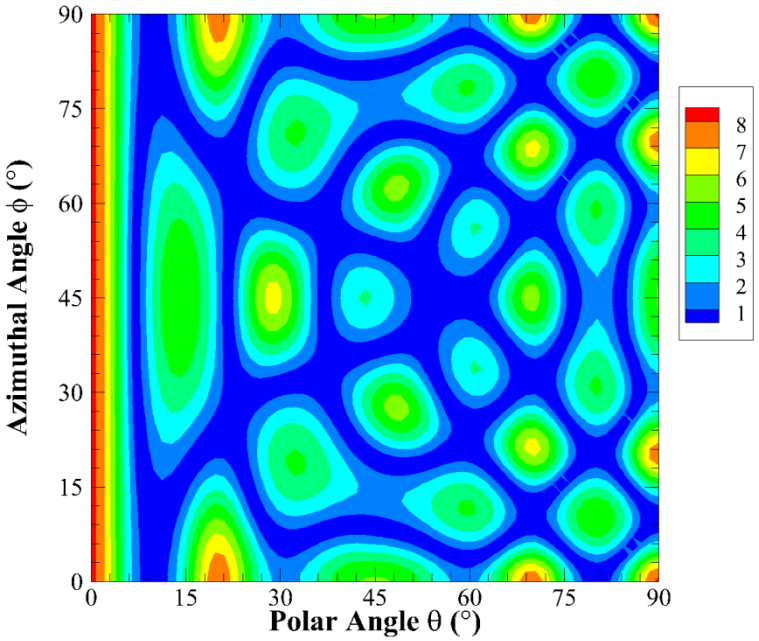

(a)

Figure 7.5: Percentage difference of discretized ballistic phase-function asymmetry factor versus azimuthal and polar angle of ballistic incidence with Legendre g = 0.8189 and M = 168

As seen previously for diffuse radiation in Chapter 4, inaccurate conservation of asymmetry factor can lead to significant errors in radiation transfer due to angular false scattering. Thus, to limit this source of error for ballistic radiation, a ballistic normalization approach that conserves both Eqs. (7.1a-b) simultaneously is desired [Hunter and Guo 2012c].

7.1.2 Hunter and Guo's 2012 Normalization for Ballistic Radiation

7.1.2.1 Mathematical Formulation

In order to ensure that ballistic out-scattered energy and ballistic asymmetry factor are accurately maintained after directional discretization, a modification of Hunter and Guo's 2012 normalization for diffuse radiation presented in Chapter 5 can be implemented to normalize $\Phi^{l^B l}$. This normalization approach for ballistic radiation is formulated as follows [Hunter and Guo 2012c, Hunter and Guo 2012e, Hunter and Guo 2014c]:

$$\widetilde{\Phi}^{l^B l} = \left(1 + A^{l^B l}\right)\Phi^{l^B l} \tag{7.3}$$

where the ballistic normalization parameters $A^{l^B l}$ are taken such that $\widetilde{\Phi}^{l^B l}$ satisfies Eqs. (7.1a-b) simultaneously, as follows:

$$\frac{1}{4\pi}\sum_{l=1}^{M} \widetilde{\Phi}^{l^B l}\, w^l = 1 \tag{7.4a}$$

$$\frac{1}{4\pi}\sum_{l=1}^{M} \widetilde{\Phi}^{l^B l} \cos\Theta^{l^B l}\, w^l = g \tag{7.4b}$$

As for diffuse radiation, the system comprised of Eqs. (7.3)-(7.4) is underdetermined, with M unknowns and 2 equations. Thus, QR factorization or least-squares can be implemented to determine the normalization parameters $A^{l^B l}$ that solve the system with the minimum norm.

It is important to mention that the ballistic normalization parameters $A^{l^B l}$ are, in general, independent of the diffuse normalization parameters $A^{l' l}$. If the direction of ballistic incidence $\hat{\boldsymbol{s}}^{\boldsymbol{l^B}}$ is identical to one of the predetermined DOM quadrature directions $\hat{\boldsymbol{s}}^{\boldsymbol{l'}}$, the

ballistic normalization parameters $A^{l^B l}$ will be identical to the diffuse normalization parameters $A^{l' l}$ generated for quadrature direction $\hat{\boldsymbol{s}}^{\boldsymbol{l}'}$ using Eqs. (5.1)-(5.2). Thus, for this case, while ballistic normalization is still required, the parameter will already be known from application of Hunter and Guo's 2012 normalization for diffuse radiation. When the direction of ballistic incidence does not match a DOM quadrature direction, the additional mathematics to solve the ballistic system of Eqs. (7.3)-(7.4) are required in order to minimize/eliminate angular false scattering errors in ballistic radiation transfer.

Use of this normalization approach to correct the ballistic scattering phase-function was first implemented in 2011, first published in 2012 [Hunter and Guo 2012c, Hunter and Guo 2012e], and expanded on recently [Hunter and Guo 2014e]. Hence, for future reference in this dissertation, this approach will be termed "Hunter and Guo's 2012 ballistic normalization".

7.1.2.2 Impact on Radiation Transfer Results

A preliminary investigation of the impact of phase-function normalization for ballistic radiation using the DOM is presented in Figure 7.6 [Hunter and Guo 2012e], in which radiative heat transfer in a benchmark, cold-walled cubic enclosure containing a cold medium irradiated at z^* = 0 by a normal, collimated incidence of unity intensity is examined. Heat fluxes in Figure 7.6 are analyzed at the centerline of the wall opposite the collimated intensity, i.e. $Q(x^*, y^* = 0.5, z^* = 1.0)$. The optical thickness and scattering albedo of the participating medium are $\tau = \omega = 1.0$, and the HG asymmetry factor is varied between g = 0.2000, 0.8000, and 0.9300. The spatial grid is taken as (27 x 27 x 27) for all simulations. DOM heat fluxes are presented for three different ballistic normalization cases: 1) no ballistic normalization, 2) ballistic out-scattered energy conservation using ballistic scattered energy averaging, and 3) Hunter and Guo's 2012 ballistic normalization. In addition to DOM predictions using M = 168, reference

Monte Carlo solutions presented by Collin et al. [2011] are also shown, to gauge DOM accuracy. For all cases, $\Phi^{l'l}$ is normalized using Hunter and Guo's 2012 normalization, as outlined in Chapter 5, in order to gauge angular false scattering errors solely due to ballistic normalization.

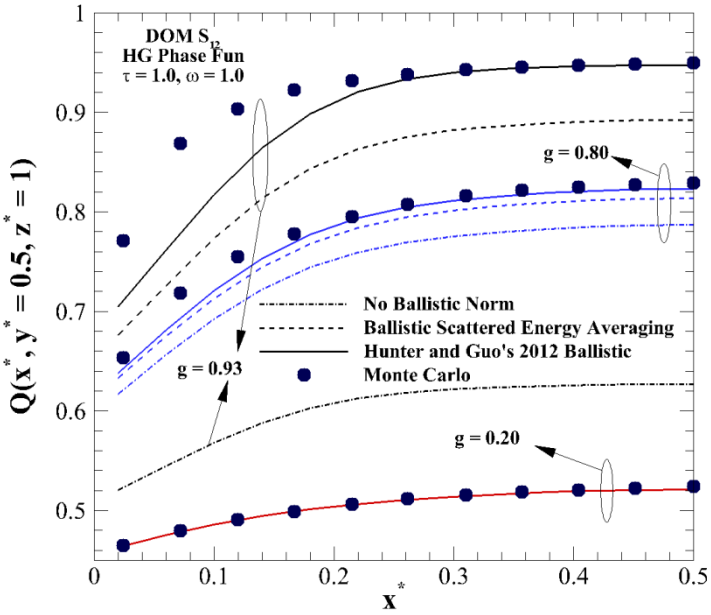

Figure 7.6: Impact of ballistic phase function normalization on Q(x*, y* = 0.5, z* = 1) for normal, ballistic heating at z* = 0 wall generated with DOM S_{12} for HG g = 0.20, 0.80, and 0.93 and comparison with Monte Carlo for optically thin medium

DOM heat fluxes generated using the three different ballistic normalization cases are nearly identical for weakly-forward scattering (g = 0.2000), conforming to the results shown in Figures 7.2a and 7.3a. Additionally, DOM heat fluxes conform within 0.6% for all locations to the benchmark MC solution. As g is increased to 0.8000, noticeable differences are witnessed between the three DOM ballistic normalization cases. When Hunter and Guo's 2012 ballistic normalization is applied, DOM solutions conform accurately to within 0.7% to MC at x^* = 0.5. For no normalization and ballistic scattered energy averaging, these differences are 5.0% and

1.8%, respectively, indicating that conservation of ballistic asymmetry factor is able to reduce angular false scattering in problems involving ballistic radiation.

For the extreme case (g = 0.9300), out-scattered energy was shown in Figure 7.2a to be extremely non-conserved without application of normalization. The lack of out-scattered energy conservation leads to errors of 34% and greater between DOM and MC heat fluxes at all locations, indicating the absolute necessity of ballistic out-scattered energy conservation. When ballistic scattered energy averaging is applied to conserve energy, the ballistic asymmetry factor in this case is altered to g = 0.8581, leading to heat flux underpredictions of 12.2%, 6.4%, and 6.0% when compared to MC at x^* = 0.12, 0.3, and 0.5, respectively. Application of Hunter and Guo's 2012 ballistic normalization results in underpredictions in heat flux with respect to MC of 7.0% near x^* = 0, which can be attributed to DOM spatial and angular discretization. However, far from the wall, the DOM heat flux conforms accurately to within 0.3% to MC at both x^* = 0.30 and 0.50. The excellent agreement near the center of the face between MC and DOM with Hunter and Guo's 2012 ballistic normalization shows that angular false scattering errors have been effectively minimized, and shows the accuracy improvement in ballistic radiation transfer resulting from conservation of ballistic out-scattered energy and asymmetry factor simultaneously [Hunter and Guo 2012e].

Figure 7.7 examines the impact of ballistic phase-function normalization on heat flux in an optically thicker (τ = 10.0) medium, with otherwise similar properties to those investigated in Figure 7.6. Results for this medium are only presented for g = 0.9300, as errors for the other two asymmetry factors are not as prominent. In addition to the MC results of Collin et al. [2011], higher order FVM results, generated with M = 840 discrete directions and no normalization, are also plotted for comparison.

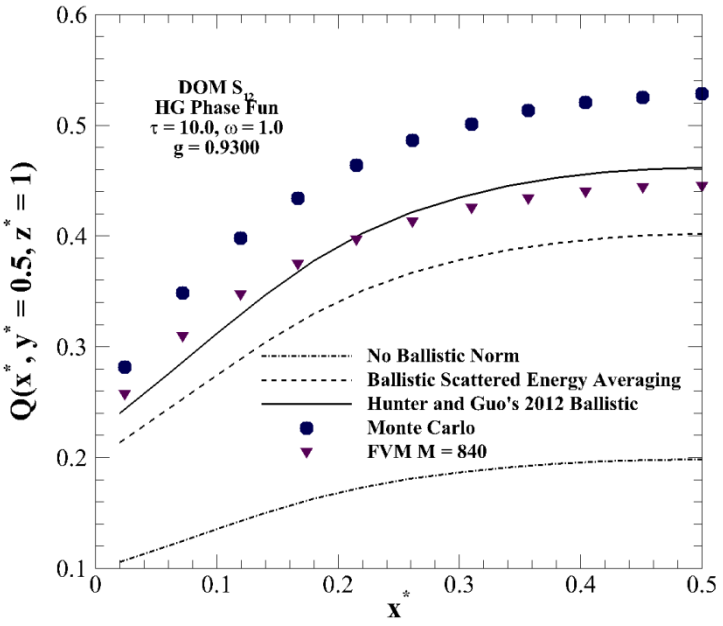

Figure 7.7: Impact of ballistic phase function normalization on Q(x^*, y^* = 0.5, z^* = 1) for normal, ballistic heating at z^* = 0 wall generated with DOM S_{12} for HG g = 0.93 and comparison with Monte Carlo and FVM results for τ = 10.0

For the optically thicker medium, discrepancies between DOM and MC solutions are much larger than for the thinner medium analyzed in Figure 7.6. When ballistic normalization is neglected entirely, the DOM heat flux profile underpredicts MC solutions by greater than 62% at all x^*, indicating that lack of scattered energy conservation has a profound impact. In fact, these results conform to the expectations garnered from Chapter 6, where it was shown that increase in optical thickness resulted in larger radiation transfer errors due to scattered energy non-conservation. When ballistic scattered energy averaging is implemented, DOM and MC differences reduce to 24% on average, indicating that angular false scattering errors exist.

Application of Hunter and Guo's 2012 ballistic normalization results in DOM heat fluxes that underpredict MC by between 12-14%, respectively. However, when the DOM with Hunter

and Guo's 2012 normalization is compared to high-order FVM with M = 840, much better agreement is witnessed, with an average difference of only 3.5%. Neither approximate method appears to accurately conform to the MC results for the thicker medium, due to both spatial and angular discretization errors, as well as challenges facing MC accuracy in thicker media. However, the fact that both approximate methods conform fairly accurately to one another gives confidence that Hunter and Guo's 2012 ballistic normalization is able to accurately conserve both scattered energy and asymmetry factor for ballistic incidence.

It is of greater interest to examine the impact of ballistic phase-function normalization on ultrafast radiative heat transfer for practical applications, such as laser-tissue interaction in biomedicine, in order to further validate the necessity of proper conservation of out-scattered energy and asymmetry factor simultaneously [Hunter and Guo 2012e]. Figures 7.8(a-b) examine the impact of ballistic phase-function normalization on the ultrafast propagation of radiant energy from a diffusely irradiated hot wall at x^* = 0 into a cold medium, with all other walls of the cubic medium treated as cold and black. Corresponding to a (27 x 27 x 27) spatial grid, the non-dimensional time step is taken to be $\Delta t^* = 0.03$, in order to ensure that the traveling distance of a ray of light is smaller than the spatial grid size during a single time step. For this ultrafast analysis, the optical thickness and scattering albedo of the medium are prescribed as τ = 25.0 and ω = 0.95, and the HG phase-function approximation with g = 0.9000 is implemented. Heat flux profiles along the side wall of the cubic enclosure, i.e. $Q(x^*, y^* = 0, z^* = 0.5)$ are presented for M = 24 and 168 in Figures 7.8(a-b), respectively. Heat fluxes are presented at four different non-dimensional times ($t^* = 0.15$, 0.45, 0.75, and 3.0) using either ballistic scattered energy averaging or Hunter and Guo's 2012 ballistic normalization.

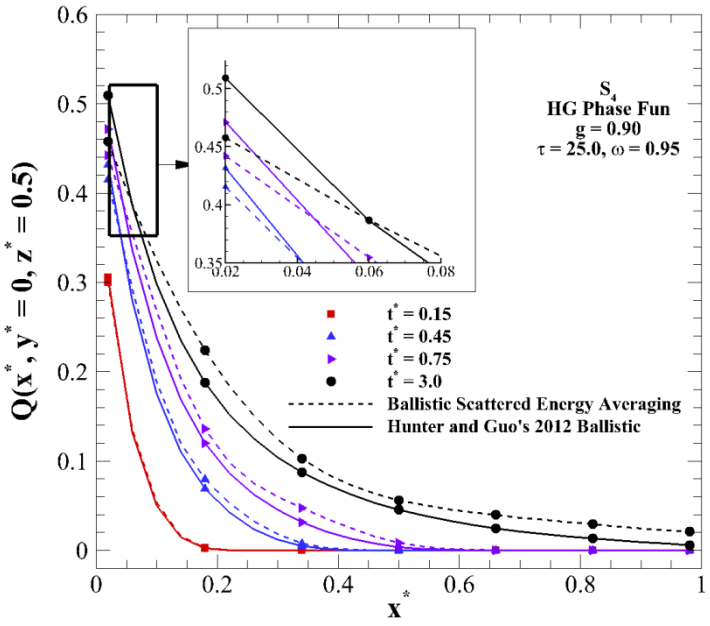

(a)

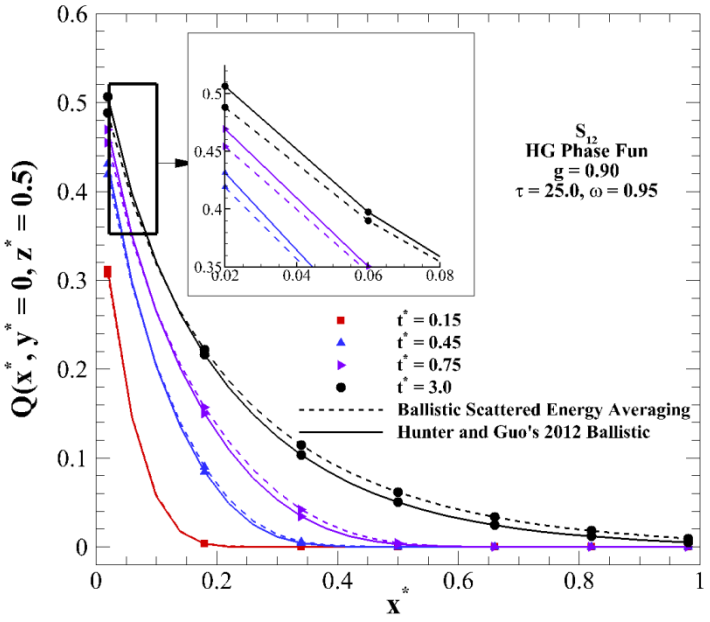

(b)

Figure 7.8: Transient propagation of $Q(x^*, y^* = 0, z^* = 0.5)$ through optically thick, highly scattering medium of the HG g = 0.90 phase function with either ballistic scattered energy or Hunter and Guo's 2012 ballistic normalizations using a) S_4 and b) S_{12} quadrature

For low discrete direction number (M = 24) in Figure 7.8a, significant discrepancies begin to manifest between the heat fluxes generated with the two ballistic normalization approaches at early times t^*. In the range where heat flux has a meaningful magnitude for t^* = 0.15 (0.02$\leq x^* \leq$ 0.26), differences of between 2-19% are witnessed between the two DOM profiles. Increasing t^* to 0.45 results in an increase in percentage difference between ballistic scattered energy averaging and Hunter and Guo's 2012 ballistic normalization. In the range x^* = 0.02-0.42, differences range between 4-77%. As steady state is approached (t^* = 3.0), a maximum overprediction of 250% occurs near the far wall when ballistic asymmetry factor is not accurately conserved. A "cross-over" in heat flux is witnessed for all non-dimensional times near the diffuse source, where heat flux predicted using ballistic scattered energy averaging underpredicts Hunter and Guo's 2012 ballistic normalization near the source, and overpredicts at locations away from the source. For the four non-dimensional times, underpredictions of 1.9%, 3.8%, 6.2%, and 10.2% are witnessed for x^* = 0.02. This "cross-over" phenomenon is actually due to angular false scattering, resulting from the false augmentation of asymmetry factor from g = 0.9000 to 0.9894. The increase in g leads to radiant energy scattering away from the wall in a stronger fashion, leading to lower fluxes near the source, and higher fluxes at the far wall.

When quadrature is refined to M = 168 in Figure 7.8b, discrepancies between ballistic scattered energy averaging and Hunter and Guo's 2012 ballistic normalizations decrease for all non-dimensional time. At this quadrature, the discretized g for ballistic radiation is altered to 0.9382 after application of ballistic scattered energy averaging, a vast improvement over 0.9894 for M = 24. At t^* = 0.15, heat flux differences between the two normalization approaches range between 1.6-8.0% in the range x^* = 0.02-0.26. The largest error occurs as steady-state is realized, with differences reaching 110% for t^* = 3.0 at the far wall. While the cross-over

phenomenon is still observed in the inlay, the weaker distortion in asymmetry factor due to angular false scattering causes the point of cross-over to move further into the medium than seen in Figure 7.8a.

For many biomedical applications, such as laser hyperthermia for cancer treatment, it is important to be able to accurately predict the amount of radiant energy absorbed by both cancerous and healthy tissues. Incorrect analysis of the medium energy absorption (or energy deposition) could result in either thermal damage and/or necrosis of healthy biological tissue during cancer irradiation, or improper destruction of cancerous tissue. The energy deposition in a medium at any given time instant or spatial location can be calculated using the traditional formulation of divergence of radiative heat flux, which is presented in Eq. (2.20).

Figures 7.9(a-b) examines contours of percent difference in cube-center energy deposition for a cold medium with a diffusely irradiating hot wall at x^* = 0 between the DOM with ballistic scattered energy averaging, and DOM with Hunter and Guo's 2012 ballistic normalization. Contours are plotted against both HG phase-function asymmetry factor and non-dimensional time t^* for the DOM S_8 quadrature in Figure 7.9a, and the DOM S_{12} quadrature in Figure 7.9b. The medium properties are taken to be τ = 25.0 and ω = 0.95.

In Figure 7.9a for M = 80 discrete directions, the percent difference in energy deposition resulting from improper ballistic asymmetry factor conservation is less than 1% for $g \leq 0.40$ for all non-dimensional times, corresponding to the fact that ballistic asymmetry factor is not strongly distorted at this asymmetry factor. As g increases, large discrepancies in energy deposition arise due to angular false scattering errors. The largest differences occur for early times, with differences of 11.5%, 7.4%, 6.1%, and 2.9% witnessed for t^* = 0.15, 0.75, 1.35, and 6.0, respectively, with g = 0.70. In general, differences reach their maximums at t^* = 0.15 for

$g \leq 0.80$, and for t^* = 0.75 for g > 0.80. The maximum overall difference occurs for g = 0.90 and t^* = 0.75, with a magnitude of ~70%. At steady-state (t^* = 6.0), the maximum difference of 20.9% occurs for g = 0.85, indicating that discrepancies due to distortion in g reduce with increasing time. When quadrature is refined to S_{12} in Figure 7.9b, the maximum overall difference in the medium decreases to 53.3% (for t^* = 0.15 and g = 0.90), while the maximum difference at steady-state is 13.7%, reaffirming that angular false scattering errors due to non-conservation of ballistic asymmetry factor are more prominent for 1) higher asymmetry factor and 2) early times.

In Section 7.1.1, the ballistic incident polar and azimuthal angles were found to have a profound effect on the discretized asymmetry factor after application of ballistic scattered energy averaging [Hunter and Guo 2012d]. In Figures 7.10(a-c), heat fluxes $Q(x^*, y^* = 0.5, z^* = 1.0)$ in a cold, cubic enclosure irradiated by ballistic incidence of unity intensity at z^* = 0 generated using the two ballistic normalization approaches are presented for varying angles of incidence [Hunter and Guo 2012e]. For all three figures, the azimuthal angle of incidence is kept constant at $\phi_i = 0°$, while the polar angle of incidence is varied between $\theta_i = 0°, 30°$, and $60°$ in Figures 7.10(a-c), respectively. The optical properties of the medium are taken as τ = 1.0 and ω = 0.95, while the HG asymmetry factor is varied between g = 0.6000 and 0.9500.

For normal incidence in Figure 7.10a, the entire wall at z^* = 1.0 experiences a direct contribution from the ballistic incidence, as well as contributions from radiative scattering. Differences in heat flux based on ballistic normalization approach are witnessed for all asymmetry factors. For g = 0.6000-0.9000, heat flux generated using ballistic scattered energy averaging overpredict those generated using Hunter and Guo's 2012 ballistic normalization by between 1-5%, corresponding to slight increases in ballistic asymmetry factor. For g = 0.9500,

the ballistic asymmetry factor is actually decreased to 0.9257, resulting in a heat flux underprediction of 2% due to angular false scattering.

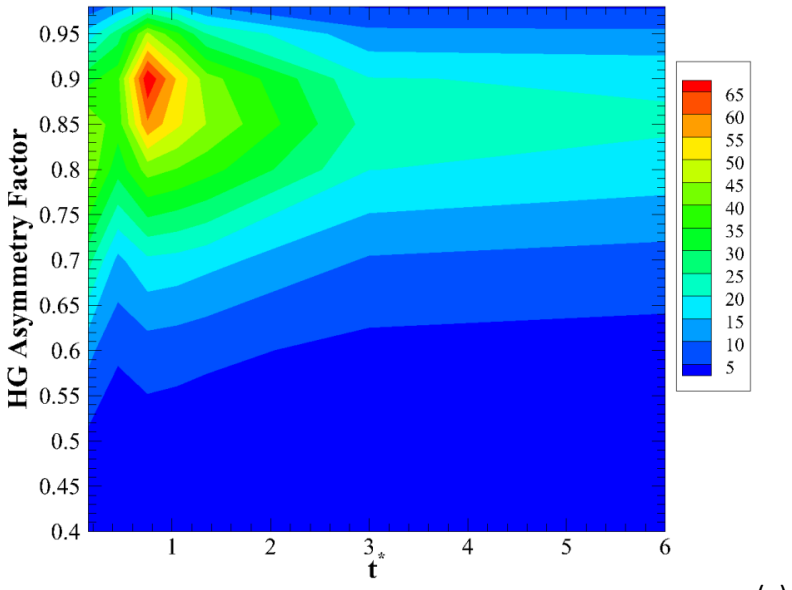

(a)

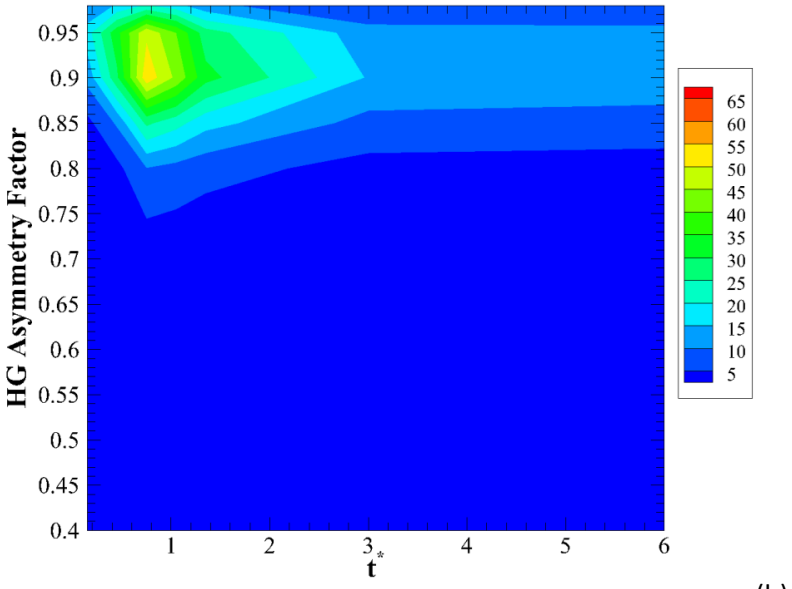

(b)

Figure 7.9: Percentage difference in ultrafast energy deposition at the cube center versus prescribed HG asymmetry factor and non-dimensional time using a) DOM S_8 and b) DOM S_{12} quadrature between ballistic scattered energy averaging and Hunter and Guo's 2012 ballistic normalization

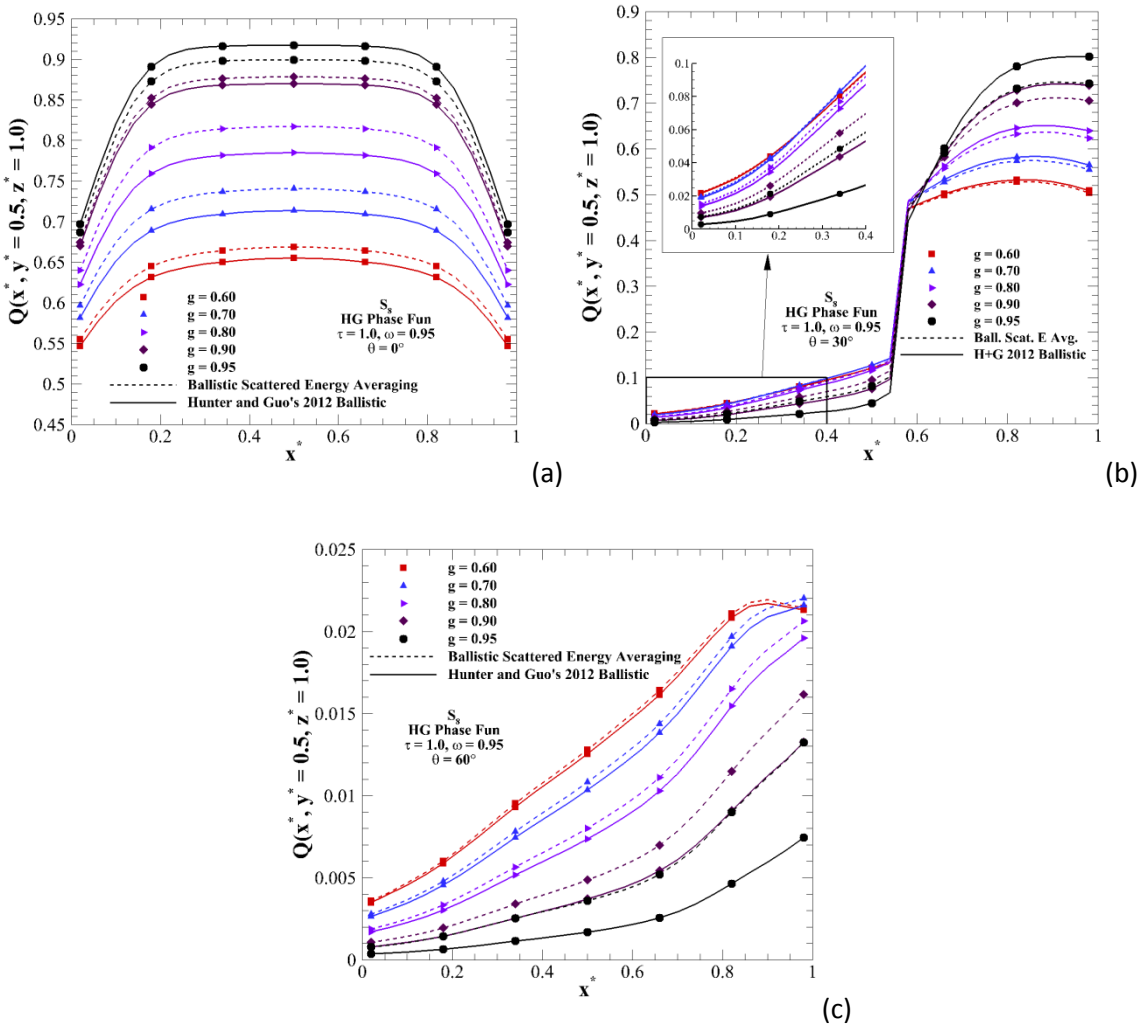

Figure 7.10: Impact of ballistic incident polar angle on Q(x*, y* = 0.5, z* = 1) for various HG asymmetry factors using ballistic scattered energy averaging and Hunter and Guo's 2012 normalization for ballistic normalization with τ = 1.0, ω = 0.95, and incident polar angle θ_i = a) 0°, b) 30°, and c) 60°

For a polar incident angle of $\theta_i = 30°$ in Figure 7.10b, only part of the wall ($x^* \geq 0.5773$) experiences a direct contribution from the ballistic incidence, resulting in the drastic change in heat flux magnitude between the two sections of the wall. Errors due to angular false scattering increase with increasing prescribed asymmetry factor, as for all cases, the discretized

asymmetry factor is reduced. In the region where no direct contribution from ballistic incidence is seen, errors in heat flux are much larger than in the opposite region, due to minimal heat flux magnitudes. The maximum errors in heat flux caused solely by scattering of the ballistic component in the range $x^* < 0.5733$ are 1.6%, 4.0%, 9.3%, 38.0%, and 145% for g = 0.6000-0.9500, respectively. In the region where ballistic incidence directly impacts the wall, the maximum errors for the same five asymmetry factors drops to 0.95%, 1.8%, 2.5%, 4.5%, and 7.3%, respectively. The massive drops in errors in this region are due to the high magnitude of ballistic intensity reaching the wall without scattering, which is not impacted by ballistic normalization.

For a polar angle of $\phi_i = 60°$ in Figure 7.10c, no direct contribution of ballistic incidence is seen at the opposite wall. However, a significant skew of heat flux towards x^* = 1.0 is observed, due to the large angle of incidence (a higher amount of energy is able to scatter towards the wall from this region). Due to DOM directional symmetry, the discretized asymmetry factors after application of ballistic scattered energy averaging are identical to those seen for $\theta_i = 30°$. Maximum errors occur near x^* = 0, in the region where heat flux is of lower magnitude due to a lack of ballistic incident energy scattering, reaching 2.6%, 5.4%, 10.0%, 35%, and 126% for g = 0.6000-0.9500, respectively. Errors decrease in magnitude as one moves towards x^* = 1.0, and the presence of the ballistic incidence is felt, with maximum errors reaching 0.6%, 2.0%, 5.3%, 21.8%, and 77.6%, respectively. For all locations x^*, angular false scattering errors due to lack of ballistic asymmetry factor conservation are significant, especially for highly anisotropic scattering.

The results in this section show that nonconservation of ballistic out-scattered energy results in large discrepancies in radiative heat flux. Use of ballistic scattered energy averaging to

conserve out-scattered energy improves radiation transfer predictions, but angular false scattering is prominent, due to lack of ballistic asymmetry factor conservation [Hunter and Guo 2012e]. This mandates the necessity of conserving both ballistic out-scattered energy and asymmetry factor simultaneously, in order to obtain accurate ultrafast radiation transfer results.

7.1.3 Hunter and Guo's 2014 Normalization for Ballistic Radiation

7.1.3.1 Mathematical Formulation

For diffuse radiation, the results in Chapter 6 showed that Hunter and Guo's 2014 normalization is a simple, efficient, and accurate method for determining radiation transfer. Though Hunter and Guo's 2014 normalization is much simpler than Hunter and Guo's 2012 approach for diffuse radiation, its application for ballistic radiation becomes more complicated [Hunter and Guo 2014e].

Due to the symmetry of DOM quadrature, if the ballistic radiation direction does not directly correspond to one of the predetermined DOM quadrature directions, there will be no forward- or backward scattering ($\cos\Theta^{l^B l} = \pm 1$) phase-function term to normalize, as discrete directions that attain those cosines with respect to the ballistic direction will not exist. It is proposed, therefore, to normalize $\Phi^{l^B l}$ only for the directions where $\cos\Theta^{l^B l}$ reaches its minimum and maximum, for a specific DOM quadrature set. Applying this idea, the ballistic out-scattered energy and asymmetry factor conservation constraints of Eqs. (7.1a-b) for Hunter and Guo's 2014 ballistic normalization can be written as follows [Hunter and Guo 2014e]:

$$\frac{1}{4\pi}\sum_{\substack{l=1 \\ l\neq l^{B+} \\ l\neq l^{B-}}}^{M} \Phi^{l^B l} w^l + \frac{N^{B+}}{4\pi}\left(1 + A^{l^{B+}}\right)\Phi^{l^B l^{B+}} w^{l^{B+}} + \frac{N^{B-}}{4\pi}\left(1 + B^{l^{B-}}\right)\Phi^{l^B l^{B-}} w^{l^{B-}} = 1 \tag{7.5a}$$

$$\frac{1}{4\pi}\sum_{\substack{l=1\\ l\neq l^{B+}\\ l\neq l^{B-}}}^{M}\Phi^{l^B l}w^{l}\cos\Theta^{l^B l}+\frac{N^{B+}}{4\pi}\left(1+A^{l^{B+}}\right)\Phi^{l^B l^{B+}}w^{l^{B+}}\cos\Theta^{l^B l^{B+}}$$
$$+\frac{N^{B-}}{4\pi}\left(1+B^{l^{B-}}\right)\Phi^{l^B l^{B-}}w^{l^{B-}}\cos\Theta^{l^B l^{B-}}=g \tag{7.5b}$$

In the above, $A^{l^{B+}}$ and $B^{l^{B-}}$ are the "forward" and backward" ballistic normalization parameters, corresponding to the discrete directions $\hat{\boldsymbol{s}}^{\boldsymbol{l^{B+}}}$ and $\hat{\boldsymbol{s}}^{\boldsymbol{l^{B-}}}$ where $\cos\Theta^{l^B l}$ attains maximum and minimum values, respectively. Additionally, the multiplicative factors N^{B+} and N^{B-} represent the number of discrete directions that attain the maximum and minimum scattering cosines with respect to the direction of ballistic incidence, as it is highly likely that multiple directions will share the same overall ballistic scattering cosine due to DOM directional symmetry. Thus, addition of these factors is necessary. Simultaneous solution of Eqs. (7.5a) and (7.5b) yields the following expressions for the "forward" and "backward" ballistic normalization parameters for Hunter and Guo's 2014 ballistic normalization:

$$A^{l^{B+}}=\left[4\pi\left(\cos\Theta^{l^B l^{B-}}-g\right)+\sum_{l=1}^{M}\Phi^{l^B l}w^{l}\left(\cos\Theta^{l^B l}-\cos\Theta^{l^B l^{B-}}\right)\right]$$
$$/\left[N^{B+}\Phi^{l^B l^{B+}}w^{l^{B+}}\left(\cos\Theta^{l^B l^{B-}}-\cos\Theta^{l^B l^{B+}}\right)\right] \tag{7.6a}$$

$$B^{l^{B-}}=\left[4\pi\left(\cos\Theta^{l^B l^{B+}}-g\right)+\sum_{l=1}^{M}\Phi^{l^B l}w^{l}\left(\cos\Theta^{l^B l}-\cos\Theta^{l^B l^{B+}}\right)\right]$$
$$/\left[N^{B-}\Phi^{l^B l^{B-}}w^{l^{B-}}\left(\cos\Theta^{l^B l^{B+}}-\cos\Theta^{l^B l^{B-}}\right)\right] \tag{7.6b}$$

In a similar fashion, redefinition for ballistic radiation phase-function normalization can be addressed for both Mishchenko's E and Kamdem Tagne's approaches, in the absence of

forward-scattering terms [Hunter and Guo 2014e]. Using the notion described for Hunter and Guo's 2014 ballistic normalization, the ballistic radiation forward-scattering parameters $A^{l^{B+}}$ for these two approaches become:

$$A^{l^{B^+}} = \left[4\pi - \sum_{l=1}^{M} \Phi^{l^B l} w^l\right] / (N^{B+} \Phi^{l^B l^{B^+}} w^{l^{B^+}}) \tag{7.7a}$$

$$A^{l^{B^+}} = \left[4\pi g - \sum_{l=1}^{M} \Phi^{l^B l} w^l \cos\Theta^{l^B l}\right] / (N^{B+} \Phi^{l^B l^{B^+}} w^{l^{B^+}} \cos\Theta^{l^B l^{B^+}}) \tag{7.7b}$$

where Eq. (7.7a) are the parameters for Mishchenko's E ballistic normalization, and Eq. (7.7b) are the parameters for Kamdem Tagne's g ballistic normalization. As with diffuse radiation, these parameters will not accurately conserve both ballistic quantities simultaneously, but can be used for comparison to Hunter and Guo's 2012 and 2014 approaches to gauge the importance of accurate conservation.

Table 7.1 lists discretized values of ballistic radiation out-scattered energy and asymmetry factor after application of Mishchenko's E and Kamdem Tagne's g ballistic normalizations to $\Phi^{l^B l}$. Data are tabulated for both the Legendre g =0.8189 and the HG g = 0.9300 phase-function approximations using the DOM with various quadrature schemes and discrete direction numbers. The direction of ballistic incidence is taken to be $\hat{\boldsymbol{s}}^{\boldsymbol{l^B}} = \overrightarrow{e_z}$ for all forthcoming analyses.

Application of Mishchenko's E normalization results in large deviations in asymmetry factor for both phase-functions and DOM quadrature schemes for low-order quadrature. Even at high-order quadratures ($N \geq 12$), the change in overall scattering effect (1-g) ranges between 0 and 20%, depending on quadrature scheme and phase-function. Conversely, for

Kamdem Tagne's g ballistic normalization, deviations in scattered energy of less than 1% are only consistently observed for $N \geq 12$. These results provide a preliminary indication that these two ballistic normalization approaches may not be able to accurately predict ballistic radiation transfer.

Table 7.1: Examination of discretized ballistic radiation scattered energy or asymmetry factor using Mishchenko's E and Kamdem Tagne's g normalizations with Legendre g = 0.8189 and HG g = 0.9300 phase-functions

Prescribed g	N	Mishchenko E - Discretized g				Kamdem Tagne g - Discretized E			
		P_NT_N	S_N	EO_N	EQ_N	P_NT_N	S_N	EO_N	EQ_N
0.8189	4	0.7213	0.7599	0.7599	0.7273	1.1134	1.0650	1.0650	1.1054
	6	0.7771	0.8016	0.8114	0.7742	1.0449	1.0179	1.0077	1.0480
	8	0.8092	0.8242	0.8102	0.8083	1.0101	0.9946	1.0088	1.0111
	10	0.8055	0.8147	0.8143	0.8058	1.0138	1.0043	1.0047	1.0135
	12	0.8154	0.8086	0.8262	0.8174	1.0036	1.0106	0.9927	1.0016
	16	0.8189	0.8164	0.8173	0.8187	1.0000	1.0025	1.0016	1.0002
0.9300	4	0.8247	0.8694	0.8694	0.8316	1.1223	1.0667	1.0667	1.1132
	6	0.8856	0.9124	0.9245	0.8851	1.0476	1.0182	1.0056	1.0482
	8	0.9075	0.9254	0.9274	0.9075	1.0235	1.0047	1.0026	1.0235
	10	0.9173	0.9228	0.9297	0.9165	1.0131	1.0073	1.0003	1.0139
	12	0.9223	0.9156	0.9301	0.9219	1.0079	1.0148	0.9999	1.0083
	16	0.9268	0.9232	0.9301	0.9265	1.0033	1.0069	0.9999	1.0036

An analysis of the "forward"- and "backward"-scattering ballistic normalization parameters generated using Hunter and Guo's 2014 normalization for ballistic radiation are presented in Figure 7.11 for varying DOM quadrature schemes and discrete direction number for HG g = 0.9300. As the HG phase-function depends solely on asymmetry factor, and both Hunter and Guo's 2012 and 2014 normalizations are suitable for HG phase-functions of diffuse radiation (as described in Chapter 6), the HG phase function is chosen to simplify the current analysis. For all directional orders and quadrature schemes, the forward-scattering ballistic normalization parameters are positive. Although not presented here, for brevity, ballistic radiation normalization using Mishchenko's E, Kamdem Tagne's g, and Hunter and Guo's 2012

ballistic normalizations result in similar forward-scattering normalization parameter magnitudes [Hunter and Guo 2014e].

Of more importance, however, are the backward-scattering parameters, in which a critical issue arises: parameters of less than -1 are observed for nearly all tested quadrature schemes and discrete direction numbers. These negative values will result in negative values of the normalized ballistic phase-function, which are physically impossible [Hunter and Guo 2014e].

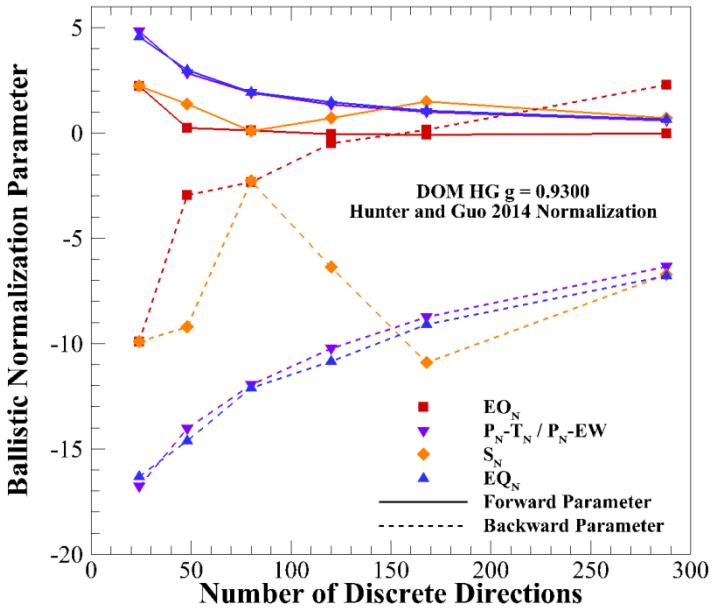

Figure 7.11: Forward and backward normalization parameters for ballistic radiation using Hunter and Guo's 2014 normalization for ballistic radiation for HG phase-function with g = 0.9300

In Figure 7.12, the backward-scattering normalization parameters generated with Hunter and Guo's 2014 ballistic normalization are compared with those generated using Hunter and Guo's 2012 ballistic normalization for the same discrete directions. As Mishchenko's E and

Kamdem Tagne's g ballistic normalizations do not involve normalization of the backward-scattering directions, they are not included in Figure 7.12.

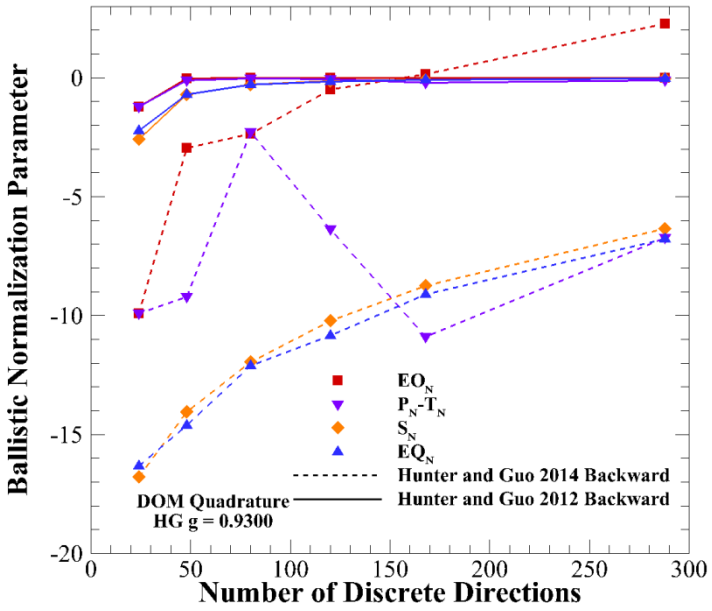

Figure 7.12: Comparison of backward-scattering normalization parameters between Hunter and Guo's 2012 and 2014 normalizations for ballistic radiation for HG phase-function with g = 0.9300

Backward-scattering ballistic normalization parameters generated using Hunter and Guo's 2014 ballistic normalization vary greatly with the chosen DOM quadrature scheme, and parameters of less than -1 are extremely common. Of concern is the fact that these negative parameters occur at the S_N directional limit (M = 288). The only quadrature where this isn't an issue over the entire range of M presented is the EO_N quadrature, where backward parameters are less than -1 for $M \leq 120$. For Hunter and Guo's 2012 ballistic normalization, parameters of less than -1 do occur, but only for the lowest quadrature order (N = 4, M = 24). The explanation for this trend stems from the fact that every value of $\Phi^{l^B l}$ is normalized/altered in Hunter and Guo's 2012 ballistic normalization. This allows for less drastic alteration of the backward-scattering terms, while maintaining ballistic out-scattered energy and asymmetry factor

conservation. The improvement in backward-scattering parameters indicates that Hunter and Guo's 2012 ballistic normalization is a more suitable approach for normalizing the ballistic radiation scattering phase function.

For normal, ballistic incidence, ballistic forward normalization parameters of < -1 do not appear for Mishchenko's E, Kamdem Tagne's g, and Hunter and Guo's 2014 ballistic normalizations. For the special case where the direction of ballistic incidence matches one of the predetermined quadrature directions, the ballistic normalization parameters will be identical to the diffuse normalization parameters for that quadrature direction. As seen in Figure 6.10, diffuse forward parameters of <-1 occur for these three simpler diffuse normalization approaches for certain directions. If the ballistic direction of incidence matches one of these specific directions, the ballistic forward parameters will also be <-1, resulting in negative phase-function values and mandating the necessity of negative intensity correction.

Additionally, for ballistic incident directions that are both non-normal and non-aligned with a predetermined quadrature direction, negative forward parameters are still encountered for certain Legendre phase-functions. For example, for the EO_8 quadrature with the g = 0.8189 Legendre phase-function, a forward ballistic normalization parameter of -1.02 occurs for ballistic incidence at polar angle $\theta = 43°$ and azimuthal angle $\phi = 5°$ after application of Hunter and Guo's 2014 ballistic normalization. Thus, for general Legendre phase-function, the existence of negative phase-function values and the necessity of negative intensity correction is always a concern. Such negative forward ballistic parameters are not encountered for the HG phase-function.

7.1.3.2 Impact on Radiation Transfer Results

The impact of ballistic normalization approach on heat fluxes $Q(x^*, y^*, z^* = 0.5)$ in the cold, cubic medium irradiated by a normal, collimated incidence of unity intensity at z^* = 1.0 (as described earlier in the chapter) is presented in Figures 7.13(a-b). DOM heat fluxes are generated using the EO_N quadrature, with M = 80 discrete directions implemented for Figure 7.13a, and M = 288 discrete directions used for Figure 7.13b. The optical thickness and scattering albedo of the medium are τ = 10.0 and ω = 1.0, while the Legendre g = 0.8189 phase-function approximation is used. DOM heat fluxes are generated using Mishchenko's E, Kamdem Tagne's g, Hunter and Guo's 2012, and Hunter and Guo's 2014 ballistic normalizations. It should also be mentioned that, for all forthcoming radiation transfer results in this section, the phase function for diffuse radiation $\Phi^{l'l}$ has been normalized using the same approach as for the ballistic component. In addition to DOM, heat fluxes generated using the FVM with a high-direction number of M = 840 are also plotted, for comparison purposes.

For M= 80 in Figure 7.13a, heat fluxes generated using Hunter and Guo's 2012 and 2014 normalizations differ from each other by less than 1% at all locations. Conversely, application of Mishchenko's E and Kamdem Tagne's g normalizations result in differences of ~2-4%, respectively. All four DOM heat fluxes with ballistic normalization overpredict the plotted FVM results by a fairly significant margin (between 4-20%), due to ray effect. Ray effect is mitigated when discrete direction number is increased to M = 288 in Figure 7.13b, resulting in accurate conformity of DOM heat fluxes with high-order FVM (maximum differences of less than 4%). Additionally, increase in discrete direction number reduces the impact of ballistic normalization approach, as the DOM heat fluxes with the four ballistic normalizations differ from each other by less than 0.2%.

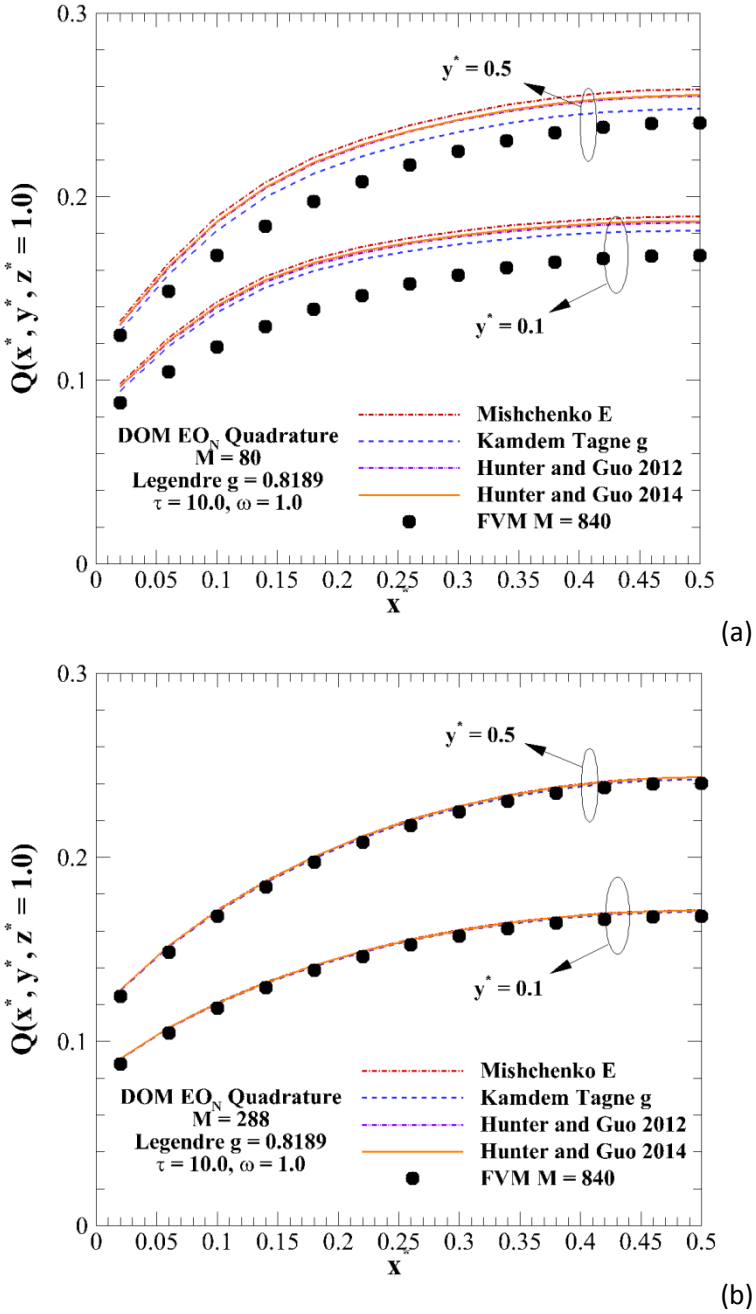

Figure 7.13: Comparison of heat flux profiles Q(x*, y*, z* = 1.0) generated using FVM and DOM with various ballistic radiation normalization techniques for Legendre g = 0.8189 with a) M = 80 and b) M = 288

Figures 7.14(a-b) present non-dimensional heat fluxes $Q(x^*, y^*, z^* = 1.0)$ for an optically thick medium with τ = 100.0 using the DOM P_N-T_N quadrature with HG g = 0.9300. All

other conditions are the same as for Figure 7.13(a-b). For both discrete direction numbers, Hunter and Guo's 2012 and 2014 normalizations result in nearly identical DOM heat flux profiles, which conform accurately to within 2% to high-order FVM. However, results generated using Mishchenko's E and Kamdem Tagne's g normalizations exhibit much stronger discrepancies.

Lack of asymmetry factor conservation in Mishchenko's E normalization leads to overpredictions in heat flux of up to 12% for M = 80 in Figure 7.14a, and up to 8% for M = 288 in Figure 7.14b. The lack of energy conservation in Kamdem Tagne's g normalization results in extreme underpredictions in heat flux as compared with FVM, with differences of >55% for M = 80 and >20% for M = 288. These results mirror the results witnessed in Figures 6.8 and 6.12, and illustrate the criticality of conserving scattered energy for applications involving optically thick media.

The highly negative backward-scattering ballistic normalization parameters in Hunter and Guo's 2014 ballistic normalization result in negative intensities in radiation transfer computation (similar to those encountered for diffuse normalization in Chapter 6), and thus negative intensity correction is required. Unlike the diffuse case, these negative intensities reappear at every iteration step, mandating the use of negative intensity correction throughout the entire simulation process. This is, in part, due to the treatment of ballistic radiation intensity using the Beer-Lambert Law in the solution of the ERT, as the ballistic radiation intensities at different medium locations have a specified value depending on optical depth. Although negative intensities occur, and negative intensity correction is necessary, the negative ballistic parameters has no appreciable impact radiation transfer results. This is because this issue only

occurs in one or a few discrete directions, and thus the overall impact is minimal [Hunter and Guo 2014e].

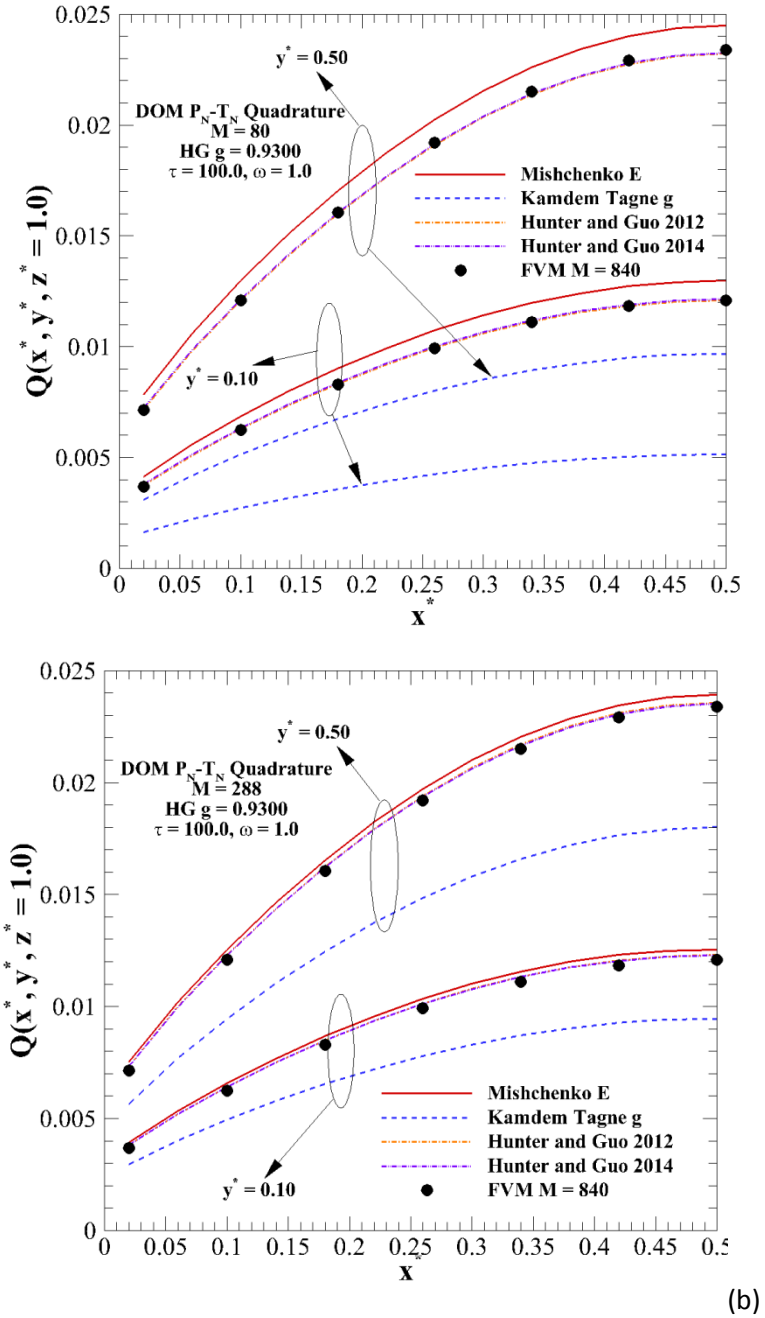

Figure 7.14: Comparison of heat flux $Q(x^*, y^*, z^* = 1.0)$ profiles generated with FVM and various DOM ballistic radiation normalization techniques in an optically thick medium with a) M = 80 and b) M = 288

In summation, the choice of ballistic normalization approach has no appreciable impact on radiation transfer results [Hunter and Guo 2014e], as long as the negative-intensity correction is enforced, except for cases where the medium is optically thick. In optically thick media, conservation of asymmetry factor and especially scattered energy is crucial, and Mishchenko's E and Kamdem Tagne's g ballistic normalization fail to conserve both simultaneously. Additionally, it should be mentioned that results are very similar for additional quadrature sets, and thus only representative quadrature results are presented. In general, in order to avoid negative intensity correction, it appears that Hunter and Guo's 2012 normalization for ballistic radiation is the most desirable method for conserving the two necessary quantities, as negative ballistic phase-function values only occur for low-order DOM quadrature.

7.2 Hunter and Guo's 2012 Normalization for Ballistic Radiation in FVM

7.2.1 Ballistic Out-Scattered Energy and Asymmetry Factor Conservation

Using the FVM, the ballistic out-scattered energy and ballistic asymmetry factor conservation conditions can be expressed as follows [Hunter and Guo 2014c]:

$$\frac{1}{4\pi}\sum_{l=1}^{M}\overline{\Phi}^{l^B l}\Delta\Omega^l = 1 \tag{7.8a}$$

$$\frac{1}{4\pi}\sum_{l=1}^{M}\overline{\Phi}^{l^B l}\cos\Theta^{l^B l}\,\Delta\Omega^l = g \tag{7.8b}$$

where the average scattering phase-function for ballistic radiation $\overline{\Phi}^{l^B l}$ is determined after implementation of solid-angle splitting for the discrete radiation directions $\hat{\boldsymbol{s}}^{\boldsymbol{l}}$, as follows:

$$\bar{\Phi}^{l^B l} = \frac{1}{\Delta\Omega^l} \sum_{l_s=1}^{M_s} \Phi^{l^B l_s} \Delta\Omega^{l_s} \tag{7.9}$$

It is crucial, for problems involving ultrafast propagation of ballistic incidence, to examine the impact of solid-angle splitting of the FVM quadrature on conservation of ballistic out-scattered energy in the system, to determine whether conservation is possible without additional treatment (as it was for diffuse radiation). This question is answered in Figure 7.15, in which deviations in ballistic scattered energy conservation after FVM discretization using M = 48, 80, 120, and 168 discrete directions are presented. Each solid angle is sub-divided into ($N_{s\phi}$ x $N_{s\theta}$) sub-angles, with $N_{s\phi}$ = $N_{s\theta}$, ranging from (4 x 4) to (24 x 24) total divisions. Ballistic scattered energy values are determined using Eq. (7.8a) for the HG phase-function approximation with g = 0.9300. Ballistic incident direction was found earlier in the chapter to have a significant effect on ballistic out-scattered energy values. In this analysis, ballistic out-scattered energy values are generated using a ballistic incident direction with polar angle θ = 0° (i.e., $\hat{\boldsymbol{s}}^{\boldsymbol{l^B}} = \overrightarrow{e_z}$) as a representative case.

Increases in solid-angle splitting directly result in convergence of ballistic out-scattered energy deviations towards zero, for a given number of discrete directions M. At high solid-angle splitting of (24 x 24), deviations from out-scattered energy conservation are less than 0.5% for all discrete direction numbers, indicating that use of a fine-enough solid-angle splitting density is able to accurately conserve ballistic out-scattered energy effectively without additional treatment after FVM directional discretization. For reference, in order to obtain conservation within 0.5%, splittings of (24 x 24), (24 x 24), (16 x 16), and (12 x 12) are required for M = 48-168, respectively.

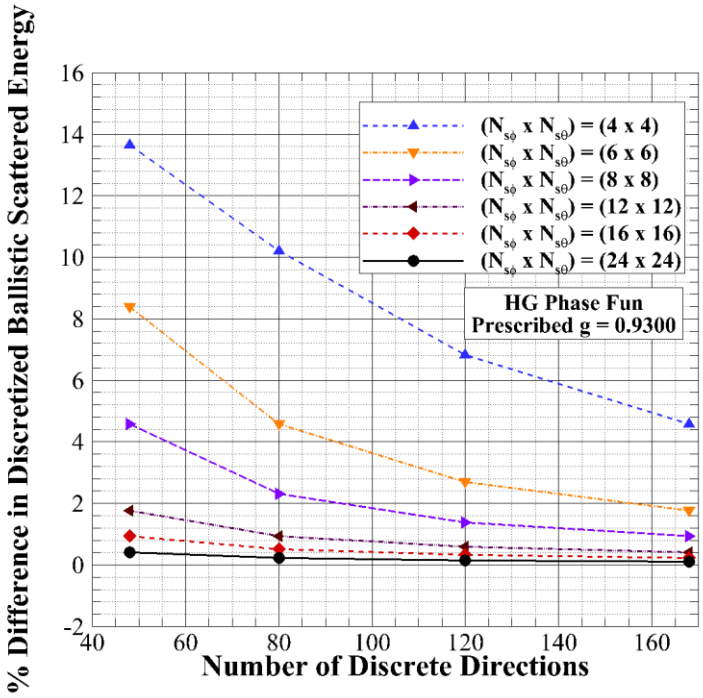

Figure 7.15: Deviation from ballistic scattered energy conservation versus number of discrete directions for HG phase function with g = 0.9300 using the FVM with various solid-angle splitting levels

In addition to the analysis in Figure 7.15, it is necessary to examine whether solid-angle splitting is able to accurately preserve the overall phase-function asymmetry factor after directional discretization [Hunter and Guo 2014c]. Recall that this was not the case for diffuse radiation, as solid-angle splitting resulted in underpredictions in g. This notion is presented in Figure 7.16, in which the deviations in ballistic asymmetry factor are plotted for the same directional quadratures and splitting levels as Figure 7.15. For low splitting resolution, asymmetry factor deviations are noticeable for all quadratures. As splitting is increased, so that ballistic out-scattered energy is conserved accurately, ballistic asymmetry factor once again tends to underpredict the prescribed value. For (24 x 24) splitting, the discretized ballistic g values are 0.9144, 0.9230, 0.9264, and 0.9280 for the four quadrature levels. These deviations

are not as large as those encountered for diffuse radiation in Chapter 4, although they may still result in significant errors due to angular false scattering. To this end, additional treatment to conserve both out-scattered energy and asymmetry factor for ballistic radiation is required.

In order to achieve simultaneous conservation after FVM discretization, Hunter and Guo's 2012 normalization for ballistic radiation can be modified for the FVM, as follows [Hunter and Guo 2014c]:

$$\widetilde{\Phi}^{l^B l} = (1 + A^{l^B l})\overline{\Phi}^{l^B l} \tag{7.10}$$

where the ballistic normalization parameters $A^{l^B l}$ are generated, using QR factorization or least-squares, such that the normalized ballistic scattering phase function $\widetilde{\Phi}^{l^B l}$ concurrently satisfies Eqs. (7.8a) and (7.8b).

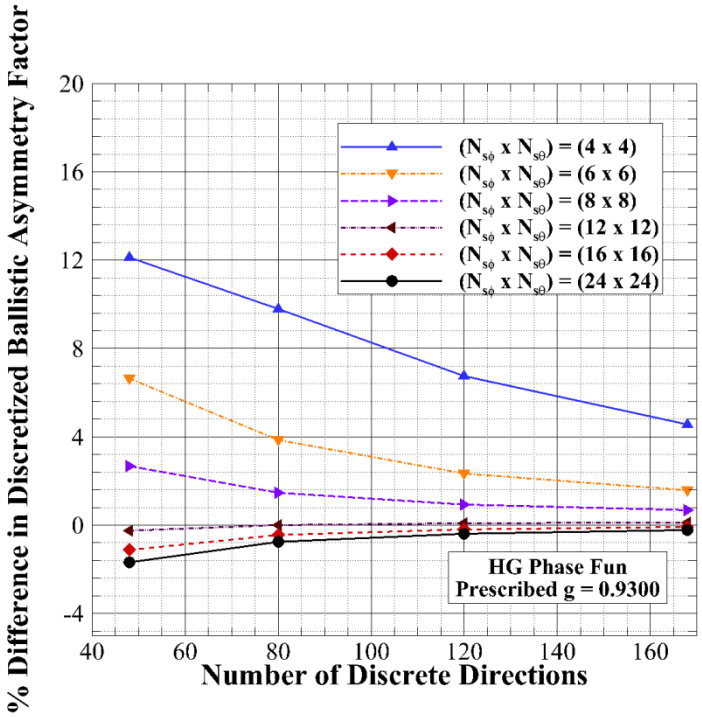

Figure 7.16: Deviation from ballistic asymmetry factor conservation versus number of discrete directions for HG phase function with g = 0.9300 using the FVM with various solid-angle splitting levels

7.2.2 Impact of Hunter and Guo's 2012 Normalization on Radiation Transfer Results

While Figures 7.15 and 7.16 provide the mathematical reasoning behind application of ballistic normalization for the FVM, analysis of the impact of normalization on ultrafast radiation transfer predictions will further show the necessity for such a treatment to avoid angular false scattering error [Hunter and Guo 2014c]. The first benchmark test problem analyzed involves ultrafast radiation transfer in an anisotropically scattering (g = 0.9300) medium housed in a cubic enclosure, with all enclosure walls taken as cold and black. The optical thickness of the medium is taken as τ = 1.0, and the scattering albedo is taken as ω = 1.0. The boundary wall at z^* = 0 is irradiated by a normal, collimated incidence of unity intensity. The spatial and temporal grid size are taken as $x^* = y^* = z^* =$ 0.04 and t^* = 0.03, respectively. As the forthcoming analyses are being performed to investigate the impact of ballistic phase function normalization only for ultrafast radiation transfer, the diffuse phase-function is normalized in order to accurately conserve scattered energy and asymmetry factor simultaneously in all cases.

Figures 7.17(a-b) investigate the impact of ballistic phase function normalization on ultrafast heat fluxes at the centerline of the wall opposite from the collimated source, i.e. $Q(x^*, y^* = 0.5, z^* = 1.0)$, generated using the FVM with and without ballistic normalization at different non-dimensional times. Heat fluxes are generated in Figure 7.17a for M = 80, and in Figure 7.17b for M = 168. FVM heat fluxes without ballistic normalization are presented for (6 x 6) and (24 x 24) solid-angle splitting, while FVM heat fluxes using Hunter and Guo's 2012 ballistic normalization are presented with (4 x 4) solid-angle splitting. In addition to FVM profiles, heat fluxes generated using the DOM with both ballistic scattered energy averaging and with Hunter and Guo's 2012 ballistic normalization are presented, for comparison. Finally, for comparison at

large t^*, steady-state MC results (originally presented by Collin et al. [2011]) are also plotted, to gauge FVM accuracy.

In both figures, DOM heat flux profiles generated using ballistic scattered energy averaging greatly underpredict both FVM and MC, due to angular false scattering. However, when Hunter and Guo's 2012 normalization is applied to both the DOM and FVM, accurate conformity of between 1-2% between the two approximate methods is witnessed at all non-dimensional times. Additionally, at the steady-state $t^* = 3.0$, normalized FVM and DOM profiles differ from MC by <1% at the wall center (x^* = 0.5) for both M = 80 and 168. The accurate conformity of the two different numerical methods to one another, as well as accuracy when compared to reference MC solutions, reinforces the premise that conservation of ballistic out-scattered energy and asymmetry factor simultaneously will result in improved ultrafast radiation transfer predictions in anisotropically scattering media.

As previously mentioned, heat flux profiles generated using the FVM without ballistic normalization and using solid-angle splitting of (6 x 6) and (24 x 24) are also presented in Figures 7.17(a-b). For M = 80 in Figure 7.17a, the percent difference between the (6 x 6) non-normalized FVM and normalized FVM is between 1-3% at x^* = 0.5 for the three non-dimensional times. Increasing splitting to (24 x 24) reduces these differences to ~1%, corresponding to more accurate conservation of ballistic scattered energy and asymmetry factor. For M = 168 in Figure 7.17b, these differences are <0.75% for all non-dimensional times. These results indicate that the non-conservation of ballistic asymmetry factor, and the resulting angular false scattering errors, are not near as significant as for the DOM, although slight discrepancies in heat flux do still arise.

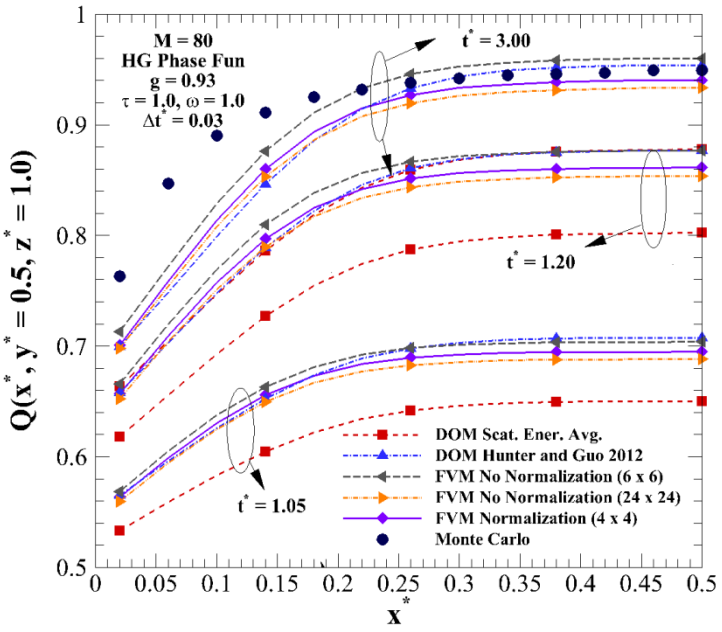

(a)

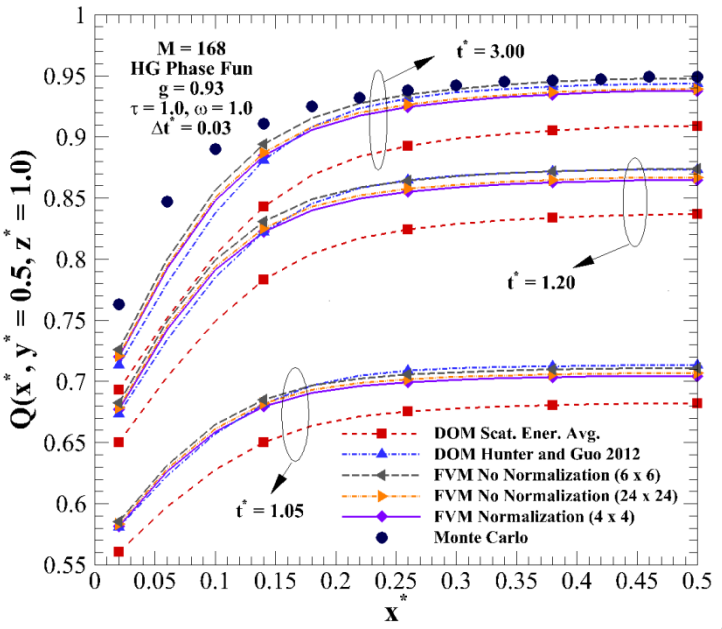

(b)

Figure 7.17: Impact of ballistic normalization on ultrafast Q(x*, y* = 0.5, z* = 1) wall at various times for an optically thinner ($\tau = 1.0$) medium with g = 0.9300 using DOM and FVM with a) M = 80 and b) M = 168 discrete directions and comparison with Monte Carlo

Figure 7.18 illustrates the impact of solid-angle splitting density on the percent difference in $Q(x^*, y^* = 0.5, z^* = 1.0)$ between FVM heat fluxes (generated both with and without ballistic phase-function normalization) and reference MC solutions at steady-state using M = 168. From Figure 7.15, (12 x 12) solid-angle splitting allows for ballistic out-scattered energy conservation to within 0.5%, while refinement to (24 x 24) improves conservation to within 0.1%. FVM heat fluxes generated using these two splitting densities underpredict MC heat fluxes by ~1.5% at the wall center, with higher differences of ~4-8% occurring near the wall. Application of Hunter and Guo's 2012 ballistic normalization using (24 x 24) splitting improves the difference between MC and FVM minimally to 1.0%. The minimal improvement occurring from normalization application conforms to the results in Figure 7.16, as without normalization, only a 2.9% change in scattering effect is observed, due to g being altered slightly from 0.9300 to 0.9280.

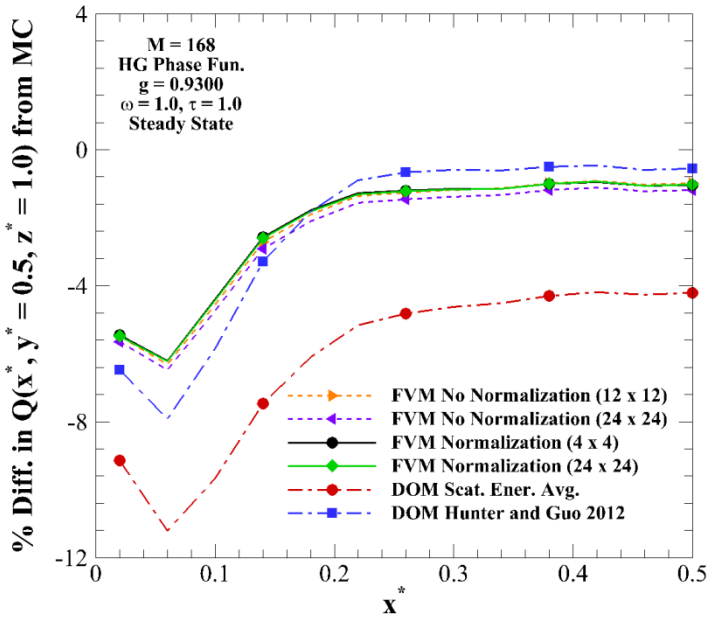

Figure 7.18: Percent difference in Q(x*, y* = 0.5, z* = 1) between MC solution and FVM solutions both with and without phase-function normalization using various solid angle splitting densities for M = 168 discrete directions

Analysis of FVM heat flux generated using Hunter and Guo's 2012 ballistic normalization with minimal (4 x 4) splitting leads to an important realization. FVM heat flux at minimal splitting is nearly identical to that generated with (24 x 24) splitting after application of ballistic normalization, with a maximum difference of less than 0.05%. This indicates that normalized results are highly independent of solid-angle splitting density, a result that was also confirmed for diffuse radiation in Figures 5.16(a-d). The ability to reduce the number of divisions per solid angle from 576 to 16, while maintaining radiation transfer accuracy, is extremely important in terms of computational efficiency.

Table 7.2 lists the computational time, in seconds, required to perform ($N_{s\phi}$ x $N_{s\theta}$) solid-angle splitting for varying numbers of discrete directions in order to calculate the average scattering phase function for FVM analysis. For M = 168, it takes 1935 seconds to perform (24 x 24) solid-angle splitting, while use of (4 x 4) splitting reduces the necessary computational time to only 1.4 seconds (a reduction of over 99%). Implementation of Hunter and Guo's 2012 ballistic normalization thus has the distinct advantage of being able to produce accurate FVM radiation transfer predictions while maximizing computational efficiency.

Table 7.2: Comparison of computational time, in seconds, required to perform solid-angle splitting for varying FVM quadrature

M	Computational Time (seconds) Required for ($N_{s\phi}$ x $N_{s\theta}$) Splitting						
	(4 x 4)	(6 x 6)	(8 x 8)	(12 x 12)	(16 x 16)	(20 x 20)	(24 x 24)
48	0.109	0.593	1.78	8.22	26.8	66.0	134
80	0.312	1.62	4.77	23.9	74.3	182	391
120	0.671	3.57	10.7	52.4	178	461	914
168	1.40	6.80	20.6	104.2	319	815	1935

Figures 7.19(a-b) examine the impact of ballistic phase function normalization on ultrafast $Q(x^*, y^* = 0.5, z^* = 1.0)$ at different non-dimensional times for both the DOM and FVM using M = 48 and M = 168 discrete directions, respectively, in an optically thicker (τ = 10.0) medium. The medium properties aside from the optical thickness are identical to those in Figures 7.17(a-b). The overall magnitude of the heat fluxes is much lower than for the optically thin medium, due to the increased number of scattering events encountered by radiant energy beams passing through the medium.

For both quadratures, use of the DOM with ballistic scattered energy averaging results in large errors, due to angular false scattering. At large t^*, the maximum differences between DOM with ballistic scattered energy averaging and Hunter and Guo's 2012 ballistic normalization are 20.6% and 8.9% for the two quadratures, respectively. Increase in directional quadrature is able to reduce, but not eliminate, angular false scattering errors.

For all non-dimensional times, increase in solid-angle splitting density improves FVM accuracy as compared to the normalized FVM. For example, for M = 48, the maximum differences between (6 x 6) FVM and FVM with Hunter and Guo's 2012 ballistic normalization are 3.9%, 4.6%, and 5.5% for t^* = 1.05, 1.50, and 4.50, respectively, while the maximum differences between (24 x 24) FVM and FVM with Hunter and Guo's 2012 ballistic normalization are 0.4%, 0.3%, and 0.1%, respectively, for the same times. Similar to the results for the optically thin medium, use of high solid-angle splitting is able to effectively conserve ballistic scattered energy and reduce angular false-scattering errors due to non-conservation of g. However, as discussed in Table 7.2, computational efficiency becomes of great concern when splitting resolution becomes extremely fine.

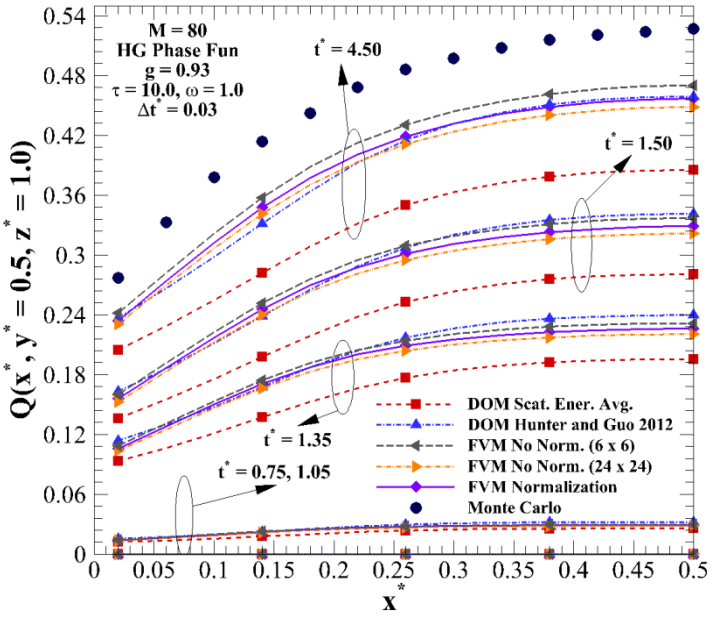

(a)

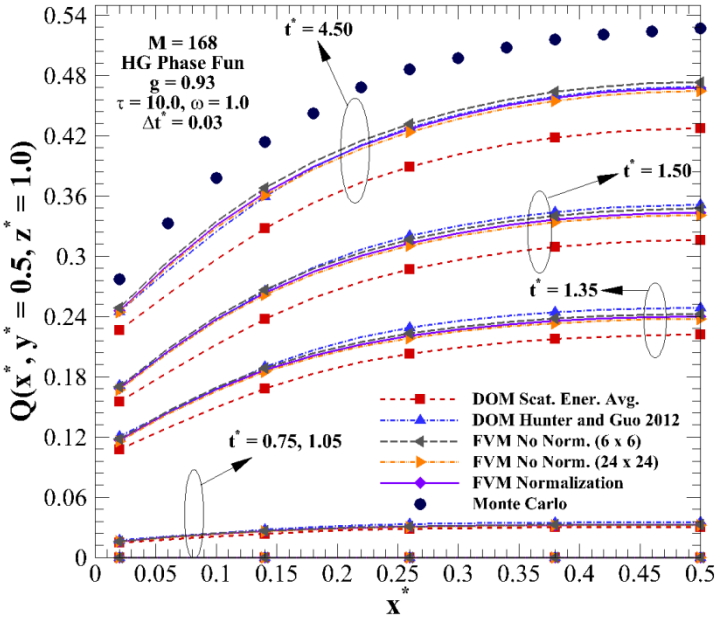

(b)

Figure 7.19: Impact of ballistic normalization on ultrafast Q(x*, y* = 0.5, z* = 1) at various times for an optically thicker ($\tau = 10.0$) medium with g = 0.9300 using DOM and FVM with a) M = 48 and b) M = 168 discrete directions and comparison with Monte Carlo

In general, for both quadrature sets, heat fluxes generated using the DOM and FVM with Hunter and Guo's 2012 ballistic normalization conform accurately to one another. At t^* =

4.50, the maximum percent differences between FVM and DOM when Hunter and Guo's 2012 ballistic normalization is applied are 7.4% and 1.9% for M = 48 and 168, respectively. The larger error for M = 48 can be attributed to ray effect. As quadrature is increased, ray effect error is effectively mitigated, and the normalized FVM and DOM profiles in Figure 7.19b conform accurately within 2% to each other at all locations.

After application of Hunter and Guo's 2012 ballistic normalization, neither approximate method is able to accurately conform to benchmark MC predictions in the optically thicker medium. For M = 48, the percent differences between the FVM and MC predictions range between -23.3% and -14.5% across the range of x^*. As quadrature is increased to M = 168, the differences become more uniform over x^*, ranging between -11.0% and -12.6%. The increase in angular quadrature is able to reduce ray effect error, but still does not result in accurate conformity between FVM and MC, conforming to the results for optically thick media witnessed in Figure 7.7 for DOM prediction of ultrafast radiation transfer in a medium with the same optical thickness.

To further support the necessity of ballistic phase-function normalization, analysis of ultrafast radiation transfer in a medium with tissue-like properties is presented in Figures 7.20-7.23. As discussed in Section 7.1.2.2, gauging the impact of ballistic phase-function normalization on the amount of energy absorbed by a medium by collimated laser irradiation is critical, in order to ensure that numerical simulations will be accurate when compared to experimental results. Strong errors due to angular false scattering in numerical results could have grave effects for *in vivo* experimentation, including damage to healthy tissue during laser hyperthermia or improper removal of cancerous tissue.

For the analyses in the forthcoming figures, the cubic enclosure and spatial grid are identical to those investigated in Figures 7.17-7.19. The optical properties are assumed to be that of human dermis [Cheong et al. 1990]: τ = 18.97, ω = 0.9858. The asymmetry factor of the medium is taken as g = 0.9300. As in the previous test problem the surface of the cubic enclosure at z^* = 0 is irradiated by a normal, collimated incidence of unity intensity. The remaining walls and medium are taken as cold. At the incident surface, a Fresnel reflection boundary condition is imposed [Kim and Guo 2004], in order to account for the mismatch in refractive index at the air/tissue interface. Additionally, the surface at z^* = 0 is taken to be a purely specular reflector. All other enclosure walls are taken as diffuse reflectors, with ρ_d = 0.5, due to the highly scattering optical thickness of turbid tissue and the theory of random walk [Guo and Kumar 2001, Guo and Kumar 2002].

Figures 7.20(a-b) investigate the impact of ballistic normalization on the ultrafast divergence of heat flux in the tissue medium at various non-dimensional times t^* using both DOM and FVM with and without ballistic normalization. Energy deposition profiles are taken along the line perpendicular to the incident surface, and passing through the cube center, i.e. $\nabla \cdot q_r(x^* = 0.5, y^* = 0.5, z^*)$. Divergence profiles in Figure 7.20a are generated using M = 80 discrete directions, while those in Figure 7.20b are generated using M = 168.

For M = 80, large discrepancies between energy deposition calculated using the DOM with ballistic scattered energy averaging and Hunter and Guo's 2012 ballistic normalization are observed at times where energy deposition is non-negligible. At $z^* = 0.02$, energy deposition calculated with ballistic scattered energy averaging is roughly ~10-12% larger than when Hunter and Guo's 2012 ballistic normalization is applied, and 11-24% smaller at z^* = 1.0. Angular false scattering, occurring due to an alteration in g from 0.9300 to 0.8364, results in radiant energy

being scattered in a less strong-forward fashion, leading to higher energy deposition near the source and lower deposition near the opposite wall.

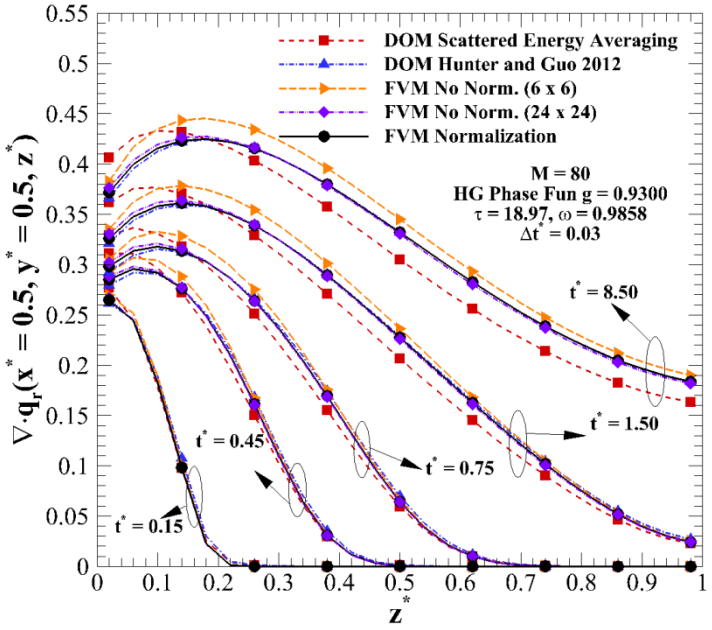

(a)

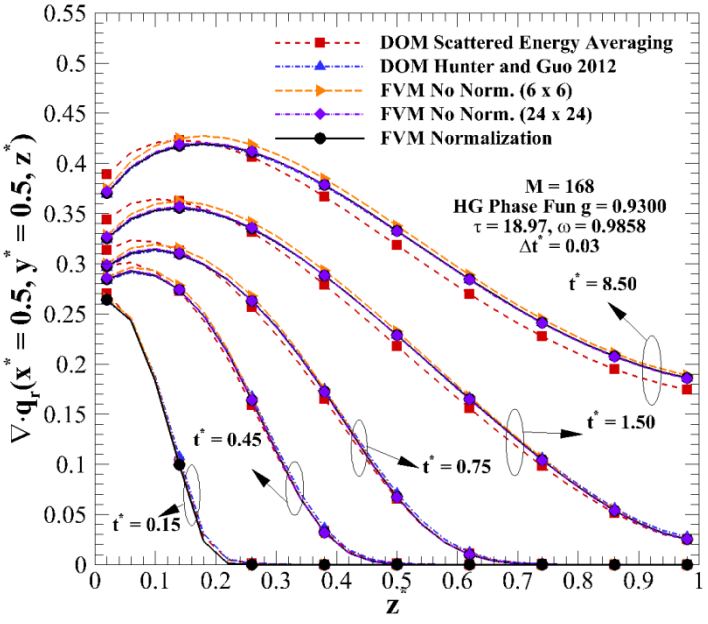

(b)

Figure 7.20: Impact of ballistic normalization on $\nabla \cdot q_r(x^* = 0.5, y^* = 0.5, z^*)$ at different non-dimensional times using DOM and FVM with a) M = 80 and b) M = 168 discrete directions in a medium with tissue-mimicking properties

The impact of solid-angle splitting for the FVM without ballistic normalization can be clearly witnessed in Figure 7.20a. Energy deposition calculated using (6 x 6) FVM with no ballistic normalization overpredicts the FVM using Hunter and Guo's 2012 ballistic normalization by maximums of 11.5%, 4.8%, and 4.8% at t^* = 0.45, 1.50, and 8.50, respectively, corresponding to a discretized g = 0.9658. Increasing splitting to (24 x 24) reduces these errors to 7.4%, 2.1%, and 1.1% at the same values of t^*, respectively, corresponding to discretized g = 0.9280. Minimal deviations in discretized asymmetry factor result in larger error at small t^*, but minimal error as the steady-state condition is approached. Accurate conformity between normalized FVM and DOM is witnessed where energy deposition is non-negligible, with a maximum difference of 1.5% occurring at t^* = 8.50.

The results in Figure 7.20b reveal a similar pattern. Energy deposition determined using DOM with ballistic scattered energy averaging overpredicts DOM with Hunter and Guo's 2012 ballistic normalization by ~5% near the source, and underpredicts by between 6-17% near the far wall, indicating a reduction in the discrepancies witnessed in Figure 7.20a due to more accurate conservation of discretized ballistic asymmetry factor (g = 0.8822) with higher discrete direction number.

Increase in discrete direction number reduces the error caused by a lack of solid-angle splitting in the FVM, as witnessed in Figure 7.20b. FVM energy deposition profiles generated without normalization using (6 x 6) solid-angle splitting result in maximum differences of 3.0%, 1.9%, and 1.8% for t^* = 0.45, 1.50, and 8.50, respectively, while (24 x 24) splitting reduces errors to 1.7%, 1.0%, and 0.4%, respectively. While these errors are minimal, use of (24 x 24) for M = 168 reduces computational efficiency by over 99% as compared to normalized FVM with (4 x 4) splitting, as seen in Table 7.2, while replicating the results accurately.

Figure 7.21 depicts contours of percent difference in divergence of radiative heat flux $\nabla \cdot q_r(x^*, y^* = 0.5, z^*)$ along the plane cutting through the center of the cubic enclosure calculated using the DOM both with ballistic scattered energy averaging and Hunter and Guo's 2012 ballistic normalization. Results are presented for M = 80 discrete directions. Near the incident source at z^* = 0.02, ballistic scattered energy averaging generates heat fluxes that are between 9-11% larger than those generated using Hunter and Guo's 2012 ballistic normalization. As distance from the source wall increases, percentage differences start to decrease, and then eventually become negative, due to a lack of energy propagation to this section of the medium stemming from alteration in discretized g to 0.8364. Near the wall opposite from the source (z^* = 0.98), the differences range between -10% and -12%, indicating the substantial impact of angular false scattering.

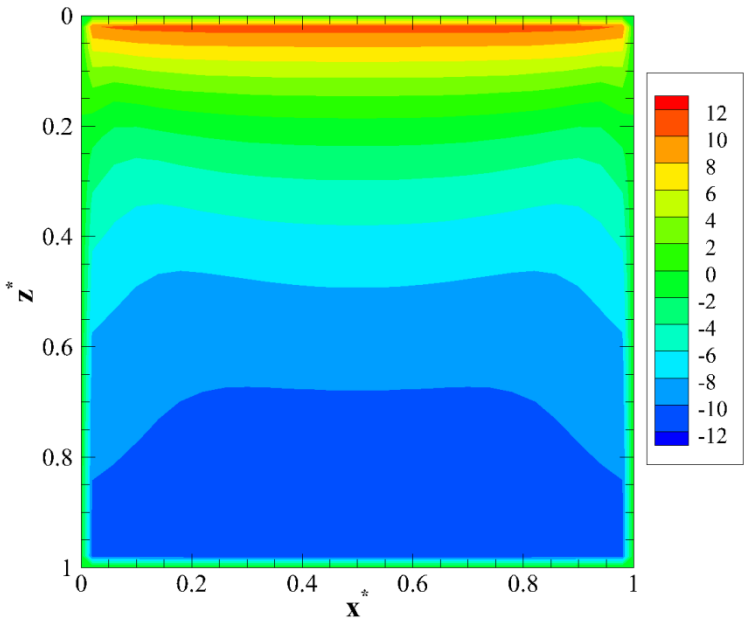

Figure 7.21: Contours of percentage difference in $\nabla \cdot q_r(x^*, y^* = 0.5, z^*)$ between DOM with ballistic energy normalization only and DOM with Hunter and Guo's ballistic normalization applied for M = 80 discrete directions in medium with tissue-mimicking properties

Figure 7.22 plots similar percentage difference contours in divergence of radiative heat flux between non-normalized FVM with (6 x 6) solid-angle splitting and normalized FVM using Hunter and Guo's 2012 ballistic normalization. At all locations in the medium, the heat flux generated using (6 x 6) splitting with no normalization overpredicts the normalized results. Near the source (z^* = 0.02), the differences are ~2-3%, while the maximum difference is ~5%. The pattern in percentage difference stems from the alteration of g to a discretized value of 0.9658 when (6 x 6) splitting is applied, indicating that the collimated irradiation scatters forward more strongly throughout the medium.

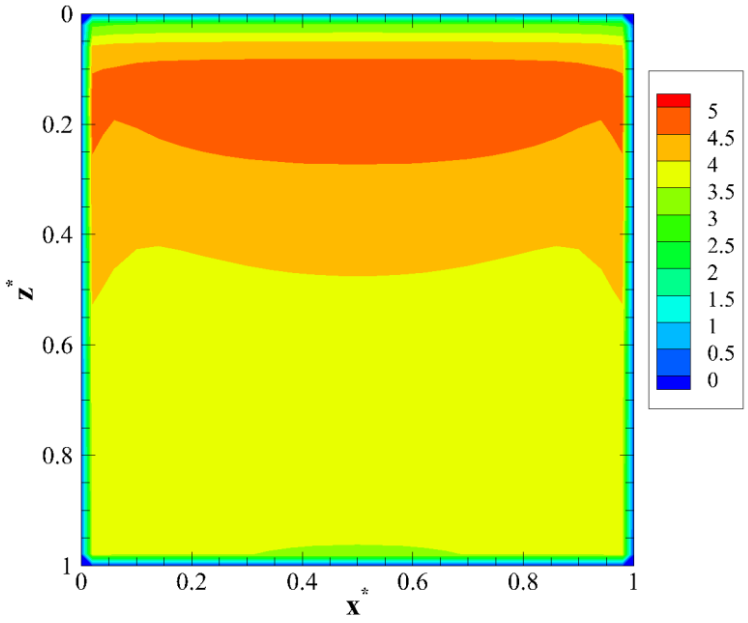

Figure 7.22: Contours of percentage difference in $\nabla \cdot q_r(x^*, y^* = 0.5, z^*)$ between FVM with and without Hunter and Guo's ballistic normalization using ($N_{s\phi}$ x $N_{s\theta}$) = (6 x 6) solid-angle splitting and M = 80 discrete directions in a medium with tissue-mimicking properties

As an additional means of justifying the use of Hunter and Guo's 2012 ballistic normalization, Figure 7.23 presents contours of percentage difference in divergence of heat flux between DOM and FVM, with Hunter and Guo's 2012 ballistic normalization implemented for

both. Throughout the entire selected slice of tissue, excellent agreement between the DOM and FVM is witnessed. The two approximate methods conform to each other within 1.5% at all locations. The accurate conformity between normalized DOM and FVM gives confidence that ballistic scattered energy and asymmetry factor are being conserved after directional discretization, leading to an improvement in numerically predicted radiation transfer results. Additionally, it indicates that either approximate method may be implemented for accurate numerical solutions to the ERT, as long as proper normalization is realized [Hunter and Guo 2014c].

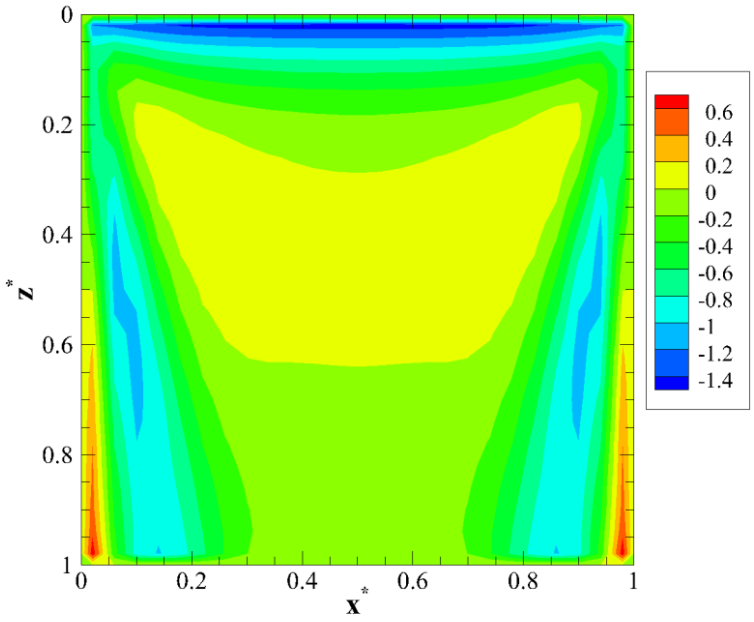

Figure 7.23: Contours of percentage difference in $\nabla \cdot q_r(x^*, y^* = 0.5, z^*)$ between FVM and DOM using Hunter and Guo's ballistic normalization for M = 80 discrete directions in medium with tissue-mimicking properties

7.3 Summary

In this chapter, the concept of phase-function normalization for ballistic radiation was introduced. The phase-function normalization approaches introduced in the previous chapters for diffuse radiation do not necessarily conserve ballistic out-scattered energy and asymmetry factor, and thus additional treatment is explored in order to limit ballistic angular false scattering errors. For the DOM, large deviations in ballistic out-scattered energy occur for highly-anisotropic scattering, with the specific angle of incidence playing a large role in the exact conservation values. Ballistic out-scattered energy can be conserved accurately using a ballistic normalization similar to Eq. (4.10). This approach, however, results in strong deviations in ballistic asymmetry factor conservation. Ballistic asymmetry factor non-conservation was shown to lead to strong angular false scattering errors in ultrafast radiation transfer predictions.

Modification of both Hunter and Guo's 2012 and 2014 normalization approaches for diffuse radiation were presented to accurately conserve both ballistic out-scattered energy and asymmetry factor simultaneously. Both methods drastically improve DOM radiation transfer predictions with respect to benchmark Monte Carlo. However, for both normalizations, negative phase-function values can occur, leading to the necessity of negative intensity correction. Negative intensity correction is required for Hunter and Guo's 2014 normalization for all directional quadratures tested, due to strongly-negative backward-scattering parameters. For Hunter and Guo's 2012 normalization, negative phase-function values for ballistic radiation are only observed for low-order DOM quadrature. For both cases, negative intensity correction does not significantly impact radiation transfer predictions.

Similar to the results found in Chapter 5 for diffuse radiation, solid-angle splitting is able to conserve ballistic out-scattered energy after FVM discretization, but slight differences in

ballistic asymmetry factor persist, and angular false scattering causes minimal discrepancies in ultrafast radiation transfer. However, the major finding for the FVM is that ballistic normalization using Hunter and Guo's 2012 approach is able to produce accurate ultrafast predictions while maximizing computational efficiency. In a comparison of energy deposition in a tissue-like medium, FVM and DOM results are very similar when normalization is implemented, while lack of normalization produces noticeable errors. These errors could be devastating in biomedical applications, such as laser hyperthermia of cancerous tissue, as inaccurate measures of medium energy absorption could lead to either necrosis/damage to healthy tissue, or inadequate destruction of cancerous tissue.

In summary, for radiation transfer problems where the ultrafast propagation of radiant energy occurs, it is necessary to normalize the ballistic scattering phase function, in order to accurately conserve ballistic out-scattered energy and asymmetry factor simultaneously. Doing so will minimize angular false scattering errors, and lead to more accurate numerical predictions, which in turn can have enormous impacts on practical applications, including *in vivo* biomedical applications.

CHAPTER 8 : CONCLUSIONS

In this dissertation, the existence and root cause behind third-type of numerical discretization error, termed as “angular false scattering” is explored. This error stems from the angular discretization of scattering anisotropy, resulting from a non-conservation of phase-function asymmetry factor. Angular false scattering is, in fact, the true “false scattering”, as the resultant errors in radiation transfer predictions stem from alteration in medium scattering properties. The use of “false scattering” to describe numerical discretization errors in the spatial domain is, in fact, a misnomer, as it has zero dependence on scattering phase-function or angular discretization. Thus, it is preferable to call such errors as “numerical smearing”, as to not offer confusion as to the mechanisms behind such numerical errors.

For highly anisotropic scattering, it is shown that the common correction approaches in the field (phase-function normalization for DOM and solid-angle splitting for FVM) are able to conserve scattered energy accurately after discretization, but are not able to conserve phase-function asymmetry factor. Thus, to limit angular false scattering error, the necessity for additional phase-function treatment for both approximate numerical methods is illustrated.

To attack the issue of improving numerical radiation transfer predictions in highly anisotropic scattering media, two novel phase-function normalization techniques are presented and formulated for use with both DOM and FVM. The first normalization approach, called Hunter and Guo’s 2012 normalization, is able to conserve both scattered energy and asymmetry factor simultaneously after angular discretization through modification of all discrete phase-function values in the system. This normalization requires solution of an underdetermined system, and thus the solution with the minimum-norm is chosen. Application of Hunter and Guo’s 2012 normalization is shown to greatly improve DOM and FVM predictions as compared

with statistical Monte Carlo. Additionally, use of proper normalization is able to greatly reduce computational requirements for both DOM and FVM, by vastly reducing both the number of discrete directions and FVM solid-angle splitting density required to produce accurate radiation transfer predictions.

The second normalization approach outlined in this study, called Hunter and Guo's 2014 normalization, draws on the simplistic mathematical approach of two other normalization techniques that are able to conserve one of the two quantities of interest, but not both. In a novel fashion, conservation of scattered energy and asymmetry factor are achieved by sole normalization of the forward- and backward-scattering phase-function terms, which reduces the computational requirement witnessed for Hunter and Guo's 2012 normalization (where all terms in the system were modified). For the HG phase function approximation, Hunter and Guo's 2014 normalization is found to be a more efficient alternative to Hunter and Guo's 2012 normalization, without sacrificing radiation transfer accuracy with respect to Monte Carlo. For Legendre phase-function approximations, however, the major issue of negative phase-function values occurs, due to highly-negative backward parameters, and negative intensity correction is required to obtain convergent ERT solutions. Application of negative intensity correction does not appear to have an appreciable impact on ERT solution accuracy.

Finally, the necessity for additional phase-function normalization for problems involving ballistic radiation transport is presented. Accurate conservation of diffuse scattered energy and asymmetry factor with Hunter and Guo's normalization approaches does not conserve ballistic out-scattered energy and asymmetry factor simultaneously, mandating the necessity for additional treatment. Hunter and Guo's 2012 and 2014 normalizations for diffuse radiation are modified for use with ballistic radiation. Ultrafast radiation transfer generated using both DOM

and FVM predict accurately with respect to Monte Carlo and each other after application of ballistic normalization. Negative intensity correction is required for Hunter and Guo's 2014 ballistic normalization for nearly all phase-function approximations and quadratures, while for Hunter and Guo's 2012 ballistic normalization, negative intensity correction is only necessary for the lowest-order quadrature.

Table 8.1 lists the crucial characteristics of the five phase-function normalization approaches discussed in this study. From the characteristics in Table 8.1, and the conclusions from the previously described results, it is recommended that Hunter and Guo's 2014 normalization is applied for highly anisotropic scattering problems governed by the HG phase-function approximation for diffuse radiation. For Legendre phase-function approximations, and for problems involving ballistic radiation transport, Hunter and Guo's 2012 normalization should be implemented, as it minimizes the necessity for negative intensity correction while maintaining radiation transfer accuracy. It is important to mention that application of phase-function normalization does not adversely impact computational time. The normalization parameters can be pre-determined for a given quadrature set and phase-function approximation. For Hunter and Guo's 2012 normalization, determination of parameters using least-squares in MATLAB takes less than 10 seconds for M = 288 discrete directions, indicating minimal impact on overall computational times. For all other normalizations, parameters are generated almost instantly, as they don't require solution of a more complex matrix equation.

In summary, the major contribution of this research is the newfound ability to accurately model radiation transfer in highly anisotropic scattering media, such as turbid tissue, using approximate ERT solution methods. Such accuracy has not been previously achieved, showcasing a major obstacle in the field of radiation transfer. The ability to accurately and

efficiently determine radiation transfer in highly anisotropic media may have an immediate and groundbreaking impact, especially for biomedical applications where accurate conformity of numerical and experimental results is paramount to the safety of human subjects in *in vivo* applications.

Table 8.1: Comparison of scattered energy averaging, Mishchenko's E, Kamdem Tagne's g, Hunter and Guo's 2012, and Hunter and Guo's 2014 normalization techniques

	Scattered Energy Avg.	Mishchenko E	Kamdem Tagne g	Hunter and Guo 2012	Hunter and Guo 2014
Scattered Energy	Conserved	Conserved	No Mechanism for Conservation	Conserved	Conserved
Asymmetry Factor	No Mechanism for Conservation	No Mechanism for Conservation	Conserved	Conserved	Conserved
Vector/Matrix Normalization	Vector	Vector	Vector	Matrix	Vector
Phase-Function Terms Normalized	All	Forward Term Corresponding to Each Incoming Direction	Forward Term Corresponding to Each Incoming Direction	All	Forward and Backward Term Corresponding to Each Incoming Direction
Occurrence of Negative Phase-Function Values	None	BOTH Diffuse and Ballistic Radiation with Legendre PFs	BOTH Diffuse and Ballistic Radiation with Legendre PFs	Only for Ballistic Radiation with the Lowest Directional Order (N = 4)	Diffuse and Ballistic Radiation with Legendre PFs and Ballistic Radiation with HG PFs
Angular False Scattering Errors	High	High for Optically Thick Media	None, but High Errors due to Energy Non-Conservation	None	None

References

Abergel, R.P., Lyons, R., Dwyer, R., White, R.R., and Uitto, J., 1986, Use of lasers for closure of cutaneous wounds: experience with Nd:YAG, argon and CO2 lasers, *Journal of Dermatologic Surgery and Oncology*, vol. 12, pp. 1181-1185.

Albini, F.A., 1985, A model for fire spread in wildland fuels by radiation, *Combustion Science and Technology*, vol. 42, pp. 229-258.

Alves, M.A., Oliveira, P.J., and Pinho, F.T., 2003, A convergent and universally bounded interpolation scheme for the treatment of advection, *International Journal for Numerical Methods in Fluids*, vol. 41, pp. 47-75.

Anderson, R.R., and Parrish, J.A., 1983, Selective photothermolysis: Precise microsurgery by selective absorption of pulsed radiation, *Science*, vol. 220(4596), pp. 524-527.

Anghileri, L.J., and Robert, J., 1986, Hyperthermia in cancer treatment, Boca Raton: CRC Press.

Angstrom, A., Solar and terrestrial radiation: 1924, Report to the international commission for solar research on actinometric investigations of solar and atmospheric radiation, *Quarterly Journal of the Royal Meteorological Society*, vol. 50, pp. 121-126.

Arkin, H., Xu, L.X., and Holmes, K.R., 1994, Recent developments in modeling heat transfer in blood perfused tissues, *IEEE Transactions on Biomedical Engineering*, vol. 41, pp. 97-107.

Baek, S.W., Kim, M.Y., and Kim, J.S., 1998, Nonorthogonal finite-volume solutions of radiative heat transfer in a three-dimensional enclosure, *Numerical Heat Transfer B*, vol. 34, pp. 419-437.

Bass, L.S., and Treat, M.R., 1985, Laser tissue welding: a comprehensive review of current and future applications, *Lasers in Surgery and Medicine*, vol. 17, pp. 315-349.

Ben Salah, M., Askri, F., Slimi, K., Ben Nasrallah, S., 2004, Numerical resolution of the radiative transfer equation in a cylindrical enclosure with the finite-volume method, *International Journal of Heat and Mass Transfer*, vol. 47, pp. 2501-2509.

Bliss, R.W., 1961, Atmospheric radiation near the surface of the ground: a summary for engineers, *Solar Energy*, vol. 5, pp. 103-120.

Borjini, M.N., Guedri, K., and Said, R., 2007, Modeling of radiative heat transfer in 3D complex boiler with non-gray sooting media, *Journal of Quantitative Spectroscopy and Radiative Transfer*, vol. 105, pp. 167-179.

Boulet, P., Collin, A., and Consalvi, J.L., 2007, On the finite volume method and the discrete ordinates method regarding radiative heat transfer in acute forward anisotropic scattering media, *Journal of Quantitative Spectroscopy and Radiative Transfer,* vol. 104, pp. 460-473.

Carlson, B.G., 1971, Tables of symmetric equal weight quadrature EQ_N over the unit sphere, *Los Alamos Scientific Lab. Rept. LA-4734*, Los Alamos, New Mexico.

Carlson, B.G., and Lathrop, K.D., 1968, Transport Theory- The Method of Discrete-Ordinates, in H. Greenspan, C.N. Kelber, and D. Okrent (eds.), *Computing Methods in Reactor Physics*, Gorden and Breach, New York.

Chai, J.C., 2003, One-dimensional transient radiation heat transfer modeling using a finite-volume method, *Numerical Heat Transfer B,* vol. 44, pp. 187-208.

Chai, J.C., 2004, Transient radiative transfer in irregular two-dimensional geometries, *Journal of Quantitative Spectroscopy and Radiative Transfer*, vol. 84, pp. 281-294.

Chai, J.C., and Moder, J.P., 2000, Radiation heat transfer calculation using an angular-multiblock procedure, *Numerical Heat Transfer B*, vol. 38, pp. 1-13.

Chai, J.C., and Patankar, S.V., 2000, Finite-volume method for radiation heat transfer, in Minkowycz, W.K., and Sparrow, E.H. (eds.), *Advances in Numerical Heat Transfer,* vol. 2, Taylor and Francis, Boca Raton.

Chai, J.C., Hsu, P.-f., and Lam, Y.C., 2004, Three-dimensional transient radiative transfer modeling using the finite volume method, *Journal of Quantitative Spectroscopy and Radiative Transfer*, vol. 86, pp. 299-313.

Chai, J.C., Lee, H.S., and Patankar, S.V., 1993, Ray effect and false scattering in the discrete ordinates method, *Numerical Heat Transfer B*, vol. 24, pp. 373-389.

Chai, J.C., Lee, H.S., and Patankar, S.V., 1994, Finite volume method for radiation heat transfer, *Journal of Thermophysics and Heat Transfer*, vol. 8, pp. 419-425.

Chai, J.C., Lee, H.S., and Patankar, S.V., 1998, Improved treatment of scattering using the discrete ordinates method, *Journal of Thermophysics and Heat Transfer*, vol. 12, pp. 605-608.

Chai, J.C., Parthasarathy, G., Lee, H.S., and Patankar, S.V., 1995, Finite-volume radiation heat transfer procedure for irregular geometries, *Journal of Thermophysics and Heat Transfer*, vol. 9, pp. 410-415.

Chen, C., and Jaluria, Y., 2007, Modeling of radiation heat transfer in the drawing of an optical fiber with multilayer structure, *Journal of Heat Transfer*, vol. 129, pp. 342-352.

Cheong, W.F., Prahl, S.A., and Welch, A.J., 1990, A review of the optical properties of biological tissues, *IEEE Journal of Quantum Electronics*, vol. 26, pp. 2166-2185.

Choi, T.Y., and Grigoropoulos, C.P., 2002, Plasma and ablation dynamics in ultrafast laser processing of crystalline silicon, *Journal of Applied Physics*, vol. 92, pp. 4918-4925.

Chowdhury, I. H., Xu, X., and Weiner, A.M., 2005, Ultrafast double-pulse ablation of fused silica, *Applied Physics Letters*, vol. 86:151110.

Chui, E.H., and Raithby, G.D., 1992, Prediction of Radiative Transfer in Cylindrical Enclosures with the Finite Volume Method, *Journal of Thermophysics and Heat Transfer*, vol. 6, pp. 605-611.

Chui, E.H., and Raithby, G.D., 1993, Computation of radiant heat transfer on a nonorthogonal mesh using the finite-volume method, *Numerical Heat Transfer B*, vol. 23, pp. 269-288.

Chui, E.H., Raithby, G.D., and Hughes, P.M.J., 1992, Prediction of radiative transfer in cylindrical enclosures with the finite volume method, *Journal of Thermophysics and Heat Transfer*, vol. 6, pp. 605-611.

Chui, E.J., Hughes, P.M.J., and Raithby, G.D., 1993, Implementation of the finite-volume method for calculating radiative transfer in a pulverized fuel flame, *Combustion Science and Technology*, vol. 92, pp. 225-242.

Coelho, P.J., 2002a, Bounded skew high-order resolution schemes for the discrete ordinates method, *Journal of Computational Physics*, vol. 175, pp. 412-437.

Coelho, P.J., 2002b, The role of ray effects and false scattering on the accuracy of the standard and modified discrete ordinates methods, *Journal of Quantitative Spectroscopy and Radiative Transfer*, vol. 73, pp. 231-238.

Collin, A., Consalvi, J.L., and Boulet, P., 2011, Acute anisotropic scattering in a medium under collimated irradiation, *International Journal of Thermal Sciences,* vol. 50, pp. 19-24.

Crosbie, A.L., and Schrenker, R.G., 1984, Radiative transfer in a two-dimensional rectangular medium exposed to diffuse radiation, *Journal of Quantitative Spectroscopy and Radiative Transfer*, vol. 31, pp. 339-372.

Cucinotta, F.A., and Durante, M., 2006, Cancer risk from exposure to galactic cosmic rays: implications for space exploration by human beings, *The Lancet Oncology,* vol. 7, pp. 431-435.

Cumber, P.S., 2000, Ray effect mitigation in jet fire radiation modeling, *International Journal of Heat and Mass Transfer*, vol. 43, pp. 935-943.

Darwish, M.S., and Moukalled, F.H., 1994, Normalized variable and space formulation for high-resolution schemes, *Numerical Heat Transfer B*, vol. 26, pp. 79-96.

Das, C., Trivedi, A., Mitra, K., and Vo-Dinh, T., 2003, Experiments and numerical analysis of short pulse laser interaction with tissue phantoms containing inhomogeneities, *Applied Optics*, vol. 42, pp. 5173-5180.

de Ris, J., 1979, Fire radiation – A review, *17th Symposium (International) on Combustion*, vol. 17, pp. 1003-1016.

Dupret, F., Nicodeme, P., Ryckmans, Y., Wouters, P., and Crochet, M.J., 1990, Global modelling of heat transfer in crystal growth furnaces, *International Journal of Heat and Mass Transfer*, vol. 33, pp. 1849-1871.

Durante, M., and Cucinotta, A., 2008, Heavy ion carcinogenesis and human space exploration, *Nature Reviews Cancer*, vol. 8, pp. 465-472.

Edwards, D.K., and Balakrishnan, A., 1973, Thermal radiation by combustion gases, *International Journal of Heat and Mass Transfer*, vol. 16, pp. 25-40.

El Wakil, N.E., and Sacadura, J.F., 1992, Some improvements of the discrete ordinates method for the solution of the radiative transport equation in multidimensional anisotropically scattering media, *ASME-HTD*, vol. 203, ASME, New York.

Elsasser, W.M., 1942, Heat transfer by infrared radiation in the atmosphere, Harvard University: Blue Hill Meterological Observatory.

Endo, T., and Yamamoto, A., 2007, Development of new solid angle quadrature sets to satisfy even- and odd-moment conditions, *Journal of Nuclear Science and Technology*., vol. 44, no. 10, pp. 1249-1258.

Farmer, J.T, and Howell, J.R., 1994, Monte Carlo prediction of radiative heat transfer in inhomogeneous, anisotropic, nongray media, *Journal of Thermophysics and Heat Transfer*, vol. 8, pp. 133-139.

Fiveland, W.A., 1984, Discrete-ordinates solutions of the radiative transport equation for rectangular enclosures, *Journal of Heat Transfer*, vol. 106, pp. 699-706.

Fiveland, W.A., 1987, Discrete-ordinates methods for radiative heat transfer in isotropically and anisotropically scattering media, *Journal of Heat Transfer*, vol. 109, pp. 809-812.

Fiveland, W.A., 1988, Three dimensional radiative heat transfer solution by the discrete-ordinates method, *Journal of Thermophysics Heat Transfer*, vol. 2, pp. 309-316.

Fiveland, W.A., 1991, The selection of discrete ordinates quadrature sets for anisotropic scattering, *Fundamentals of Radiation Heat Transfer* ASME-HTD, vol. 160.

Flock, S.T., Wilson, B.C., and Patterson, M.S., 1989, Monte Carlo modeling of light propagation in highly scattering tissues – II: Comparison with measurements in phantoms, *IEEE Transactions on Biomedical Engineering*, vol. 36, pp. 1169-1173.

Fried, N.M., Hung, V.C., and Walsh, J.T. Jr., 1999, Laser tissue welding: Laser spot size and beam profile studies, *IEEE Journal of Selected Topics in Quantum Electronics*, vol. 5, pp. 1004-1012.

Gaskell, P.H., and Lau, A.K.C., 1988, Curvature compensated convective transport: SMART, a new boundedness preserving transport algorithm, *International Journal for Numerical Methods in Fluids*, vol. 8, pp. 617-641.

Goody, R.M., and Yung, Y.L., 1995, Atmospheric radiation: Theoretical basis, Oxford University Press.

Gordon, W.E., 1958, Incoherent scattering of radio waves by free electrons with applications to space exploration by radar, *Proceedings of the IRE*, vol. 46, pp. 1824-1829.

Gratzel, M., 2005, Mesoscopic solar cells for electricity and hydrogen production from sunlight, *Chemistry Letters*, vol. 34, pp. 8-13.

Guedri, K., Abbassi, M.A., Borjini, M.N., Halouani, K., and Said, R., 2009, Application of the finite-voluem method to study the effects of baffles on radiative heat transfer in complex enclosures, *Numerical Heat Transfer A*, vol. 55, pp. 780-806.

Guo, Z., Aber, J., Garetz, B., and Kumar, S., 2002, Monte Carlo simulation and experiments of pulsed radiative transfer, *Journal of Quantitative Spectroscopy and Radiative Transfer*, vol. 73, pp. 159-168.

Guo, Z., and Kumar, S., 2000, Equivalent isotropic scattering formulation for transient short-pulse radiative transfer in anisotropic scattering planar media, *Applied Optics*, vol. 39, pp. 4411-4417.

Guo, Z., and Kumar, S., 2001, Discrete-ordinates solution of short-pulsed laser transport in two-dimensional turbid media, *Applied Optics*, vol. 40, pp. 3156-3163.

Guo, Z., and Kumar, S., 2002, Three-dimensional discrete ordinates method in transient radiative transfer, *Journal of Thermophysics and Heat Transfer*, vol. 16, pp. 289-296.

Guo, Z., and Maruyama, S., 1999, Scaling anisotropic scattering in radiative transfer in three-dimensional nonhomogeneous media, *International Communications in Heat and Mass Transfer*, vol. 26, pp. 997-1007.

Guo, Z., and Maruyama, S., 2000, Radiative heat transfer in nonhomogeneous, nongray, and anisotropic scattering media, *International Journal of Heat and Mass Transfer*, vol. 43, pp. 2325-2336.

Guo, Z., Kumar, S., and San, K.C., 2000, Multidimensional Monte Carlo simulation of short-pulse laser transport in scattering media, *Journal of Thermophysics and Heat Transfer*, vol. 14, pp. 504-511.

Guo, Z., Maruyama, S., and Tagawa, S., 1998, Combined heat transfer in floating zone growth of large silicon crystals with radiation on diffuse and specular surfaces, *Journal of Crystal Growth*, vol. 194, pp. 321-330.

Guo, Z., Wan, S.K., Kim, K.H., and Kosaraju, C., 2003, Comparing diffusion approximation with radiation transfer analysis for light transport in tissues, *Optical Review*, vol. 10, pp. 415-421.

Guo, Z., Wang, X.L., and Huan, H., 2010, Plasma-mediated ablation of biofilm contamination, *Applied Surface Science*, vol. 257, pp. 1247-1253.

Guo, Z., and Hunter, B., 2013, Advances in ultrafast radiative transfer modeling and applications: A review, *Heat Transfer Research*, vol. 44, pp. 303-344.

Harten, A., 1983, High resolution schemes for hyperbolic conservation laws, *Journal of Computational Physics*, vol. 49, pp. 357-393.

Hatano, M., Moon, S., Lee, M., Suzuki, K., and Grigoropoulos, C.P., 2000. Excimer laser-induced temperature field in melting and resolidification of silicon thin films, *Journal of Applied Physics*, vol. 87, pp. 36-43

Howell, J.R., 1998, The Monte Carlo method in radiative heat transfer, *ASME Journal of Heat Transfer*, vol. 120, pp. 547-560.

Huang, H., and Guo, Z., 2009a, Ultra-short pulsed laser PDMS thin-layer separation and micro-fabrication, *Journal of Micromechanics and Microengineering*, vol. 19:005007.

Huang, H., and Guo, Z., 2009b, Human dermis separation via ultra-short pulsed laser plasma-mediated ablation, *Journal of Physics D: Applied Physics*, vol. 42:165204.

Huang, H., and Guo, Z., 2010, Ultrashort pulsed laser ablation and stripping of freeze-dried dermis, *Lasers in Medical Science*, vol. 25, pp. 517-524.

Hunter, B., and Guo, Z., 2012c, Phase function normalization for accurate analysis of ultrafast collimated radiative transfer, *Applied Optics*, vol. 51, pp. 2192-2201.

Hunter, B., and Guo, Z., 2011, Comparison of discrete-ordinates method and finite volume method for steady-state and ultrafast radiative transfer analysis in cylindrical coordinates, *Numerical Heat Transfer B*, vol. 59, pp. 339-359.

Hunter, B., and Guo, Z., 2012a, Conservation of asymmetry factor in phase function discretization for radiative transfer analysis in anisotropic scattering media, *International Journal of Heat and Mass Transfer*, 2011, vol. 55, nos. 5-6, pp. 1544-1552.

Hunter, B., and Guo, Z., 2012b, Reduction of angle splitting and computational time for the finite volume method via phase function normalization, *International Journal of Heat and Mass Transfer*, 2011, vol. 55, nos. 9-10, pp. 2449-2460.

Hunter, B., and Guo, Z., 2012d, Phase-function normalization in 3-D discrete-ordinates solution of radiative transfer – Part I: Conservation of scattered energy and asymmetry factor, *Numerical Heat Transfer* B, vol. 62, pp. 203-222.

Hunter, B., and Guo, Z., 2012e. Phase-function normalization in 3-D discrete-ordinates solution of radiative transfer – Part II: Benchmark comparisons, *Numerical Heat Transfer B*, vol. 62, pp. 223-242.

Hunter, B., and Guo, Z., 2013, Comparison of quadrature schemes in DOM for anisotropic scattering radiative transfer analysis, *Numerical Heat Transfer B*, vol. 63, pp. 485-507.

Hunter, B., and Guo, Z., 2014a, Normalization of various phase functions for radiative heat transfer analysis in a solar absorber tube, *Heat Transfer Engineering*, vol. 35, no. 6-8, pp. 791-801.

Hunter, B., and Guo, Z., 2014b, A new and simple technique to normalize HG phase function for conserving scattered energy and asymmetry factor, *Numerical Heat Transfer B*, vol. 65, pp. 195-217

Hunter, B., and Guo, Z., 2014c, Improved treatment of anisotropic scattering for ultrafast radiative transfer analysis, *Journal of Heat Transfer*, *submitted for review.*

Hunter, B., and Guo, Z., 2014d, Improved treatment of anisotropic scattering in radiative transfer analysis using the finite volume method, *Heat Transfer Engineering*, *submitted for review.*

Hunter, B., and Guo, Z., 2014e, Applicability of phase-function normalization techniques for radiation transfer computation with DOM, *Numerical Heat Transfer B*, *submitted for review*

Jamaluddin, A.S., and Smith, P.J., 1988, Predicting radiative transfer in axisymmetric cylindrical enclosures using the discrete ordinates method, *Combustion Science and Technology*, vol. 62, pp. 173-186.

Jaunich, M., Raje, S., Kim, K.H., Mitra, K., and Guo, Z., 2008, Bio-Heat Transfer Analysis during Short Pulse Laser Irradiation of Tissues, *International Journal of Heat and Mass Transfer*, vol. 51, pp. 5511-5521.

Jendoubi, S., Lee, H.S., and Kim, T.K., 1993, Discrete ordinates solutions for radiatively participating media in a cylindrical enclosure, *Journal of Thermophysics and Heat Transfer*, vol. 7, pp. 213-219.

Jessee, J.P., and Fiveland, W.A., 1997, Bounded, high-resolution differencing schemes applied to the discrete ordinates method, *Journal of Thermophysics and Heat Transfer,* vol. 11, pp. 540-548.

Jiao, J., and Guo, Z., 2009, Thermal Interaction of Short-Pulsed Laser Focused Beams with Skin Tissues, *Physics in Medicine and Biology.*, vol. 54, pp. 4225-4241.

Jiao, J., and Guo, Z., 2011, Modeling of ultrashort pulsed laser ablation in water and biological tissues in cylindrical coordinates, *Applied Physics B*, vol. 103, pp. 195-205.

Kamdem Tagne, H.T., 2013, Phase-function normalization in discrete ordinate method, *Journal of Thermophysics and Heat Transfer, submitted for review.*

Kamdem Tagne, H.T., and Ballis, D.D., 2005, Radiative heat transfer using isotropic scaling approximation: application to fibrous medium, *Journal of Heat Transfer*, vol. 127, pp. 1115-1123.

Kamel, G., Naceur, B.M., Rachid, M., and Rachid, S., 2006, Formulation and testing of the FTn finite volume method for radiation in 3-D complex inhomogeneous participating media, *Journal of Quantitative Spectroscopy and Radiative Transfer*, vol. 98, pp. 425-445.

Karni, J., Kribus, A., Rubin, R., and Doron, P., 1998, The 'Porcupine': a novel high-flux absorber for volumetric solar receivers, *Journal of Solar Energy-Transactions of the ASME*, vol. 120, pp. 85-95.

Kim, B.-M., Feit, M.D., Rubenchik, A.M., Joslin, E.M., Celliers, P.M., Eichler, J. et al., 2001, Influence of pulse duration on ultrashort laser pulse ablation of biological tissues, *Journal of Biomedical Optics*, vol. 6, pp. 332-338.

Kim, K.H., and Guo, Z., 2004, Ultrafast radiation heat transfer in laser tissue welding and soldering, *Numerical Heat Transfer A*, vol. 46, pp. 23-40.

Kim, K.H., and Guo, Z., 2007, Multi-time-scale heat transfer modeling of turbid tissues exposed to short-pulsed irradiations, *Computer Methods and Programs in Biomedicine*, vol. 86, pp. 112-123.

Kim, M.Y., 2008, Assessment of the axisymmetric radiative heat transfer in a cylindrical enclosure with the finite volume method, *International Journal of Heat and Mass Transfer*, vol. 51, pp. 5144-5153.

Kim, M.Y., and Baek, S.W., 1997, Analysis of radiative transfer in cylindrical enclosures using the finite volume method, *Journal of Thermophysics and Heat Transfer*, vol. 11, pp. 246-252.

Kim, M.Y., Baek, S.W., and Park, J.H., 2001, Unstructured finite-volume method for radiative heat transfer in a complex two-dimensional geometry with obstacles, *Numerical Heat Transfer B*, vol. 39, pp. 617-635.

Kim, S.H., and Huh, K.Y., 2000, A new angular discretization scheme of the finite volume method for 3-D radiative heat transfer in absorbing, emitting, and anisotropically scattering media, *International Journal of Heat and Mass Transfer*, vol. 43, pp. 1233-1242.

Kim, T.K., and Lee, H., 1988, Effect of anisotropic scattering on radiative heat transfer in two-dimensional rectangular enclosures, *International Journal of Heat and Mass Transfer*, vol. 31, pp. 1711-1721.

Kim, T.K., and Lee, H., 1990, Scaled isotropic results for two-dimensional anisotropic scattering media, *Journal of Heat Transfer*, vol. 112, pp. 721-727.

Korkin, S.V., Lyapustin, A.I., and Rozanov, V.V., 2012, Modifications of discrete ordinate method for computations with high scattering anisotropy: comparative analysis, *Journal of Quantitative Spectroscopy and Radiative Transfer*, vol. 113, pp. 2040-2048.

Kumar, S., and Mitra, K., 1999, Microscale aspects of thermal radiation transport and laser applications, *Advances in Heat Transfer*, vol. 33, pp.187-294.

Lee, H., and Buckius, R.O., 1982, Scaling anisotropic scattering in radiation heat transfer for a planar medium, *Journal of Heat Transfer*, vol. 104, pp. 68-75.

Leonard, B.P., 1987, Locally modified quick scheme for highly convective 2-D and 3-D flows, in Taylor, C., and Morgan, K. (eds.), *Numerical Methods in Laminar and Turbulent Flows*, Pineridge Press, Swansea, UK.

Li, B-W., Yao, Q., Cao, X-Y., and Cen, K-F., 1998, A new discrete ordinates quadrature scheme for three-dimensional radiative heat transfer, *Journal of Heat Transfer*, vol. 120, pp. 514-518.

Li, X., Weiqiang, K., Wang, Z., Chang, C., and Bai, F., 2010, Thermal model and thermodynamic performance of molten salt cavity receiver, *Renewable Energy*, vol. 35, pp. 981-988.

Liu, F., Becker, H.A., and Pollard, A., 1996, Spatial differencing schemes of the discrete-ordinates method, *Numerical Heat Transfer B*, vol. 30, pp. 23-43.

Liu, F., Yoo, K.M., and Alfano, R.R., 1993, Ultrafast laser-pulse transmission and imaging through biological tissues, *Applied Optics*, vol. 32, pp. 554-558.

Liu, L.H., Ruan, L.M., and Tan, H.P., 2002, On the discrete ordinates method for radiative heat transfer in anisotropically scattering media, *International Journal of Heat and Mass Transfer,* vol. 45, pp. 3259-3262.

Liu, X., Du, D., and Mourou, G., 1997, Laser ablation and micromachining with ultrashort laser pulses, *IEEE Journal of Quantum Electronics*, vol. 33, pp. 1706-1716.

Loesel, F.H., Fischer, J.P., Gotz, M.H., Horvath, C., Juhasz, T., Noack, F. et al., 1998, Non-thermal ablation of neural tissue with femtosecond laser pulses, *Applied Physics B*, vol. 66, pp. 121-128.

Longoni, G., and Haghighat, A., 2001, Development of new quadrature sets with the "ordinate splitting" technique, *Proceedings of 2001 ANS International Meeting on Mathematical Methods for Nuclear Applications*, Salt Lake City, Utah, Sept. 9-13.

Lu, X., and Hsu, P.-f., 2004, Reverse Monte Carlo for transient radiative transfer in participating media, *Journal of Heat Transfer*, vol. 126, pp. 621-627.

Lu, X., and Hsu, P.-f., 2005, Reverse Monte Carlo simulations of light pulse propagation in nonhomogeneous media, *Journal of Quantitative Spectroscopy and Radiative Transfer*, vol. 93, pp. 349-367.

Lubatschowski, H., Heisterkamp, A., Will, F., Singh, A.I., Serbin, J., Ostendorf, A. et al., 2003, Medical applications for ultrafast laser pulses, *Proceedings of SPIE 2002*, 4633.

Ma, J., Sun, Y-S., and Li, B-W., 2013, Analysis of radiative transfer in a one-dimensional nonlinear anisotropic scattering medium with space-dependent scattering coefficient using spectral collocation method, *International Journal of Heat and Mass Transfer*, vol. 67, pp. 569-574.

Maltby, J.D., and Burns, P.J., 1991, Performance, accuracy, and convergence in a three-dimensional Monte Carlo radiative heat transfer simulation, *Numerical Heat Transfer B*, vol. 19, pp. 191-209.

Menguc, M.P., and Viskanta, R., 1986, Radiative transfer in axisymmetric finite cylindrical enclosures, *Journal of Heat Transfer*, vol. 108, pp. 271-276.

Mishchenko, M.I., Dlughach, J.M., Vanovitskij, E.G., and Zakharova, N.T., 1999, Bidirectional reflectance of flat, optically thick particulate layers: an efficient radiative transfer solution and applications to snow and soil surfaces, *Journal of Quantitative Spectroscopy and Radiative Transfer*, vol. 63, pp. 409-432.

Mishra, S.C., and Krishna, C.H., 2011, Analysis of radiative transport in a cylindrical enclosure – an application of the modified discrete ordinate method, *Journal of Quantitative Spectroscopy and Radiative Transfer*, vol. 112, pp. 1065-1081.

Mishra, S.C., Chugh, P., Kumar, P, and Mitra, K., 2006, Development and comparison of the DTM, the DOM and the FVM formulations for the short-pulse laser transport through a participating medium, *International Journal of Heat and Mass Transfer,* vol. 49, pp. 1820-1832.

Mishra, S.C., Roy, H.K., and Misra, N., 2006, Discrete ordinate method with a new and simple quadrature scheme, *Journal of Quantitative Spectroscopy and Radiative Transfer*, vol. 101, pp. 249-262

Mitra, K., and Kumar, S., 1999, Development and comparison of models for light-pulse transport through scattering-absorbing media, *Applied Optics*, vol. 40, pp. 3156-3163.

Modest, M.F., 2003, *Radiative Heat Transfer*, 2nd ed., pp. 263-284, 498-530, Academic Press, New York.

Murray, L.W., Su, L., White, G.E., and White, R.A., 1989, Cross linking of extracellular matrix proteins: A preliminary report on a possible mechanism of argon laser welding, *Lasers in Surgery and Medicine*, vol. 9, pp. 490-496.

Murthy J.Y., and Mathur S.R., 1998, Finite volume method for radiative heat transfer using unstructured meshes, *Journal of Thermophysics and Heat Transfer*, vol. 12, pp. 313-321.

Muthukumaran, R., and Mishra, S.C., 2008a, Transient response of a planar participating medium subjected to a train of short-pulse irradiation, *International Journal of Heat and Mass Transfer*, vol. 51, pp. 2418-2432.

Muthukumaran, R., and Mishra, S.C., 2008b, Thermal signatures of a localized inhomogeneity in a 2-D participating medium subjected to an ultra-fast step-pulse laser wave, *Journal of Quantitative Spectroscopy and Radiative Transfer*, vol. 109, pp. 705-726.

Niemz, M.H., Klancnik, E.G., and Bille, J.F., 1991, Plasma-mediated ablation of corneal tissue at 1053 nm using a Nd:YLF oscillator/regenerative amplifier laser, *Lasers in Surgery and Medicine*, vol. 11, pp. 426–431.

Quan, H., and Guo, Z., 2004, Fast 3-D optical imaging with transient fluorescence signals, *Optics Express,* vol. 12, pp. 449-457.

Rahmani, R.K., Ayasoufi, A., and Molavi, H., 2009, Numerical simulation of transient radiative heat transfer applying finite volume method on generalized computational grid, *Proceedings of ASME Early Career Technical Conference*, New York: ASME.

Raithby, G.D., 1999, Evaluation of discretization errors in finite-volume radiant heat transfer predictions, *Numerical Heat Transfer B*, vol. 36, pp. 241-264.

Raithby, G.D., and Chui, E.H., 1990, A finite-volume method for predicting a radiant heat transfer in enclosures with participating media, *Journal of Heat Transfer*, vol. 112, pp. 415-423.

Ridouane, E., and Campo, A., 2006, Numerical computation of the temperature evolution in the human eye, *Heat Transfer Research*, vol. 37, pp. 607-617.

Sadoghi, P., 2006, Discrete ordinates method for propagation of light in highly scattering vascular tissues, *Optics Communications*, vol. 266, pp. 359-363.

Sajjadi, A.Y., Mitra, K., and Guo, Z., 2013, Thermal analysis and experiments of laser–tissue interactions: A review, *Heat Transfer Research*, vol. 44, pp. 345-388.

Sakami, M., Mitra, K., and Hsu, P., 2002, Analysis of light-pulse transport through two-dimensional scattering-absorbing media, *Journal of Quantitative Spectroscopy and Radiative Transfer*, vol. 73, pp. 169-179.

Seo, T, Kaminski, D.A.., and Jensen, M.K., 2002, Combined convection and radiation in simultaneously developing flow and heat transfer with nongray gas mixtures, *Numerical Heat Transfer A*, vol. 26, pp. 49-66.

Serafetinides, A.A., Khabbaz, M.G., Makropoulou, M.I., and Kar, A.K., 1999, Picosecond laser ablation of dentine in endodontics, *Lasers in Medical Science,* vol. 14, pp. 168-174.

Shokri, M., and Beyler, C.L., 1989, Radiation from large pool fires, Journal of Fire Protection Engineering, vol. 1, pp. 141-149.

Siegel, R., and Howell, J., 2002, *Thermal Radiation Heat Transfer*, 4th ed., pp. 371-490, Taylor and Francis, New York.

Solovjov, V.P., and Webb, B.W., An efficient method for modeling radiative transfer in multicomponent gas mixtures with soot, Journal of Heat Transfer, vol. 123, 2001, pp. 450-457.

Strassl, M., Kasenbacher, A., and Wintner, E., 2002, Ultrashort laser pulses in dentistry, *Journal of Oral Laser Applications*, vol. 2, pp. 213-222.

Taine, J., and Soufiani, A., 1999, Gas IR radiative properties: from spectroscopic data to approximate models, *Advances in Heat Transfer*, vol. 33, pp. 295-414.

Thurgood, C.P., Pollard, A., and Becker, H.A., 1995, The T_N quadrature set for the discrete ordinates method, *Journal of Heat Transfer*, vol. 117, pp. 1068-1070.

Tien, C.L., and Lee, S.C., 1982, Flame radiation, *Progress in Energy and Combustion Science*, vol. 8, pp. 41-59.

Truelove, J.S., 1988, Three-dimensional radiation in absorbing-emitting-scattering media using the discrete ordinates approximation, *Journal of Quantitative Spectroscopy and Radiative Transfer*, vol. 39, pp. 27-31.

Tuncer, O., Acharya, S., and Uhm, J.H., 2009, NOx and flashback characteristics of confined premixed hydrogen-enriched methane flames, *International Journal of Hydrogen Energy*, vol. 34, pp. 496-506.

Turner, J.A., 1999, A realizable renewable energy future, *Science* 30, vol. 285, no. 5428, pp. 687-689.

Tzen, E., and Morris, R., 2003, Renewable energy sources for desalination, *Solar Energy*, vol. 75, pp. 375-379.

Van Leer, B., 1979, Towards the ultimate conservation difference scheme. V. A second-order sequel to Godunov's method, *Journal of Computational Physics*, vol. 32, pp. 101-136.

Vandenberghe, L., 2011, The QR Factorization, Class Lecture – Applied Numerical Computing EE103, UCLA, http://www.ee.ucla.edu/~vandenbe/103/lectures/qr.pdf (accessed March 2011)

Villringer, A., and Chance, B., 1997, Non-invasive optical spectroscopy and imaging of human brain function, *Trends in Neurosciences*, vol. 20, pp. 435-42.

Walters, D.V., and Buckius, R.O., 1992, Monte Carlo methods for radiative heat transfer in scattering media, in *Annual Review of Heat Transfer*, vol. 5, Hemisphere, New York, pp. 131-176.

Wang, F., Shuai, Y., Yuan, Y., Yang, G., and Tan, H., 2010, Thermal stress analysis of eccentric tube receiver using concentrated solar radiation, *Solar Energy*, vol. 84, pp. 1809-1815.

Wang, L., Ho, P.P., Liu, C., Zhang, G., and Alfano, R.R., 1991, Ballistic 2-D imaging through scattering walls using an ultrafast optical kerr gate, *Science*, vol. 253, pp. 769-771.

Wang, X., and Guo, Z., 2010, Effective removal of adhering cells via ultrashort laser pulses, *Optics and Laser Technology*, vol. 42, pp. 447-451.

Wiscombe, W.J., 1976, On initialization, error and flux conservation in the doubling method, *Journal of Quantitative Spectroscopy and Radiative Transfer*, vol. 16, pp. 637-658.

Wu, H.L., and Fricker, N., 1971, An investigation of the behaviour of swirling jet flames in a narrow cylindrical furnace, *2nd Members Conference of the International Flame Research Foundation*, Ijmuiden, The Netherlands.

Yamada, Y., 1995, Light-tissue interaction and optical imaging in biomedicine, *Annual Review on Heat Transfer*, vol. 6, pp. 1-59.

Yang, W.J., Taniguchi, H., and Kudo, K., 1995, Radiative heat transfer by the Monte Carlo method, *Advances in Heat Transfer*, vol. 27, pp. 1-215.

Yodh, A., and Chance, B., 1995, Spectroscopy and imaging with diffuse light, *Physics Today*, pp. 34-40.

Yoo, K.M., and Alfano, R.R., 1993, Ultrafast time-gated imaging in thick tissues: a step toward optical mammography, *Optical Letters,* vol. 18, pp. 1092-1094.